RUHR-UNIVERSITÄT BOCHUM

RUB

SFB 837
Interaction Modeling in Mechanized Tunneling

Efficient Simulation of Crack Propagation at Finite Strains through Brittle and Ductile Microstructures given by Voxel Data

Dennis Wingender

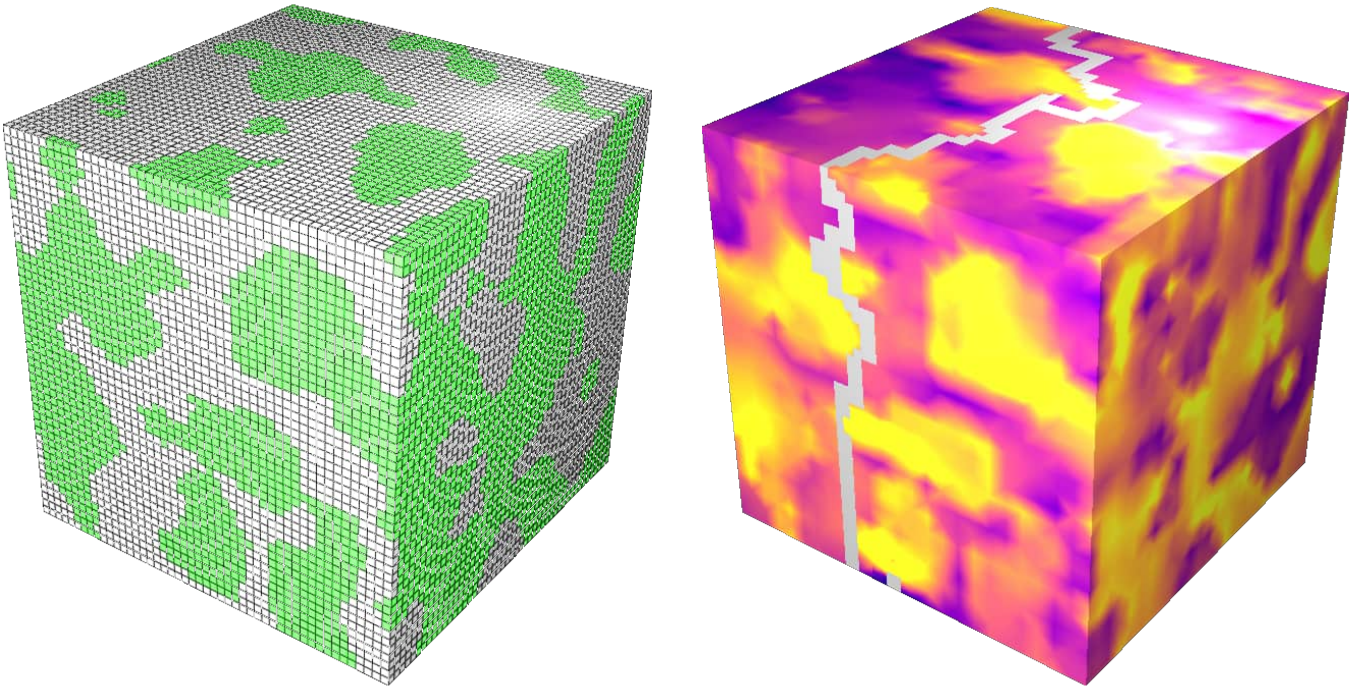

Efficient Simulation of Crack Propagation at Finite Strains through Brittle and Ductile Microstructures given by Voxel Data

Dissertation
zur
Erlangung des Grades
Doktor-Ingenieur

der
Fakultät für Maschinenbau
der Ruhr-Universität Bochum

von
Dennis Wingender
aus Essen

Bochum 2022

Mitteilungen aus dem Institut für Mechanik
Nr. 190

Publisher:

Institute for Mechanics
Ruhr-University Bochum
D-44780 Bochum

Prof. Dr.-Ing. habil. Daniel Balzani
Chair for Continuum Mechanics

Herausgeber:

Institut für Mechanik
Ruhr-Universität Bochum
D-44780 Bochum

Prof. Dr.-Ing. habil. Daniel Balzani
Lehrstuhl für Kontinuumsmechanik

ISBN: 978-3-935892-68-1

Copyright © 2023 by Dennis Wingender

All rights reserved.
No parts of this work may be reproduced or used in any matter without written permission of the copyright holder.

Dieses Werk ist urheberrechtlich geschützt.
Alle Rechte, einschließlich der Vervielfältigung, Veröffentlichung, Bearbeitung und Übersetzung, bleiben vorbehalten.

Dissertation eingereicht am (Thesis submission):	18.10.2022
Mündliche Prüfung am (Thesis Defense):	23.01.2023
Erstgutachter (First referee):	Prof. Dr.-Ing. Daniel Balzani
Zweitgutachter (Second referee):	Prof. Dr. rer. nat. Klaus Hackl
Prüfungsvorsitz (Committee chair):	Prof. Dr.-Ing. Sebastian Weber

Preface

Since May 2016, I have worked as a research assistant at the Chair of Continuum Mechanics at the Ruhr-University Bochum where I generated the content of this work. My first topic dealt with the artificial construction and homogenization of asphalt concrete microstructures. This work was supervised by Professor Ralf Jänicke, the former head of the chair. When he followed his professorship to the Chalmers University of Technology in Gothenburg, I stayed in Bochum. Under the supervision of Professor Daniel Balzani, who was the new head of the chair, I got the opportunity to be part of the Sonderforschungsbereich 837 "Interaction Modeling in Mechanized Tunneling" since 2019 in which I worked on the topic that is primarily presented in this thesis. I would like to express my deepest gratitude to all the amazing people who supported me with their technical knowledge and wisdom and thus, had a huge impact on this work.

First of all, I would like to thank Professor Daniel Balzani for giving me the opportunity to research on a very interesting topic. This work would not have been possible without his excellent guidance, wisdom, and inspiration. I am grateful for the time I could work under his supervision and for the freedom he gave me to develop my research in certain directions. Especially, I am thankful that he always had an open ear to elaborate solutions to research problems in hour-long discussions whenever it was needed.

Secondly, I would like to thank Professor Ralf Jänicke for introducing me into the world of professional research in mechanics. His knowledge and encouragement were a huge help to start my career in science. I also like to thank Professor Klaus Hackl, not only for evaluating my thesis, but for the chance to learn from him in his classes since my first semester throughout my bachelor's and master's degrees. Additionally, I am grateful for the cooperation with Professor Arne Röttger and Lukas Brackmann, who supplied data from laboratory experiments. Their expertise in material science helped to gain knowledge about the physics behind the complex field of crack propagation through metallic microstructures. Furthermore, I would like to thank Professor Philip Junker for his support on material modeling questions and his motivational spirit before Daniel Balzani started as new head of the Chair for Continuum Mechanics.

During the last years, I encountered many amazing colleagues who supported me a lot and made my time in my office interesting and entertaining. Because the list of these is too long to mention them all, I would like to empathize a few of those, At first, I would like to thank my former office roommate Malte Sauerwein for the amazing time we had in the office and the many fruitful discussions. I greatly enjoyed the many occasions when we played office table tennis or watched soccer in the VFL stadium. Furthermore, the expertise and advice of Dennis Ogiermann concerning mathematics and programming questions were a huge help when I was struggling with software or hardware issues. As my second office roommate, he made the time in the office fun, creative and interesting. I also thank Hendrik Dorn (Dennis 1) for the great work and the deep theoretical discussions about mechanics as well as the rest of the world.

Lastly, my special thanks go to my parents, my brother and my sister in law for their continuous and unconditional support throughout the phases of my PhD. as well as the rest of my life.

Zusammenfassung

Die Effizienz des mechanisierten Tunnelvortriebs wird stark von dem Verschleiß der Abbauwerkzeuge beeinflusst, da die verschlissenen Teile ersetzt werden. Für den Abbau weicher Böden werden Schälmesser eingesetzt, die aus einem metallischen Körper bestehen, auf dem Bewehrungen aus einem Metallmatrixkompositen aufgebracht sind. Mikroskopisch bestehen Metallmatrixkomposite aus harten Carbiden, die in einer duktilen Metallmatrix eingebettet sind. Aufgrund der Penetration der Bewehrungen durch die Gesteinspartikel im Boden tritt Verschleiß in Form von Abrasion und Oberflächenzerrütung auf. Die Oberflächenzerrüttung besteht primär aus unterkritischer Rissausbreitung auf der Mikroskale unter zyklischer Belastung. Daher ist Ziel dieser Arbeit, eine rechentechnisch effiziente Methode zur Simulation von Rissausbreitung auf der Mikroskale zu entwickeln, um diese Verschleißart zu untersuchen und die Mikrostruktur ihr gegenüber zu verbessern. Dazu wird die bestehende Eigenerosionsmethode, die sich vorher nur für die Simulation von Rissausbreitung spröder Materialien geeignet hat, auf Rissausbreitung durch metallische Materialien erweitert. Da die Morphologie des Werkstoffs als Voxeldaten gegeben ist, die aus einem μCT-Scan resultieren, wird zusätzlich die Finite Zellmethode angewandt, die für diese Art Daten besonders geeignet ist. Anhand eines Beispielmaterials, hier Ferro-Titanit, das als Material für die Bewehrungen auf den Abbauwerkzeugen verwendet wird, wird die Plausibilität des entwickelten Frameworks im Vergleich zu Experimenten gezeigt. Um die Komplexität einer realen Mirkostruktur zur Verringerung des Rechenaufwands zu reduzieren, werden zusätzlich kleinere repräsentative Volumenelemente konstruiert und deren Aussagekraft über die Rissausbreitung anhand von Simulationen gezeigt. In weiteren Simulationen an künstlichen, vereinfachten Mikrostrukturen eines Kaltarbeitstahls mit verschiedenen Morphologien, die aus verschiedenen Herstellungsarten resultieren, wird demonstriert, dass sich der entwickelte Framework dazu eignet, die Morphologie mit dem größten Widerstand gegen Rissausbreitung und somit die Mikrostruktur mit dem größten Verschleißwiderstand zu identifizieren. Dadurch ist gezeigt, dass die entwickelte Simulationsmethode ihren Zweck erfüllt.

Abstract

The efficiency of mechanized tunneling is strongly influenced by the wear acting on the mining tools, because the worn parts have to be replaced. For the excavation of soft soils, chisels are used, which consist of a metallic body armored with layers made of metal matrix composites. Microscopically, metal matrix composites consist of hard carbides embedded in a ductile metal matrix. Due to the penetration of the chisel layers by particles of the soil, wear occurs in the form of abrasion and surface spalling. Surface spalling is primarily governed by subcritical crack propagation at the microscale under cyclic loading. Therefore, the objective of this work is to develop a computationally efficient method to simulate crack propagation on the microscale in order to study this wear mechanism and to improve the microstructure regarding surface spalling. To this end, the existing eigenerosion method, which has previously been suitable only for simulating crack propagation through brittle materials, is extended to crack propagation through metallic materials. Since the morphology of the material is given as voxel data resulting from a μCT scan, the Finite Cell Method, which is particularly suitable for this type of data, is also applied. On the basis of an example material, in this case Ferro-Titanit used as metal matrix composite layers of the mining tools, the plausibility of the developed framework is shown in comparison to laboratory experiments. In order to reduce the complexity of a real microstructure to decrease the computational effort, smaller representative volume elements are constructed and their predictive power of crack propagation is shown by simulations. In further simulations on artificial, simplified microstructures of a cold work steel with different morphologies resulting from different manufacturing methods, it is demonstrated that the developed framework is suitable to identify the morphology with the highest resistance to crack propagation and thus, the microstructure with the highest wear resistance. Hence, it is shown that the developed simulation method serves its purpose.

Contents

1. Introduction 1

1.1. Wear on the mining tools of tunnel boring machines 1
  1.1.1. Mining tools in the tunnel drilling process 1
  1.1.2. Basic wear mechanisms 3
  1.1.3. Surface spalling and subcritical crack propagation in metallic microstructures 4
  1.1.4. Ductile crack propagation and fatigue 5
1.2. Aims of this work 6
1.3. State of the art 7
1.4. Outline 9

2. Simulation of mechanical problems 11

2.1. Continuum mechanics 11
  2.1.1. Kinematic and deformation measures 11
  2.1.2. Mechanical stresses and internal power 14
  2.1.3. Equilibrium equations 15
2.2. Finite Element framework 17
  2.2.1. Variational formulation 17
  2.2.2. Discretization of the continuous body 18
  2.2.3. Approximation of the displacements in the discretized body 19
  2.2.4. Time discretization 22
  2.2.5. Solving procedure 23
2.3. Constitutive laws 24
  2.3.1. Neo-Hookean hyperelasticity 25
  2.3.2. Finite strain J_2-elasto-plasticity 25
  2.3.3. Extension to rate-dependent elasto-viscoplastic material behavior for regularization 30
  2.3.4. Tension-compression split 32
  2.3.5. Crack criteria 33

3. Eigenerosion approach 37

3.1. Regularization of the crack propagation problem 37
3.2. Application on spatial discretizations 40
3.3. Staggered algorithm 43
3.4. Technical remarks 44

4. Mesh convergence of the eigenerosion approach 47

4.1. Brittle fracture 47
  4.1.1. Plate with initial crack 47
  4.1.2. Plate without initial crack 48
  4.1.3. Influence radius, critical Griffith-type constant and specimen size . . . 48
  4.1.4. Energetic relations 50
4.2. Ductile crack propagation 51
  4.2.1. Elasto-plastic specimen 52

4.2.2. Ductile crack propagation with regularization . . . 55
4.2.3. Influence of regularization intensity . . . 56
4.2.4. Simulation with cyclic loading . . . 57

5. Eigenerosion for heterogeneous structures 63
5.1. The standard FCM . . . 63
5.1.1. Basic concept . . . 63
5.1.2. Volume integration . . . 65
5.2. Hanging node constraints . . . 67
5.3. Adaptive mesh refinement . . . 70
5.3.1. Mechanical equilibrium . . . 71
5.3.2. Element and subcell erosion . . . 73
5.3.3. Technical remarks . . . 74
5.4. Discretization of the voxel data . . . 75
5.4.1. Generation of voxel data from μCT-scan . . . 76
5.4.2. Properties of discretizations . . . 78
5.4.3. Voxel decomposition techniques . . . 80
5.4.4. Discretization of voxel data for the proposed approach . . . 84
5.4.5. Proof of concept with artificial microstructure . . . 86

6. Construction of artificial representative volume elements 95
6.1. SSRVE construction . . . 96
6.1.1. Basic approach . . . 96
6.1.2. Statistical descriptors . . . 97
6.1.3. Applications of the objective functions . . . 100
6.1.4. Parameterizations of the inclusions . . . 101
6.1.5. Application on Ferro-Titanit . . . 102
6.2. Statistical volume elements . . . 107
6.2.1. Properties of asphalt concrete . . . 107
6.2.2. Computational generation of SVEs . . . 108
6.2.3. Numerical examples of SVEs . . . 114
6.2.4. Generalized Maxwell model . . . 116
6.2.5. Mechanical test on SVEs . . . 118
6.3. Comparison of SSRVE for MMCs with SVEs for asphalt concrete . . . 119

7. Calibrated simulations of crack propagation on microstructures 121
7.1. Parameter identification . . . 121
7.2. Validation with three-point bending test . . . 122
7.2.1. Macroscopic experiment . . . 122
7.2.2. Extraction of boundary conditions of the microscale simulations . . . 124
7.2.3. Validation of the numerical and material parameters with homogeneous microstructure . . . 125
7.3. Crack propagation through Ferro-Titanit . . . 126
7.3.1. Voxel data from scan . . . 126
7.3.2. SSRVE . . . 129
7.4. Influence of microstructure morphology of cold work tool steel . . . 131
7.4.1. Linearly increasing load . . . 132
7.4.2. Cyclic load . . . 137

8. Conclusion and outlook 139

A. Voigt notation 143

B. SSRVE data **144**

List of Tables **147**

List of Figures **155**

1. Introduction

1.1. Wear on the mining tools of tunnel boring machines

1.1.1. Mining tools in the tunnel drilling process

Tunneling enables many possibilities in subsurface constructions for multiple applications because it generates additional space. In particular in cities, tunneling gains importance because it expands the limited space on the surface by underground constructions. As the major application, tunnels are used in traffic, e.g., for railways and streets through cities and mountains so that tunneling increases the mobility. Hence, tunneling is an up-to-date topic. For instance, figure 1.1a underlines this fact by showing the increase in the number of tunnels and tunnel length in Germany. From 1996 to 2017, within 21 years, the number of tunnels as well as the tunnel length have more than doubled. For the excavation, three different methods are applied: the Cut-and-Cover method, the New Austrian Method (NATM) and the Mechanized Tunneling. As shown in figure 1.1b, all three methods were widely used in the period from 1999 to 2019. In 11 of these 20 years, the major part of driven tunnel length is excavated by mechanized tunneling because of its advantages. It allows prefabrication of tunnel lining segments, consumes a low amount of time and money compared to the other methods and the excavation process is automatized. Because of these advantages, this work focuses on the mechanized tunneling as a subproject of the Sonderforschungsbereich (SFB) 837 "Interaction Modeling in Mechanized Tunneling" funded by the Deutsche Forschungsgemeinschaft (DFG). During the mechanized tunneling, the cylindrical tunnel boring machine (TBM), cf. figure 1.2a&b, drives forward into its axial direction while its cutting wheel in the front rotates and excavates the soil with its applied mining tools. For excavating hard soils, e.g., rocks, cutting disks are used whereas chisels are applied for middle-hard and soft soils, e.g., clay. Conveyor belts transport the soil out of the tunnel. When the TBM has proceeded a certain

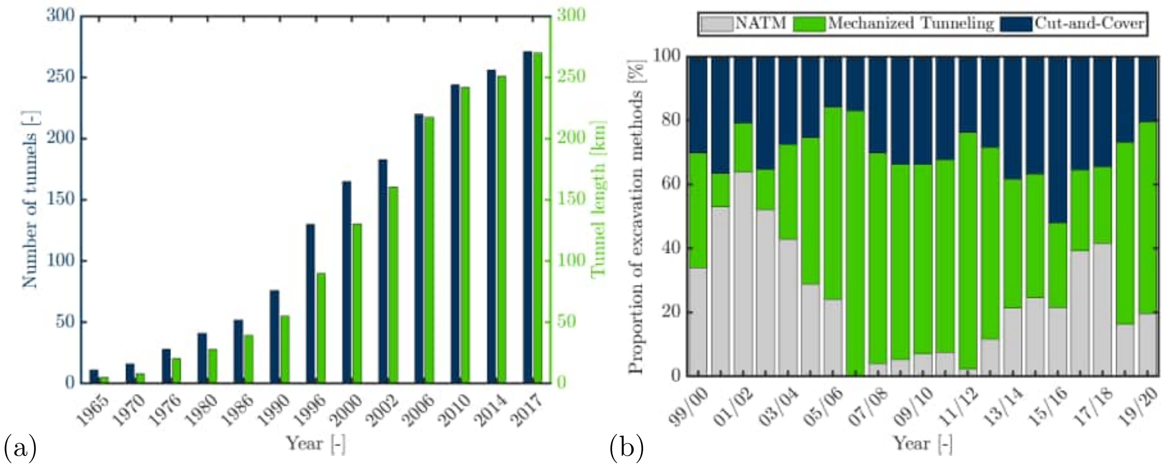

Figure 1.1.: (a) Overall number of tunnels and tunnel length in Germany from 1965 until 2017 [43], and (b) proportion of three excavation methods, namely NATM, Mechanized Tunneling and Cut-and-Cover method, for tunneling for underground, urban and rapid transit systems in Germany from 1999 until 2020 related to driven length [120].

distance, it yields until the prefabricated tunnel lining segments are installed at the newly generated tunnel surface. Afterwards, the TBM advances again and the process is repeated until the whole tunnel is drilled. General information about the engineering in tunneling can be found in standard books, e.g., Maidl et al. [81, 82].

If the mining tools that are applied on the cutting wheel fail due to wear occurring during excavation, they have to be exchanged which leads to an increased cost and time consumption. This motivates the necessity for an investigation of the wear mechanisms on the mining tools. This work focuses on the chisels and their wear. Frenzel et al. [38] state that chisels require a high material strength in order to withstand high mechanical stresses due to contact with the soil during the excavation process in order to quarry soil without being deformed plastically. In contrast to that, a high fracture toughness is necessary to ensure that brittle fracture, either spontaneously or due to fatigue, and wear in the form of surface spalling are avoided. Additionally, wear in the form of abrasion has to be prevented at the surfaces in contact with the soil. Therefore, a high hardness of the mining tool's surface is required. The hardness counteracts with the fracture toughness, because hard materials tend to have a low fracture toughness and vice versa. Further information on the maintenance of cutting tools in mechanized tunneling can be found in Conrads [23]. To fulfill the requirements for the mining tools, their main body consists of low-cost steels, e.g., construction steels or quenched and tempered steels, because of their high toughness and strength. At the surfaces that touch the soil, metal matrix composites (MMC) are applied because of their additional hardness, to prevent abrasion. MMC is a material class whose materials are metallic mixtures. The inclusions of the MMC consist of brittle and stiff carbides which are compounds of metal and carbon atoms. The carbide inclusions ensure a high hardness that is necessary to resist scratching and are of the size of a few $\mu\mathrm{m}^3$. They are surrounded by a ductile metal matrix, which provides the high fracture toughness and material strength. However, during the excavation, the material may still fail because of boulders and geological inhomogeneities that lead to an impact due to which the material strength is exceeded locally. The morphology of the inclusions on the microscopic level as well as their volume fraction within the whole structure depend on the specific material, that is chosen for the technical application. Because the length scale of the components is of a few micrometers, the morphology of the material's microstructure only becomes visible on the so-called "microscale". In contrast to that, length scale of the mining tool is given in centimeters and meters, on the so-called "macroscale" so that the microstructure morphology is not visible. The material on the macroscale has the homogenized material properties of the microstructure on the microscale so that the properties of the macroscopic material can be modified by adjusting the properties of the material's microstructure. Hence, the mining tool's resistance against surface spalling depends on the microstructure of the MMC.

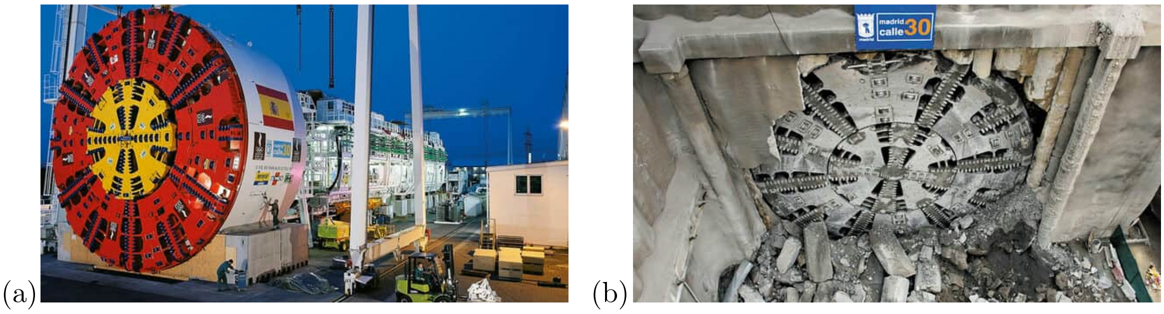

Figure 1.2.: (a) Tunnel boring machine (TBM) in Madrid and (b) front view on its cutter head at the tunnel breakthrough by the company AG [2]

1.1.2. Basic wear mechanisms

Wear is defined as the loss of material at the surface of a solid body that results from mechanical loads induced by contact and relative movement of a solid, liquid or gaseous counter body as, e.g., explained in Czichos and Habig [24]. It appears in the form of wear particles that break out of the material. Together with friction, wear belongs to the scientific and engineering field of tribology, which deals with the investigation of interacting surfaces in relative motion to each other, including lubrication. Hence, friction and wear have to be viewed as system properties and not as material properties. In the excavation process, the wear is divided into primary and secondary wear. The wear of the cutting tools, that are in contact with the soil, is considered as the primary wear. In contrast to that, wear that occurs on other parts of the cutter head are considered as secondary wear. This work focuses on the primary wear. Its tribological system is shown in figure 1.3a. It consists of the chisel tool which scratches the tunnel face, which serves as counter body, in a rotational move while the TBM advances towards the tunnel face. No lubricant is applied. In general, the primary wear is divided into four categories contributing separately or in combination:

- **Adhesion**: Here, the contact surfaces undergo adhesive connections, which are sheared off during relative motion. The material division occurs at the interface or near the adhesive zone, so that material transfer from one side to the other is possible. This type of wear primarily takes place between metallic materials due to their adhesive affinities. However, in terms of the mining tools, this effect occurs between the cutting tools and fine-grained soils due to missing lubricants. According to Köhler et al. [64], varying pressure conditions lead to changing soil pore pressure which may become negative when the water is pressed out. This induces a vacuum at the material interfaces which leads to the suction of the soil on the mining tool's surface and thus, to adhesion.

- **Abrasion**: This wear mechanism takes place in tribological systems, in which a harder body scratches the surface of a softer one. Thereby, plastic deformations in the softer material increases with every load cycle until material loss occurs at the surface. In terms of the mechanized tunneling, hard particles within the soil scratch and groove the cutting tools' surfaces so that parts of it are removed during the excavation process, cf. Röttger et al. [117]. This mechanism appears in the form of microploughing, microcracking, microfatigue and microcutting. Furthermore, it is mostly considered as the main the form of wear on the mining tools. Its influence on the shape of the chisels is shown in figure 1.3b. The mining tool's body in this figure is scraped off at multiple areas. This wear mechanism has recently been investigated experimentally in Küpferle et al. [67, 69] and numerically in Hoormazdi et al. [54].

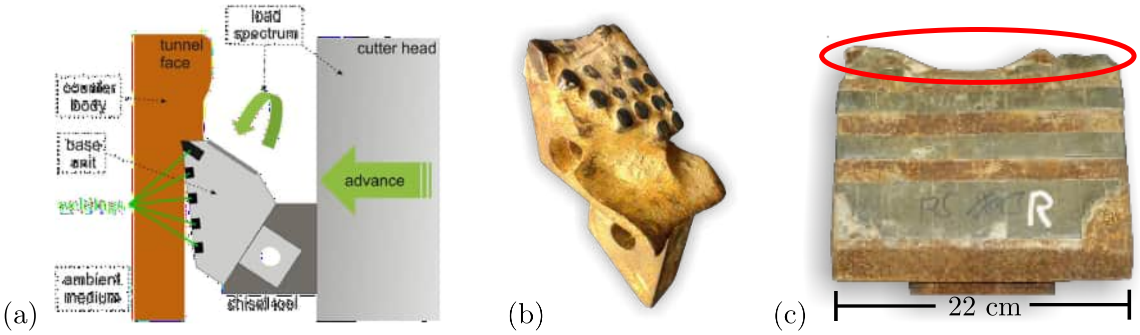

Figure 1.3.: (a) Schematic structure of the tribological system of the TBM mining tool, (b) chisel subject to abrasive wear and (c) top-view on chisel subject to surface spalling, taken from Küpferle et al. [69]

- **Surface spalling/ surface degradation**: This type of wear occurs under changing mechanical loads at the surface and is caused by crack propagation and fatigue. These to effects lead to damage and loss in the stiffness of the tool. With increasing load cycles, micro-cracks and plastic deformations on the microscale increase. If multiple cracks unite, parts of the surface breaks out. In figure 1.3c, the parts of the chisel's surface broke away due to the surface spalling. This is the wear mechanism, which this work focuses on, and is described in detail in the subsection 1.1.3.

- **Tribochemical reaction**: As the name states, a chemical reaction may occur between the lubricant/environment and the surface as for example shown in Hsu et al. [56]. These reactions are divided into two types. The first one only occurs under contact conditions and is usually governed by reactions directly at the surface. The second type of reactions takes place independently under the pressures and temperatures induced by the process. Both types of reactions influence each other. At the mining tools on the TBM, this effect occurs in the form of corrosion whose influence on the life time of the cutting tool is small compared to the other wear mechanisms. Therefore, it may be neglected as a wear mechanism by itself, but affects the abrasion, as stated in Espallargas et al. [35].

In the tunnel drilling process, the wear on the mining tools is mainly governed by abrasion and surface spalling. Their effect on the chisels' shape is shown in figure 1.3b&c. This work focuses on the numerical investigation of surface spalling while Hoormazdi et al. [54] investigates the abrasion.

1.1.3. Surface spalling and subcritical crack propagation in metallic microstructures

Due to the surface spalling, parts of the mining tools' surfaces break out under cyclic loading until the tool fails. This is effect on the material has been investigated experimentally in Küpferle et al. [68] for cemented carbides, a special type of MMCs. Herein, the plastic deformations appearing on the microscopic level increase over time due to cyclic load. One load cycle consists of one loading and one unloading step. The change in the plastic deformations lead to a change of the mechanical fields which results in crack initiation. Gurson [48], Chu and Needleman [22] investigated crack initiation and divided it into three steps. Firstly, the voids nucleate and secondly, they grow due to the cyclic load. Thirdly, the voids connect in such a way that they form microcracks. These cracks propagate through the material. As schematically shown in figure 1.4a, the crack propagation firstly behaves subcritically, which means that material inhomogeneities and plastic deformations prevent the crack fro immediately propagating through the whole structure by capturing some of the locally increased energy due to the crack. This leads to a rest of the crack. Hence, the crack propagates with increasing cycle number until it becomes critical, meaning that the crack propagates until the material boundaries are reached so that the structure fails. Thus, the microstructure morphology and material properties strongly determine the subcritical crack propagation as experimentally shown in Brackmann et al. [15], and therefore, the resistance against surface spalling. For example, the speed of the subcritical crack propagation and the crack path vary with the microstructure. It may primarily develop straight, through one of the constituents, along the material interfaces or around certain a material phase depending on the properties of the phases. Two microscopic images of the crack path through metallic microstructures are shown in figure 1.4b. Additionally, other effects in the form of stress-induced phase transitions or interface layers may occur within the material and influence the crack behavior. In order to find an improvement of the material regarding surface spalling, different microstructure morphologies as well as different materials for the constituents have to be tested. Hereby,

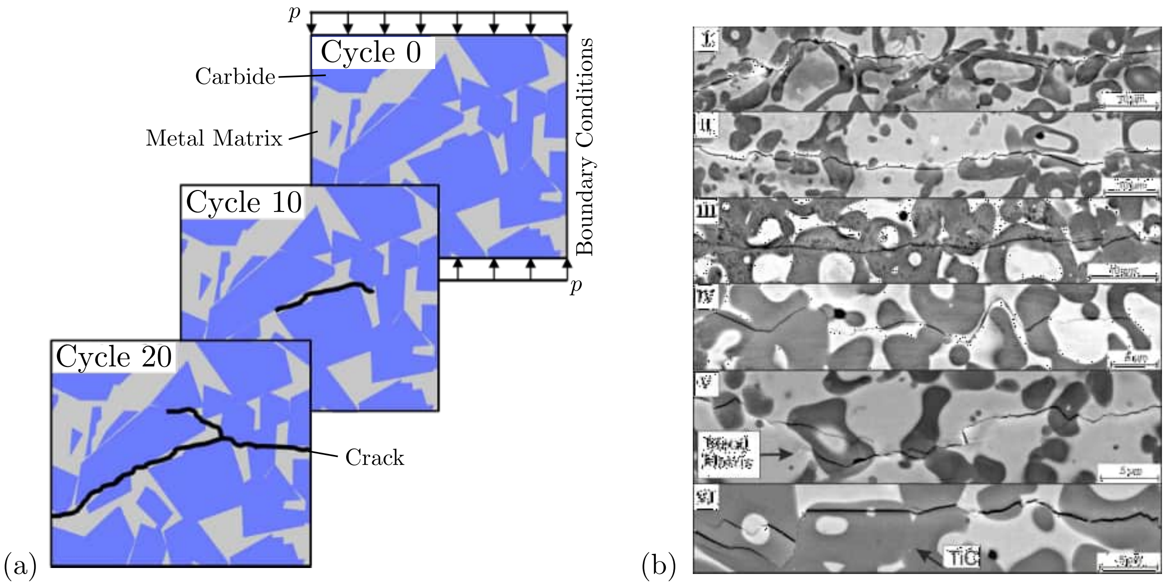

Figure 1.4.: (a) Schematic illustration of subcritical crack propagation under cyclic loading and (b) scanning electron micrograph of MMC Ferro-Titanit microstructure consisting of titanium carbides (TiC) within metal matrix including crack, taken from Küpferle [66]

physical restrictions of the choice of materials and the morphologies apply, because, e.g., different inclusion materials and different ways of production of the material lead to different inclusion shapes. For example, tungsten carbide inclusions appear as spheres, whereas titanium carbide inclusions form shells. In this work, the microstructures of different classes of metallic mixtures are investigated. Here, hard metals, MMCs and cold work tools steels are investigated. They all consist of brittle carbide inclusions surrounded by a ductile matrix. The carbide inclusions are extremely stiff and brittle. They provide the hardness to the overall material which is necessary to avoid the material loss of the mining tool due to the hard particles in the soil. Because the carbides are brittle and have a low resistance against crack propagation, they are surrounded by a ductile matrix which increases the overall fracture toughness. In some materials, interface layers which influence the material properties as well may occur additionally. The overall material properties strongly depend on the choice of the volume fraction of the phases, of the constituent materials, of the interface properties and of the microstructure morphology. The morphology is determined by the microscopic materials and the way they are manufactured. The investigation of these effects by examining complex mechanical experiments and visualizing the crack path on the microscopic level, e.g., via μCT scans, consumes a high amount of money, machine capacities and personnel resources. Furthermore, the modification of the microscopic morphology is limited to manufacturing processes which prohibits the optimization of the morphology regarding wear. Additionally, numerical simulations enable the visualization of the mechanical fields which helps to gain knowledge of the governing processes. Hence, a numerical setup for simulating the crack propagation on the microscale becomes promising due to its low costs and flexibility.

1.1.4. Ductile crack propagation and fatigue

Brittle crack propagation has firstly been investigated by Griffith [46] in 1921. He discovered that in a crack propagates by an area increment in an elastic material if the elastic energy surpasses a certain energy level. This criterion is known as the Griffith criterion, in which the constant energy level per crack area increment is known as the Griffith energy release rate. This constant is equal to the surface energy that is needed to produce a certain surface. In this approach, it is assumed that this process works irreversible and that the crack surfaces

are stress-free. Later, Irwin [57] investigated metals with ductile material behavior and found out that plasticity plays an important role for the crack propagation. For example, necking of tensile specimen occurs before cracking, as seen in Onat and Prager [104]. Additionally, the crack path changes. Furthermore, Irwin extended the original Griffith criterion for brittle materials to ductile materials by additionally considering the energy that dissipates into plastic deformation near the crack tip before the crack propagates.
A special form of crack propagation is the so-called fatigue. It describes the damage of a structure due to cyclic loading, which firstly was investigated by Wöhler [157]. Motivated by the investigation of train axles that broke in an incident in the 19th century, as seen in [145], he discovered that structures might fail under cyclic loading even though the load amplitude is lower than the maximum static load. The original Wöhler experiment consists of a beam which is loaded with a weight on one side rotated axially until it breaks. Here, the load oscillates sinusoidal, whereas in physical applications other minimum and maximum loads may occur. To classify those, e.g., into asymmetric tension-compression, repeated tension or alternating tension, the technically important ratio of the minimum load divided by the maximum load is taken into account. With the result from the cyclic experiments, the so-called Wöhler curves, as seen in Orowan [105], are produced which capture the number of cycles till failure dependent on the load amplitude. With these, lifetime predictions of structures under certain loadings can be made. The importance of Wöhler curves is underlined by the fact that they are part of DIN norms, e.g., DIN-50100 [28]. For metallic materials, fatigue is divided into low-cycle fatigue (LCF) and high-cycle fatigue (HCF). The number of load cycles in the LCF regime usually lies between 10^2 and 10^4. Here, the load is chosen with such an amplitude that the structure endures at least one cycle but macroscopic plastic deformations occur. Due to those, the plastic deformation changes increases with every load cycle so that plastic hysteresis becomes visible. This leads to crack initiation, propagation and finally failure of the material. In opposite to that, HCF occurs under loads that are low enough not to cause any macroscopic plastic deformation and damage so that the structure behaves purely elastically. Here, the fatigue is governed by effects on the microscale. On this scale, plastic deformations and microcracking occurs until the microcracks form cracks large enough to cause cracks on the macroscopic level and finally failure of the macroscopic structure. Hence, the wear mechanism surface spalling is regarded as one form of HCF. The number of cycles in the HFC regime often lies above 10^4. Because a clear limit between the governing effects is not observable, the LCF and HCF regime are not clearly separable. For further information about fatigue, standard books like Bathias and Pineau [12].

1.2. Aims of this work

The main goal of the work is the development of a novel numerical simulation framework for the investigation of surface spalling on the mining tools of TBMs and the improvement of their microstructure morphology against wear. This requires the simulation of crack propagation on the microscale of metallic structures. Therefore, computational methods capable of handling geometrical nonlinearities, finite strain elasto-plasticity and crack propagation along arbitrary crack paths through complex three-dimensional structures based on voxel data are mandatory. Additionally, computational efficiency is desired. The simulation of crack propagation remains a challenging task in engineering science. The reason for that is that the continuum mechanics requires continuity in the mechanical fields. However, cracks lead to discontinuities in the form of jumps in the displacement and stress fields, which leads to numerical problems in simulations, due to their requirement of continuity. Especially, in the numerical investigation of ductile crack propagation, most approaches suffer from numerical instabilities, mesh-dependency and/or inefficiency.

In this work, the **Finite Element Method** (FEM), cf., e.g., Bathe [10], Zienkiewicz et al. [165], is chosen as a basis for simulation of solid mechanics problems. As an extension of the FEM, the so-called **eigenerosion**, that implies element erosion, as introduced in Pandolfi and Ortiz [106] based on the variational formulation in Schmidt et al. [127], supplies independence of the spatial discretization. Therein, the Griffith criterion is applied based on a regularized crack evaluated by a length scale parameter ϵ, which leads to Γ convergence of the regularized energy dissipation functional to the unregularized one as ϵ goes to zero, as shown in Schmidt et al. [127]. Resulting from this, the crack path, crack propagation and thus, the overall structural converge with finer discretization. In the sense of FE discretizations, the eroded elements are able to undergo eigendeformations for which no further energy has to be imposed. The original implementation in Pandolfi and Ortiz [106] only considers small strains and brittle material behavior. Because the investigated metallic materials underly ductile material behavior, the eigenerosion framework is extended to ductile crack propagation in this work. Therefore, the fracture criterion and the material models are modified. Additionally, inertia effects are considered by application of the Newmark scheme, cf. Newmark [101]. The discretization of the microstructures based on voxel data from μCT-scans is complicated and costly. Additionally, a huge amount of elements occur which leads to high computational costs. To circumvent these problems, an enhancement of the FEM, the so-called **Finite Cell Method** (FCM), as introduced in Parvizian et al. [109], is additionally considered. In combination with the eigenerosion, this framework is additionally extended by refining the discretization near the crack tip. For this new approach, a suitable decomposition of voxel data is applied.

In order to obtain results from microscale simulations that are comparable to results from laboratory experiments, the parameters are calibrated by simulating macroscopic experiments under cyclic loads in line with experiments. With these parameters, simulations on the microscale based on cutouts of the voxel data obtained from μCT-scans are carried out and the resulting crack paths, compared to results from laboratory experiments by application of the proposed algorithm. Because simulations on the full microstructure are computationally demanding due to its high complexity, smaller, less complex microstructures are constructed. This are called **Representative Volume Elements** (RVE). Here, the concept of **Statistically similar representative volume elements** (SSRVE), cf. Scheunemann et al. [125] is applied on the voxel data. Simulations of crack propagation are carried out on the constructed SSRVEs. Additionally, the crack propagation through different microstructure morphologies of the same macroscopic material, that are chosen in line with real morphologies that develop due to different manufacturing processes, are calculated.

1.3. State of the art

The phenomenon of wear was firstly investigated in Wöhler [157] and still is an up-to-date topic in mechanical engineering. The latest results from laboratory experiments on materials underlying wear in the tunnel drilling process can be seen in, e.g., Brackmann et al. [15], Küpferle et al. [69, 67, 68], Röttger et al. [117]. Numerical simulations for the investigation of the other governing form of wear occurring on the surface of mining tools, abrasion, are presented in, e.g., Hoormazdi [53], Hoormazdi et al. [55], and summarized in Butt et al. [19]. Conceptually, the numerical simulation of surface spalling requires a simulation framework which is capable of handling cracks along a priori unknown and complex crack paths through 3D microstructures based on voxel data under the assumption of nonlinear geometry and elasto-plastic material behavior. Additionally, computational efficiency is desired. In Shakoor et al. [132] multiple approaches for simulations including crack propagation on the microscale are summarized. The simulation of crack propagation and fracture remains challenging in engineering because cracks lead to discontinuities in the form of jumps in the mechanical fields, i.e., displacement and stress fields. The discontinuities lead to numerical problems in simulations because the underlying physics in the form of the continuum mechanics requires continuity which is necessary for numerical methods, e.g., the FEM. Especially the numerical investigation of ductile crack propagation, most approaches suffer from numerical problems, mesh-dependency and/or inefficiency. To circumvent the numerical problems that occur in simulations that demand continuity of the mechanical fields like the FEM, mesh-free methods, for instance, the peridynamics presented by Silling et al. [133], Madenci and Oterkus [80], avoid classical continuum mechanical descriptions and thus, numerical issues caused by cracks. On the microscale, brittle simulations are shown in Guski et al. [49] and in Nayak et al. [99]. As a drawback, these methods suffer from missing continuum mechanical links, especially in terms of plasticity. For ductile materials, plasticity is of great importance for the crack propagation, in particular for the investigation of the surface spalling. Because these links are important to gain knowledge about the surface spalling, Additionally, only the velocity and not the displacements are prescribed in the Peridynamics which restricts the possible boundary value problems. Because of these advantages, mesh-free methods are avoided in this work.

Due to the enormous influence of the mechanical fields on the crack propagation, most approaches for simulating of crack propagation extend the FEM because of its capability to accurately resolve the mechanical fields. For example, the Extended Finite Element Method (XFEM) in Belytschko and Black [14], Fries et al. [39] incorporates cracking by considering enhanced shape functions. Following this, Sukumar et al. [139] shows microscale simulations with brittle crack propagation and Beese et al. [13] for ductile crack propagation at finite strains. However, the XFEM is technically demanding and conceptually not straightforward. Additionally, remeshing is required for large deformations. Another approach is the phase-field method by Miehe et al. [91] in which a continuous damage field is considered which represents the sharp crack as a smooth field. Applications on microstructures can be seen in, for instance, Nguyen et al. [102] assuming small deformations and brittle material behavior, in Shahba and Ghosh [131] for elastic polycrystals and in Cheng et al. [21] assuming crystal plasticity. The disadvantage of this technique lies in the high computational costs resulting from an additional degree of freedom representing the damage field. As another continuous approach, a gradient-enhanced damage model as, for instance, introduced in Junker et al. [59] for small strains and in Junker et al. [60] for finite strains, also assumes a smooth damage field for the sharp crack. In this model, a neighbored element method is applied to derive the gradient terms. However, these models suffer from missing descriptions for failure and, therefore, do not suit for numerical simulation of surface spalling.

Furthermore, cohesive-zone models, as introduced in Barenblatt [9] for brittle and Dugdale [32] for ductile materials and applied on the FE framework in Hillerborg et al. [52], make use of elements, e.g., interface elements, that underly decohesion due to damage and cracks. Here, the existence of a fracture process zone around the crack tip is considered in which small-scale yielding, micro-cracking and void nucleation, growth and coalescence lead to material degradation. Examples of this technique for the debonding of the inclusion to matrix are shown in Liang and Sofronis [76], Meng and Wang [86]. These methods may suffer from erroneous crack patterns, as shown in Schellekens and De Borst [121]. Additionally, if the crack path is unknown, interface elements have to be applied between all elements, cf., e.g., Xu and Needleman [158], leading to a high number of elements and thus, high computational costs. Other approaches, for example, early element erosion techniques at the microscale, as, e.g., in Wulf et al. [156], suffer from localization effects and inefficiency.

In this work, the eigenerosion approach, as implemented in Pandolfi and Ortiz [106] based on the variational formulation in Schmidt et al. [127], is applied because it fulfills the requirements for the simulation of subcritical crack propagation through metallic microstructures. The eigenerosion method has been used in implementations other than the original one in Pandolfi and Ortiz [106] before. In Qinami et al. [112], an extension to small strain Drucker-Prager elasto-plasticity is given and the influence of the load speed on the crack propagation is investigated. Furthermore, mesh-free variations are shown in Pandolfi et al. [107], Li et al. [75], Navas et al. [98], for example, for the simulation of fragmentation and high-impact loading. In Pandolfi et al. [108], the computational advantage of the eigenerosion compared to the previously mentioned phase-field method is demonstrated. For the efficient simulation directly on voxel data, the FCM introduced in Parvizian et al. [109] as an enhancement of the FEM and applied on three-dimensional structures in Düster et al. [33] is combined with the eigenerosion. Different cell decomposition techniques for the FCM have been exploited in Fangye et al. [36]. As shown in Yang et al. [159], the FCM circumvents the complicated and computational costly meshing procedure of, the complex microstructures as presented in, e.g., Schneider et al. [128]. Other approaches for crack propagation have already made use of the FCM for this problem. For example, the phase-field approach has been applied for crack initiation by Ranjbar et al. [114] and for small strain brittle crack propagation in Nagaraja et al. [97]. Furthermore, refinement approaches, e.g., in the form of local enrichment, cf. Düster et al. [34], have already been investigated. However, a split of the finite cells into finite elements has not been performed in literature according to the authors knowledge. Because of this, the consideration of the split of the finite cells has not been incorporated for the cell decomposition techniques before, since additional assumptions for the properties of the cells are necessary.

For the reduction of the computational costs of simulations based on voxel data obtained from a μCT-scan of a complex microstructure, smaller, less complex RVEs are constructed. Multiple definitions for RVEs are given, cf., e.g., Zeman [163], Hill [51], Drugan and Willis [31]. They may either be cutouts of a larger microstructure or artificially constructed. Here, the concept of SSRVEs, as introduced in Schröder et al. [129] and extended in Balzani et al. [8], Scheunemann et al. [124] and Scheunemann et al. [125] for dual phase steel, is applied. Therein, inclusions appear as ellipses and ellipsoids. Other shapes, e.g., cylinders, have not been exploited for the construction of the SSRVEs in the original papers. Other methods for the construction of RVEs are presented in Fritzen et al. [42], Fritzen and Böhlke [41] for crystalline microstructures and in Ghossein and Lévesque [45], Wriggers and Moftah [155] for concrete microstructures. Yin et al. [160] introduces the term statistical volume elements for these kind of microstructures. These algorithms only generate inclusions or material phases which are convex with sharp edges. A similar approach, which serves as the second method next to the SSRVEs in this work, is presented in Schüler et al. [130]. Therein, asphalt concrete microstructures are constructed based on CT-scans.

1.4. Outline

The outline of this work is as follows: In chapter 2, the basic equations of the FEM for solids are summarized. Therefore, the necessary fundamental equations of the continuum mechanics are given firstly. Additionally, the constitutive laws that mathematically describe the behavior of the investigated materials, namely Neo-Hookean hyperelasticity, finite strain J_2-elasto-plasticity, as seen Simo [134], Simo and Miehe [136], Simo et al. [137] and the elasto-viscoplasticity according to Perzyna [110], are presented.

For the simulation of crack propagation, the eigenerosion approach as presented in Pandolfi and Ortiz [106] is implemented. This implementation is described in chapter 3. Additionally, the extension of the eigenerosion approach to geometric nonlinearity and ductile fracture are given. Furthermore, an improved method for the derivation of the regularized crack area necessary for calculating the crack resistance and handling inertia effects are implemented.

In chapter 4, the plausibility of the extended eigenerosion is demonstrated. Therefore, the results of tension tests on brittle as well as ductile specimen according to Miehe et al. [92] under uniformly increasing load are shown. Herein, the mesh convergence of the occurring shear bands (only in the case of elasto-plastic and elasto-viscoplastic material behavior), of the crack path and structural response is shown. Furthermore, tests under cyclic loads are simulated in order to show the capability of the framework to generate Wöhler curves.

Then, the proposed algorithm for the efficiently application of the eigenerosion on voxel data of microstructures obtained from μCT-scans is described in chapter 5. Therefore, the standard FCM presented firstly. Afterwards, the combination of the eigenerosion with the FCM and all of its key components are presented. In this framework, the implementation of hanging node constraints is necessary. Furthermore, the discretization of the voxel-based microstructure for this algorithm is a crucial ingredient. Then, a benchmark experiment is shown to demonstrate the plausibility and the efficiency.

Afterwards, the construction of simplified artificial microstructures for the reduction of computational costs is presented in chapter 6. Therein, the concept of the construction of statistically similar representative volume elements (SSRVE) and its application on the metal matrix composite Ferro-Titanit is described. This concept is compared to an alternative approach, namely the construction of statistical volume element (RVE), applied on the microstructure of asphalt concrete.

Chapter 7 presents the results of simulations of crack propagation through metallic microstructures. Therefore, the calibration and validation of the material and numerical parameters is shown firstly. Afterwards, the results of microstructures based on μCT-scans, SSRVEs and different artificial morphologies of cold work tool steel are presented.

Finally, this work is summarized and concluded in chapter 8. Furthermore, an outlook on further investigations is made.

2. Simulation of mechanical problems

For the numerical simulation of crack propagation, different numerical methods can be used, cf. section 1.3. In this work, the Finite Element Method (FEM) is applied as presented in this chapter. Therefore, the basic equations of the continuum mechanics for solids, on which the FEM is based, are recapitulated firstly. Afterwards, the FE framework including the variational form, the discretization and solving procedure is described. Additionally, the constitutive laws of the materials, that the microstructures consist of, are given.

2.1. Continuum mechanics

For the mechanical description of crack propagation and its application a the FE framework, a short introduction into continuum mechanics is given in this section. The continuum mechanics contains the analysis of deformation and stress states of a body subject to loads and prescribed deformations. As a basis for that, a continuum is considered as a material body of a certain volume which consists of an infinite amount of material points. These have physical quantities in the form of material properties, e.g., the bulk modulus or the density, and field quantities, e.g., the displacement, mechanical stress or temperature. These fields have to be continuous over the whole body. Hence, no jumps in those are allowed. Note, that the material points do not represent atoms, which would lead to a discretization of the body and therefore, to discontinuities, but imaginary points capturing the characteristics of the body locally instead. In the following, kinematics, stress measures and balance equations of these continua necessary for the FE formulation are described based on the works of Marsden and Hughes [83] and Mase [84] on the basics of continuum mechanics.

2.1.1. Kinematic and deformation measures

The kinematic is often defined as the branch of dynamics, that describes the motion and deformation of bodies without consideration of forces and masses. For this purpose, the existence of different states of a body at different times is considered. Firstly, the undeformed body $\mathcal{B}_0$ with the volume V consists of material points at the position $\boldsymbol{X} \in \mathcal{B}_0$ with their mechanical quantities at the time $t = t_0$, as shown in figure 2.1. This state is assumed as reference configuration. Secondly, at the time $t > t_0$, the body $\mathcal{B}_t$ with the volume v is deformed due to any kind of loading, e.g., mechanically or thermally, so that the material points move to the position $\boldsymbol{x} \in \mathcal{B}_t$ in the current configuration. With this assumption, space dependent quantities, e.g., the density ρ, can now be expressed either in the reference configuration, in the case of the density, with ρ_0 at $t = t_0$, or in the current configuration, in the case of the density, with ρ at $t > t_0$. In continuum mechanics, the physical quantities of both configurations are represented by scalars and tensors. In this work, we assume a three-dimensional orthonormal Cartesian basis for both configurations with the Cartesian basis vectors $\boldsymbol{E}_1$, $\boldsymbol{E}_2$ and $\boldsymbol{E}_3$ in the reference configuration and, respectively, $\boldsymbol{e}_1$, $\boldsymbol{e}_2$ and $\boldsymbol{e}_3$ in the current configuration. Based on these, the tensors can be represented in index notation, e.g., a first-rank tensor $\boldsymbol{a} = a_i \boldsymbol{e}_i$, a second-rank tensor $\boldsymbol{A} = A_{ij} \boldsymbol{e}_i \otimes \boldsymbol{e}_j$ or a fourth-rank tensor $\mathbb{A} = \mathbb{A}_{ijkl} \boldsymbol{e}_i \otimes \boldsymbol{e}_j \otimes \boldsymbol{e}_k \otimes \boldsymbol{e}_l$. Here, $\otimes$ denotes the dyadic product. Due to the orthonormality of the basis vectors, their vector product $\boldsymbol{e}_i \cdot \boldsymbol{e}_j = \delta_{ij}$ results in the Kronecker Delta δ_{ij} for which

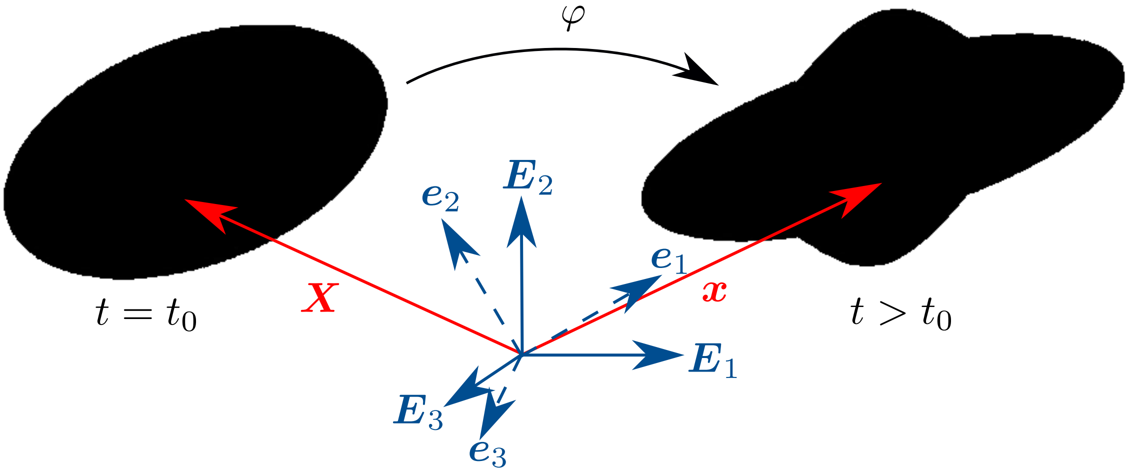

Figure 2.1.: Undeformed body $\mathcal{B}_0$ in the reference configuration at $t = t_0$ and deformed body $\mathcal{B}_t$ in the current configuration at $t > t_0$.

$\delta_{ij} = 1$, if $i = j$, and $\delta_{ij} = 0$, otherwise holds. Because of the linearity and homogeneity of tensors between coordinate systems and therefore, their configurations, the physical laws are formulated in tensor equations that are invariant regarding their configuration. Furthermore, these transformations are bijective. The nonlinear deformation

$$\boldsymbol{x} = \varphi(\boldsymbol{X}, t) \tag{2.1}$$

maps the material points $\boldsymbol{X}$ from the space of the reference body $\mathcal{B}_0$ onto the space of the current body $\mathcal{B}_t$, here denoted with $\boldsymbol{x}$. The position vectors of both configurations are related over the displacement

$$\boldsymbol{u} := \boldsymbol{x} - \boldsymbol{X} \tag{2.2}$$

which describes the motion of the material points over time t. The velocity is considered as the partial derivative

$$\boldsymbol{v} := \dot{\boldsymbol{u}} = \frac{\partial \boldsymbol{u}}{\partial t} \tag{2.3}$$

with respect to the time t and, analogously, the acceleration as the second derivative

$$\boldsymbol{a} := \dot{\boldsymbol{v}} = \frac{\partial \boldsymbol{v}}{\partial t} = \ddot{\boldsymbol{u}} = \frac{\partial^2 \boldsymbol{u}}{\partial t^2}. \tag{2.4}$$

Note, that the notations of the time derivatives $\dot{\bullet} = \frac{\partial \bullet}{\partial t}$ and $\ddot{\bullet} = \frac{\partial^2 \bullet}{\partial t^2}$ are used in the rest of this work. Additionally, spatial derivatives are applied in the form of gradient, namely $\mathrm{Grad}(\bullet) = \frac{\partial \bullet}{\partial \boldsymbol{X}}$ with respect to the reference and $\mathrm{grad}(\bullet) = \frac{\partial \bullet}{\partial \boldsymbol{x}}$ with respect to the current configuration. Analogously, the divergence, namely $\mathrm{Div}(\bullet) = (\frac{\partial \bullet}{\partial \boldsymbol{X}}) : \boldsymbol{I}$ with respect to the reference and $\mathrm{div}(\bullet) = (\frac{\partial \bullet}{\partial \boldsymbol{x}}) : \boldsymbol{I}$ with respect to the current configuration with the second order identity tensor $\boldsymbol{I} = \delta_{ij} \boldsymbol{E}_i \otimes \boldsymbol{E}_j$ are derived, in order to describe local deformation states of the material points. The deformation gradient

$$\boldsymbol{F} := \mathrm{Grad}(\boldsymbol{x}) = \frac{\partial \boldsymbol{x}}{\partial \boldsymbol{X}} = \boldsymbol{I} + \frac{\partial \boldsymbol{u}}{\partial \boldsymbol{X}} \tag{2.5}$$

suits for describing the deformation, especially, because of its characteristic $\mathrm{d}\boldsymbol{x} = \boldsymbol{F} \cdot \mathrm{d}\boldsymbol{X}$. This represents the relation of an infinitesimal line segment $\mathrm{d}\boldsymbol{x}$ in the current configuration with the infinitesimal line segment $\mathrm{d}\boldsymbol{X}$ in the reference configuration. Hence, the deformation gradient $\boldsymbol{F}$ holds one basis vector in reference and one basis vector in the reference configuration. As another property of the deformation gradient, its Jacobian determinant

$$J := \det(\boldsymbol{F}) \tag{2.6}$$

represents the change in the infinitesimal volume of the current configuration $\mathrm{d}v = J\,\mathrm{d}V$ compared to the volume of the reference configuration $\mathrm{d}V$. From a physical point of view, the volume cannot become negative and thus, $J > 0$ holds as a constraint for the deformation gradient $\boldsymbol{F}$. Based on these assumptions, different deformation measures in the reference as well as in the current configuration are defined. The vector product of the increment of the position vector

$$\mathrm{d}\boldsymbol{x} \cdot \mathrm{d}\boldsymbol{x} = (\boldsymbol{F} \cdot \mathrm{d}\boldsymbol{X}) \cdot (\boldsymbol{F} \cdot \mathrm{d}\boldsymbol{X}) = \mathrm{d}\boldsymbol{X} \cdot \underbrace{\boldsymbol{F}^{\mathrm{T}} \cdot \boldsymbol{F}}_{:=\boldsymbol{C}} \cdot \mathrm{d}\boldsymbol{X} \tag{2.7}$$

is examined from which the right Cauchy-Green stretch tensor $\boldsymbol{C}$ results. This second-rank tensor holds its basis vectors in the reference configuration. Analogously, the left Cauchy-Green stretch tensor $\boldsymbol{b}$ is determined by

$$\mathrm{d}\boldsymbol{X} \cdot \mathrm{d}\boldsymbol{X} = (\boldsymbol{F}^{-1} \cdot \mathrm{d}\boldsymbol{x}) \cdot (\boldsymbol{F}^{-1} \cdot \mathrm{d}\boldsymbol{x}) = \mathrm{d}\boldsymbol{X} \cdot (\underbrace{\boldsymbol{F} \cdot \boldsymbol{F}^{\mathrm{T}}}_{:=\boldsymbol{b}})^{-1} \cdot \mathrm{d}\boldsymbol{X} \tag{2.8}$$

with both basis vectors in the current configuration. Based on these, the strains in the form of the Green-Lagrange tensor in the reference configuration and the Almansi tensor in the current configuration are defined by

$$\boldsymbol{E} := \tfrac{1}{2}(\boldsymbol{C} - \boldsymbol{I}) \qquad \text{and} \qquad \boldsymbol{A} := \tfrac{1}{2}(\boldsymbol{I} - \boldsymbol{b}^{-1}). \tag{2.9}$$

Another form to capture the deformation based on those tensors is obtained by the spectral decomposition into their eigenvalues λ_i^2, which are seen as the square of the principal stretches λ_i, and their eigenvectors $\boldsymbol{N}_i$ in reference and $\boldsymbol{n}_i$ in the current configuration. Physically, the principal stretches represent the ratio of the elongations to the reference length into the directions of the corresponding eigenvectors. The eigenvalues and eigenvectors solve the eigenvalue problems

$$(\boldsymbol{C} - \lambda_i^2\,\boldsymbol{I}) \cdot \boldsymbol{N}_i = \boldsymbol{0} \qquad \text{and} \qquad (\boldsymbol{b} - \lambda_i^2\,\boldsymbol{I}) \cdot \boldsymbol{n}_i = \boldsymbol{0} \tag{2.10}$$

with $i = 1, 2, 3$. With this relation, the Cauchy stretch tensors can be reconstructed in the form

$$\boldsymbol{C} = \sum_{i=1}^{3} \lambda_i^2\,\boldsymbol{N}_i \otimes \boldsymbol{N}_i \qquad \text{and} \qquad \boldsymbol{b} = \sum_{i=1}^{3} \lambda_i^2\,\boldsymbol{n}_i \otimes \boldsymbol{n}_i. \tag{2.11}$$

Resulting from this, the deformation gradient can also be rewritten as $\boldsymbol{F} = \sum_{i=1}^{3} \lambda_i\,\boldsymbol{n}_i \otimes \boldsymbol{N}_i$. Another important measures for the description of material laws are the tensor invariants of the Cauchy-Green stretch tensors

$$\begin{aligned} I_1 &= \operatorname{tr}\boldsymbol{C} = \operatorname{tr}\boldsymbol{b} = \lambda_1^2 + \lambda_2^2 + \lambda_3^2 \\ I_2 &= \tfrac{1}{2}((\operatorname{tr}\boldsymbol{C})^2 - \operatorname{tr}\boldsymbol{C}^2) = \tfrac{1}{2}((\operatorname{tr}\boldsymbol{b})^2 - \operatorname{tr}\boldsymbol{b}^2) = \lambda_1^2\,\lambda_2^2 + \lambda_1^2\lambda_3^2 + \lambda_2^2\lambda_3^2 \\ I_3 &= \det\boldsymbol{C} = \det\boldsymbol{b} = J^2 = \lambda_1^2\,\lambda_2^2\,\lambda_3^2 \end{aligned} \tag{2.12}$$

that reduce the second-rank tensors to three coordinate system independent values. Note, that the invariants of the right Cauchy-Green stretch tensor $\boldsymbol{C}$ coincide with the ones of the left Cauchy-Green stretch tensor $\boldsymbol{b}$. The derivatives

$$\begin{aligned} \frac{\partial I_1}{\partial \boldsymbol{C}} &= \boldsymbol{I} & \frac{\partial I_1}{\partial \boldsymbol{b}} &= \boldsymbol{I} \\ \frac{\partial I_2}{\partial \boldsymbol{C}} &= I_1\,\boldsymbol{I} - \boldsymbol{C} & \frac{\partial I_2}{\partial \boldsymbol{b}} &= I_1\,\boldsymbol{I} - \boldsymbol{b} \\ \frac{\partial I_3}{\partial \boldsymbol{C}} &= I_3\,\boldsymbol{C}^{-1} & \frac{\partial I_3}{\partial \boldsymbol{b}} &= I_3\,\boldsymbol{b}^{-1} \end{aligned} \tag{2.13}$$

are of importance for the evaluation of material laws in section 2.3. For the sake of splitting the deformation into a volumetric and a deviatoric part, the isochoric Cauchy stretch tensors

$$\bar{\boldsymbol{C}} := J^{-\frac{2}{3}}\boldsymbol{C} \qquad \text{and} \qquad \bar{\boldsymbol{b}} := J^{-\frac{2}{3}}\boldsymbol{b} \tag{2.14}$$

with the relations

$$\frac{\partial \bar{\boldsymbol{C}}}{\partial \boldsymbol{C}} = J^{-\frac{2}{3}}\left(\mathbb{I} - \tfrac{1}{3}\,\boldsymbol{C} \otimes \boldsymbol{C}^{-1}\right) \qquad \text{and} \qquad \frac{\partial \bar{\boldsymbol{b}}}{\partial \boldsymbol{b}} = J^{-\frac{2}{3}}\left(\mathbb{I} - \tfrac{1}{3}\,\boldsymbol{b} \otimes \boldsymbol{b}^{-1}\right) \tag{2.15}$$

are introduced. $\mathbb{I}$ denotes the fourth order unit tensor $\delta_{ij}\delta_{kl}\boldsymbol{E}_i \otimes \boldsymbol{E}_k \otimes \boldsymbol{E}_j \otimes \boldsymbol{E}_l$. Furthermore, the spectral decomposition enables the derivation of the logarithmic strain tensor

$$\boldsymbol{\varepsilon} := \sum_{i=1}^{3} \varepsilon_i\, \boldsymbol{n}_i \otimes \boldsymbol{n}_i \qquad \text{with the logarithmic principal strains} \qquad \varepsilon_i = \ln \lambda_i. \tag{2.16}$$

This strain measure is used for some material laws because of advantages due to its logarithmic properties. In particular, for those including crack propagation, it enables the tension-compression split of the strain tensor

$$\boldsymbol{\varepsilon} := \boldsymbol{\varepsilon}_+ + \boldsymbol{\varepsilon}_- \qquad \text{with} \qquad \boldsymbol{\varepsilon}_\pm := \sum_{i=1}^{3} \langle \varepsilon_i \rangle_\pm\, \boldsymbol{n}_i \otimes \boldsymbol{n}_i \tag{2.17}$$

with the Macaulay bracket $\langle \bullet \rangle_\pm = (\bullet \pm |\bullet|)/2$ into a tension part with positive principal strains $\boldsymbol{\varepsilon}_+$ and into a compression part with negative principal strains $\boldsymbol{\varepsilon}_-$.

2.1.2. Mechanical stresses and internal power

The second part of the continuum mechanics, next to the kinematics, deals with mechanical stresses and their connection to the strains. These stresses can be expressed in both configurations and therefore, hold different meanings in the engineering context. They are based on the consideration of a traction vector $\boldsymbol{t} = \frac{\mathrm{d}\boldsymbol{f}}{\mathrm{d}a}$ which relates the force vector $\boldsymbol{f}$ to the current cut surface area a, that it is subjected to. By assuming the surface area vector $\boldsymbol{a} := a\,\boldsymbol{n}$ which contains the normal vector $\boldsymbol{n}$ of the cut surface in the current configuration, the Cauchy stress

$$\boldsymbol{\sigma} := \frac{\mathrm{d}\boldsymbol{f}}{\mathrm{d}\boldsymbol{a}} \tag{2.18}$$

results. From this, the Cauchy theorem

$$\boldsymbol{t} = \boldsymbol{\sigma} \cdot \boldsymbol{n} \tag{2.19}$$

follows. The Cauchy stress is also known as „true stress“ because both, the force vector $\boldsymbol{f}$ as well as the surface $\boldsymbol{a}$, exist in the current configuration. Another important stress measure, especially for metal plasticity, is the Kirchhoff stress tensor

$$\boldsymbol{\tau} := J\,\boldsymbol{\sigma}. \tag{2.20}$$

Note, that these two stress tensors hold symmetry, whereas the first Piola-Kirchoff stress

$$\boldsymbol{P} := J\,\boldsymbol{\sigma} \cdot \boldsymbol{F}^{-\mathrm{T}} = \boldsymbol{\tau} \cdot \boldsymbol{F}^{-\mathrm{T}} \tag{2.21}$$

does not provide symmetry due to the multiplication of the symmetric Cauchy stress $\boldsymbol{\sigma}$ with the asymmetric deformation gradient $\boldsymbol{F}$. This stress measure is also known also „technical stress“ or „engineering stress“ because it relates the current force vector $\boldsymbol{f}$ to the reference surface area A, which in technical applications is easy to measure compared to the current surface area a. Lastly, the second Piola-Kirchhoff stress

$$\boldsymbol{S} := J\,\boldsymbol{F}^{-1} \cdot \boldsymbol{\sigma} \cdot \boldsymbol{F}^{-\mathrm{T}} \tag{2.22}$$

represents the pullback of the Kirchhoff stress $\boldsymbol{\tau}$ into the reference configuration. Based on these, the internal power is expressed in the different configurations by

$$P := \int\limits_{\mathcal{B}_t} \boldsymbol{\sigma} : \boldsymbol{d}_s \,\mathrm{d}v = \int\limits_{\mathcal{B}_0} \boldsymbol{P} : \dot{\boldsymbol{F}} \,\mathrm{d}V = \int\limits_{\mathcal{B}_0} \boldsymbol{S} : \dot{\boldsymbol{E}} \,\mathrm{d}V \tag{2.23}$$

in which $\bullet : \bullet$ denotes the double contraction which is applied to multiply the stress measures with their corresponding deformation rate measures. Here, the time derivatives $\boldsymbol{d}_s = \boldsymbol{F}^{-1} \cdot \dot{\boldsymbol{E}} \cdot \boldsymbol{F}^{-\mathrm{T}}$, $\dot{\boldsymbol{F}}$ and $\dot{\boldsymbol{E}} = \dot{\boldsymbol{C}}/2$ are considered. The spatial time derivative $\boldsymbol{d}_s = \frac{1}{2}(\boldsymbol{l} + \boldsymbol{l}^{\mathrm{T}})$ can also be expressed in terms of $\boldsymbol{l} = \dot{\boldsymbol{F}} \cdot \boldsymbol{F}^{-1}$.

2.1.3. Equilibrium equations

In solid mechanics, certain fundamental balance equations hold for the equilibrium of a body locally and globally. In the following, the ones necessary for modeling crack propagation in the FE framework are presented. Firstly, the balance of mass in global form

$$\dot{m} = 0 \rightarrow m = \int\limits_{\mathcal{B}_t} \rho \,\mathrm{d}V = \int\limits_{\mathcal{B}_0} \rho_0 \,\mathrm{d}v \tag{2.24}$$

and in local form

$$\rho_0 = \frac{\mathrm{d}m}{\mathrm{d}V} = \frac{\mathrm{d}m}{\mathrm{d}v}\frac{\mathrm{d}v}{\mathrm{d}V} = \rho\, J \tag{2.25}$$

is considered because of the assumption that no mass m is either generated or destroyed during the processes of interest. Secondly, the balance of momentum

$$\dot{I} = \boldsymbol{p} \tag{2.26}$$

with the sum of external forces

$$\boldsymbol{p} = \int\limits_{\mathcal{B}_t} \rho\, \boldsymbol{b}_0 \,\mathrm{d}v + \int\limits_{\partial\mathcal{B}_t} \boldsymbol{t}^{\mathrm{s}} \,\mathrm{d}a, \tag{2.27}$$

namely the integrated volume acceleration $\boldsymbol{b}_0$ and surface tractions $\boldsymbol{t}^{\mathrm{s}}$ in the current configuration is assumed. Here,

$$I = \int\limits_{\mathcal{B}_t} \rho\, \dot{\boldsymbol{x}} \,\mathrm{d}v = \int\limits_{\mathcal{B}_0} \rho_0\, \dot{\boldsymbol{x}} \,\mathrm{d}V. \tag{2.28}$$

represents the momentum resulting from the inertia. From this, the final global form

$$\int\limits_{\mathcal{B}_t} \rho\, \boldsymbol{b}_0 \,\mathrm{d}v + \int\limits_{\partial\mathcal{B}_t} \boldsymbol{t}^{\mathrm{s}} \,\mathrm{d}a = \frac{\partial}{\partial t} \int\limits_{\mathcal{B}_t} \rho\, \dot{\boldsymbol{x}} \,\mathrm{d}v \tag{2.29}$$

follows that states that the sum of the integrated volume acceleration and surface tractions $\rho_0\, \boldsymbol{b}_0$ and $\boldsymbol{t}^{\mathrm{s}}$ equals the inertia. This equilibrium is given in the local form as

$$\mathrm{Div}\,(\boldsymbol{P}) + \rho_0\, \boldsymbol{b}_0 = \rho_0\, \ddot{\boldsymbol{x}} \tag{2.30}$$

in the reference configuration. Because the stresses depend on the displacements $\boldsymbol{u}$, these equations are differential equations. These underly the Dirichlet boundary condition $\boldsymbol{u} =$

$\boldsymbol{u}_{\mathrm{B}}$, which prescribes the displacement at the Dirichlet boundary to $\boldsymbol{u}_{\mathrm{B}}$, and the Neumann boundary condition, which prescribes the surface traction $\boldsymbol{t} = \boldsymbol{t}_B$ at the Neumann boundary. Analogously, the angular momentum balance

$$\dot{I}_m = \boldsymbol{p}_m \tag{2.31}$$

with the moment of the force around the point p at the arbitrary position $\boldsymbol{x}_p$

$$\boldsymbol{p}_m = \int\limits_{\mathcal{B}_t} (\boldsymbol{x} - \boldsymbol{x}_p) \times \rho_0 \, \boldsymbol{b}_0 \, \mathrm{d}v + \int\limits_{\partial\mathcal{B}_t} (\boldsymbol{x} - \boldsymbol{x}_p) \times \boldsymbol{t}^{\mathrm{s}} \, \mathrm{d}a \tag{2.32}$$

and the angular momentum

$$I_m = \int\limits_{\mathcal{B}_t} (\boldsymbol{x} - \boldsymbol{x}_p) \times \rho \, \dot{\boldsymbol{x}} \, \mathrm{d}v = \int\limits_{\mathcal{B}_0} (\boldsymbol{x} - \boldsymbol{x}_p) \times \rho \, \dot{\boldsymbol{x}} \, \mathrm{d}V \tag{2.33}$$

hold as the third equilibrium. This leads to the global form

$$\int\limits_{\mathcal{B}_t} (\boldsymbol{x} - \boldsymbol{x}_p) \times \rho \, \dot{\boldsymbol{x}} \, \mathrm{d}v = \int\limits_{\mathcal{B}_t} (\boldsymbol{x} - \boldsymbol{x}_p) \times \rho_0 \, \boldsymbol{b}_0 \, \mathrm{d}v + \int\limits_{\partial\mathcal{B}_t} (\boldsymbol{x} - \boldsymbol{x}_p) \times \boldsymbol{t}^{\mathrm{s}} \, \mathrm{d}a. \tag{2.34}$$

The local form of this equation results in the symmetry conditions of the second Piola-Kirchhoff stress and Cauchy stress

$$\boldsymbol{S} = \boldsymbol{S}^{\mathrm{T}} \qquad \text{and} \qquad \boldsymbol{\sigma} = \boldsymbol{\sigma}^{\mathrm{T}} \tag{2.35}$$

as mentioned in the previous subsection. In general, the first Piola-Kirchhoff stress $\boldsymbol{P} = \boldsymbol{F}^{-1} \cdot \boldsymbol{S}$ is asymmetric due to the general asymmetry of the deformation gradient $\boldsymbol{F}$. These symmetries provide numerical advantages in particular less storage and calculation operations for these stresses. The fourth balance equation

$$W^{\mathrm{ext}} - W^{\mathrm{int}} = \int\limits_{\mathcal{B}_t} \tfrac{1}{2} \, \rho \, \dot{\boldsymbol{x}} \cdot \dot{\boldsymbol{x}} \, \mathrm{d}v = \int\limits_{\mathcal{B}_0} \tfrac{1}{2} \, \rho_0 \, \dot{\boldsymbol{x}} \cdot \dot{\boldsymbol{x}} \, \mathrm{d}V \tag{2.36}$$

with the difference of the externally imposed energy W^{ext} and the internal energy

$$W^{\mathrm{int}} = \int_{\mathcal{B}_0} \psi \, \mathrm{d}V \tag{2.37}$$

on the left-hand side and the kinetic energy on the right-hand side holds. This balance equation includes the first law of thermodynamics which states that energy can neither be destroyed or generated but only changes its form. Here, the free Helmholtz energy ψ denotes the specific energy stored in local form. Lastly, the second law of thermodynamics is considered. It states that the dissipation

$$\mathcal{D} = \boldsymbol{S} : \dot{\boldsymbol{E}} - \dot{\psi} = \boldsymbol{\tau} : \boldsymbol{d}_s - \dot{\psi} \geq 0, \tag{2.38}$$

here in the form of the Clausius-Duhem inequality, may only increase over time and not decrease. Thus, irreversibility is ensured for dissipative processes. It defines the dissipation as the difference of the imposed power minus the power of the strain energy.

2.2. Finite Element framework

In order to calculate the internal stresses and crack propagation through solids, the previously shown balance equations have to be solved. Since the solution becomes very complex, even for simple structures, it can only be found analytically in a few special cases. In order to circumvent this problem, the analytical solution is approximated numerically. Therefore, the **Finite Element Method** (**FEM**), which is commonly used for solid mechanics, as shown in, e.g., Taylor and Zienkiewicz [141], Bathe [10] and, for large deformations, Bathe et al. [11], is applied for the numerical simulations in this work. The main concept of the FEM is based on the spatial discretization of the continuous body into multiple finite elements. In these, the shape of the field variable functions are assumed to be known as so-called "Ansatz" functions, e.g., in the form of piecewise linear functions. Hence, only the parameters of these functions have to be found. In our case, the FE software **FEAP**, cf. Taylor [142] is applied.

2.2.1. Variational formulation

In this subsection, the system of differential equation necessary for the FE framework for solid mechanics is described. Therefore, the so-called **weak form** of the momentum balance has to be derived. For this purpose, the momentum balance in equation 2.30 in terms of the first Piola-Kirchhoff stress $\boldsymbol{P}$ is considered. For solving this equation, boundary conditions on the surface $\partial\mathcal{B}_0 = \partial_{\mathrm{D}}\mathcal{B}_0 \cup \partial_{\mathrm{N}}\mathcal{B}_0$ have to be assumed. On the Dirichlet boundary $\partial_{\mathrm{D}}\mathcal{B}_0$ the displacements $\boldsymbol{u}_{\mathrm{B}}$ are prescribed, and on the Neumann boundary $\partial_{\mathrm{N}}\mathcal{B}_0$ the surface tractions $\boldsymbol{t}_{\mathrm{B}}$ are prescribed. Here, the two types of boundary must not overlap so that the relation $\partial_{\mathrm{D}}\mathcal{B}_0 \cap \partial_{\mathrm{N}}\mathcal{B}_0 = \emptyset$ holds. Combining all of this, one obtains the strong form of the differential system of equations

$$\mathrm{Div}\,(\boldsymbol{P}) + \rho_0\,\boldsymbol{b}_0 = \rho_0\,\ddot{\boldsymbol{x}} \;\text{ with }\; \boldsymbol{u} = \boldsymbol{u}_{\mathrm{B}} \;\text{ on }\; \partial_{\mathrm{D}}\mathcal{B}_0 \;\text{ and }\; \boldsymbol{P}\cdot\boldsymbol{N} = \boldsymbol{t}_{\mathrm{B}} \;\text{ on }\; \partial_{\mathrm{N}}\mathcal{B}_0 \tag{2.39}$$

including the Cauchy theorem $\boldsymbol{P}\cdot\boldsymbol{N} = \boldsymbol{t}_{\mathrm{B}}$ with the surface normal $\boldsymbol{N}$ in the reference configuration. This representation of the system of differential equations is called the "strong form" and has to be solved for the variable $\boldsymbol{u}$ since the first Piola-Kirchhoff stress $\boldsymbol{P}$ and the acceleration of the displacements $\ddot{\boldsymbol{u}} = \ddot{\boldsymbol{x}}$ depend on it. The relation of the first Piola-Kirchhoff stress $\boldsymbol{P}$ to the displacements $\boldsymbol{u}$ depends on the material properties. To reformulate the strong form from the material point description to the global form, or so-called "weak form", the differential equation is multiplied by the variation of the displacement $\delta\boldsymbol{u}$, which represents an arbitrary test function with the property $\delta\boldsymbol{u} = 0$ on $\partial_{\mathrm{D}}\mathcal{B}_0$. By integration over the volume of the body $\mathcal{B}_0$, the virtual work results in

$$\delta\Pi = -\int\limits_{\mathcal{B}_0} \delta\boldsymbol{u}\cdot\mathrm{Div}(\boldsymbol{P})\,\mathrm{d}V - \int\limits_{\mathcal{B}_0} \rho_0\,\delta\boldsymbol{u}\cdot(\boldsymbol{b}_0 - \ddot{\boldsymbol{x}})\,\mathrm{d}V = 0. \tag{2.40}$$

In order to reduce the order of this differential equation, the Gauß theorem is applied so that we obtain

$$\delta\Pi = \int\limits_{\mathcal{B}_0} \mathrm{Grad}(\delta\boldsymbol{u}) : \boldsymbol{P}\,\mathrm{d}V - \int\limits_{\partial\mathcal{B}_0} \delta\boldsymbol{u}\cdot\boldsymbol{P}\cdot\boldsymbol{N}\,\mathrm{d}A - \int\limits_{\mathcal{B}_0} \rho_0\,\delta\boldsymbol{u}\cdot(\boldsymbol{b}_0 - \ddot{\boldsymbol{x}})\,\mathrm{d}V = 0. \tag{2.41}$$

Because the variation of the displacements $\delta\boldsymbol{u}$ is zero at the Dirichlet boundary $\partial_{\mathrm{D}}\mathcal{B}_0$, only the surface integral over the Neumann boundary remains. By application of the relation $\ddot{\boldsymbol{x}} = \ddot{\boldsymbol{X}} + \ddot{\boldsymbol{u}} = \ddot{\boldsymbol{u}}$ and the Cauchy theorem $\boldsymbol{P}\cdot\boldsymbol{N} = \boldsymbol{t}_{\mathrm{B}}$, the form

$$\delta\Pi = \int\limits_{\mathcal{B}_0} \mathrm{Grad}(\delta\boldsymbol{u}) : \boldsymbol{P}\,\mathrm{d}V - \int\limits_{\partial_{\mathrm{N}}\mathcal{B}_0} \delta\boldsymbol{u}\cdot\boldsymbol{t}_{\mathrm{B}}\,\mathrm{d}A - \int\limits_{\mathcal{B}_0} \rho_0\,\delta\boldsymbol{u}\cdot(\boldsymbol{b}_0 - \ddot{\boldsymbol{u}})\,\mathrm{d}V = 0 \tag{2.42}$$

is obtained. This weak form of virtual work is taken into account for FE approximations. From the physical point of view, this virtual work represents the first variation of the total potential energy

$$\Pi = \int\limits_{\mathcal{B}_0} W \,\mathrm{d}V - \int\limits_{\partial_\mathrm{N}\mathcal{B}_0} \boldsymbol{u} \cdot \boldsymbol{t}_\mathrm{B} \,\mathrm{d}A - \int\limits_{\mathcal{B}_0} \rho_0 \left(\boldsymbol{b}_0 - \ddot{\boldsymbol{u}}\right) \cdot \boldsymbol{u} \,\mathrm{d}V \tag{2.43}$$

with the specific energy $W = \boldsymbol{F} : \boldsymbol{P}$. It is minimized with respect to the displacements $\boldsymbol{u}$, because of the natural axiom that systems tend to the state of lowest potential. This total potential energy $\Pi = \Pi^\mathrm{int} + \Pi^\mathrm{ext}$ is divided into the internal potential energy Π^int and the external potential energy Π^ext, whose variations

$$\delta\Pi^\mathrm{int} = \int\limits_{\mathcal{B}_0} \delta W \,\mathrm{d}V = \int\limits_{\mathcal{B}_0} \delta\boldsymbol{F} \cdot \frac{\partial W}{\partial \boldsymbol{F}} \,\mathrm{d}V \tag{2.44}$$

containing the relations $\boldsymbol{P} = \frac{\partial W}{\partial \boldsymbol{F}}$ and $\delta\boldsymbol{F} = \mathrm{Grad}(\delta\boldsymbol{u})$ and

$$\delta\Pi^\mathrm{ext} = - \int\limits_{\partial_\mathrm{N}\mathcal{B}_0} \delta\boldsymbol{u} \cdot \boldsymbol{t}_\mathrm{B} \,\mathrm{d}V - \int\limits_{\mathcal{B}_0} \rho_0 \,\delta\boldsymbol{u} \cdot \left(\boldsymbol{b}_0 - \ddot{\boldsymbol{u}}\right) \mathrm{d}V \tag{2.45}$$

are obtained from the variation of the total energy potential $\delta\Pi = \delta\Pi^\mathrm{int} + \delta\Pi^\mathrm{ext}$.

2.2.2. Discretization of the continuous body

Because the solution of the variational potential energy $\delta\Pi = 0$ cannot be solved for $\boldsymbol{u}$ analytically in most cases, the solution is approximated by the FEM. In this approach, the original body $\mathcal{B}_0$ is spatially discretized into n^el finite elements. Each element K takes a part of the space of the body $\mathcal{B}_K$ with the surface $\partial\mathcal{B}_K$. Combining all elements, the original body

$$\mathcal{B}_0 \approx \mathcal{B}^\mathrm{FE} = \bigcup_{K=1}^{n^\mathrm{el}} \mathcal{B}_K \tag{2.46}$$

is approximated by $\mathcal{B}^\mathrm{FE}$, as shown in figure 2.2. The boundaries of adjacent elements overlap. These overlaps are defined as two-dimensional “faces” in three-dimensional bodies and one-dimensional “edges” in two-dimensional bodies respectively. The faces of the elements match in such a way that the remaining free surfaces result in the surface of the discretized body $\partial\mathcal{B}^\mathrm{FE}$. In each of these elements, the spatial distribution of the field variable for which the differential equation has to be solved, in our case, the displacements $\boldsymbol{u}^\mathrm{FE}$, is assumed to be given as a sum of known functions N^m, for instance a trilinear function in the case of hexahedra. This function N^m is called the “shape function” or “Ansatz function”. Assuming this, the displacement

$$\boldsymbol{u}(\boldsymbol{X}) \approx \boldsymbol{u}^\mathrm{FE}(\boldsymbol{X}) = \sum_{m=1}^{n^\mathrm{en}} N^m \boldsymbol{d}_K^m \quad \forall \quad \boldsymbol{X} \in \mathcal{B}_K \tag{2.47}$$

is interpolated by the summation of these shape functions $N^m = N^m(\boldsymbol{X})$, that depend on the location $\boldsymbol{X}$ multiplied by the displacements $\boldsymbol{d}_K^m$ at n^en specific points, the so-called “nodes”, within the element K. The differential equation only has to be solved for the nodal displacements $\boldsymbol{d}_K^m$ in order to obtain the approximated field of displacements $\boldsymbol{u}$ by minimizing the total potential energy. This approach is also called “Galerkin method”. It is assumed that with increasing refinement of the discretization, the approximated solution of the displacements $\boldsymbol{u}^\mathrm{FE}$ converges towards the analytical solution $\boldsymbol{u}$ of the original differential equation because the

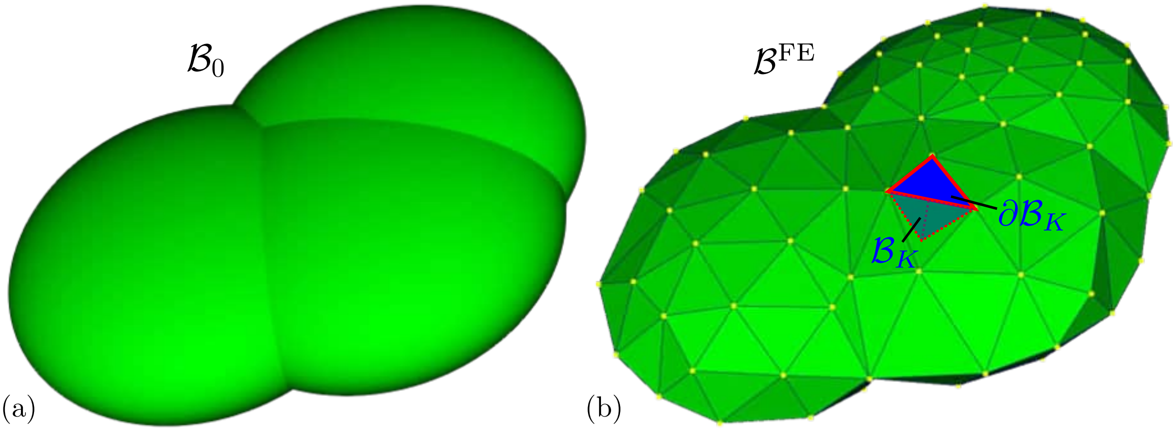

Figure 2.2.: (a) Body $\mathcal{B}$ and (b) its discretization $\mathcal{B}^{\mathrm{FE}}$ into tetrahedral elements with their edges (black) and nodes (yellow) including the body $\mathcal{B}_K$ of the element K and its outer surface $\partial\mathcal{B}_K$.

more elements exist, the smoother is the approximation to the original function. The two common ways of refinement are the h-refinement, that decreases the characteristic element size h, e.g., the edge length of the elements, and the p-refinement, that increases the polynomial degree p of the Ansatz functions N^m in the case of polynomial Ansatz functions, so that the displacements are approximated more accurately. Both refinement methods lead to an increased number of nodes and thus, the number of degrees of freedom, for which the differential equation has to be solved. This leads to an increase in computational cost. Furthermore, the so-called C_0-continuity is required which means that the displacement fields match at the element surfaces with the ones of the coinciding surface of the neighboring element so that no jumps in the displacement field $\boldsymbol{u}$ occur. Otherwise, the jumps in the displacement fields would destroy the continuity assumption which is necessary for the continuum mechanical basis of the system of differential equations. The discretization $\mathcal{B}^{\mathrm{FE}}$ including nodes and elements is called “mesh”.

2.2.3. Approximation of the displacements in the discretized body

In order to derive the displacements $\boldsymbol{u}^{\mathrm{FE}}$ from the weak form in equation (2.42) globally, equation (2.47) is applied element-wise. The geometry of each element is transformed into the isoparametric space, cf. figure 2.3, with the coordinate vector $\boldsymbol{\xi}$ containing the components ξ_1, ξ_2, $\xi_3 \in [-1, 1]$. Now, the shape function is rewritten as a function $N^m = N^m(\boldsymbol{\xi})$ depending on the isoparametric coordinate vector $\boldsymbol{\xi}$. Therefore, the coordinates $\boldsymbol{X}$ have to be transformed into the coordinates $\boldsymbol{\xi}$ of the isoparametric space, in which the form of the shape functions is defined, in our case, in the form of polynomials. Hence, the displacement field $\boldsymbol{u}_K^{\mathrm{FE}}$ results in

$$\boldsymbol{u}_K^{\mathrm{FE}} = \sum_{m=1}^{n^{\mathrm{en}}} N^m(\boldsymbol{\xi})\, \boldsymbol{d}_K^m \tag{2.48}$$

as the sum of the shape function $N^m(\boldsymbol{\xi})$ multiplied with the nodal displacements $\boldsymbol{d}_K^m$ of the node m corresponding to the element K in the isoparametric space from $m = 1$ to the number of nodes per element n^{en}. For simplicity, the dependence on $\boldsymbol{\xi}$ is dropped in the following. The shape functions have the property that they are of the value 1 at the corresponding node and zero at all other nodes. Additionally, the sum of all shape functions equals 1 in every point. For mapping the vector $\boldsymbol{X}$ in the reference configuration onto the isoparametric space, the Jacobian

$$\boldsymbol{J} = \frac{\partial \boldsymbol{X}}{\partial \boldsymbol{\xi}} \tag{2.49}$$

is evaluated for each element K. By reordering the shape functions N^m to the matrix

$$\underline{\boldsymbol{N}} = \left[\begin{array}{cc|cc|c|cc} N^1 & 0 & N^2 & 0 & \cdots & N^{n^{\text{en}}} & 0 \\ 0 & N^1 & 0 & N^2 & \cdots & 0 & N^{n^{\text{en}}} \end{array}\right] \tag{2.50}$$

in the two-dimensional case or

$$\underline{\boldsymbol{N}} = \left[\begin{array}{ccc|ccc|c|ccc} N^1 & 0 & 0 & N^2 & 0 & 0 & \cdots & N^{n^{\text{en}}} & 0 & 0 \\ 0 & N^1 & 0 & 0 & N^2 & 0 & \cdots & 0 & N^{n^{\text{en}}} & 0 \\ 0 & 0 & N^1 & 0 & 0 & N^2 & \cdots & 0 & 0 & N^{n^{\text{en}}} \end{array}\right] \tag{2.51}$$

in the three-dimensional case and, we obtain the displacements

$$\boldsymbol{u}_K = \underline{\boldsymbol{N}} \cdot \boldsymbol{d}_K \quad \text{and} \quad \delta\boldsymbol{u}_K = \underline{\boldsymbol{N}} \cdot \delta\boldsymbol{d}_K \tag{2.52}$$

within the element K. Therein, the nodal displacements $\boldsymbol{d}_K^m$ are summarized to the elemental displacement vector $\boldsymbol{d}_K = \left[(\boldsymbol{d}_K^1)^{\text{T}},\, (\boldsymbol{d}_K^2)^{\text{T}},\, ...,\, (\boldsymbol{d}_K^{n^{\text{en}}})^{\text{T}}\right]^{\text{T}}$. Furthermore, the gradient of the shape functions is evaluated by

$$\tilde{\underline{\boldsymbol{B}}} = \text{Grad}(\underline{\boldsymbol{N}}) = \frac{\partial \underline{\boldsymbol{N}}}{\partial \boldsymbol{X}} = \frac{\partial \underline{\boldsymbol{N}}}{\partial \boldsymbol{\xi}} \cdot \frac{\partial \boldsymbol{\xi}}{\partial \boldsymbol{X}} = \frac{\partial \underline{\boldsymbol{N}}}{\partial \boldsymbol{\xi}} \cdot \boldsymbol{J}^{-1}. \tag{2.53}$$

which is rewritten into the matrix form $\underline{\boldsymbol{B}} = \left[\underline{\boldsymbol{B}}^1 | \underline{\boldsymbol{B}}^2 | \cdots | \underline{\boldsymbol{B}}^{n^{\text{en}}}\right]$ with the partial B-matrices $\underline{\boldsymbol{B}}^m$ of the node m. These partial matrices are of the form

$$\underline{\boldsymbol{B}}^m = \begin{bmatrix} \frac{\partial N^m}{\partial X_1} & 0 & 0 & \frac{\partial N^m}{\partial X_2} & 0 & \frac{\partial N^m}{\partial X_3} & 0 & 0 & 0 \\ 0 & \frac{\partial N^m}{\partial X_2} & 0 & 0 & \frac{\partial N^m}{\partial X_3} & 0 & \frac{\partial N^m}{\partial X_1} & 0 & 0 \\ 0 & 0 & \frac{\partial N^m}{\partial X_3} & 0 & 0 & 0 & 0 & \frac{\partial N^m}{\partial X_2} & \frac{\partial N^m}{\partial X_1} \end{bmatrix}^{\text{T}}. \tag{2.54}$$

The transformation with the two matrices $\underline{\boldsymbol{N}}$ and $\underline{\boldsymbol{B}}$ is inserted into the total energy potential (2.42), so that elemental form

$$\begin{aligned} \Pi_K = \int\limits_{\mathcal{B}_K} (\underline{\boldsymbol{B}} \cdot \boldsymbol{d}_K) \cdot \underline{\boldsymbol{P}}\, \text{d}V - \int\limits_{\partial_{\text{N}}\mathcal{B}_K} (\underline{\boldsymbol{N}} \cdot \boldsymbol{d}_K) \cdot \boldsymbol{t}_{\text{B}}\, \text{d}A \\ - \int\limits_{\mathcal{B}_K} \rho_0\, (\underline{\boldsymbol{N}} \cdot \boldsymbol{d}_K) \cdot (\boldsymbol{b}_0 - \underline{\boldsymbol{N}} \cdot \ddot{\boldsymbol{d}}_K)\, \text{d}V \end{aligned} \tag{2.55}$$

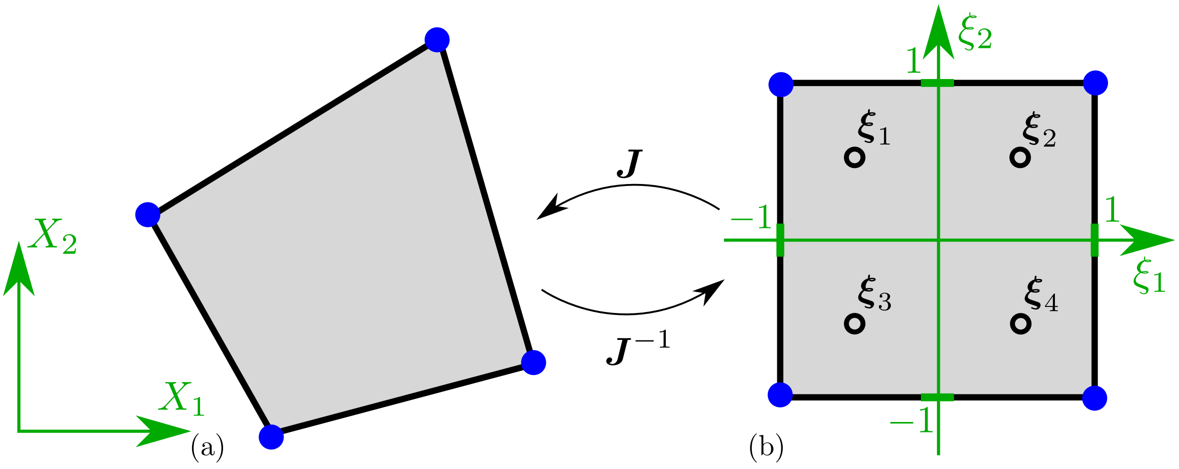

Figure 2.3.: (a) Quadrilateral element of a mesh in the reference configuration which is transformed into (b) the isoparametric space in order to evaluate the material response at the Gauß points $\boldsymbol{\xi}_l$.

follows. The underline $\underline{\bullet}$ indicates that the corresponding tensor is transformed into the Voigt notation which simplifies the numerical implementation by reducing the second order tensors to vectors and fourth order tensors to matrices, cf. appendix A. For example, the second order deformation gradient $\boldsymbol{F} = \mathrm{Grad}(\boldsymbol{u}) + \boldsymbol{I}$ is rewritten into $\underline{\boldsymbol{F}} = \underline{\boldsymbol{B}} \cdot \boldsymbol{d}_K + \underline{\boldsymbol{I}}$. By derivation of the first variation, one obtains the weak form of the potential energy

$$\begin{aligned}\delta\Pi_K = \delta\boldsymbol{d}_K \cdot \frac{\partial \Pi_K}{\partial \boldsymbol{d}_K} = \int\limits_{\mathcal{B}_K} (\underline{\boldsymbol{B}} \cdot \delta\boldsymbol{d}_K) \cdot \underline{\boldsymbol{P}}\,\mathrm{d}V - &\int\limits_{\partial_\mathrm{N}\mathcal{B}_K} (\underline{\boldsymbol{N}} \cdot \delta\boldsymbol{d}_K) \cdot \boldsymbol{t}_\mathrm{B}\,\mathrm{d}A \\ - &\int\limits_{\mathcal{B}_K} \rho_0\,(\underline{\boldsymbol{N}} \cdot \delta\boldsymbol{d}_K) \cdot (\boldsymbol{b}_0 - \underline{\boldsymbol{N}} \cdot \ddot{\boldsymbol{d}}_K)\,\mathrm{d}V.\end{aligned} \tag{2.56}$$

By considering the relation $\delta\Pi_K := \delta\boldsymbol{u} \cdot \boldsymbol{f}_K$, one obtains the vector of forces

$$\boldsymbol{f}_K = \underbrace{\int\limits_{\mathcal{B}_K} \underline{\boldsymbol{B}}^\mathrm{T} \cdot \underline{\boldsymbol{P}}\,\mathrm{d}V}_{:=\boldsymbol{r}_K} \underbrace{- \int\limits_{\partial_\mathrm{N}\mathcal{B}_K} \underline{\boldsymbol{N}}^\mathrm{T} \cdot \boldsymbol{t}_\mathrm{B}\,\mathrm{d}A - \int\limits_{\mathcal{B}_K} \rho_0\,\underline{\boldsymbol{N}}^\mathrm{T} \cdot \boldsymbol{b}_0\,\mathrm{d}V}_{:=\boldsymbol{q}_K} + \underbrace{\int\limits_{\mathcal{B}_K} \rho_0\,\underline{\boldsymbol{N}}^\mathrm{T} \cdot \underline{\boldsymbol{N}} \cdot \ddot{\boldsymbol{d}}_K\,\mathrm{d}V}_{:=\boldsymbol{r}_K^\mathrm{m}} \tag{2.57}$$

of element K on its nodes. Herein, the force $\boldsymbol{f}_K = \boldsymbol{r}_K + \boldsymbol{q}_K + \boldsymbol{r}_K^\mathrm{m}$ is split into a part of the internal forces $\boldsymbol{r}_K$, of the external forces $\boldsymbol{q}_K$ and of the inertia $\boldsymbol{r}_K^\mathrm{m}$. For evaluation of the integrals, the element K is transformed into the isoparametric space $\mathcal{B}_K^\mathrm{iso}$, so that they are derived for any field variable $v(\boldsymbol{X})$ by the integral

$$\int\limits_{\mathcal{B}_K} v\,(\boldsymbol{X})\ \mathrm{d}V = \int\limits_{\mathcal{B}_K^\mathrm{iso}} v\,(\boldsymbol{\xi})\ \det\left(\boldsymbol{J}\,(\boldsymbol{\xi})\right)\ \mathrm{d}V \tag{2.58}$$

over the isoparametric location variables $\boldsymbol{\xi}$. Hence, the matrix of shape functions $\underline{\boldsymbol{N}}$ and of derivatives of the shape functions $\underline{\boldsymbol{B}}$ are the same for all elements with the same geometrical shapes and assumed shape functions. For computation of the volume and surface integrals, the Gauß quadrature is applied. In this scheme, the volume integral of any field variable $v(\boldsymbol{X})$ is approximated by the sum

$$\int\limits_{\mathcal{B}_K} v\,(\boldsymbol{X})\ \mathrm{d}V \approx \sum_{l=1}^{n^\mathrm{GP}} w_l\,(\boldsymbol{\xi})\ v\,(\boldsymbol{\xi})\ \det\left(\boldsymbol{J}\,(\boldsymbol{\xi})\right)\big|_{\boldsymbol{\xi}_l} \tag{2.59}$$

of the field variable $v(\boldsymbol{X})$ evaluated at n^GP Gauß points with the coordinates $\boldsymbol{\xi}_l$ in the isoparametric space multiplied by the weighting factors w_l. Herein, the Gauß point coordinates $\boldsymbol{\xi}_l$ and their weighting factors w_l depend on the chosen types of shape functions, in our case n^en Lagrange polynomials. In terms of the elemental forces $\boldsymbol{f}_K$, the stress $\underline{\boldsymbol{P}}$, the matrices $\underline{\boldsymbol{N}}$, $\underline{\boldsymbol{B}}$ and the volume forces $\boldsymbol{b}_0$ are evaluated at the n^GP Gauß points. Applying this, the contributors to the nodal forces result in

$$\begin{aligned}\boldsymbol{r}_K &\approx \sum_{l=1}^{n^\mathrm{GP}} w_l\ \det(\boldsymbol{J})\,\underline{\boldsymbol{B}}^\mathrm{T} \cdot \underline{\boldsymbol{P}}\big|_{\boldsymbol{\xi}_l} \\ \boldsymbol{q}_K &\approx -\sum_{l=1}^{n^\mathrm{GP}} w_l\ \det(\boldsymbol{J})\,\left(\underline{\boldsymbol{N}}^\mathrm{T} \cdot \boldsymbol{t}_\mathrm{B} + \rho_0\,\underline{\boldsymbol{N}}^\mathrm{T} \cdot \boldsymbol{b}_0\right)\big|_{\boldsymbol{\xi}_l} \\ \boldsymbol{r}_K^\mathrm{m} &\approx \sum_{l=1}^{n^\mathrm{GP}} w_l\ \det(\boldsymbol{J})\,\rho_0\,\underline{\boldsymbol{N}}^\mathrm{T} \cdot \underline{\boldsymbol{N}} \cdot \ddot{\boldsymbol{d}}_K\Big|_{\boldsymbol{\xi}_l}.\end{aligned} \tag{2.60}$$

Note, that the dependencies on the variables $\boldsymbol{\xi}$ are dropped in the following for the sake of simplicity. The vector of internal forces $\boldsymbol{r}_K$ and external forces $\boldsymbol{q}_k$ are directly be evaluated based on $\boldsymbol{d}_K$, while the acceleration $\ddot{\boldsymbol{d}}_K$ which is necessary for the inertia $\boldsymbol{r}^{\mathrm{m}}$ has to be derived by numerical time integration.

2.2.4. Time discretization

The continuous time t is also discretized in order to solve the momentum balance. Therefore, the time is split into n^{t} time steps, so that the differential equation is evaluated at the time steps t_0, t_1, ..., t_n, t_{n+1}, ..., t_{n^t} in series. For the derivation of the displacements $\boldsymbol{d}$ in the so-called "current" time step t_{n+1}, the values of the previous time step t_n are taken into account. All necessary values of the previous time step are assumed to be known whereas the ones of the current time step are calculated. At the initial time t_0, the initial values have to be prescribed. Here, with decreasing increment $\Delta t = t_{n+1} - t_n$, the FE solution of the differential equation converges to the one of the original momentum balance. Hence, Δt has to be chosen small enough for an accurate approximation. Furthermore, a small time step size may increase numerical stability of the calculations. For the numerical integration of the acceleration $\ddot{\boldsymbol{u}}_{n+1}$ at the time step t_{n+1}, the Newmark-β method, as introduced in Newmark [101] is applied. This method provides the basic equations

$$\dot{\boldsymbol{u}}_{n+1} = \dot{\boldsymbol{u}}_n + \Delta t \left[(1-\gamma)\, \ddot{\boldsymbol{u}}_n + \gamma\, \ddot{\boldsymbol{u}}_{n+1} \right] \tag{2.61}$$

$$\mathbf{u}_{n+1} = \mathbf{u}_n + \Delta t\, \dot{\boldsymbol{u}}_n + \Delta t^2 \left[\left(\frac{1}{2} - \beta \right) \ddot{\boldsymbol{u}}_n + \beta\, \ddot{\boldsymbol{u}}_{n+1} \right] \tag{2.62}$$

with the Newmark parameters $0 \leq \beta \leq 1$ and $0 \leq \gamma \leq 1$. The parameter γ controls the interpolation of the acceleration between $\ddot{\boldsymbol{u}}_n$ and $\ddot{\boldsymbol{u}}_{n+1}$ for the calculation of the current velocity $\dot{\boldsymbol{u}}_{n+1}$ whereas the parameter γ controls the influence of these accelerations on the current displacement $\mathbf{u}_{n+1}$. By rearranging these equations, one obtains the current accelerations and velocities

$$\ddot{\boldsymbol{u}}_{n+1} = \frac{1}{\beta\,\Delta t^2} \left(\boldsymbol{u}_{n+1} - \boldsymbol{u}_n \right) - \frac{1}{\beta\,\Delta t}\, \dot{\boldsymbol{u}}_n - \left(\frac{1}{2\,\beta} - 1 \right) \ddot{\boldsymbol{u}}_n \tag{2.63}$$

and

$$\dot{\boldsymbol{u}}_{n+1} = \frac{\gamma}{\beta\,\Delta t} \left(\mathbf{u}_{n+1} - \mathbf{u}_n \right) + \left(1 - \frac{\gamma}{\beta} \right) \dot{\boldsymbol{u}}_n + \left(1 - \frac{\gamma}{2\,\beta} \right) \Delta t\, \ddot{\boldsymbol{u}}_n \tag{2.64}$$

that are derived and saved in every time step based on the current displacements $\boldsymbol{u}_{n+1}$ and the known displacements $\boldsymbol{u}_n$ and its derivatives of the previous time step. If $1/2 \leq \gamma \leq 2\,\beta$ holds, then the Newmark-β method is unconditionally stable regardless of the time step size Δt. If the parameters are set to $\beta = \frac{1}{4}$ and $\gamma = \frac{1}{2}$, average constant acceleration is obtained. By applying the time discretization and the Newmark scheme and by considering the nodal accelerations $\ddot{\boldsymbol{d}}$ instead of the accelerations $\ddot{\boldsymbol{u}}$, one obtains the inertia

$$\begin{aligned} \boldsymbol{r}_K^{\mathrm{m}} &= \int\limits_{\mathcal{B}_K} \rho_0\, \underline{\boldsymbol{N}}^{\mathrm{T}} \cdot \underline{\boldsymbol{N}} \cdot \left(\frac{1}{\beta\,\Delta t^2} \left(\boldsymbol{d}_K - \boldsymbol{d}_{K,n} \right) - \frac{1}{\beta\,\Delta t}\, \dot{\boldsymbol{d}}_{K,n} - \left(\frac{1}{2\,\beta} - 1 \right) \ddot{\boldsymbol{d}}_{K,n} \right) \mathrm{d}V \\ &\approx \sum_{l=1}^{n^{\mathrm{GP}}} w_l\, \det(\boldsymbol{J})\, \rho_0\, \underline{\boldsymbol{N}}^{\mathrm{T}} \cdot \underline{\boldsymbol{N}} \cdot \left(\frac{1}{\beta\,\Delta t^2} \left(\boldsymbol{d}_K - \boldsymbol{d}_{K,n} \right) - \frac{1}{\beta\,\Delta t}\, \dot{\boldsymbol{d}}_{K,n} - \left(\frac{1}{2\,\beta} - 1 \right) \ddot{\boldsymbol{d}}_{K,n} \right) \Bigg|_{\boldsymbol{\xi}_l} \end{aligned} \tag{2.65}$$

of the force vector $\boldsymbol{f}_K$. For simplicity, the index $\bullet_{n+1}$ of all variables at the current time step is dropped. Here, $\boldsymbol{d}_K$ in the current time step is the unknown which the overall system is solved for. Afterwards, the accelerations $\ddot{\boldsymbol{u}}$ and the velocities $\ddot{\boldsymbol{u}}$ are derived for the incorporation of the dynamics in the next time step.

2.2.5. Solving procedure

Resulting from the first variation of the potential $\delta\Pi = \delta\boldsymbol{u}\cdot\boldsymbol{f} = \boldsymbol{0}$, the global force vector $\boldsymbol{f} = \boldsymbol{0}$ has to vanish in order to ensure, that this equation holds for any $\delta\boldsymbol{u}$. In terms of FEM, $\boldsymbol{f}$ is considered as the global vector of nodal forces which results from the elemental forces $\boldsymbol{f}_K$. In order to determine the global vector of displacements $\boldsymbol{D}$, which contains the components of the elemental displacement vector $\boldsymbol{d}_K$ of all elements, the nonlinear equation $\boldsymbol{f}(\boldsymbol{D})$ is solved iteratively with the Newton-Raphson scheme. Therefore, the linearization of the nonlinear system of equations is required. Here, the elemental force vector is linearized by

$$\operatorname{lin}(\boldsymbol{f}_K) = \boldsymbol{f}_K + \frac{\partial \boldsymbol{f}_K}{\partial \boldsymbol{d}_K} \cdot \Delta\boldsymbol{d}_K \tag{2.66}$$

with respect to the unknown nodal displacements $\boldsymbol{d}_K$. The term $\Delta\boldsymbol{d}_K$ denotes an increment of the nodal displacements $\boldsymbol{d}_K$. Here, the derivative

$$\frac{\partial \boldsymbol{f}_K}{\partial \boldsymbol{d}_K} = \underbrace{\frac{\partial \boldsymbol{r}_K}{\partial \boldsymbol{d}_K}}_{:=\boldsymbol{k}_K} + \underbrace{\frac{\partial \boldsymbol{q}_K}{\partial \boldsymbol{d}_K}}_{=\boldsymbol{0}} + \underbrace{\frac{\partial \boldsymbol{r}_K^{\mathrm{m}}}{\partial \boldsymbol{d}_K}}_{:=\boldsymbol{m}_K} \tag{2.67}$$

is evaluated. Note, that the derivative $\frac{\partial \boldsymbol{q}_K}{\partial \boldsymbol{d}_K}$ becomes zero because the external forces are independent from the nodal movements. Inserting the relations of the equations (2.57) and (2.60), one obtains the elemental stiffness matrix

$$\boldsymbol{k}_K = \int\limits_{\mathcal{B}_K} \underline{\boldsymbol{B}}^{\mathrm{T}} \cdot \frac{\partial \underline{\boldsymbol{P}}}{\partial \boldsymbol{d}_K} \,\mathrm{d}V = \int\limits_{\mathcal{B}_K} \underline{\boldsymbol{B}}^{\mathrm{T}} \cdot \underbrace{\frac{\partial \underline{\boldsymbol{P}}}{\partial \underline{\boldsymbol{F}}}}_{:=\underline{\mathbb{A}}} \cdot \underbrace{\frac{\partial \underline{\boldsymbol{F}}}{\partial \boldsymbol{d}_K}}_{=\underline{\boldsymbol{B}}} \,\mathrm{d}V \approx \sum_{l=1}^{n^{\mathrm{GP}}} w_l \,\det(\boldsymbol{J})\, \underline{\boldsymbol{B}}^{\mathrm{T}} \cdot \underline{\mathbb{A}} \cdot \underline{\boldsymbol{B}}\Big|_{\boldsymbol{\xi}_l} \tag{2.68}$$

containing the nominal material tangent $\mathbb{A} := \frac{\partial \boldsymbol{P}}{\partial \boldsymbol{F}}$, which depends on the mechanical properties at the Gauß point. The stresses and material tangents are derived from the material law which may not necessarily provide these values in the same configuration as the first Piola-Kirchhoff stress $\boldsymbol{P}$ and nominal material tangent $\mathbb{A}$. Here, the material laws are formulated in the spatial description with the Kirchhoff stress $\boldsymbol{\tau} = \boldsymbol{P} \cdot \boldsymbol{F}^{\mathrm{T}}$ and the spatial material tangent $\mathfrak{c}_{\boldsymbol{\tau}} = 2\frac{\partial \boldsymbol{\tau}}{\partial \boldsymbol{b}} \cdot \boldsymbol{b}$. To include these in the given FE equations, the first Piola-Kirchhoff stress is evaluated by equation 2.21 and the components of the nominal material tangent by the expression $[\mathbb{A}]_{ijkl} = \left([\mathfrak{c}_{\boldsymbol{\tau}}]_{ijkl} + \delta_{ik}\,[\boldsymbol{\tau}]_{ijkl}\right) F^{-1}_{mj} F^{-1}_{nl}$. In our implementation of the FEM, different mass matrices $\boldsymbol{m}_K$ are considered. Analogously to the stiffness matrix $\boldsymbol{k}_K$, the consistent mass matrix

$$\boldsymbol{m}_K^{\mathrm{CMM}} = \int\limits_{\mathcal{B}_K} \frac{\rho_0}{\beta\,\Delta t^2}\, \underline{\boldsymbol{N}}^{\mathrm{T}} \cdot \underline{\boldsymbol{N}} \,\mathrm{d}V \approx \sum_{l=1}^{n^{\mathrm{GP}}} w_l \,\det(\boldsymbol{J})\, \frac{\rho_0}{\beta\,\Delta t^2}\, \underline{\boldsymbol{N}}^{\mathrm{T}} \cdot \underline{\boldsymbol{N}}\Bigg|_{\boldsymbol{\xi}_l} \tag{2.69}$$

is derived. This matrix is commonly applied in FE approaches. If the consistent mass matrix $\boldsymbol{m}^{\mathrm{CMM}}$ is considered as the mass matrix $\boldsymbol{m}_K$, the inertia effects of every node influences the nodal forces at every other node of the element. In many applications, this property is desired, but if the nodes are supposed to be able to move independently from each other, the lumped mass matrix

$$\left[\boldsymbol{m}_K^{\mathrm{LMM}}\right]_{ij} = \begin{cases} \sum\limits_{i} \left[\boldsymbol{m}_K^{\mathrm{CMM}}\right]_{ij} & \text{if } i = j \\ 0 & \text{otherwise} \end{cases} , \tag{2.70}$$

which is evaluated based on the components of the consistent mass matrix $[\boldsymbol{m}_K^{\mathrm{CMM}}]_{ij}$, is chosen. This method to evaluate the lumped mass matrix is called “row sum method”. Therein, only the entries of the diagonal are occupied with nonzero values. Hence, the mass of the element is spread onto the nodes. This leads to the decoupling of the nodal movements in terms of inertia. Because of this property, the lumped mass matrix $\boldsymbol{m}_K^{\mathrm{LMM}}$ is applied in the eigenerosion framework for crack propagation, to ensure that the crack surfaces are traction-free. To solve the global equilibrium $\boldsymbol{f} = \boldsymbol{0}$, the displacements of all nodes are summarized in the global displacement vector $\boldsymbol{D}$. For the projection of the nodal displacements $\boldsymbol{d}_K$ of the elements onto the global vector $\boldsymbol{D}$, the unification operator $\bigcup$ is applied. Using this, the relations

$$\boldsymbol{D} = \bigcup_{K=1}^{n^{\mathrm{el}}} \boldsymbol{d}_K \qquad \text{and} \qquad \Delta\boldsymbol{D} = \bigcup_{K=1}^{n^{\mathrm{el}}} \Delta\boldsymbol{d}_K \tag{2.71}$$

for the global vector of displacements $\boldsymbol{D}$ and its increment $\Delta\boldsymbol{D}$ are obtained. Note, that the degrees of freedom, that are prescribed as Dirichlet boundary conditions, do not occur in these vectors. Furthermore, the global stiffness matrix $\boldsymbol{K}$, the global mass matrix $\boldsymbol{M}$, the global vector of internal forces $\boldsymbol{R}$, the global vector of inertia forces $\boldsymbol{R}^{\mathrm{m}}$ and the global vector of external forces $\boldsymbol{Q}$ are evaluated by

$$\boldsymbol{K} := \mathop{\mathsf{A}}_{K=1}^{n^{\mathrm{el}}} \boldsymbol{k}_K, \quad \boldsymbol{M} := \mathop{\mathsf{A}}_{K=1}^{n^{\mathrm{el}}} \boldsymbol{m}_K, \quad \boldsymbol{R} := \mathop{\mathsf{A}}_{K=1}^{n^{\mathrm{el}}} \boldsymbol{r}_K, \quad \boldsymbol{R}^{\mathrm{m}} := \mathop{\mathsf{A}}_{K=1}^{n^{\mathrm{el}}} \boldsymbol{r}_K^{\mathrm{m}} \text{ and } \boldsymbol{Q} := \mathop{\mathsf{A}}_{K=1}^{n^{\mathrm{el}}} \boldsymbol{q}_K. \tag{2.72}$$

The assembly operator A indicates that the entries of the elemental vectors and matrices are added up in global vectors and matrices under the consideration of the location of the degrees of freedom in the global displacement vector $\boldsymbol{D}$. With these, the global force vector

$$\boldsymbol{f} = \boldsymbol{R} + \boldsymbol{R}^{\mathrm{m}} + \boldsymbol{Q} \tag{2.73}$$

and its linearization

$$\operatorname{lin}(\boldsymbol{f}) = \boldsymbol{R} + \boldsymbol{R}^{\mathrm{m}} + \boldsymbol{Q} + (\boldsymbol{K} + \boldsymbol{M}) \cdot \Delta\boldsymbol{D} \tag{2.74}$$

are obtained. In the Newton-Raphson scheme, the system of equations $\operatorname{lin}(\boldsymbol{f}) \overset{!}{=} \boldsymbol{0}$, which leads to

$$(\boldsymbol{K} + \boldsymbol{M}) \cdot \Delta\boldsymbol{D} = -\boldsymbol{R} - \boldsymbol{R}^{\mathrm{m}} - \boldsymbol{Q}, \tag{2.75}$$

which is solved for $\Delta\boldsymbol{D}$ in every iteration step. Afterwards, the global displacement vector $\boldsymbol{D} \Leftarrow \boldsymbol{D} + \Delta\boldsymbol{D}$ is updated. This process is repeated until a chosen convergence criterion, e.g., the displacement norm $|\Delta\boldsymbol{D}|$, the residual norm $|\boldsymbol{R} + \boldsymbol{R}^{\mathrm{m}} + \boldsymbol{Q}|$ or the energy norm $|\Delta\boldsymbol{D} \cdot (\boldsymbol{R} + \boldsymbol{R}^{\mathrm{m}} + \boldsymbol{Q})|$ becomes lower than a specified tolerance *tol*. With this procedure, the displacement field $\boldsymbol{u}$, which fulfills the mechanical equilibrium is approximated. The number of linearized equations in the Newton-Raphson scheme is defined as n_{eq} and strongly influences the computational effort. The global vectors $\boldsymbol{R}$, $\boldsymbol{R}^{\mathrm{m}}$, $\boldsymbol{Q}$ are of the size $n_{\mathrm{eq}} \times 1$ and the global matrices $\boldsymbol{K}$ and $\boldsymbol{M}$ of the size $n_{\mathrm{eq}} \times n_{\mathrm{eq}}$. For comparison of different approaches, the computational effort is divided into two parts. The first one results from the assembly of the system of linearized equations of the Newton-Raphson scheme, whereas the second part is the effort for solving the system of linearized equations.

2.3. Constitutive laws

In this section, the material models or so-called **constitutive laws** are presented. In terms of the FEM, the material models describe the relation between a deformation measure to the resulting stress and material tangent. Technically, they are implemented into material routines that take the deformation gradient as input and derive the stresses and material tangent as output for every Gauß point. In particular, the focus lies on the Neo-Hookean hyperelasticity model, the J_2-elasto-plasticity and an extension to elasto-viscoplasticity at large strains that represent typical material behavior of metallic materials and carbides. Here, the elastic material behavior is assumed for the brittle carbides and the elasto-plastic and elasto-viscoplastic material behavior for the metal matrices. Here, the material models underlie finite strains instead of small strains because it is a known from, e.g., Schüler et al. [130] that in microstructures large strains may occur even though only small strains are applied macroscopically.

2.3.1. Neo-Hookean hyperelasticity

As the first material model, the Neo-Hookean hyperelasticity for compressible solids, as seen in Rivlin [116] is introduced. Here, the free Helmholtz energy density reads

$$\psi = \frac{\kappa}{2}\,\ln(J)^2 + \frac{\mu}{2}\,(\mathrm{tr}(\bar{\boldsymbol{C}}) - 3) \tag{2.76}$$

with the bulk modulus κ and the shear modulus μ. This energy is split into a volumetric part which describes the energy due to pure change in the volume of a body J without the change of the shape and the isochoric part that only considers the pure deviation by taking into account the purely isochoric right Cauchy stretch tensor $\bar{\boldsymbol{C}}$. For the derivation of the stress, the derivative

$$\boldsymbol{S} = \frac{\partial\psi}{\partial\boldsymbol{E}} = \frac{\partial\psi}{\partial\boldsymbol{C}} : \frac{\partial\boldsymbol{C}}{\partial\boldsymbol{E}} = 2\,\frac{\partial\psi}{\partial\boldsymbol{C}} = 2\,\frac{\partial\psi}{\partial J}\frac{\partial J}{\partial I_3}\frac{\partial I_3}{\partial\boldsymbol{C}} + 2\,\frac{\partial\psi}{\partial\bar{\boldsymbol{C}}} : \frac{\partial\bar{\boldsymbol{C}}}{\partial\boldsymbol{C}} \tag{2.77}$$

is evaluated with the chain rule and the derivatives in equations 2.13, so that the second Piola-Kirchhoff stress

$$\boldsymbol{S} = \kappa\,\ln(J)\,\boldsymbol{C}^{-1} + \mu\,J^{-\frac{2}{3}}\,(\boldsymbol{I} - \tfrac{1}{3}\,I_1\,\boldsymbol{C}^{-1}) \tag{2.78}$$

in the reference configuration and, by application of the pushforward operation, the Kirchhoff stress

$$\boldsymbol{\tau} = 2\,\boldsymbol{b}\cdot\frac{\partial\psi}{\partial\boldsymbol{b}} = \boldsymbol{F}\cdot\boldsymbol{S}\cdot\boldsymbol{F}^{\mathrm{T}} = \kappa\,\ln(J)\,\boldsymbol{I} + 2\,\mu\,\mathrm{dev}(\bar{\boldsymbol{b}}) \tag{2.79}$$

follow. Furthermore, the material tangent $\mathfrak{c}_{\boldsymbol{\tau}}$ regarding the Kirchhoff stress is evaluated by the derivation

$$\begin{aligned}\mathfrak{c}_{\boldsymbol{\tau}} &= 4\,\boldsymbol{b}\cdot\frac{\partial^2\psi}{\partial\boldsymbol{b}^2}\cdot\boldsymbol{b} = 2\,\frac{\partial\boldsymbol{\tau}}{\partial\boldsymbol{b}}\cdot\boldsymbol{b} = 2\,\frac{\partial\boldsymbol{\tau}}{\partial J}\frac{\partial J}{\partial I_3}\otimes\frac{\partial I_3}{\partial\boldsymbol{b}}\cdot\boldsymbol{b} + 2\,\frac{\partial\boldsymbol{\tau}}{\partial\bar{\boldsymbol{b}}} : \frac{\partial\bar{\boldsymbol{b}}}{\partial\boldsymbol{b}}\cdot\boldsymbol{b} && (2.80)\\ &= \frac{\kappa}{J}\,\boldsymbol{I}\otimes\boldsymbol{I} + 2\,\mu J^{-\frac{2}{3}}\left[\tfrac{1}{4}\,(\boldsymbol{I}\otimes\boldsymbol{b})^{\overset{23}{\mathrm{T}}} + \tfrac{1}{4}\,(\boldsymbol{I}\otimes\boldsymbol{b})^{\overset{24}{\mathrm{T}}} - \tfrac{1}{3}\,\boldsymbol{I}\otimes\boldsymbol{b} - \tfrac{1}{3}\,\boldsymbol{b}\otimes\boldsymbol{I} + \tfrac{1}{9}\,\mathrm{tr}(\boldsymbol{b})\,\boldsymbol{I}\otimes\boldsymbol{I}\right], && (2.81)\end{aligned}$$

as shown in Simo and Hughes [135], which is necessary for the implementation in FE frameworks.

2.3.2. Finite strain J_2-elasto-plasticity

For modeling the ductile crack propagation through metallic materials, an elasto-plastic material model is necessary. Here, the von Mises or so-called J_2-elasto-plasticity at finite strains with isotropic hardening, as seen Simo [134], Simo and Miehe [136], Simo et al. [137], is applied. For the numerical implementation see Miehe et al. [89] and Klinkel [63]. For this material model, the concept of mechanical configurations is extended by an intermediate configuration, as seen in figure 2.4, following the basic concept of Kröner [65] and Lee [74]. By

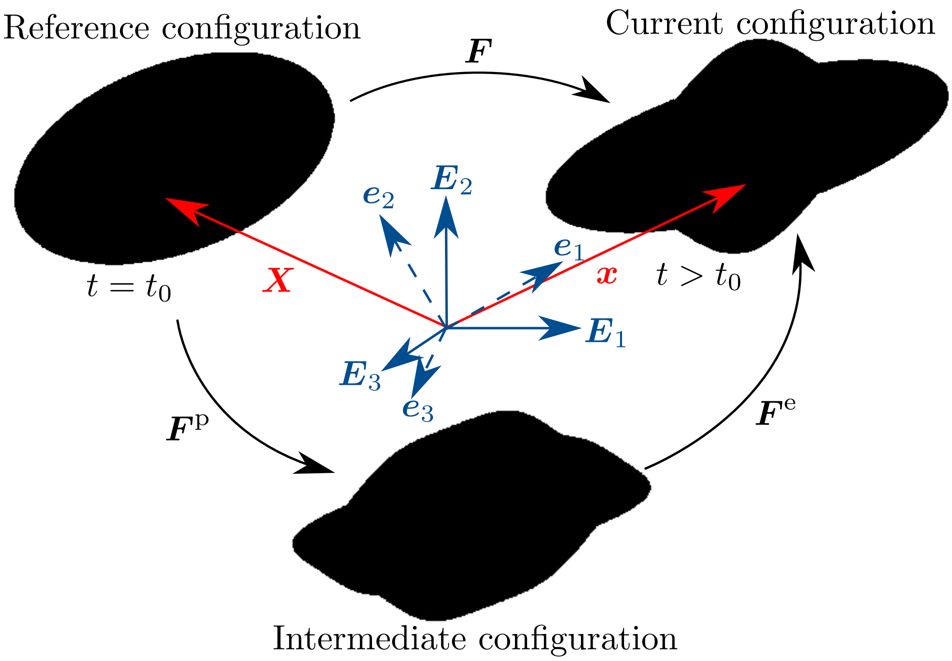

Figure 2.4.: Undeformed body $\mathcal{B}_0$ in the reference configuration at $t = t_0$, deformed body $\mathcal{B}_{\mathrm{i}}$ in the intermediate and $\mathcal{B}_t$ in the current configuration at $t > t_0$.

considering this additional configuration, the deformation gradient is split multiplicatively

$$\boldsymbol{F} = \boldsymbol{F}^{\mathrm{e}} \cdot \boldsymbol{F}^{\mathrm{p}} \tag{2.82}$$

into a purely plastic part $\boldsymbol{F}^{\mathrm{p}}$, which maps from the reference configuration $\mathcal{B}_0$ onto the plastic intermediate configuration $\mathcal{B}_{\mathrm{i}}$, and a purely plastic part $\boldsymbol{F}^{\mathrm{p}}$, which maps from intermediate $\mathcal{B}_{\mathrm{i}}$ onto the current configuration $\mathcal{B}_t$. Here, it is assumed that no stresses occur in the intermediate configuration $\mathcal{B}_{\mathrm{i}}$ and that the stresses exclusively result from elastic deformations between the intermediate and the current configuration. Analogously to the basic continuum mechanics in which only two configurations are assumed, the deformation measures can be derived between the different configurations. Therefore, the elastic left Cauchy-Green tensor, that describes the purely elastic deformation between the intermediate and current configuration, and its spectral decomposition result in

$$\boldsymbol{b}^{\mathrm{e}} := \boldsymbol{F}^{\mathrm{e}} \cdot \boldsymbol{F}^{\mathrm{eT}} = \sum_{i=1}^{3} (\lambda_i^{\mathrm{e}})^2 \, \boldsymbol{n}_i \otimes \boldsymbol{n}_i \tag{2.83}$$

with the square root of the elastic eigenvalues λ_i^{e}, that are physically seen as the principal elastic stretches, and the corresponding eigenvectors $\boldsymbol{n}_i$ in the current configuration. With the application of the principal logarithmic elastic strains $\varepsilon_i^{\mathrm{e}} = \log(\lambda_i^{\mathrm{e}})$, the elastic strain tensor

$$\boldsymbol{\varepsilon}^{\mathrm{e}} := \sum_{i=1}^{3} \varepsilon_i^{\mathrm{e}} \, \boldsymbol{n}_i \otimes \boldsymbol{n}_i \tag{2.84}$$

is constructed in the logarithmic representation. This enables the additive split of the strain $\boldsymbol{\varepsilon} = \boldsymbol{\varepsilon}^{\mathrm{e}} + \boldsymbol{\varepsilon}^{\mathrm{p}}$ into an elastic part $\boldsymbol{\varepsilon}^{\mathrm{e}}$ and a plastic part and $\boldsymbol{\varepsilon}^{\mathrm{p}}$. The Helmholtz energy density

$$\psi = \psi^{\mathrm{e}}(\boldsymbol{\varepsilon}^{\mathrm{e}}) + \psi^{\mathrm{p}}(\alpha) \tag{2.85}$$

is divided into an elastic part $\psi^{\mathrm{e}}(\boldsymbol{\varepsilon}^{\mathrm{e}})$ only depending on the elastic strains $\boldsymbol{\varepsilon}^{\mathrm{e}}$ and the plastic part $\psi^{\mathrm{p}}(\alpha)$ that depends on the equivalent plastic strain α. For the elastic part, the quadratic elastic free energy function

$$\psi^{\mathrm{e}} = \frac{\kappa}{2}\,\mathrm{tr}(\boldsymbol{\varepsilon}^{\mathrm{e}})^2 + \mu\,\mathrm{dev}(\boldsymbol{\varepsilon}^{\mathrm{e}}) : \mathrm{dev}(\boldsymbol{\varepsilon}^{\mathrm{e}}) \tag{2.86}$$

containing the compression modulus κ and the shear modulus μ is assumed. Note, that Raoult [115] proved that in this free energy density the polyconvexity condition with respect to the deformation gradient $\boldsymbol{F}$, as introduced in Ball [6] is not fulfilled so that uniqueness of the solution of the global momentum balance is not guaranteed anymore. The plastic dissipation potential

$$\psi^{\mathrm{p}} = y_0\,\alpha + (y_\infty - y_0)\,\left[\alpha + \frac{\exp(-h^{\exp}\,\alpha) - 1}{h^{\exp}}\right] + \frac{1}{2}\,h^{\mathrm{lin}}\,\alpha^2 \tag{2.87}$$

is chosen as superposition of linear and exponential type hardening, as seen in Voce [144], with the equivalent plastic strain α and the material parameters in the form of the degree of exponential hardening $h^{\exp}$, the slope of the superimposed linear hardening h^{lin}, the initial yield strength y_0 and the plastic yield strength y_∞ at the beginning of the purely linear hardening. By derivation, we obtain the hardening function

$$\beta = \frac{\partial\,\psi^{\mathrm{p}}}{\partial\,\alpha} = y_0 + (y_\infty - y_0)\,\left[1 - \exp(-h^{\exp}\,\alpha)\right] + h^{\mathrm{lin}}\,\alpha. \tag{2.88}$$

For the decision if the plastic flow occurs, the flow condition

$$\phi(\boldsymbol{\tau}, \alpha) = \tau^{\mathrm{vM}}(\boldsymbol{\tau}) - \beta(\alpha) \leq 0, \tag{2.89}$$

is assumed, which compares the isotropic hardening function β to the von Mises stress

$$\tau^{\mathrm{vM}}(\boldsymbol{\tau}) = \sqrt{\frac{3}{2}}\,||\mathrm{dev}(\boldsymbol{\tau})||. \tag{2.90}$$

This measure ensures plastic incompressibility which means that the plastic deformation only occurs in the deviatoric part of the stress tensor which is observed in metal plasticity. This assumption results in a cylindrical yield surface in the principal stress space (τ_1,τ_2,τ_3), as seen in figure 2.5. Plasticity deformations occur, if a stress state lies on the surface of the cylinder. If the stress state is in the cylinder, the plastic deformations do not increase. Stress states outside the cylinder are prohibited. Note, that the name J_2-elasto-plasticity origins from the second deviatoric invariant $J_2 = \frac{1}{2}\,\mathrm{dev}(\boldsymbol{\tau}) : \mathrm{dev}(\boldsymbol{\tau})$ which appears in the derivation of the von Mises stress $\tau^{\mathrm{vM}}(\boldsymbol{\tau})$. Together with the plastic internal variable $\lambda^{\mathrm{p}} \geq 0$, the Kuhn-Tucker

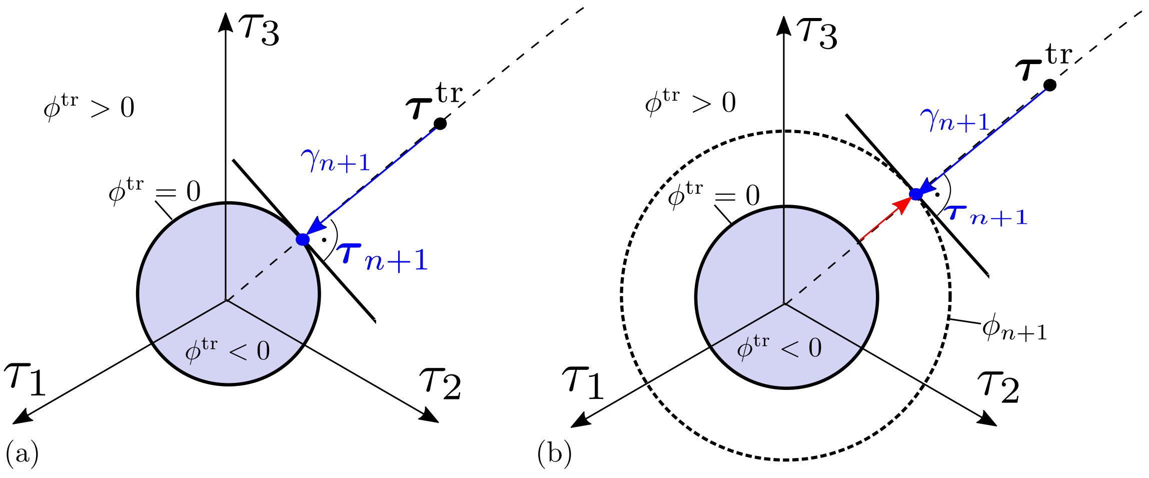

Figure 2.5.: Yield surface in the principal stress space (τ_1,τ_2,τ_3) with a trial stress $\boldsymbol{\tau}^{\mathrm{tr}}$ for elasto-plasticity (a) without hardening and (b) with hardening.

condition

$$\phi\,\lambda^{\mathrm{p}} = 0 \tag{2.91}$$

is fulfilled, in which the Lagrange multiplier λ^{p} describes the plastic flow. This equation holds, because either $\lambda^{\mathrm{p}} = 0$ if purely elastic deformations occur ($\phi < 0$) or $\phi = 0$ if the plastic deformations increase with the internal variable λ^{p}. To derive the plastic flow, the dissipation inequality in equation 2.38 has to be evaluated under consideration of the Kuhn-Tucker condition so that the minimization problem

$$-\,\mathcal{D} + \phi\,\lambda^{\mathrm{p}} = -\boldsymbol{\tau} : \boldsymbol{d} + \dot{\psi} + \phi\,\lambda^{\mathrm{p}} = -\boldsymbol{\tau} : \boldsymbol{d} + \frac{\partial \psi^{\mathrm{e}}}{\partial \boldsymbol{b}^{\mathrm{e}}} \cdot \dot{\boldsymbol{b}}^{\mathrm{e}} + \frac{\partial \psi^{\mathrm{p}}}{\partial \alpha}\dot{\alpha} + \phi\,\lambda^{\mathrm{p}} \leq 0 \tag{2.92}$$

has to be solved to maximize the dissipation $\mathcal{D}$. Therefore, the time derivative

$$\dot{\boldsymbol{b}}^{\mathrm{e}} = \boldsymbol{l} \cdot \boldsymbol{b}^{\mathrm{e}} + \boldsymbol{b}^{\mathrm{e}} : \boldsymbol{l}^{\mathrm{T}} + \mathcal{L}(\boldsymbol{b}^{\mathrm{e}}) \tag{2.93}$$

is applied to extend the minimization problem to

$$\left(-\boldsymbol{\tau} + 2\,\frac{\partial \psi}{\partial \boldsymbol{b}^{\mathrm{e}}} \cdot \boldsymbol{b}^{\mathrm{e}}\right) \cdot \boldsymbol{d}_s + \left(2\,\frac{\partial \psi}{\partial \boldsymbol{b}^{\mathrm{e}}} \cdot \boldsymbol{b}^{\mathrm{e}}\right) : \left(\tfrac{1}{2}\mathcal{L}(\boldsymbol{b}^{\mathrm{e}}) \cdot (\boldsymbol{b}^{\mathrm{e}})^{-1}\right) + \frac{\partial \psi^{\mathrm{p}}}{\partial \alpha}\dot{\alpha} + \phi\,\lambda^{\mathrm{p}} \leq 0. \tag{2.94}$$

To ensure, that this inequality holds for arbitrary $\boldsymbol{d}_s$, it is assumed that the factor in front of it becomes zero. Hence, the equation

$$\boldsymbol{\tau} = 2\,\frac{\partial \psi^{\mathrm{e}}}{\partial \boldsymbol{b}^{\mathrm{e}}} \cdot \boldsymbol{b}^{\mathrm{e}} = 2\,\frac{\partial \psi^{\mathrm{e}}}{\partial \boldsymbol{\varepsilon}^{\mathrm{e}}} \cdot \sum_{i=1}^{3} \frac{\partial \boldsymbol{\varepsilon}^{\mathrm{e}}}{\partial \lambda_i^{\mathrm{e}}} \frac{\partial \lambda_i^{\mathrm{e}}}{\partial (\lambda_i^{\mathrm{e}})^2} \frac{\partial (\lambda_i^{\mathrm{e}})^2}{\partial \boldsymbol{b}^{\mathrm{e}}} \cdot \boldsymbol{b}^{\mathrm{e}} = \kappa\,\mathrm{tr}(\boldsymbol{\varepsilon}^{\mathrm{e}})\,\boldsymbol{I} + 2\,\mu\,\mathrm{dev}(\boldsymbol{\varepsilon}^{\mathrm{e}}). \tag{2.95}$$

holds for the Kirchhoff stress $\boldsymbol{\tau}$. With this assumption, the dissipation inequality is simplified to

$$f_{\mathcal{D}} := \boldsymbol{\tau} : \left(\tfrac{1}{2}\mathcal{L}(\boldsymbol{b}^{\mathrm{e}}) \cdot (\boldsymbol{b}^{\mathrm{e}})^{-1}\right) + \beta\,\dot{\alpha} + \phi\,\lambda^{\mathrm{p}} \leq 0. \tag{2.96}$$

To find the minimum of $f_{\mathcal{D}}$, the derivatives with respect to $\boldsymbol{\tau}$, β and λ^{p} are derived and set to zero. Based on this, the evolution equations are evaluated to

$$\frac{\partial f_{\mathcal{D}}}{\partial \boldsymbol{\tau}} = \left(\tfrac{1}{2}\mathcal{L}(\boldsymbol{b}^{\mathrm{e}}) \cdot (\boldsymbol{b}^{\mathrm{e}})^{-1}\right) + \lambda^{\mathrm{p}}\frac{\partial \phi}{\partial \boldsymbol{\tau}} \overset{!}{=} 0 \rightarrow \quad \left(\tfrac{1}{2}\mathcal{L}(\boldsymbol{b}^{\mathrm{e}}) \cdot (\boldsymbol{b}^{\mathrm{e}})^{-1}\right) = -\lambda^{\mathrm{p}}\frac{3}{2}\,\frac{\mathrm{dev}(\boldsymbol{\tau})}{\tau^{\mathrm{vM}}(\boldsymbol{\tau})} \tag{2.97}$$

$$\frac{\partial f_{\mathcal{D}}}{\partial \beta} = \dot{\alpha} + \lambda^{\mathrm{p}}\frac{\partial \phi}{\partial \beta} \overset{!}{=} 0 \rightarrow \quad \dot{\alpha} = \lambda^{\mathrm{p}} \tag{2.98}$$

$$\frac{\partial f_{\mathcal{D}}}{\partial \lambda^{\mathrm{p}}} = \phi \overset{!}{=} 0 \rightarrow \quad \phi = 0 \tag{2.99}$$

so that the plastic flow λ^{p} is the last variable to determine the evolution of the plastic deformation. For the case that $\phi < 0$ holds, no additional plastic deformations occur and thus, $\dot{\alpha} = \lambda^{\mathrm{p}} = 0$ holds for the Lagrange multiplier. Otherwise, if $\phi = 0$ holds, the plastic deformations increase and thus, the Lagrange multiplier λ^{p} becomes larger than zero. Furthermore, $\phi > 0$ is not allowed.

As a basic concept for the algorithmic treatment, the trial value of the Kirchhoff stress

$$\boldsymbol{\tau}^{\mathrm{tr}} = \boldsymbol{\tau}(\boldsymbol{\varepsilon}_{n+1} - \boldsymbol{\varepsilon}_n^{\mathrm{p}}), \tag{2.100}$$

which is derived on the basis of the plastic deformations of the previous time step $\boldsymbol{\varepsilon}_n^{\mathrm{p}}$, is compared to the current isotropic hardening $\beta(\alpha_n)$, so that the trial flow condition

$$\phi^{\mathrm{tr}} = \phi(\boldsymbol{\tau}^{\mathrm{tr}}, \alpha_n) \tag{2.101}$$

decides whether additional plastic deformations occur or not within the corresponding time step. This procedure is also called **predictor** step. If the trial stress $\boldsymbol{\tau}^{\mathrm{tr}}$ lies within the cylinder in the principal stress space, so that $\phi^{\mathrm{tr}} < 0$ holds, no further plastic deformations occur. Hence, the current internal variables $\alpha_{n+1} = \alpha_n$ and $\boldsymbol{\varepsilon}_{n+1} = \boldsymbol{\varepsilon}_n$ equal to the previous ones and the stress $\boldsymbol{\tau}_{n+1} = \boldsymbol{\tau}^{\mathrm{tr}}$ equals the trial stress in that case. Furthermore, the material tangent results in the purely elastic derivative

$$\mathfrak{c}^{\mathrm{e}}_{\boldsymbol{\tau}} = \frac{\partial \boldsymbol{\tau}}{\partial \boldsymbol{\varepsilon}^{\mathrm{e}}} = \kappa\, \boldsymbol{I} \otimes \boldsymbol{I} + 2\,\mu\,\mathbb{P} \tag{2.102}$$

with the tensor $\mathbb{P} = \mathbb{I} - \frac{1}{3}\boldsymbol{I} \otimes \boldsymbol{I}$. However, if $\phi^{\mathrm{tr}} > 0$, additional plastic deformation occurs and therefore, the equivalent plastic strain α_{n+1} has to be updated in such a way that $\phi_{n+1}(\boldsymbol{\tau}_{n+1}, \alpha_{n+1}) \overset{!}{=} 0$ holds. This update is also known as **plastic corrector** step. In terms of the yield surface in the principal stress space, cf. figure 2.5b, this procedure represents the radial return of the trial stress $\boldsymbol{\tau}^{\mathrm{tr}}$ onto the increased yield surface. Based on this, the evolution of the equivalent plastic strain is assumed as

$$\alpha_{n+1} = \alpha_n + \gamma_{n+1} \tag{2.103}$$

with the increase in the equivalent plastic strains γ_{n+1} so that

$$\boldsymbol{\varepsilon}^{\mathrm{p}}_{n+1} = \boldsymbol{\varepsilon}^{\mathrm{p}}_{n} + \frac{3}{2}\frac{\gamma_{n+1}}{\tau^{\mathrm{vM}}(\boldsymbol{\tau}_{n+1})}\,\mathrm{dev}(\boldsymbol{\tau}_{n+1}) \tag{2.104}$$

follows considering the radial return. Additionally, we consider the relation

$$\boldsymbol{\tau}_{n+1} = \mathfrak{c}^{\mathrm{e}}_{\boldsymbol{\tau}} : \boldsymbol{\varepsilon}^{\mathrm{e}}_{n+1} = \mathfrak{c}^{\mathrm{e}}_{\boldsymbol{\tau}} : (\boldsymbol{\varepsilon}_{n+1} - \boldsymbol{\varepsilon}^{\mathrm{p}}_{n+1}), \tag{2.105}$$

which takes advantage of the linear relation of the elastic logarithmic strain $\boldsymbol{\varepsilon}^{\mathrm{e}}_{n+1}$ to the Kirchhoff stress $\boldsymbol{\tau}_{n+1}$. On this equation, the deviator

$$\mathrm{dev}(\boldsymbol{\tau}_{n+1}) = 2\,\mu\,\mathbb{P} : \left(\boldsymbol{\varepsilon}_{n+1} - \boldsymbol{\varepsilon}^{\mathrm{p}}_{n} - \frac{3}{2}\frac{\gamma_{n+1}}{\tau^{\mathrm{vM}}(\boldsymbol{\tau}_{n+1})}\,\mathrm{dev}(\boldsymbol{\tau}_{n+1})\right) \tag{2.106}$$

is applied. By reformulation, one obtains the deviatoric Kirchhoff stress

$$\mathrm{dev}(\boldsymbol{\tau}_{n+1}) = \frac{1}{1 + 3\mu\frac{\gamma_{n+1}}{\tau^{\mathrm{vM}}(\boldsymbol{\tau}_{n+1})}}\,\mathrm{dev}(\boldsymbol{\tau}^{\mathrm{tr}}). \tag{2.107}$$

Based on this, we get the difference

$$\tau^{\mathrm{vM}}(\boldsymbol{\tau}_{n+1}) = \tau^{\mathrm{vM}}(\boldsymbol{\tau}^{\mathrm{tr}}) - 3\,\mu\,\gamma_{n+1} \tag{2.108}$$

by application of the von Mises stress on both sides and reordering afterwards. Based on this, the final form of the Kirchhoff stress

$$\begin{aligned} \boldsymbol{\tau}_{n+1} &= \tfrac{1}{3}\,\mathrm{tr}(\boldsymbol{\tau}^{\mathrm{tr}})\,\boldsymbol{I} + \frac{\tau^{\mathrm{vM}}(\boldsymbol{\tau}^{\mathrm{tr}}) - 3\mu\,\gamma_{n+1}}{\tau^{\mathrm{vM}}(\boldsymbol{\tau}^{\mathrm{tr}})}\,\mathrm{dev}(\boldsymbol{\tau}^{\mathrm{tr}}) && (2.109) \\ &= \left(\kappa\,\boldsymbol{I} \otimes \boldsymbol{I} + \frac{\tau^{\mathrm{vM}}(\boldsymbol{\tau}^{\mathrm{tr}}) - 3\,\mu\,\gamma_{n+1}}{\tau^{\mathrm{vM}}(\boldsymbol{\tau}^{\mathrm{tr}})}\mathbb{P}\right)(\boldsymbol{\varepsilon}_{n+1} - \boldsymbol{\varepsilon}^{\mathrm{p}}_{n+1}) && (2.110) \end{aligned}$$

follows under consideration of equation 2.105. The last missing part, the update of the equivalent plastic strains γ_{n+1}, is derived by application of the Newton scheme to solve the non-linear equation $\phi_{n+1}(\gamma_{n+1}) \overset{!}{=} 0$. Therefore, the first terms of the Taylor approximation

$$\phi^{k+1}_{n+1} = \phi^{k}_{n+1} + \frac{\mathrm{d}\phi^{k}_{n+1}}{\mathrm{d}\gamma^{k}_{n+1}}\,\Delta\gamma^{k}_{n+1} + \cancelto{0}{\frac{\mathrm{d}^2\phi^{k}_{n+1}}{(\mathrm{d}\gamma^{k}_{n+1})^2}(\Delta\gamma^{k}_{n+1})^2} + \ldots \approx \phi^{k}_{n+1} + \frac{\mathrm{d}\phi^{k}_{n+1}}{\mathrm{d}\gamma^{k}_{n+1}}\,\Delta\gamma^{k}_{n+1} \overset{!}{=} 0 \tag{2.111}$$

leads to the update of the increase in equivalent plastic strain

$$\gamma_{n+1}^{k+1} = \gamma_{n+1}^{k} + \Delta\gamma_{n+1}^{k} = \gamma_{n+1}^{k} - \frac{\gamma_{n+1}^{k}}{\frac{\mathrm{d}\phi_{n+1}^{k}}{\mathrm{d}\gamma_{n+1}^{k}}} \tag{2.112}$$

with every iteration step k of the Newton algorithm. Together the derivative

$$\frac{\mathrm{d}\phi_{n+1}^{k}}{\mathrm{d}\gamma_{n+1}^{k}} = \frac{\partial\phi_{n+1}^{k}}{\partial\boldsymbol{\tau}_{n+1}^{k}} \cdot \frac{\partial\boldsymbol{\tau}_{n+1}^{k}}{\partial\gamma_{n+1}^{k}} + \frac{\partial\phi_{n+1}^{k}}{\partial\beta_{n+1}^{k}}\frac{\partial\beta_{n+1}^{k}}{\partial\alpha_{n+1}^{k}}\frac{\partial\alpha_{n+1}^{k}}{\partial\gamma_{n+1}^{k}} \tag{2.113}$$

$$= -\left(3\mu + (y_\infty - y_0)\, h^{\exp}\exp(-h^{\exp}\alpha_{n+1}^{k}) + h^{\mathrm{lin}}\right), \tag{2.114}$$

the increase in equivalent plastic strains γ_{n+1}^{k+1} and therefore, of the equivalent plastic strains α_{n+1}^{k+1} is approximated until the flow condition $|\phi_{n+1}^{k+1}| < tol$ falls below a chosen tolerance value. When this limit is reached, the logarithmic plastic strains $\boldsymbol{\varepsilon}_{n+1}^{\mathrm{p}}$ and the Kirchhoff stress $\boldsymbol{\tau}_{n+1}$ are determined. Additionally, the elasto-plastic material tangent $\mathfrak{c}_{\boldsymbol{\tau}}^{\mathrm{ep}}$ in the plastic regime is required for implementing the elasto-plastic material model. By the total derivation of the Kirchhoff stress $\boldsymbol{\tau}_{n+1}$ for the strain $\boldsymbol{\varepsilon}_{n+1}$ in the current time step $n+1$, the elasto-plastic material tangent

$$\mathfrak{c}_{\boldsymbol{\tau}}^{\mathrm{ep}} = \frac{\mathrm{d}\boldsymbol{\tau}_{n+1}}{\mathrm{d}\boldsymbol{\varepsilon}_{n+1}} = \frac{\partial\boldsymbol{\tau}_{n+1}}{\partial\boldsymbol{\varepsilon}_{n+1}} + \frac{\partial\boldsymbol{\tau}_{n+1}}{\partial\gamma_{n+1}} \otimes \frac{\partial\gamma_{n+1}}{\partial\boldsymbol{\varepsilon}_{n+1}} \tag{2.115}$$

$$= \kappa\,\boldsymbol{I}\otimes\boldsymbol{I} + \frac{\tau^{\mathrm{vM}}(\boldsymbol{\tau}^{\mathrm{tr}}) - 3\,\mu\,\gamma_{n+1}}{\tau^{\mathrm{vM}}(\boldsymbol{\tau}^{\mathrm{tr}})}\mathbb{P} \tag{2.116}$$

$$+\,2\,\mu\left(1 - \frac{\tau^{\mathrm{vM}}(\boldsymbol{\tau}_{n+1})}{\tau^{\mathrm{vM}}(\boldsymbol{\tau}^{\mathrm{tr}})}\right)\frac{\operatorname{dev}(\boldsymbol{\tau}^{\mathrm{tr}})}{||\operatorname{dev}(\boldsymbol{\tau}^{\mathrm{tr}})||} \otimes \frac{\operatorname{dev}(\boldsymbol{\tau}^{\mathrm{tr}})}{||\operatorname{dev}(\boldsymbol{\tau}^{\mathrm{tr}})||} \tag{2.117}$$

$$-\,2\,\mu\,\frac{3\,\mu}{3\mu + (y_\infty - y_0)\,h^{\exp}\exp(-h^{\exp}\alpha_{n+1}) + h^{\mathrm{lin}}}\frac{\operatorname{dev}(\boldsymbol{\tau}^{\mathrm{tr}})}{||\operatorname{dev}(\boldsymbol{\tau}^{\mathrm{tr}})||} \otimes \frac{\operatorname{dev}(\boldsymbol{\tau}^{\mathrm{tr}})}{||\operatorname{dev}(\boldsymbol{\tau}^{\mathrm{tr}})||} \tag{2.118}$$

results.

2.3.3. Extension to rate-dependent elasto-viscoplastic material behavior for regularization

In order to avoid mesh dependence that might appear due to too strong plastic localization, the elasto-plastic material model is extended to Perzyna-type elasto-viscoplasticity, cf. Perzyna [110], Junker et al. [58] and in terms of the phase-field approach, cf. Miehe et al. [92, 93], Aldakheel [3]. In contrast to the elasto-plastic material model, we assume the rate-dependent evolution equation

$$\dot{\alpha}^{\mathrm{vp}} = \lambda^{\mathrm{vp}} = \frac{1}{\eta}\,\langle\phi\rangle_{+} \tag{2.119}$$

with the Macaulay bracket $\langle\bullet\rangle_{\pm} = (\bullet \pm |\bullet|)/2$ and the viscosity η, which leads to relaxation of the material. For our applications, the viscous part does not represent any physical behavior but only serves for regularization. In terms of the principal stress space, this leads to a radial return of the trial stress $\boldsymbol{\tau}^{\mathrm{tr}}$ towards the coordinate origin, cf. figure 2.6, which may end either within the cylinder surrounded by the yield surface or outside the cylinder. This depends on the viscosity η and, in numerical implementations, on the time step size Δt and the loading speed of the structure. Based on this, the change of equivalent viscoplastic strains in explicit numerical implementations reads

$$\gamma_{n+1}^{\mathrm{vp}} = \frac{\Delta t}{\eta}\,\langle\phi^{\mathrm{tr}}\rangle_{+} \tag{2.120}$$

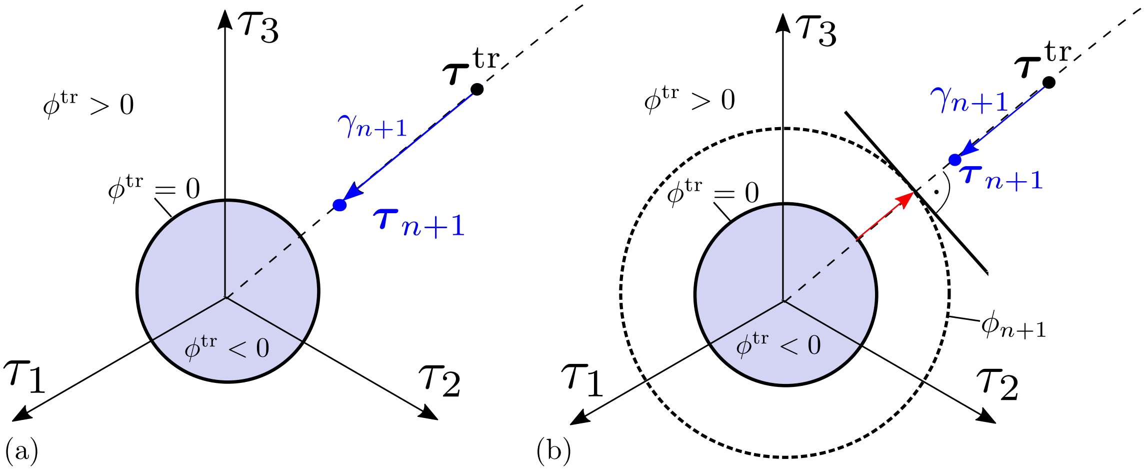

Figure 2.6.: Yield surface in the principal stress space (τ_1,τ_2,τ_3) with a trial stress $\boldsymbol{\tau}^{\text{tr}}$ for elasto-viscoplasticity (a) without hardening and (b) with hardening.

so that the equivalent viscoplastic strains result in

$$\alpha_{n+1}^{\text{vp}} = \alpha_n^{\text{vp}} + \gamma_{n+1}^{\text{vp}} = \alpha_n^{\text{vp}} + \frac{\Delta t}{\eta} \left\langle \phi^{\text{tr}} \right\rangle_+ \tag{2.121}$$

and respectively the logarithmic viscoplastic strains

$$\boldsymbol{\varepsilon}_{n+1}^{\text{vp}} = \boldsymbol{\varepsilon}_n^{\text{vp}} + \frac{3}{2} \frac{\gamma_{n+1}}{\tau^{\text{vM}}(\boldsymbol{\tau}^{\text{tr}})} \operatorname{dev}(\boldsymbol{\tau}^{\text{tr}}) \tag{2.122}$$

analogously to the previously described plastic evolutions. Herein, no Newton algorithm has to be applied because the evolutions are derived explicitly based on the trial flow condition ϕ^{tr} which is independent from the internal variables of the current time t_{n+1}. As another consequence of the explicit derivation, for both, the case of purely elastic as well as the case of elasto-viscoplastic deformations, the stress holds $\boldsymbol{\tau}_{n+1} = \boldsymbol{\tau}_{n+1}(\boldsymbol{\varepsilon}_{n+1}, \alpha_n) = \boldsymbol{\tau}^{\text{tr}}$. Thus, the elasto-viscoplastic material tangent results in the purely elastic one

$$\mathfrak{c}_{\boldsymbol{\tau}}^{\text{vp}} = \frac{\mathrm{d}\boldsymbol{\tau}_{n+1}}{\mathrm{d}\boldsymbol{\varepsilon}_{n+1}} = \frac{\partial \boldsymbol{\tau}_{n+1}}{\partial \boldsymbol{\varepsilon}_{n+1}} + \cancelto{0}{\frac{\partial \boldsymbol{\tau}_{n+1}}{\partial \gamma_{n+1}}} \otimes \frac{\partial \gamma_{n+1}}{\partial \boldsymbol{\varepsilon}_{n+1}} = \kappa\, \boldsymbol{I} \otimes \boldsymbol{I} + 2\,\mu\, \mathbb{P} = \mathfrak{c}_{\boldsymbol{\tau}}^{\text{e}}. \tag{2.123}$$

As a difference to the rate-independent model, in which the internal variables are evaluated, so that $\phi = 0$ holds, the evolution equation 2.119 of the rate-dependent model will lead to $\phi > 0$ if the viscosity η is chosen large enough. Hence, the development of the plastic deformations is delayed. If η is chosen too small, $\phi < 0$ may result, which results in an increased plastic deformation. In order to be able to adjust the plastic regimes over the body, the hardening function is modified to

$$\beta = y_0 \exp(-\delta\, \alpha) + (y_\infty - y_0)\, \left[1 - \exp(-h^{\text{exp}}\, \alpha)\right] + h^{\text{lin}}\, \alpha \tag{2.124}$$

with the localization parameter δ, which reduces the yield stress, that is necessary to imply additional plastic deformation after plasticity once has taken place. With this parameter the plastic localization is controlled. With increasing values for the localization parameter δ, the thickness of the regime of plastic deformations is reduced independently from the spatial discretization. Here, the resulting plastic dissipation potential is modified to

$$\psi^p = \frac{y_0}{\delta} \left[1 - \exp(-\delta\, \alpha)\right] + (y_\infty - y_0) \left[\alpha + \frac{\exp(-h^{\text{exp}}\, \alpha) - 1}{h^{\text{exp}}}\right] + \frac{1}{2}\, h^{\text{lin}}\, \alpha^2. \tag{2.125}$$

2.3.4. Tension-compression split

For the simulation of fatigue, the material laws have to be extended in order only erode the tensile part and not the compressive part of the cracked elements. This is considered because it is assumed that crack surfaces don't transfer tensile forces towards each other but compression forces due to the contact of the crack surfaces. Therefore, we split the elastic energy

$$\psi^{\mathrm{e}} = (1 - D)\, \psi^{\mathrm{e}}_{+} + \psi^{\mathrm{e}}_{-} \tag{2.126}$$

density into a tensile part ψ^{e}_{+} and a compressive part ψ^{e}_{-} analogously to the implementation Miehe et al. [90] for the phase-field method. Here, the damage variable D indicates whether the material is cracked ($D = 1$) or still intact ($D = 0$). Hence, if the material is cracked, the tensile part of the elastic energy density ψ^{e}_{+} vanishes while the compressive part ψ^{e}_{-} remains. In contrast to the original implementation in Miehe et al. [90], in which the damage variable D can be any number between zero and one, it is binary since it is only able to be zero in intact elements and one in eroded elements. In the latter case, it is assumed for simplicity that no further plastic deformation takes place in eroded elements so that no update of the internal variable occurs. This tension-compression split is applied on both, the elasto-plastic and the elasto-viscoplastic material models.

Spectral decomposition approach Multiple approaches for the decomposition of the energy density are possible. These influence the fracture criterion and thus, the crack propagation. Here, we apply the spectral decomposition approach, as shown in Miehe et al. [90] which is commonly used in phase field simulations considering mode I cracks. Here, the two parts of the free Helmholtz energy density read

$$\psi^{\mathrm{e}}_{\pm} = \frac{\lambda}{2}\, \langle \mathrm{tr}(\boldsymbol{\varepsilon}^{\mathrm{e}}) \rangle^{2}_{\pm} + \mu\, \boldsymbol{\varepsilon}^{\mathrm{e}}_{\pm} : \boldsymbol{\varepsilon}^{\mathrm{e}}_{\pm} \tag{2.127}$$

with the Lamé parameter $\lambda = \kappa - 2/3\, \mu$ and the elastic logarithmic strains

$$\boldsymbol{\varepsilon}^{\mathrm{e}} = (1 - D)\, \boldsymbol{\varepsilon}^{\mathrm{e}}_{+} + \boldsymbol{\varepsilon}^{\mathrm{e}}_{-} \qquad \text{with} \qquad \boldsymbol{\varepsilon}^{\mathrm{e}}_{\pm} = \sum_{i=1}^{3} \langle \varepsilon^{\mathrm{e}}_{i} \rangle_{\pm}\, \boldsymbol{n}_i \otimes \boldsymbol{n}_i, \tag{2.128}$$

that are split into tensile and compressive parts as well, based on the sign of the principal logarithmic elastic strains $\varepsilon^{\mathrm{e}}_{i}$. Considering this, one obtains tensile and compressive parts of the Kirchhoff stress

$$\begin{aligned} \boldsymbol{\tau}_{\pm} &= 2\, \boldsymbol{b}^{\mathrm{e}} \cdot \frac{\partial \psi^{\mathrm{e}}_{\pm}}{\partial \boldsymbol{b}^{\mathrm{e}}} = 2\, \boldsymbol{b}^{\mathrm{e}} \cdot \left(\frac{\partial \psi^{\mathrm{e}}_{\pm}}{\partial \boldsymbol{\varepsilon}^{\mathrm{e}}} + \frac{\partial \psi^{\mathrm{e}}_{\pm}}{\partial \boldsymbol{\varepsilon}^{\mathrm{e}}_{+}} : \frac{\partial \boldsymbol{\varepsilon}^{\mathrm{e}}_{+}}{\partial \boldsymbol{\varepsilon}^{\mathrm{e}}} + \frac{\partial \psi^{\mathrm{e}}_{\pm}}{\partial \boldsymbol{\varepsilon}^{\mathrm{e}}_{-}} : \frac{\partial \boldsymbol{\varepsilon}^{\mathrm{e}}_{-}}{\partial \boldsymbol{\varepsilon}^{\mathrm{e}}} \right) \cdot \sum_{i=1}^{3} \frac{\partial \boldsymbol{\varepsilon}^{\mathrm{e}}}{\partial \lambda^{\mathrm{e}}_{i}} \frac{\partial \lambda^{\mathrm{e}}_{i}}{\partial (\lambda^{\mathrm{e}}_{i})^{2}} \frac{\partial (\lambda^{\mathrm{e}}_{i})^{2}}{\partial \boldsymbol{b}^{\mathrm{e}}} \\ &= \lambda\, \langle \mathrm{tr}(\boldsymbol{\varepsilon}^{\mathrm{e}}) \rangle_{\pm}\, \mathbf{I} + 2\, \mu\, \boldsymbol{\varepsilon}^{\mathrm{e}}_{\pm} \qquad \text{combined to} \qquad \boldsymbol{\tau} = (1 - D)\, \boldsymbol{\tau}_{+} + \boldsymbol{\tau}_{-}\,. \end{aligned} \tag{2.129}$$

In the case of $D = 1$, only the compressive stresses $\boldsymbol{\tau}_{-}$ resulting from negative strains remain whereas the tensile part $\boldsymbol{\tau}_{+}$ vanishes. This prohibits intersection of the two sides of the crack. Otherwise, if $D = 0$, both parts of the stresses are active. Based on this, the material tangent is derived by

$$\mathfrak{c}_{\boldsymbol{\tau}} = (1 - D)\, \mathfrak{c}_{\boldsymbol{\tau}\,+} + \mathfrak{c}_{\boldsymbol{\tau}\,-} \tag{2.130}$$

with the tension part $\mathfrak{c}_{\boldsymbol{\tau}+}$ and compression part $\mathfrak{c}_{\boldsymbol{\tau}-}$. According to Miehe and Lambrecht [88], they are derived by

$$
\begin{aligned}
\mathfrak{c}_{\boldsymbol{\tau}\pm} = 2\,\frac{\partial \boldsymbol{\tau}^{\mathrm{e}}_{\pm}}{\partial \boldsymbol{b}^{\mathrm{e}}} \cdot \boldsymbol{b}^{\mathrm{e}} = 2\left(\frac{\partial \boldsymbol{\tau}^{\mathrm{e}}_{\pm}}{\partial \boldsymbol{\varepsilon}^{\mathrm{e}}} + \frac{\partial \boldsymbol{\tau}^{\mathrm{e}}_{\pm}}{\partial \boldsymbol{\varepsilon}^{\mathrm{e}}_{+}} : \frac{\partial \boldsymbol{\varepsilon}^{\mathrm{e}}_{+}}{\partial \boldsymbol{\varepsilon}^{\mathrm{e}}} + \frac{\partial \boldsymbol{\tau}^{\mathrm{e}}_{\pm}}{\partial \boldsymbol{\varepsilon}^{\mathrm{e}}_{-}} : \frac{\partial \boldsymbol{\varepsilon}^{\mathrm{e}}_{-}}{\partial \boldsymbol{\varepsilon}^{\mathrm{e}}}\right) \cdot \sum_{i=1}^{3} \frac{\partial \boldsymbol{\varepsilon}^{\mathrm{e}}}{\partial \lambda^{\mathrm{e}}_{i}} \frac{\partial \lambda^{\mathrm{e}}_{i}}{\partial (\lambda^{\mathrm{e}}_{i})^2} \frac{\partial (\lambda^{\mathrm{e}}_{i})^2}{\partial \boldsymbol{b}^{\mathrm{e}}} \cdot \boldsymbol{b}^{\mathrm{e}} \\
&= \lambda\, \mathcal{H}(\pm \mathrm{tr}(\boldsymbol{\varepsilon}^{\mathrm{e}}))\, \mathbf{I} \otimes \mathbf{I} + 2\,\mu \sum_{i=1}^{3} \mathcal{H}(\pm \varepsilon^{\mathrm{e}}_{i})\, \boldsymbol{n}_i \otimes \boldsymbol{n}_i \otimes \boldsymbol{n}_i \otimes \boldsymbol{n}_i \\
&\quad + \mu \sum_{i=1}^{3} \sum_{j\neq i, \varepsilon^{\mathrm{e}}_j \neq \varepsilon^{\mathrm{e}}_i}^{3} \frac{\langle \varepsilon^{\mathrm{e}}_i \rangle_{\pm} - \langle \varepsilon^{\mathrm{e}}_j \rangle_{\pm}}{\varepsilon^{\mathrm{e}}_i - \varepsilon^{\mathrm{e}}_j} (\mathbb{G}_{ij} + \mathbb{G}_{ji}) + \mu \sum_{i=1}^{3} \sum_{j\neq i,\, \varepsilon^{\mathrm{e}}_j = \varepsilon^{\mathrm{e}}_i}^{3} \mathcal{H}(\pm \varepsilon^{\mathrm{e}}_i)(\mathbb{G}_{ij} + \mathbb{G}_{ji})
\end{aligned}
\tag{2.131}
$$

containing the fourth order tensor $\mathbb{G}_{ij} = \boldsymbol{n}_i \otimes \boldsymbol{n}_j \otimes \boldsymbol{n}_i \otimes \boldsymbol{n}_j + \boldsymbol{n}_i \otimes \boldsymbol{n}_j \otimes \boldsymbol{n}_j \otimes \boldsymbol{n}_i$ and the Heaviside function

$$
\mathcal{H}(x) = \begin{cases} 0 & \text{if}\, x \leq 0 \\ 1 & \text{otherwise.} \end{cases}
\tag{2.132}
$$

Due to the Heaviside function, jumps in the material tangent at the logarithmic principal strains $\varepsilon^{\mathrm{e}}_i \approx 0$ and at the trace $\mathrm{tr}(\boldsymbol{\varepsilon}^{\mathrm{e}}) \approx 0$ occur in material points with $D = 1$, which may lead to numerical instabilities during the solving process with the Newton-Raphson scheme. If $D = 0$, this material tangent coincides with the elastic one $\mathfrak{c}^{\mathrm{e}}_{\boldsymbol{\tau}}$ of the elasto-plastic and elasto-viscoplastic material formulation.

Alternative approaches Note, that alternative approaches for splitting the energy into a tension and compression part have been examined, mostly for brittle materials. For example, Amor et al. [4] proposes a volumetric-deviatoric split

$$
\psi^{\mathrm{e,Amor}}_{+} = \frac{\kappa}{2}\, \langle \mathrm{tr}(\boldsymbol{\varepsilon}^{\mathrm{e}}) \rangle^2_{+} + \mu\, \mathrm{dev}(\boldsymbol{\varepsilon}^{\mathrm{e}}) : \mathrm{dev}(\boldsymbol{\varepsilon}^{\mathrm{e}}) \quad \text{and} \quad \psi^{\mathrm{e,Amor}}_{-} = \frac{\kappa}{2}\, \langle \mathrm{tr}(\boldsymbol{\varepsilon}^{\mathrm{e}}) \rangle^2_{-}
\tag{2.133}
$$

in which the expansive volumetric part and the deviatoric part are considered as the tensile part. Thus, only the compressive volumetric part remains if $D = 1$ holds. For the simulation of mode II shear cracks, Lancioni and Royer-Carfagni [70] introduced

$$
\psi^{\mathrm{e,Lancioni}}_{+} = \mu\, \mathrm{dev}(\boldsymbol{\varepsilon}^{\mathrm{e}}) : \mathrm{dev}(\boldsymbol{\varepsilon}^{\mathrm{e}}) \quad \text{and} \quad \psi^{\mathrm{e,Lancioni}}_{-} = \frac{\kappa}{2}\, \mathrm{tr}(\boldsymbol{\varepsilon}^{\mathrm{e}})^2
\tag{2.134}
$$

which only allows crack propagation under deviatoric strains. In order to be able to simulate mode I as well as mode II cracks with one framework, Zhang et al. [164] propose the separation of the occurring term $\psi^{\mathrm{e,Zhang}}/G_c = \psi^{\mathrm{e,Zhang}}_{I}/G_{c,I} + \psi^{\mathrm{e,Zhang}}_{II}/G_{c,II}$ into mode I and mode II energy densities and therefore, individual Griffith-type energy release rates $G_{c,I}$ and $G_{c,II}$. Another concept for imposing tensile-compression asymmetry into the algorithm is the application of so-called representative crack elements (RCE), as introduced in Storm et al. [138]. Here, the full degraded material state is taken into account to construct the stresses and material tangent. However, the approach of the previous subsubsection is chosen for our application because of its simplicity and the primarily assumed mode I tension crack propagation.

2.3.5. Crack criteria

For the simulation of the crack propagation, the imposed work in the material points, that dissipates before or during the element erosion process, has to be evaluated in every Gauß point. Therefore, this work has to be determined thermodynamically consistently for each used material, with or without tension-compression split. Originally, Pandolfi and Ortiz [106] proposed to derive the element energy $U_K = 0.5\,\hat{\boldsymbol{u}}_K \cdot \boldsymbol{k}_K \cdot \hat{\boldsymbol{u}}_K$ by considering the element stiffness $\boldsymbol{k}_K$ and element displacement vector $\hat{\boldsymbol{u}}_K$ which is valid for linear elastic materials and linearized geometrical assumptions, but leads to wrong results for any other material law and nonlinear deformation measures. Hence, the imposed work U_K is modified:

- in the case of brittle materials with the Neo-Hookean hyperelasticity without the tension-compression asymmetry, we assume that the fully imposed element energy
$$U_K = \int\limits_{\mathcal{B}^{\mathrm{e}}} \psi \,\mathrm{d}V \tag{2.135}$$
is eroded and therefore, taken into account for the criterion if the corresponding element K is eroded. For small strains, this energy equals to the element energy of the original implementation in Pandolfi and Ortiz [106], but has to be extended for the hyperelasticity, because of the geometric nonlinearity. Here, the imposed work in the element equals exactly the released energy if this element is eroded. Thus, this fracture criterion conserves the thermodynamic consistency.

- For the elasto-plastic material model without tension-compression asymmetry, the full imposed work
$$U_K = \int\limits_{\mathcal{B}^{\mathrm{e}}} (\psi^{\mathrm{e}} + \psi^{\mathrm{p}}) \,\mathrm{d}V \tag{2.136}$$
is taken into account. This work contains the elastic energy ψ^{e} that is released during the erosion process plus the work that dissipates in the crack tip due to plastic deformation ψ^{p}. Here, the dissipation in the Clausius-Duhem inequality evaluated from the equations 2.115 and 2.92
$$\mathcal{D} = -\frac{3}{2}\,\lambda^{\mathrm{p}} \boldsymbol{\tau} : \frac{\operatorname{dev}(\boldsymbol{\tau})}{\boldsymbol{\tau}^{\mathrm{vM}}} + \beta\,\dot{\alpha} = -\lambda^{\mathrm{p}} \left(\boldsymbol{\tau}^{\mathrm{vM}} - \beta\right) = -\lambda^{\mathrm{p}} \phi = 0 \tag{2.137}$$
becomes zero in the case of plastic deformations. If no plastic deformations occur in the time step, only elastic deformations occur and thus, the dissipation $\mathcal{D}$ becomes zero as well. Hence, this part is not considered for the crack criterion. This criterion was chosen in line with Irwin [57] who summarized the plastic dissipation as well as the dissipation due to crack propagation into one critical Griffith-type constant $G_c = G_c^{\mathrm{crack}} + G_c^{\mathrm{plasticity}}$ which is used to characterize the material's strength against crack propagation. This extension results from laboratory experiments in which only the full dissipated energy can be measured. The experiments lack of the capability to determine which part of the energy has dissipated into plasticity and which part into crack propagation. For ductile materials, it is often assumed that the plastic part $G_c^{\mathrm{plasticity}} \gg G_c^{\mathrm{crack}}$ surpasses the part of the crack propagation by far. Furthermore, this criterion is built analogously to the one used in the phase field approach in, e.g., Miehe et al. [93].

- If the elasto-viscoplastic material model is applied, the viscous dissipation becomes $\mathcal{D}^{\mathrm{vis}} = \frac{1}{2}\eta\,\dot{\alpha}^2$ so that the imposed work is extended to
$$U_K = \int\limits_{\mathcal{B}^{\mathrm{e}}} \left(\psi^{\mathrm{e}} + \psi^{\mathrm{p}} + \int\limits_{t} \mathcal{D}^{\mathrm{vis}} \,\mathrm{d}t \right) \mathrm{d}V \tag{2.138}$$
containing the time integral over the dissipation $\mathcal{D}^{\mathrm{vis}}$ which additionally occurs before the crack propagates. Numerically, this term is evaluated by
$$\int\limits_{0}^{t_{n+1}} \mathcal{D}^{\mathrm{vis}} \,\mathrm{d}t = \int\limits_{0}^{t_n} \mathcal{D}^{\mathrm{vis}} \,\mathrm{d}t + \frac{\eta}{2} \int\limits_{t_n}^{t_{n+1}} \dot{\alpha}^2 \,\mathrm{d}t \approx \bar{\mathcal{D}}_n^{\mathrm{vis}} + \frac{\eta}{2} \left(\frac{\gamma_{n+1}}{\Delta t}\right)^2 \Delta t = \bar{\mathcal{D}}_n^{\mathrm{vis}} + \frac{\eta}{2} \frac{\gamma_{n+1}^2}{\Delta t}$$

based on the integrated dissipation of the previous time step $\bar{\mathcal{D}}_n^{\text{vis}}$. Computationally, this variable is saved as an additional history variable.

- If the tension-compression asymmetry of the elastic energy $\psi^{\text{e}} = (1-D)\psi_+^{\text{e}} + \psi_-^{\text{e}}$ is applied, the imposed work

$$U_K = \int\limits_{\mathcal{B}^{\text{e}}} \left(\psi_+^{\text{e}} + \psi^{\text{p}} + \int\limits_t \mathcal{D}^{\text{vis}} \, \text{d}t \right) \text{d}V \tag{2.139}$$

  is reduced by the compression part ψ_-^{e} because this part remains after the erosion and does not dissipate so that thermodynamic consistency remains. This criterion can also be applied on elasto-plastic materials by setting $\mathcal{D}^{\text{vis}} = 0$ and on elastic materials by setting $\psi^{\text{p}} = 0$ additionally.

3. Eigenerosion approach

In order to implement crack propagation into the FE framework, the eigenerosion approach as firstly shown in Schmidt et al. [127], Pandolfi and Ortiz [106] is applied. This approach is chosen because of its robustness and mesh independence. In this chapter, the basic equations of this approach and its mesh-independence due to Γ-convergence are described. Furthermore, the extension to ductile crack propagation at finite strains, cf. Wingender and Balzani [150], and its implementation are shown.

3.1. Regularization of the crack propagation problem

Based on the work of Griffith [46] about the theory of brittle fracture, the existence of a Griffith-type energy release rate

$$G := - \lim_{\Delta|C| \to 0} \frac{\Delta U(\boldsymbol{u})}{\Delta|C|} \tag{3.1}$$

is assumed. It describes the energy change ΔU, that is released if the crack set C enlarges by a small extension of the crack set ΔC as schematically shown in figure 3.1. If the crack propagates, the crack set C increases so that the crack surface $|C|$ grows by the increment $\Delta|C|$. ΔU denotes the increment in the potential energy U, which is stored by imposing mechanical work. In the fully elastic case, the energy U only depends on the displacements $\boldsymbol{u}$. Here, it is assumed, that the change in the stored elastic energy ΔU completely dissipates into the crack propagation and thus, into expansion of the crack surface. Furthermore, the original Griffith energy release rate only refers to completely brittle crack propagation. Hence, for the application on crack propagation through ductile materials, this relation is referred as **Griffith-type energy release rate** because additional assumptions to this are required so that the relation of the stored potential energy U to the crack set C has to be adjusted in this case. In this work, irreversibility of crack propagation and no healing of the material are

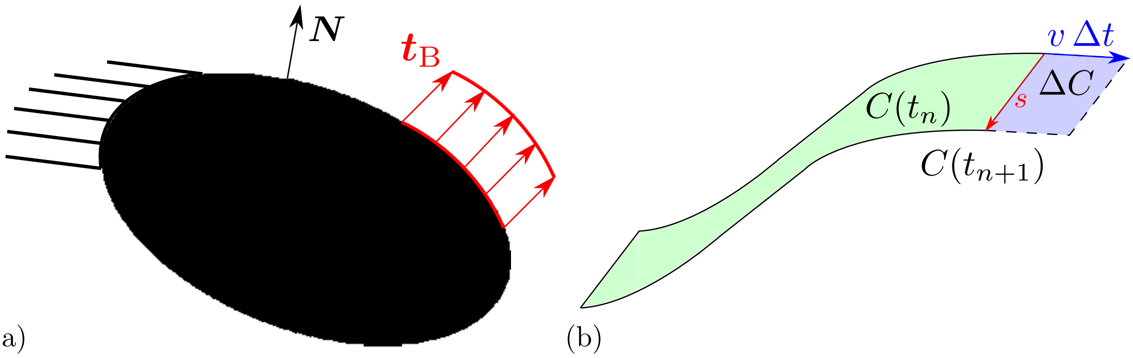

(a) (b)

Figure 3.1.: (a) Body $\mathcal{B}_0$ with crack C and Dirichlet boundary conditions as well as Neumann boundary conditions. (b) crack plane within the body with previous crack plane $C(t)$ (green), of the crack area ΔC (blue) with the crack width s and the crack velocity v.

taken into account so that the monotonicity constraint

$$C(t_n) \subset C(t_{n+1}) \tag{3.2}$$

holds for the crack set $C(t_n)$ at time t_n. It is a subset of the crack set $C(t_{n+1})$ at the later time t_{n+1} so that the crack set cannot be reduced over time. Note, that the Griffith-type crack criterion only describes crack propagation but not crack initiation. It neglects effects that are necessary for modeling these, e.g., void nucleation, void clustering and microcracking. These effects are investigated, e.g., in Gurson [48], Chu and Needleman [22] and modeled in the Gurson-Tveergard-Needlemen (GTN) model Needleman and Tvergaard [100]. Experimentally, the crack initiation and crack propagation are handled separately since the crack initiation is additionally governed by different effects. Thus, in physical experiments as well as in simulations based on eigenerosion, an initial crack has to be imposed. By reformulation of the basic equation 3.1 under the assumption of small changes in the crack set C as well as potential energy, the equation yields to

$$G = -\frac{\partial U(\boldsymbol{u})}{\partial |C|} \leq G_c \tag{3.3}$$

which serves as the basis for the eigenerosion approach in [127]. The critical Griffith-type energy release rate G_c relates the energy, that is necessary to increase the area, divided by the expansion of the crack area. If the energy release rate G reaches the critical value of Griffith-type energy release rate G_c, the crack propagates with the crack front velocity v. Otherwise, the crack rests and its crack tip velocity v becomes 0. Taking these requirements into account, the relations

$$v \begin{cases} = 0, & \text{if} \quad G - G_c < 0 \\ > 0, & \text{if} \quad G - G_c = 0 \end{cases} \qquad \text{and thus,} \quad (G - G_c)\, v = 0 \tag{3.4}$$

are obtained. Additionally, the unilateral contact constraint

$$[\![\boldsymbol{u}]\!] \cdot \boldsymbol{n}_c^+ \geq 0 \tag{3.5}$$

with the jump of the displacement field $[\![\boldsymbol{u}]\!] = \boldsymbol{u}^+ - \boldsymbol{u}^-$ between the displacements $\boldsymbol{u}^+$ and $\boldsymbol{u}^-$ at the opposite sides of the crack surface and the normal vector $\boldsymbol{n}_c^+$ and $\boldsymbol{n}_c^-$ of the crack surfaces prohibits the two sides of the crack to intersect. If $[\![\boldsymbol{u}]\!] \cdot \boldsymbol{n}_c^+ = 0$ and thus, $[\![\boldsymbol{u}]\!] \cdot \boldsymbol{n}_c^- = 0$ hold, the crack is fully closed and if $[\![\boldsymbol{u}]\!] \cdot \boldsymbol{n}_c^+ > 0$ and thus, $[\![\boldsymbol{u}]\!] \cdot \boldsymbol{n}_c^- < 0$, the crack surfaces move away from each other so that the crack opens. The crack surfaces would intersect if $[\![\boldsymbol{u}]\!] \cdot \boldsymbol{n}_c^+ < 0$. This jump in the displacement field $[\![\boldsymbol{u}]\!]$ is responsible for the discontinuity of the mechanical field variables. Analytically, the stress at the crack tip becomes infinitely large. Additionally, it is assumed that the two sides of the crack surfaces are traction-free because of the consideration of no contact between those. Hence, the traction vectors at the two crack surfaces become $\boldsymbol{t}_c^+ = \boldsymbol{\sigma}^+ \cdot \boldsymbol{n}_c^+ = 0$ and $\boldsymbol{t}_c^- = \boldsymbol{\sigma}^- \cdot \boldsymbol{n}_c^- = 0$ at the crack surface with the Cauchy stresses $\boldsymbol{\sigma}^+$ and $\boldsymbol{\sigma}^-$ at the two crack surfaces. In opposite to that, this dissertation considers the possibility of tractions at the crack surfaces under compression and traction-free crack surfaces under tension by assuming the tension-compression split in some material models. In that case,

$$\boldsymbol{t}_c^+ = \boldsymbol{\sigma}^+ \cdot \boldsymbol{n}_c^+ \leq 0 \quad \text{and} \quad \boldsymbol{t}_c^- = \boldsymbol{\sigma}^- \cdot \boldsymbol{n}_c^- \leq 0 \tag{3.6}$$

holds. These traction-free crack surfaces under tension enable deformations at the crack for which no additional mechanical work is required. This results from the missing connection between two material points on opposite sides of the crack surfaces. These deformations are called **Eigendeformations**. Note, that the Griffith-type fracture criterion assumes the crack to propagate rate-independently. However, time-dependent effects like inertia or rate-dependent material formulations enable the crack propagation over time under static load. The energy-dissipation functional is formulated as

$$F = U(\boldsymbol{u}) + G_c|C| \tag{3.7}$$

considering the Griffith-type energy release rate in equation 3.3 and the monotonicity constraint in equation 3.2, which guarantees that the dissipated energy $G_c|C|$ may only increase and not decrease over the time t. This ensures that the second law of thermodynamics is fulfilled. The energy-dissipation potential F has to be minimized according to Mielke and Ortiz [94] with respect to the displacement field $\boldsymbol{u}$ and the crack set C at all times t. If this criterion is directly applied on simulation frameworks using spatial discretization in particular finite element simulations, the crack propagation will depend on the chosen mesh size h, because the energy near the crack tip localizes. This effect results from the stresses near the crack tip which become infinitely large in analytical solutions due to the discontinuity imposed by the crack. To circumvent this problem and to ensure independency from the spatial discretization, the energy dissipation functional requires regularization, either in the form of regularization of the stored potential energy U or of the crack set C. in the case of the eigenerosion approach, the regularization

$$F_\epsilon = U + G_c \frac{|C_\epsilon|}{2\,\epsilon} \tag{3.8}$$

of the energy-dissipation functional F is applied, now considering the ϵ-neighborhood C_ϵ of the crack set C with the influence radius $\epsilon > 0$. Here, the regularization of the crack set C to its ϵ-neighborhood C_ϵ leads to an increase in its dimension. For example, the crack set C of a two-dimensional crack plane becomes a three-dimensional volume C_ϵ. Hence, the dimension of the ϵ-neighborhood C_ϵ of the crack set is reduced by dividing by two times the influence radius ϵ. This division additionally supplies the normalization with respect to the influence radius ϵ. To ensure that this regularization leads to mesh-independent and numerically converging results, mathematical prove of the convergence of the regularized energy-dissipation functional F_ϵ to the unregularized energy-dissipation functional F as $\epsilon \to 0$ is required. Therefore, the Γ-convergence was proven in Schmidt et al. [127] by demonstrating that the two required conditions for Γ-convergence as, e.g., shown in Dal Maso [25], hold. Firstly, the lower bound

$$\forall \boldsymbol{u}_\epsilon \to \boldsymbol{u} \quad \liminf_{\epsilon \to 0} F_\epsilon(\boldsymbol{u}_\epsilon) \geq F(\boldsymbol{u}) \tag{3.9}$$

states that the lower bound of the regularized energy-dissipation functional for the influence radius $\epsilon \to 0$ and for all displacement fields $\boldsymbol{u}_\epsilon \to \boldsymbol{u}$ of the regularized problem coincides with the unregularized energy-dissipation functional $F(\boldsymbol{u})$. Secondly, the recovery sequence

$$\exists \boldsymbol{u}_\epsilon \to \boldsymbol{u} \quad \limsup_{\epsilon \to 0} F_\epsilon(\boldsymbol{u}_\epsilon) \leq F(\boldsymbol{u}) \tag{3.10}$$

ensures that the lower bound is optimal due to the existence of a displacement field $\boldsymbol{u}_\epsilon$ for which the upper bound of the regularized energy-dissipation functional F_ϵ again coincides with unregularized energy-dissipation functional $F(\boldsymbol{u})$. Combining these two conditions for the Γ-convergence, the consequence

$$\exists \boldsymbol{u}_\epsilon \to \boldsymbol{u} \quad \lim_{\epsilon \to 0} F_\epsilon(\boldsymbol{u}_\epsilon) = F(\boldsymbol{u}) \tag{3.11}$$

implies the existence of at least one displacement field $\boldsymbol{u}_\epsilon$ for which the regularized energy-dissipation functional $F_\epsilon(\boldsymbol{u}_\epsilon)$ yields to the unregularized one $F(\boldsymbol{u})$ as $\epsilon \to 0$. Hence, the regularization of the crack area is mathematically justified.

3.2. Application on spatial discretizations

The regularized energy dissipation functional F_ϵ is applied on spatially discretized bodies, in our case, with FEM discretizations. Here, the erosion of finite elements is considered. If an element is eroded, it is assumed to be cracked, so that it represents the crack. Eroded elements are able to undergo eigendeformations for which no additional work is required. Therefore, the element stiffness $\boldsymbol{k}_K$ is set to zero in the case of assuming traction-free crack surfaces, as seen in the original implementation in Pandolfi et al. [107]. If a tension-compression split is considered, the stresses and material tangents in the evaluated material points have to be modified. Therefore, the additional element damage variable D is passed into the material subroutines at the corresponding Gauß points in the FE software. This binary damage variable D indicates whether the element is eroded ($D = 1$) or still intact ($D = 0$). For further information on the modified constitutive laws, see 2.3. To technically evaluate the Griffith-type criterion in every discrete time step t_n, the difference in the energetic states ΔU_K in the element K due its erosion is considered. The energy of eroded elements is reduced to zero under the assumption of no tension-compression split. The energy before erosion is the total imposed energy U_K, so that the difference becomes $\Delta U_K = 0 - U_K = -U_K$. In the original implementation in Pandolfi et al. [107], difference in the potential is derived by $-\Delta U_K = 0.5\,\boldsymbol{d}_K \cdot \boldsymbol{k}_K \cdot \boldsymbol{d}_K$ by considering the element stiffness $\boldsymbol{k}_K$ and element displacement vector $\boldsymbol{d}_K$. This is only valid in simulations assuming linear elastic material behavior and linear geometry. For application on other material laws, the energy difference $-\Delta U_K$ is derived based on the energy at the Gauß point level. After these are evaluated, the elemental energy difference $-\Delta U_K$ is calculated by the numerical volume integration over the element's volume. This additionally enables the implementation of nonlinear material laws and the split of the material laws into a tension and compression part which is necessary for eroded elements to transmit forces under compression. This energy difference $-\Delta U_K$ is compared to the maximally tolerable energy $G_c\,\Delta A_K$ that considers the increase in the crack area ΔA_K if element K is eroded. ΔF_K is assumed to be the energy that additionally has to be imposed into element K to erode it. Hence, $-\Delta F_K$, the so-called **net energy gain**, can be interpreted as the remaining energy, that does not dissipate after erosion but is imposed into the remaining intact elements. It is evaluated by

$$-\Delta F_K := -\Delta U_K - G_c\,\Delta A_K \tag{3.12}$$

in each time step t_n after solving the mechanical equilibrium and represents the term $G - G_c$ of the Griffith-type fracture criterion. This criterion is applied to determine whether the crack propagates ($-\Delta F_K \geq 0$) or rests ($-\Delta F_K < 0$). Herein, the change in the stored potential energy $-\Delta U_K$ competes with the crack resistance $G_c\,\Delta A_K$. Hence, if the stored potential energy $-\Delta U_K$ surpasses the crack resistance $G_c\,\Delta A_K$, it is energetically more favorable to remove the stored potential energy $-U_K$ while an increase in the dissipation $G_c\,\Delta A_K$ is accepted to minimize the net energy gain $-\Delta F_K$. Due to the monotonicity constraint in equation 3.2, the erosion of an element happens irreversibly so that a back transformation into an intact element is prohibited.

In order to derive the net energy gain $-\Delta F_K$, the effective crack area ΔA_K is evaluated in every intact element K. This evaluation is the crucial difference of the eigenerosion approach to other forms of nonlocal approaches. Here, the increment of the regularized crack area is defined as

$$\Delta A_K := \frac{|\,(C \cup K)_\epsilon \setminus C_\epsilon|}{2\,\epsilon}. \tag{3.13}$$

It represents only that part of the neighborhood area which would additionally be considered if the element domain K was eroded, as seen in figure 3.2. The ϵ-neighborhood C_ϵ of the current crack set C contains the ϵ-neighborhood of the currently eroded elements. It is subtracted from the ϵ-neighborhood $(C \cup K)_\epsilon$ of the unification $C \cup K$ of the current crack set C and

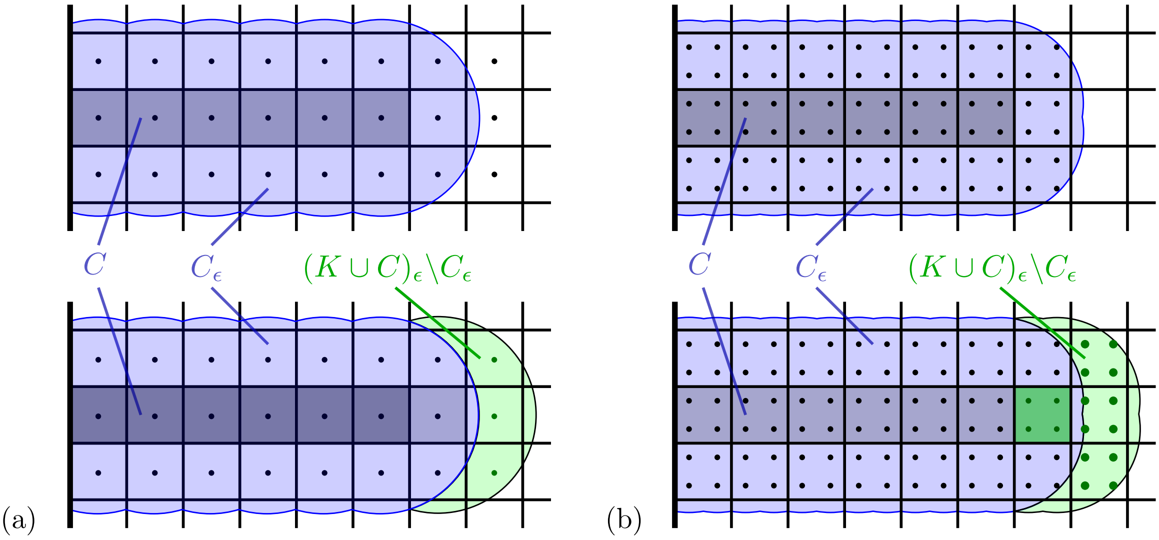
C
C_ϵ
$(K \cup C)_\epsilon \backslash C_\epsilon$
(a)
C
C_ϵ
$(K \cup C)_\epsilon \backslash C_\epsilon$
(b)

Figure 3.2.: Mesh with eroded elements C (dark gray), their ϵ-neighborhood C_ϵ (dark blue) and additional crack area $(C \cup K)_\epsilon \backslash C_\epsilon$ for element domain K (green) based on (a) the center of masses and (b) the Gauß points, taken from Wingender and Balzani [150].

element K. Their unified area $|(C \cup K)_\epsilon \backslash C_\epsilon|$ is normalized by 2ϵ. For the derivation of the ϵ-neighborhood the every intact element, the original work in Pandolfi and Ortiz [106] proposes taking into account the center of masses of each element K, as shown in figure 3.2a. Here, the distances of the element center of mass of element K to the center of masses of all other elements are evaluated. The elements with the distance lower than the influence radius ϵ temporarily saved to a list for this element. Thereby, the ϵ-neighborhood of each element K results in a sphere. Afterwards, this list is reduced by all elements that lie within the lists of eroded elements. Then $(C \cup K)_\epsilon \backslash C_\epsilon$ is evaluated by summing up the volumes of the elements within the remaining list of element K. In contrast to that, our implementation considers the Gauß point coordinates that are used for the Gauß point quadrature and their Gauß point volumes that are already computed for the evaluation of the element stresses and material tangents. Here, the Gauß point lists of all Gauß points within the element K are summarized to one list so that they represent the union of spheres around the Gauß points of element K. Based on this, the incremental crack area

$$\Delta A_K = \frac{\sum_{l=1}^{n_K^{\text{GPlist}}} V_l^K}{2\,\epsilon} \tag{3.14}$$

is computed by summing up the n_K^{GPlist} volumes V_l^K assigned to the Gauß points in the Gauß point list of the element K. The volumes are derived by

$$V_l^K = w_l^K \det(\boldsymbol{J}_K) \tag{3.15}$$

involving the weighting factor w_l^K of the Gauß point l within its element K and the Jacobian $\boldsymbol{J}_K$ of the element K. Note, that the Gauß point volume of the reference configuration instead of the current configuration are taken into account in order to avoid an artificial change of the crack resistance due to deformation. For example, an element with an large volume increase would enforce an unphysical increase in the incremental crack area ΔA_K if the volumes of the current configuration were considered. The reason for considering the Gauß points instead of the center of masses is that, for higher-order shape functions, e.g., quadratic approximation of the displacements, the center of masses may be located far from the straight

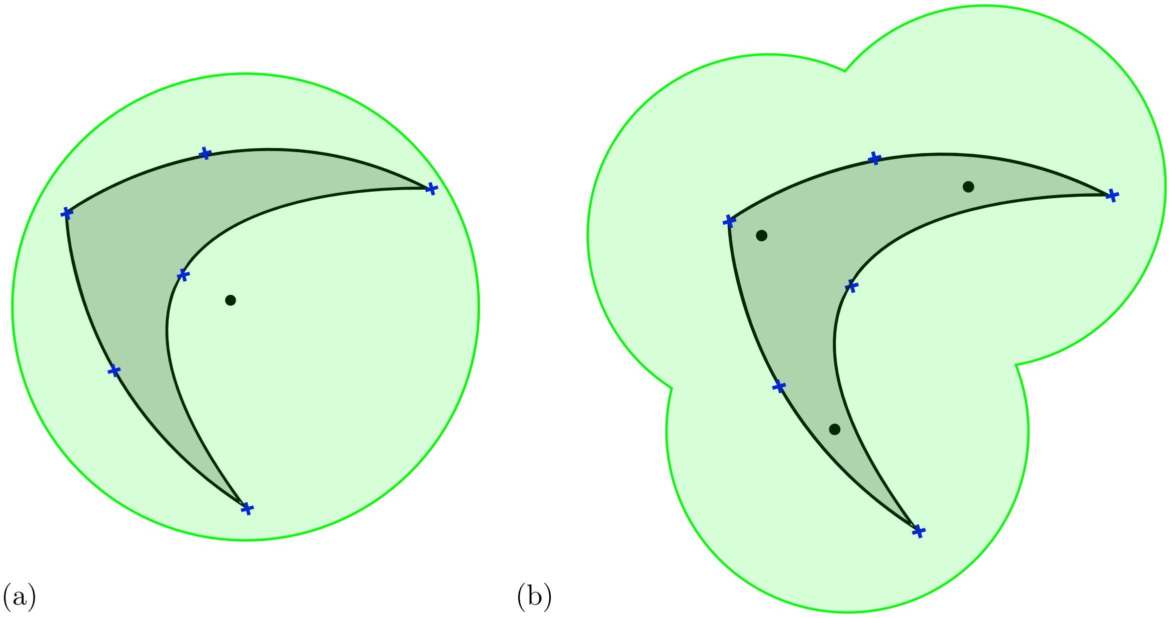

Figure 3.3.: (a) Banana-shaped triangular element with quadratic shape function with influence area (green) based on (a) barycenter and (b) Gauß points (black).

connections of the corner nodes if the element formulation is not reduced to straight-edge elements. In this case, the center of mass may lie far away so that ϵ-neighborhoods with small influence radii ϵ may not capture these elements and therefore, may result in a bad regularization. In order to avoid such cases, a method which considers more points in one elements is applied, namely the Gauß point based regularization. An example is demonstrated in figure 3.3. Therein, the center of mass lies outside the element so that the influence area badly represents the area around the element. The influence area in figure 3.3b better represents the shape of the element because the three Gauß points lie within the element. For the choice of the influence radius ϵ, two restrictions hold. On the one hand, it requires a certain size to capture the Gauß points of neighboring elements to ensure a proper regularization, but on the other hand, has to be chosen small enough to ensure that $F_\epsilon(\boldsymbol{u}_\epsilon) \to F(\boldsymbol{u})$ holds. As a counter example for the latter case, if the influence radius ϵ is chosen in such a away that one element's Gauß point list contains all Gauß points of all elements in the investigated structure, all element will erode in one time step because their crack resistance vanishes if this element erodes. Schmidt et al. [127] proposes to derive the influence radius $\epsilon = \epsilon(h)$ depending on the mesh size h for the barycentric approach. Here, the additional restriction $h\,\epsilon^{-1} \to 0$ as $h \to 0$ holds mathematically due the Γ-convergence, which states that the mesh size h has to go faster to zero than ϵ. However, the relation

$$\epsilon(h) = C_h\, h \tag{3.16}$$

is used in our implementation as proposed in Pandolfi et al. [107] as it provides numerical convergence as demonstrated in chapter 4. For simplicity, a constant global influence radius ϵ is chosen based on the maximum element edge size h in order to ensure a sufficient nonlocal ϵ-neighborhood K_ϵ of the large elements which leads to reasonable results, as shown in chapter 7. Note that the choice of C_h and the size of the simulated structure strongly influence the crack propagation because ΔA_K varies with these parameters. Hence, the Griffith-type energy release rate G_c in the simulations does not necessarily coincide with the physical one, but is rather seen as a numerical parameter instead of a physical material parameter. In order to perform the simulation according to physical structures, the critical Griffith-type energy release rate G_c has to be adjusted for a certain influence radius ϵ and cannot simply be obtained from literature. This numerical parameter is obtained by fitting the numerical results to results

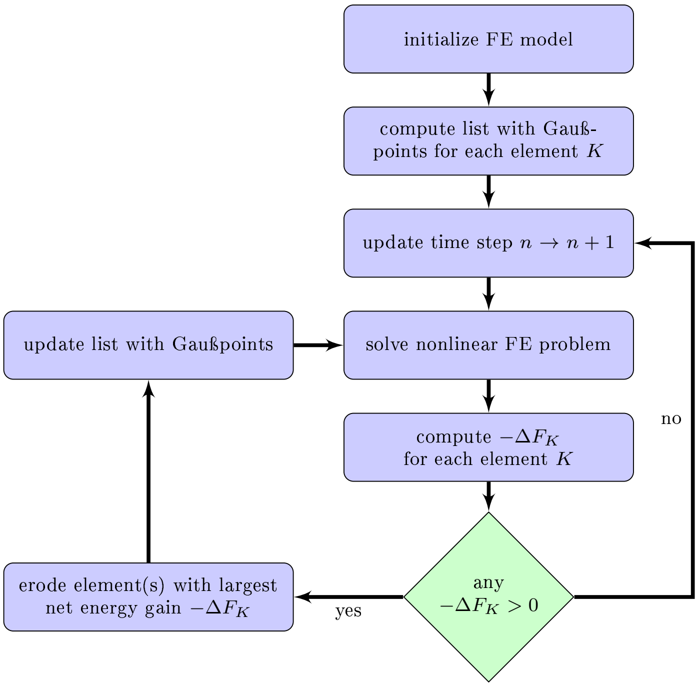
initialize FE model
compute list with Gauß-points for each element K
update time step $n \to n+1$
update list with Gaußpoints
solve nonlinear FE problem
compute $-\Delta F_K$ for each element K
no
any $-\Delta F_K > 0$
yes
erode element(s) with largest net energy gain $-\Delta F_K$

Figure 3.4.: Schematic illustration of the considered eigenerosion algorithm within a finite element framework, taken from Wingender and Balzani [150].

of laboratory experiments. One example is demonstrated in chapter 7. Furthermore, the Gauß point list has to be saved which leads to additional consumption of computational costs. The size of the list increases in general with ϵ^3 in three-dimensional calculations considering a constant mesh. With low influence radii ϵ, the additional computational effort is kept low.

3.3. Staggered algorithm

In the eigenerosion approach, the momentum balance as well as the minimization of the regularized energy-dissipation potential have to be fulfilled simultaneously in every time step t_{n+1}. Therefore, they are solved for the nodal displacement field $\boldsymbol{D}$ as well as the crack set $C(t_{n+1})$, in our case, in an iterative, staggered scheme. Therein, both fields are solved in series, as shown in figure 3.4. In every time step t_{n+1}, the mechanical equilibrium equations are solved first. Afterwards, the net energy gain $-\Delta F_K$ is evaluated for each element K. If the net energy gain $-\Delta F_K$ of at least one element becomes larger than zero, it becomes a candidate for erosion. Out of all erosion candidates, the one with the highest net energy gain $\max(-\Delta F_K)$ is eroded by setting its element damage variable D to one and subtracting all of the Gauß points in its ϵ-neighborhood from the Gauß point list of the remaining intact elements. In order to enable the crack path to branch into multiple directions simultaneously, elements, whose net energy gain $-\Delta F_K$ only differs in a numerical tolerance tol_{NEG} from the highest net energy gain $\max(-\Delta F_K)$, are eroded as well. In our implementation this tolerance criterion is applied as the relative comparison $1 - (-\Delta F_K)/\max(-\Delta F_K) > \text{tol}_{NEG}$ because the dimension of the net energy gain varies largely with different structure sizes and with time step sizes Δt_{n+1}. The reason for that is that smaller time step sizes lead to smaller net energy gain $-\Delta F_K$ because with smaller time step sizes Δt_{n+1}, the critical crack resistance only is surpassed by a small amount. $\text{tol}_{NEG} = 10^{-6}$ has been empirically found to supply reasonable results. For instance in simulations with perfectly symmetric geometry, as shown in figure 3.5, the crack is able to propagate into both directions simultaneously. Otherwise, the crack would firstly propagate into one direction and afterwards, into the other one. However,

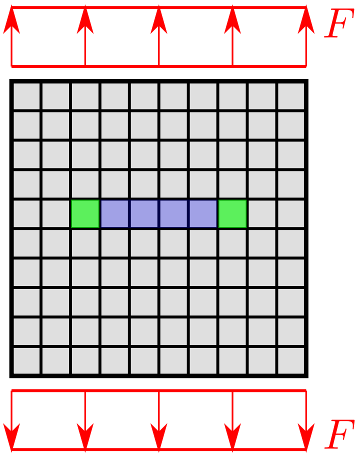

Figure 3.5.: Mesh with intact elements (gray), eroded elements (blue) and elements that might erode simultaneously (green).

this algorithm is capable of simulating the bifurcation of the crack path without any special treatment, as shown in Qinami et al. [112]. After the element erosion, the solve of the mechanical equilibrium and the check for erosion are repeated until no further elements erode in this time step. Then, the time step is updated as in the usual finite element method. Hence, the finite element algorithm is extended by another loop in every time step for the eigenerosion algorithm which increases the computational effort by one solve of the mechanical equilibrium for each eroded element except in the case of bifurcation. However, the solving procedure may still be fast compared to other methods, which solve the displacement field $\boldsymbol{D}$ and the crack set C monolithically because in these methods, the number of equations surpasses the one of the staggered schemes by far. Conceptually, the calculation of the net energy gain $-\Delta F_K$ can be seen as trial step and the element erosion as a corrector step. Although it may intuitive, the question remains if the staggered scheme leads to the absolute minimum of the regularized energy-dissipation functional F_ϵ of the current time step. For instance, in the case of two cracks close to each other, the ϵ-neighborhoods might influence each other in such a way that the crack paths are not represented accurately. However, such cases have not been observed yet but still require further investigations.

3.4. Technical remarks

The eigenerosion approach within the FE framework leads to additional sources of numerical instabilities that might prevent the Newton algorithm for solving the mechanical equilibrium equation from converging. Firstly, the element stiffness is reduced or even may become zero which might break the structure into to multiple parts or single unconnected nodes in the erosion process. This leads to an unsolvable system of equations due not sufficiently statically bounded parts and therefore, numerical instabilities. To circumvent this problem, some numerical approaches for simulating crack propagation as, e.g., in Miehe et al. [91], impose a small remaining stiffness in cracked parts which leaves a small connection between all elements and nodes. As a disadvantage, this impedes a clear crack and proper structural responses. For instance, nodes that are only attached to eroded elements are able to move independently from any elements. Hence, numerical stability has to be improved, in our a case by imposing Newmark-dynamics. This method imposes additional stiffness and residual terms to the system of equations which strengthens the solvability. In general, the consisting mass matrix $\boldsymbol{M}^{\mathrm{CMM}}$, is applied. This mass matrix has the property that nodes transmit forces onto each other due to inertia. To avoid dynamic effects of the different nodes onto each other, the element mass matrix of the eroded elements is converted to the lumped mass matrix $\boldsymbol{M}^{\mathrm{LMM}}$

that ensures the mass conservation and separated nodes due to its diagonal form. The switch of the mass matrices leads to inaccuracies of the dynamics in eroded elements during the time step of their erosion because of the rearrangement of masses. Thus, simulations with high velocities influencing the crack propagation are not recommended for simulations with this implementation. For the simulations of this work, low velocities at the Dirichlet boundaries are assumed to be imposed so that this circumstance may be neglected. Additionally, not all nodes are connected to intact elements anymore and thus, do not contribute their masses to the total mass of the structure. Exemplarily, figure 3.6a shows a mesh consisting of hexahedral elements under the assumption of linear shape functions. Therein, all nodes of eroded elements are connected to nodes of other elements. However, if two adjacent rows of elements are eroded, as shown in figure 3.6b, some nodes are disconnected from all intact elements. Their mass is not attached to either side of the crack. Hence, the effective mass of the structure is reduced by their amount. The same effect occurs if elements with quadratic shape functions are chosen, cf. figure 3.6c. Here, nodes in the center of eroded elements are disconnected from intact elements. Therefore, the whole structure's mass is artificially reduced by the masses of these nodes. However, the dynamic terms of these nodes are necessary because otherwise, the stiffness matrix would be zero for all entries that are connected to this element. In that case, the global linearized system of equations of the Newton-Raphson scheme would not be solvable anymore. In general, it would be possible to ensure the mass conservation by searching the disconnected nodes and spreading their masses onto the nodes of the neighboring intact elements. However, since the dynamic effects in the simulations of this work are relatively small compared to other effects, this has not been implemented yet.

A second source for numerical instabilities results from localization of mechanical fields near the crack tip. Especially in time steps in which elements erode, the large change in the mesh leads to large changes in these fields that may prevent the Newton-Raphson scheme to converge because the starting point of the Newton-Raphson iteration, namely the previous solution of the displacements, lies too far away from the current solution. This effect can be circumvented by reducing the size of the elements that are going to be eroded. This reduces the changes in the mesh and energy released due to cracking. A second possibility is decreasing the time step size which may decrease the number of elements that erode in one time step and slightly reduces the net energy gain $-\Delta F_K$. Thirdly, in the case of ductile materials, the application of a numerically more stable constitutive law may lead to stabilization of the calculations. For instance, the internal variables of the elasto-plastic material model are derived implicitly by application of the Newton scheme to solve a nonlinear equation. This scheme may fail if the starting point for the Newton iteration lies too far away from the actual solution. In contrast to that, the history variables of the elasto-viscoplastic material model are calculated explicitly so that instabilities due to their calculation is circumvented.

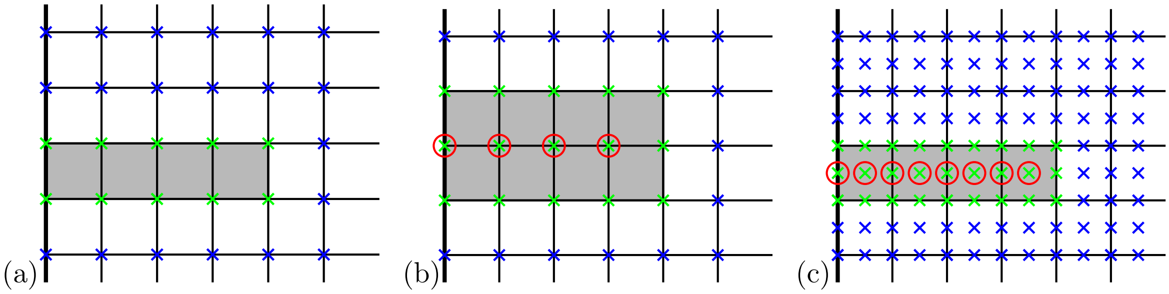

Figure 3.6.: Mesh with its nodes (blue) and eroded elements (gray) with the nodes attached to these (green) in the case (a) and (b) of linear shape functions and (c) quadratic shape functions. Nodes that are connected to any element anymore are marked with a red circle.

4. Mesh convergence of the eigenerosion approach

To demonstrate the plausibility of the extension of the eigenerosion approach to ductile crack propagation at finite strains, the results of different simulations of a benchmark experiment are analyzed. Here, we consider a dogbone-shaped specimen under tension as, for example, examined in Miehe et al. [93] or Aldakheel [3]for which the results are known. In particular, we focus on the analysis of the crack path and integral values, here in the form of the resulting reaction force and displacement curves.

4.1. Brittle fracture

First investigations of the algorithm are carried out for brittle fracture. Here, two different initial conditions for the crack are demonstrated to circumvent the problem that the proposed algorithm is only capable of the accurate simulation of crack propagation and not crack initiation. The effects of the crack initiation depend on effects on a lower scale. Firstly, a specimen with an initial crack and secondly, a specimen without a crack but with a small perturbation of the structure are examined. The specimen and its geometry parameter are presented in figure 4.1.

4.1.1. Plate with initial crack

In the first simulations, the specimen is sledged with an initial crack length a at the time $t = 0$, as shown in figure 4.1a. The specimen is loaded with constantly increasing displacement $\bar{u} = t \cdot 0.05$ mm/s. The specimen's mesh consists of 27-node hexahedral elements with quadratic shape functions. The characteristic element size h represents the minimum in-plane element edge length. In four different meshes, the characteristic element sizes $h = 0.22, 0.11, 0.065, 0.0325$ mm were chosen. The element's thickness is of the size of the specimen thickness T, so that only one layer of elements is considered. This leads to a high aspect ratio of the elements. Nevertheless, this does not affect the numerical accuracy since the mechanical stress and strain fields are constant in thickness direction. The Neo-Hookean material law is assumed under the consideration of the bulk modulus $\kappa = 164883.0$ MPa, the shear modulus $\mu = 76100.0$ MPa, the critical Griffith-type energy release rate $G_c = 2$ N/mm and the density $\rho = 7810$ kg/m^3.

The resulting final crack paths are shown in figure 4.2. As expected for brittle crack propagation, the crack propagates strictly horizontally through the specimen in every chosen discretization. In later numerical examples, it will be shown that the positive results of the crack paths are not controlled by the element borders and that the crack path is also able to propagate across the element borders. In figure 4.3a, the resultant force $\bar{Q}$ at the upper Dirichlet boundary of the specimen is plotted over the prescribed displacement $\bar{u}$ for the different initial crack lengths. Therein, the force increases linearly until it drops to zero and stays constant from that point on. This immediate drop is expected in tension tests with a homogeneous brittle specimen. When the first element erodes, the cross section of the specimen lateral to the direction of the prescribed displacements decreases. This leads to a higher stress in

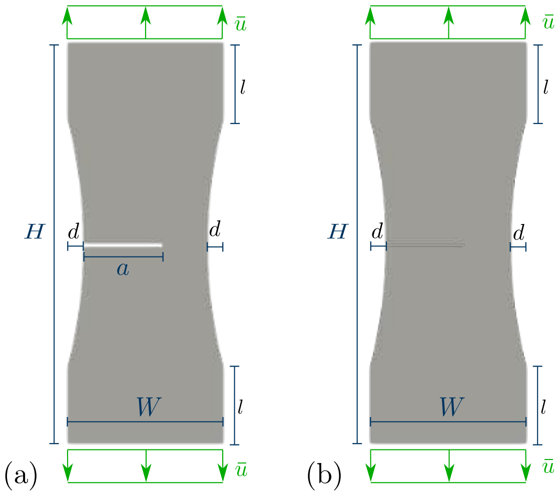

Geometric parameter	Value in mm
W	3.0
H	7.75
d	0.3
l	1.5
T	0.2727

(c)

Figure 4.1.: (a) Specimen for tension test with initial crack at time t_0, (b) specimen for tension test without crack, and (c) considered geometric parameters; T denotes the thickness of the specimens, taken from Wingender and Balzani [150].

the element next to the eroded one. Additionally, the incremental crack area ΔA_K becomes smaller in the neighboring element so that this element erodes in the same time step. This process repeats until the specimen breaks into two parts. All curves of the resultant force converge with decreasing mesh size h in all scenarios. Thus, the mesh-independency of the extension of the eigenerosion approach to finite strains is confirmed for brittle specimens.

4.1.2. Plate without initial crack

Because the method to impose the initial crack by modifying the geometry might be complicated in some cases, a second method is presented in the next example. Here, the geometry is kept but a small perturbation is imposed. Therefore, an area with the horizontal length of $(W - 2d)/10$ at the center of the specimen is weakened, where the crack is expected to propagate through in laboratory experiments, cf. figure 4.4. In vertical direction, only one row of elements is affected so that its vertical length is of the size h. The weakened area is slightly shifted away from the center to avoid artificial symmetrization of the setup. If the weakened area was symmetric, the crack would propagate horizontally into both directions simultaneously, which would be unphysical. In the weakened area, the critical Griffith-type release rate is set to the small value $G_c = 0.0001$ N/mm. The affected elements erode within the first time step of the simulation and thus, impose an initial crack. The approach is equivalent to assuming the elements to be eroded before the simulation starts since the affected elements erode in one of the first time steps. As in the previous example, the crack grows horizontally for all discretizations, even though the initial crack is considered at different horizontal locations, as shown in figure 4.5. Because the perturbation is slightly shifted to the right, the elements to the right erode first before the elements to the left erode. Additionally, the structural response in the form of the load-displacement curve in figure 4.3b converges with decreasing mesh size h. Altogether, the mesh independence for brittle crack propagation is demonstrated for this type of crack initiation.

4.1.3. Influence radius, critical Griffith-type constant and specimen size

In order to perform simulations including crack propagation qualitatively and quantitatively correctly, knowledge about the numerical parameters is crucial. To gain this knowledge, the simulations for brittle crack propagation through the specimen which is sledged with a length of $a = 0.57$ mm are repeated for multiple different Griffith-type energy release rates G_c and

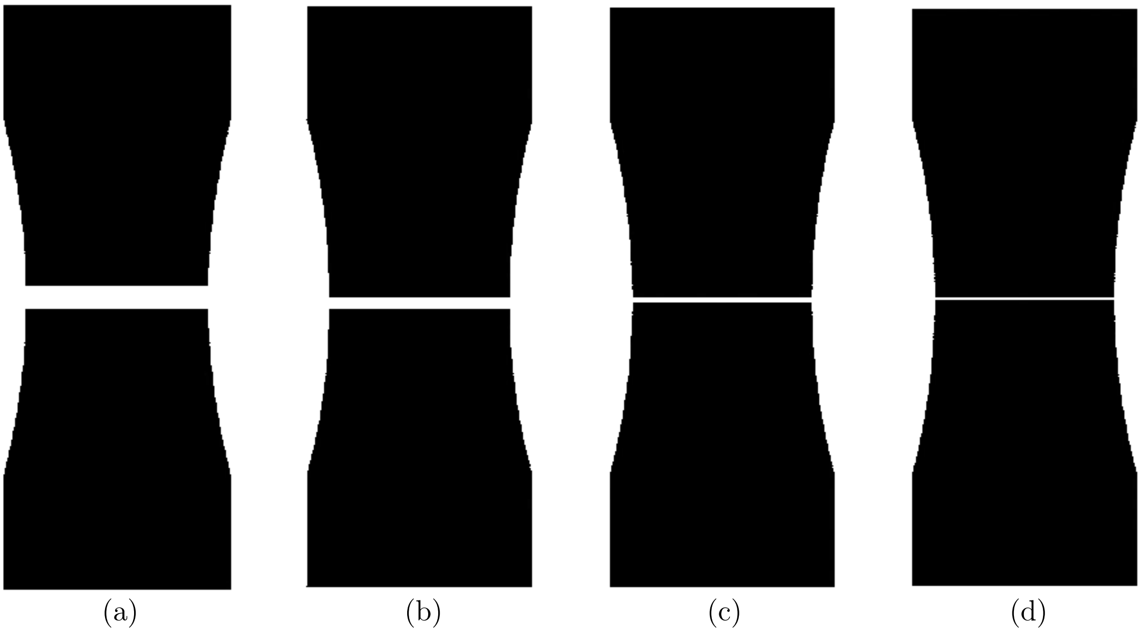
(a) (b) (c) (d)

Figure 4.2.: Final crack through specimen in tension test with the initial crack length $a = 0.95$ mm for the different element sizes (a) $h = 0.22$ mm, (b) $h = 0.11$ mm, (c) $h = 0.065$ mm, and (d) $h = 0.0325$ mm, taken from Wingender and Balzani [150]. The eroded elements are removed from these images.

different influence radii constant C_h which scales the influence radius $\epsilon = C_h\, h$ with the mesh size h. As shown in figure 4.6a, an increase in the Griffith-type energy release rate G_c leads to an increase in the displacement $\bar{u}$ that is necessary for the crack to propagate, as expected. In the investigated range of the Griffith-type energy release rate, G_c does not affect the crack path. However, in more complex simulations, this might be the case. For example, if the Griffith-type energy release rate G_c is decreased in elasto-plastic materials, a transition from ductile to brittle crack propagation and therefore, the crack path might occur. In figure 4.6b, it is shown that an increasing influence radius ϵ leads to an increased displacement $\bar{u}$ at which the crack propagates. This effect occurs because the number of Gauß points in the Gauß point list increases approximately quadratically with the influence radius, cf. figure 4.6c. Because the incremental crack area ΔA_K is derived based on these Gauß points' volumes and divided by the influence radius ϵ, the crack resistance $G_c\, \Delta A_K$ increases approximately linearly with the influence radius ϵ as long as ϵ is small compared to the structure. For computational efficiency and because of the property that the regularized energy-dissipation functional F_ϵ converges to the unregularized one F, the influence radius is supposed to be kept small. In figure 4.6d, the resulting stress $\frac{\bar{Q}}{WT}$ is shown for different sizes of the specimen. Its lengths H and W are multiplied by the factor 2, 4 and 8, whereas the critical Griffith-type energy release rate rate G_c and the influence radius constant C_h are kept constant. With increasing size, the macroscopic strain $\frac{\bar{u}_c}{H}$, at which the crack propagates, is increased. This contradicts the observation from experiments that the brittle specimens crack at a certain macroscopic stress and strain independently from the specimen size. If the critical Griffith-type energy release rate G_c is increased by the same factor as the length of specimen edges, the crack occurs at the exact same macroscopic. Note, that the resultant reaction force with increased critical energy release rate is not plotted here.

Because only one displacement $\bar{u}_c$ at which the crack propagates matches with comparable experiments, the two numerical parameters, namely the Griffith-type energy release rate G_c as well as the influence radius ϵ, have to be adjusted accordingly. For example, tensile test are suitable to find the Griffith-type energy release rate G_c for a chosen influence radius

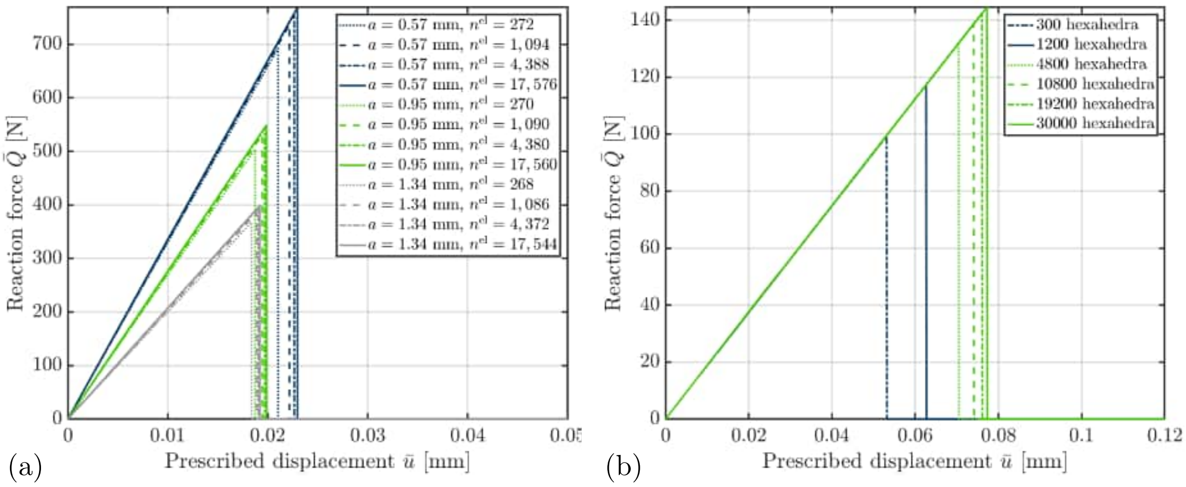

Figure 4.3.: Force-displacement curve for brittle material (a) with and (b) without prescribed initial crack, taken from Wingender and Balzani [150]. The converging response indicates mesh-independence.

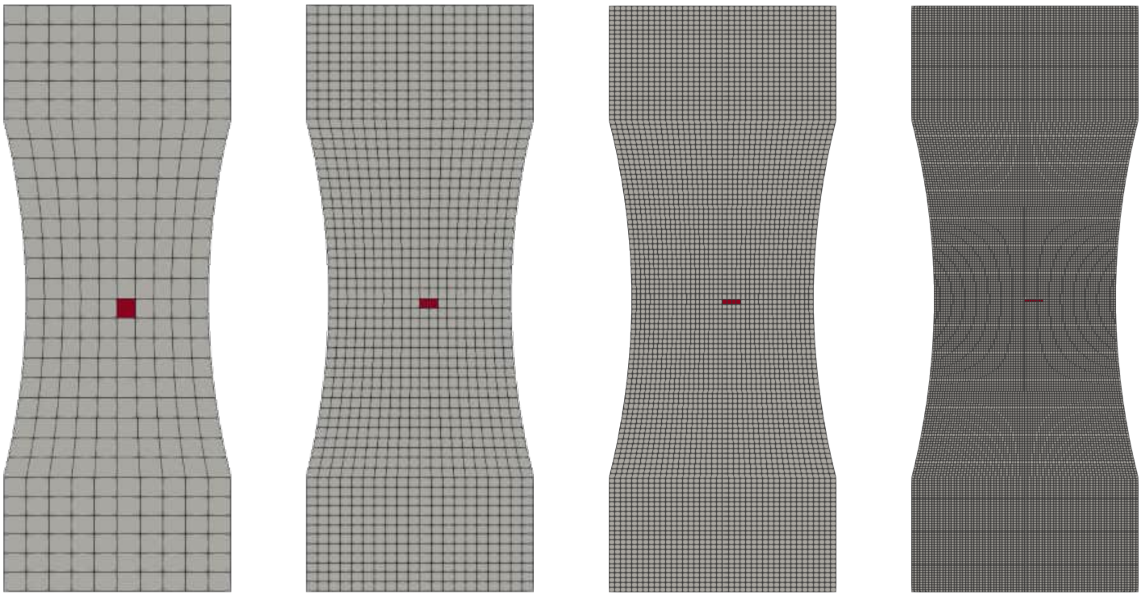
(a) (b) (c) (d)

Figure 4.4.: Specimen with weakened area (red) for different mesh sizes (a) $h = 0.22$ mm, (b) $h = 0.11$ mm, (c) $h = 0.065$ mm and (d) $h = 0.0325$ mm, taken from Wingender and Balzani [150].

constant C_h and for a chosen specimen size. As another conclusion from these simulations, the Griffith-type energy release rate G_c cannot be taken from literature to simulate a crack through a certain material, but has to be fitted with numerical simulations in comparison to results of laboratory experiments. Thereby, the simulations are to be carried out on the same length scales as the later calculated structure since the critical Griffith-type energy release rate depends on the structure size.

4.1.4. Energetic relations

The energetic relations for the crack criterion are investigated for brittle fracture in a specimen with a sledge or perturbation compared to a specimen without initial crack. The figures 4.7a&c show the average energy $\bar{\psi} = \int_{\mathcal{B}^{\mathrm{e}}} \psi \, \mathrm{d}V / V^{\mathrm{e}}$ in the element that is going to be eroded first. in the case of the weakened specimen, the first element after the erosion of the weakened element

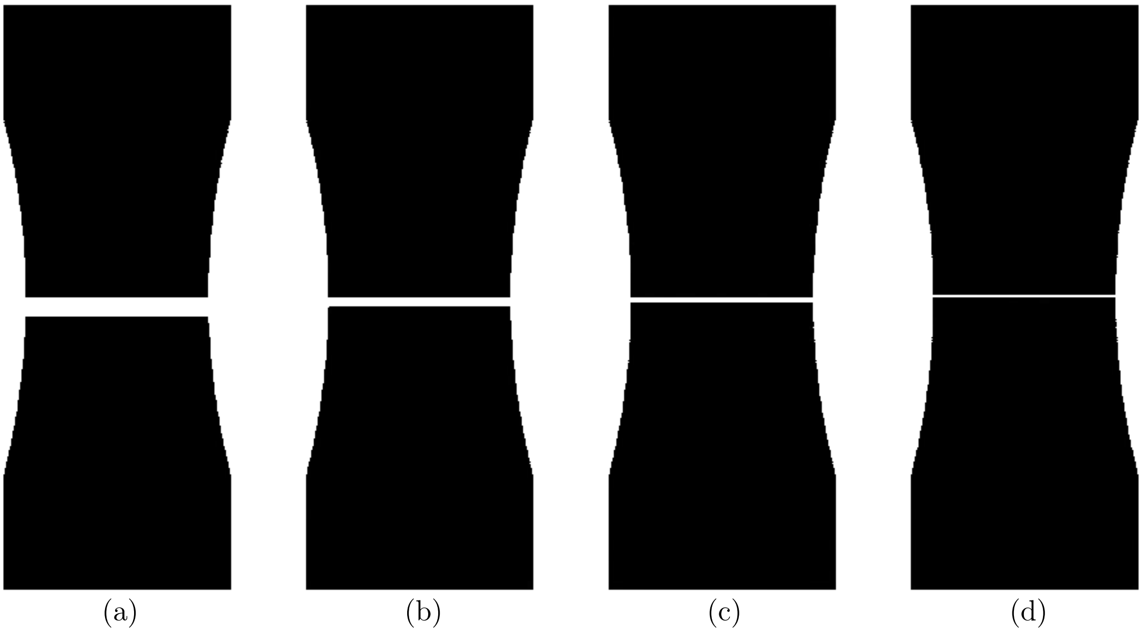

Figure 4.5.: Final crack through brittle specimen with weakened area in the tension test with the different element sizes (a) $h = 0.22$ mm, (b) $h = 0.11$ mm, (c) $h = 0.065$ mm, and (d) $h = 0.0325$ mm, taken from Wingender and Balzani [150].

is considered. An increase in the average energy density with decreasing in-plane edge length h is observable in the case of the specimen with an initial crack or weakness. This increase results from the localization of the stresses near the crack tip, that become infinitely large in analytical solutions. in the case of the weakened specimen, this effect only becomes visible after the erosion of the weakened elements. In contrast to that, the energy density $\bar{\psi}$ stays almost constant in the case of the specimen without an initial crack. As a consequence of this observation, the imposed energy $-\Delta U_K \approx \bar{\psi}\, h^2 t$ becomes approximately linear for the modified but stays constant for the unmodified specimen without initial crack with respect to the in-plane edge length h. In contrast to that, the incremental crack area $\mathrm{d}A_K$ of the element that will be eroded next increases linearly with increasing in-plane edge length h for the modified as well as for the unmodified specimen. As a consequence, the crack resistance $G_c\, \Delta A_K$ increases linearly as well. Hence, comparing the element energy $-\Delta U_K$ to this crack resistance, it becomes clear that an initial crack or material weakness is necessary. Note, that this study has only been carried out for brittle materials to understand the occurring effects. If inelastic material behavior is assumed, these relation become more complicated.

4.2. Ductile crack propagation

To prove the extension of the eigenerosion approach to ductile crack propagation, numerical examples under additional consideration of plasticity are calculated. Therein, the specimen with weakened area in figure 4.1b is taken into account. In table of figure 4.8b, the material parameters are shown. They are adjusted in line with stress-strain curves in figure 4.8a from real tensile tests of iron alloys. The critical Griffith-type energy release rate is set to $G_c = 11$ N/mm under the assumption of the influence radius constant $C_h = 0.5$. Both plastic material laws, namely elasto-plasticity and elasto-viscoplasticity, are applied.

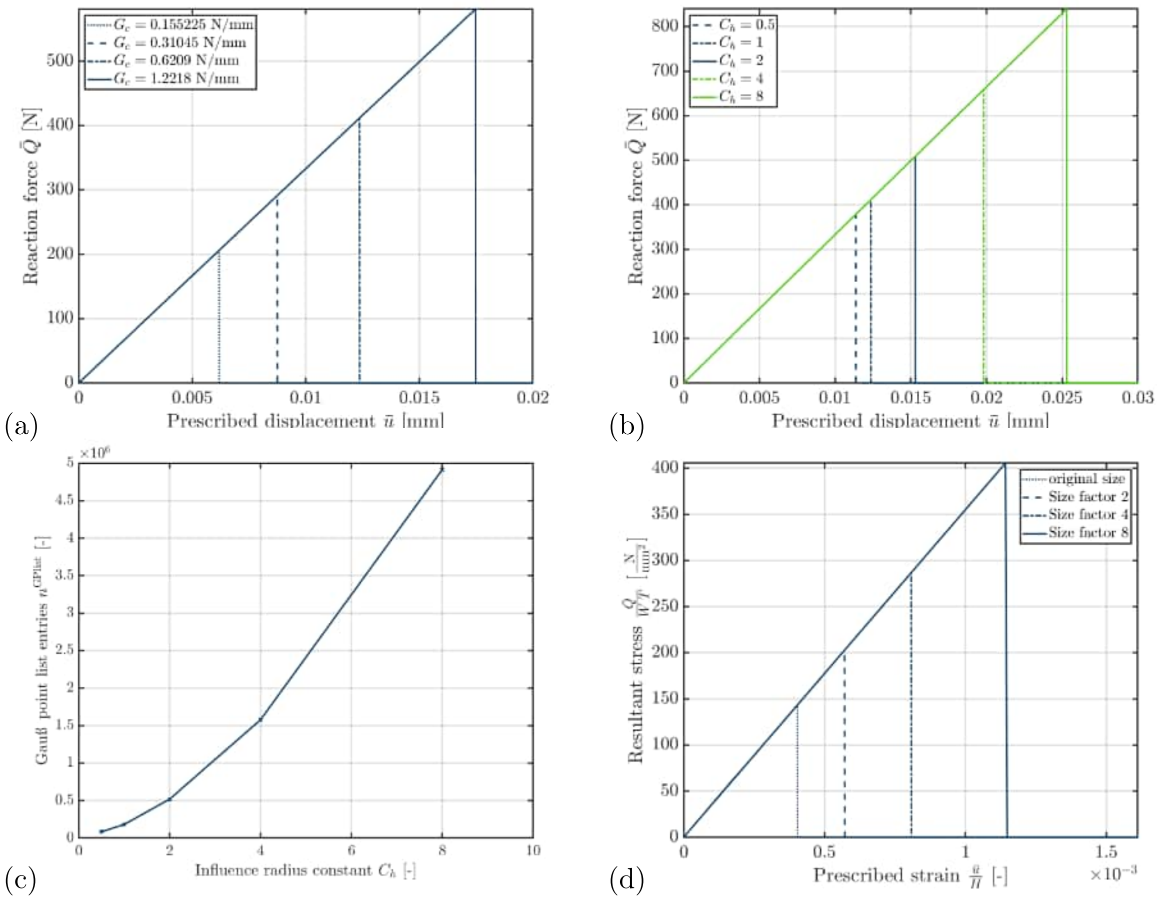

Figure 4.6.: (a)Reaction force $\bar{Q}$ over displacement $\bar{u}$ of brittle specimen for different Griffith-type energy release rates G_c, (b) different influence radii constants C_h that determine the influence radius $\epsilon = C_h\, h$ and (c) number of entries in Gauß point list over influence radius constant C_h.

4.2.1. Elasto-plastic specimen

At first, the elasto-plastic material formulation in section 2.3.2 without regularization is applied on the specimen with different mesh sizes. In figure 4.9, the resulting equivalent plastic strain α in shown for an external displacement of $\bar{u} = 0.2$ mm. The lines of plastic deformations, the so-called **shear bands**, evolve diagonally. This coincides with the results of the analytical investigations in Onat and Prager [104]. Because of the asymmetric imposition of the weakness and therefore, the initial crack, the shear bands loose their symmetry and only appear in one of the two possible directions. However, the intensity of the plastic strains increases and the thickness of the shear bands decreases with decreasing element size h. This effect occurs due to the development of the plastic deformations. When a certain deformation $\bar{u}$ is reached, the plastic yield stress in one row of elements is surpassed so that they deform plastically. Due to plasticity, their stiffness is reduced so that further deformations primarily occur in those because their resistance against further deformation is lower compared to the ones of the neighboring elements. Hence, only one row of elements deforms plastically and thus, the plastic deformations are mesh-dependent. The elements outside the shear band only deform elastically. Thus, the energy $-\Delta U_K$ imposed in those solely consists of the contribution from the elastic part ψ^{e} of the energy density. In contrast to that, the imposed energy within the shear bands is increased by the contribution of the plastic part ψ^{p}. Therefore, their imposed energy is higher than the one of the surrounding elements and thus, only they erode, as shown in figure 4.11. Because of this, the crack evolves diagonally along the shear bands

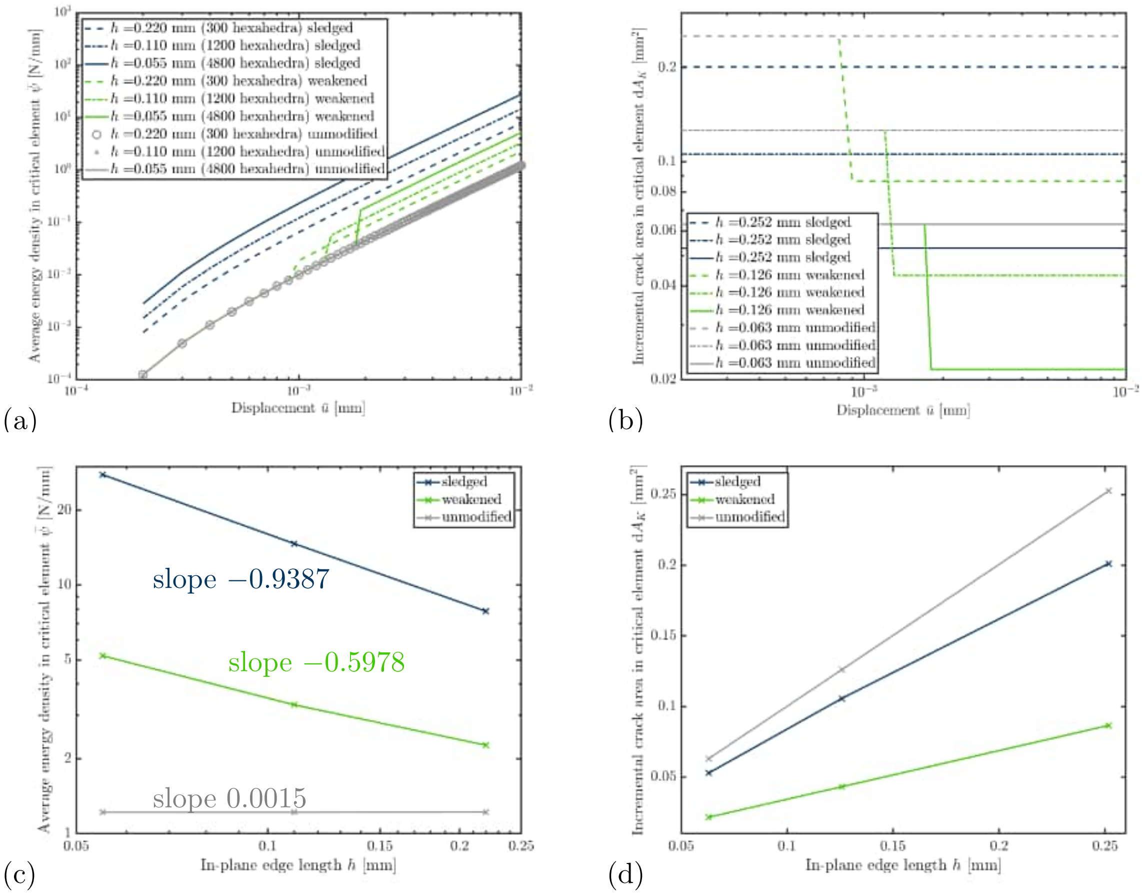

Figure 4.7.: Average energy $\bar{\psi}$ of the element that is going to be eroded first over (a) macroscopic displacement $\bar{u}$ and (c) critical average energy $\bar{\psi}$ at which this element erodes over the characteristic in-plane edge length h at the displacement $\bar{u} = 0.01$ mm, and incremental crack area $\mathrm{d}A_K$ over (b) the macroscopic displacement $\bar{u}$ and over (d) the characteristic in-plane edge length h at the displacement $\bar{u} = 0.01$ mm.

as expected for ductile crack propagation in this experiment whereas it evolves straightly in brittle specimen without plasticity. This crack path is obtained for all different discretizations. Furthermore, it is demonstrated that the crack path is able to propagate across the element

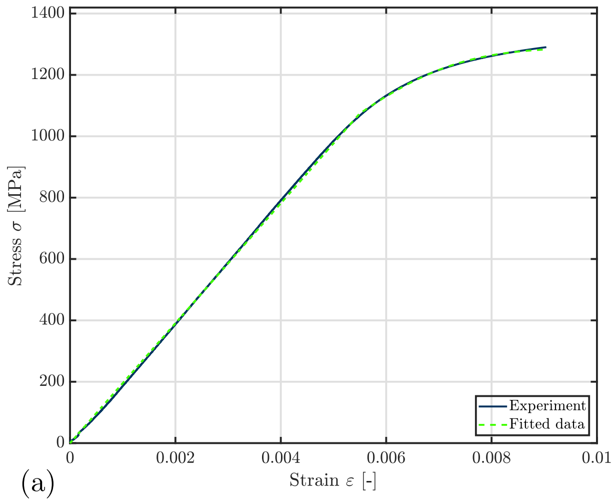

(a)

Parameter	Value	Unit
κ	164883.0	MPa
μ	76100.0	MPa
y_0	1073.47	MPa
y_∞	1289.57	MPa
h^{exp}	1394.84	-
h^{lin}	67.22	MPa

(b)

Figure 4.8.: (a) Adjusted stress-strain curve of elasto-plastic material (iron alloy) and (b) material parameters, taken from Wingender and Balzani [150].

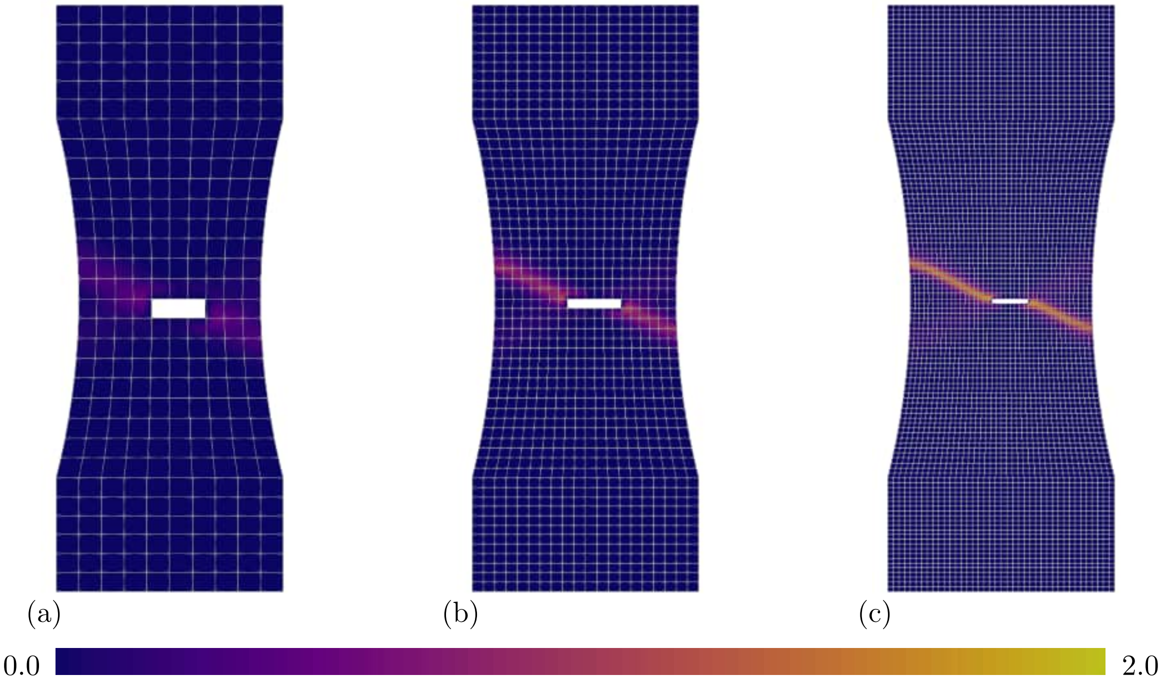

(a) (b) (c)

Figure 4.9.: Distribution of equivalent plastic strain α at $\bar{u} = 0.2$ mm using the unregularized elasto-plastic formulation for different element sizes (a) $h = 0.22$ mm, (b) $h = 0.11$ mm and (c) $h = 0.065$ mm, taken from Wingender and Balzani [150].

orientation so that it can be assumed that the element shape does not affect the crack path. Because the intensity of the plastic deformations increases with decreasing element size h, the time t_c at which the crack propagates, varies with different discretizations. Hence, the plastic deformations localize too strongly to obtain a mesh-independent framework for ductile crack crack propagation if the elasto-plastic material law without regularization is considered. This effect is observable in the resulting force-displacement curves in figure 4.10. Therein, no convergence with decreasing element size h can be observed. Hence, for the investigation of mesh convergence of a simulation framework that includes crack propagation, it is not

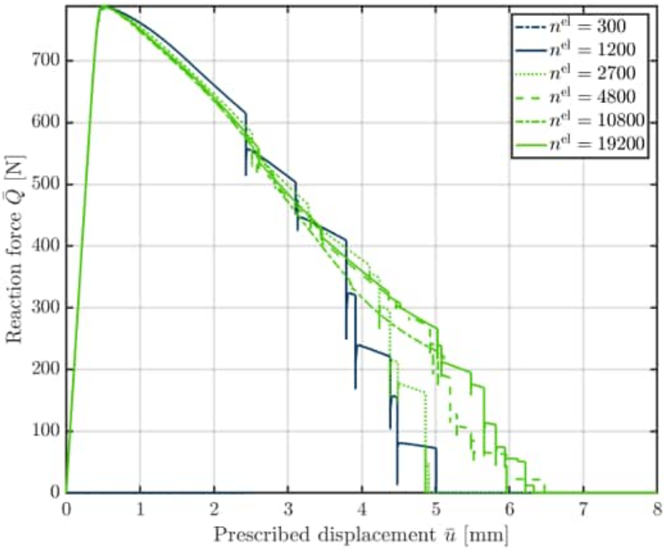

Figure 4.10.: Force-displacement curve for the unregularized elasto-plastic material formulation. Clearly, convergence cannot be observed, taken from Wingender and Balzani [150].

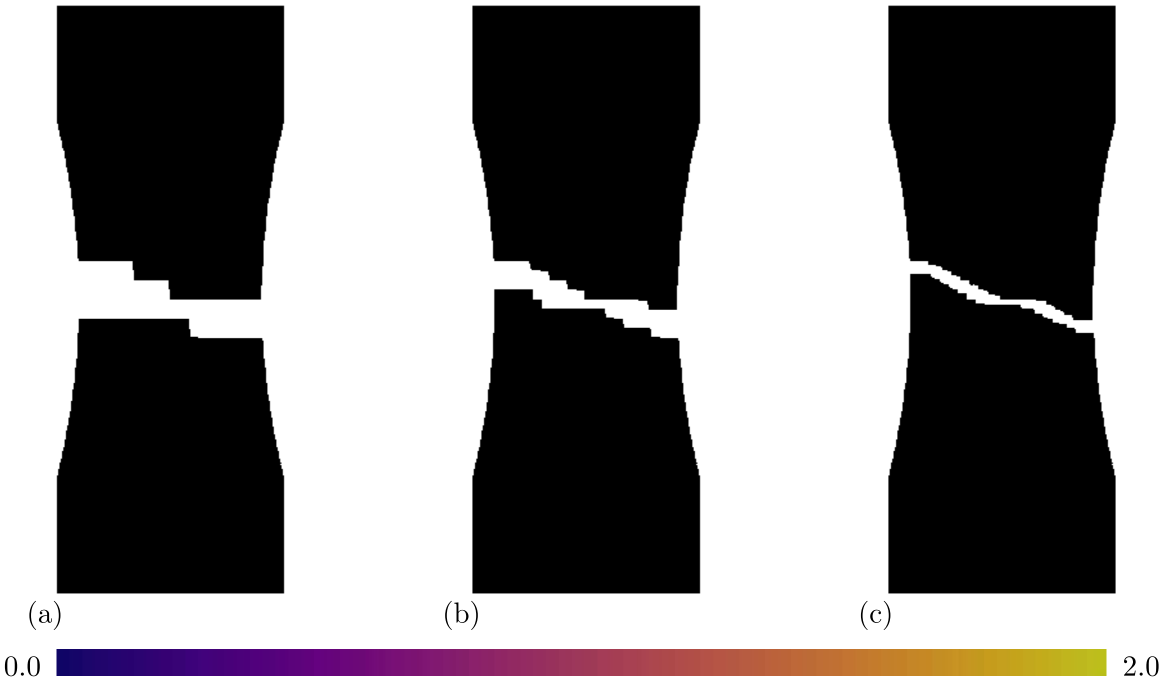

Figure 4.11.: Crack path and equivalent plastic strain α resulting from unregularized elasto-plastic formulation for different element sizes (a) $h = 0.22$ mm, (b) $h = 0.11$ mm and (c) $h = 0.065$ mm, taken from Wingender and Balzani [150].

sufficient to only consider the crack path. The structural response has to be regarded as well. In the shown force-displacement curves, finite jumps are observable at times when the crack propagates. Here, the crack propagates in multiple time steps instead of one time step as in brittle specimen. This effect occurs because the neighboring elements partially capture the energy, that is released due to the element erosion, because the additional energy dissipates into additional plastic deformation.

4.2.2. Ductile crack propagation with regularization

In order to obtain a framework with mesh-independence in the crack path as well as in the structural response, the exaggerated localization of the plastic deformation has to be reduced to remove the mesh-dependence of the time t_c at which the crack propagates. Therefore, the elasto-viscoplastic material law in which the plasticity is regularized due to the delaying viscosity is considered. Here, the specimen is simulated with the viscosity $\eta = 300\,\mathrm{MPa\,s}$ and the localization parameter $\delta = 0.2$. In figure 4.12, the effect of the regularization becomes visible: Here, the plastic deformations converge with decreasing mesh size h. Due to the viscosity, the plasticity is delayed so that the elements in the row in which plasticity occurs firstly are kept from loosing too much stiffness. Because of that, the stresses in the neighboring elements are higher compared to the elasto-plastic example. This triggers plastic deformations in these as well. Hence, the shear bands spread over more than only one row of elements. Furthermore, the delay of the plasticity allows a second diagonal shear band with a lower intensity to form. Again, the crack path develops diagonally and converges with decreasing element size h, as shown in figure 4.13. Since the plastic deformations converge, the resulting reaction force $\bar{Q}$ also converges, cf. figure 4.14. Thus, the viscosity, as applied here, prevents the plasticity from localizing too strongly and therefore, prevents mesh-dependence due to plastic localization effects. Hence, the qualitative and quantitative mesh-independence of the presented framework for ductile crack propagation is demonstrated.

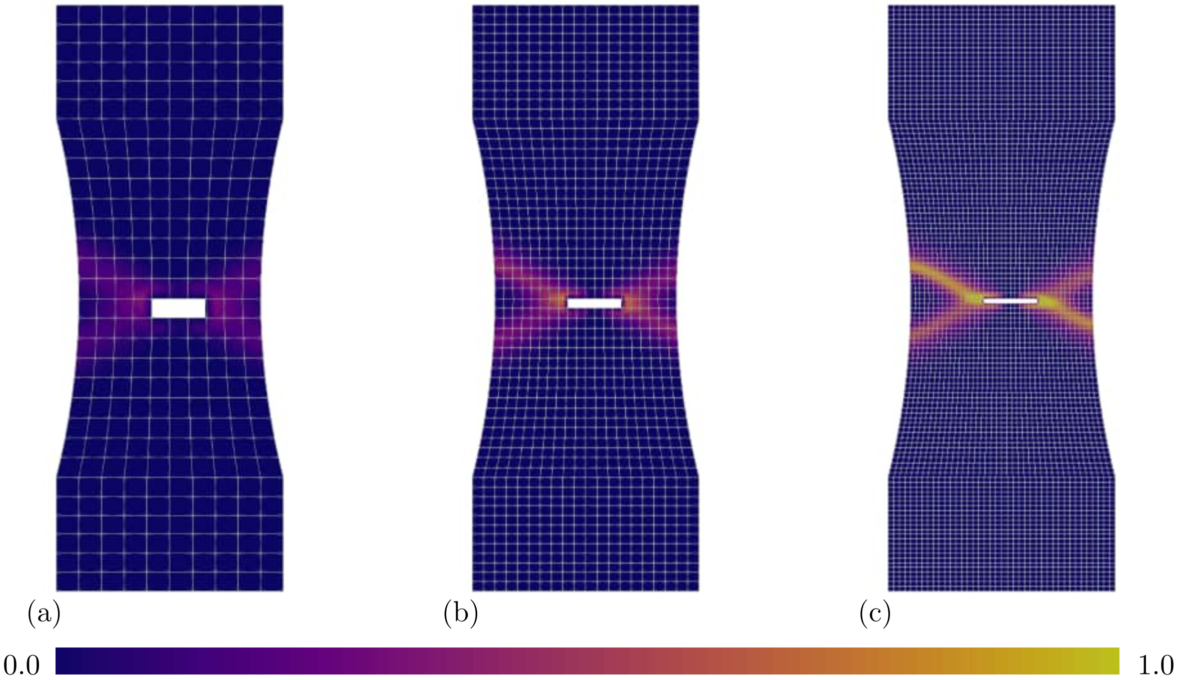

Figure 4.12.: Distribution of equivalent plastic strain α at $\bar{u} = 0.25$ mm using the regularized elasto-viscoplastic formulation for different mesh sizes (a) $h = 0.22$ mm, (b) $h = 0.11$ mm and (c) $h = 0.065$ mm, taken from Wingender and Balzani [150].

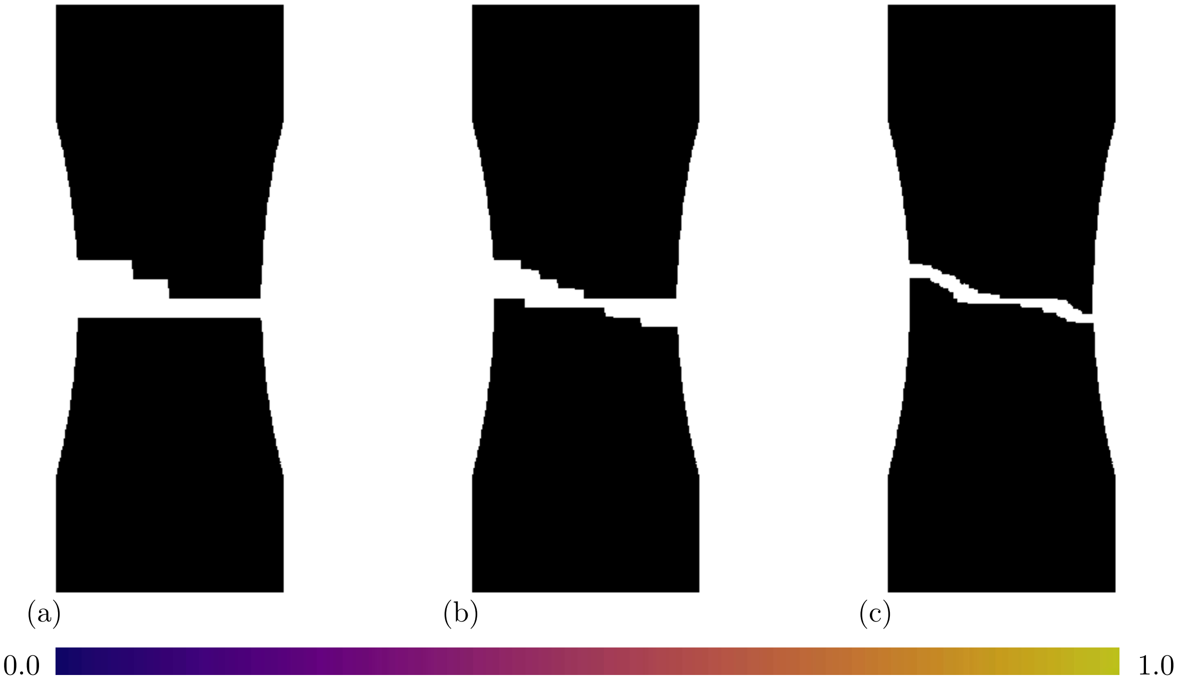

Figure 4.13.: Crack path resulting from regularized elasto-plastic formulation for different element sizes (a) $h = 0.22$ mm, (b) $h = 0.11$ mm and (c) $h = 0.065$ mm, taken from Wingender and Balzani [150].

4.2.3. Influence of regularization intensity

To achieve the mesh-independence and physically reasonable results, the regularization parameters, namely the viscosity η and the localization parameter δ, have to be adjusted properly. To analyze the effect of these two parameters on the distribution of the plastic deformations, the tensile test on the weakened specimen as well as on an unmodified specimen is simulated again. Hereby, the viscosity η and the localization parameter δ are varied. The resultant

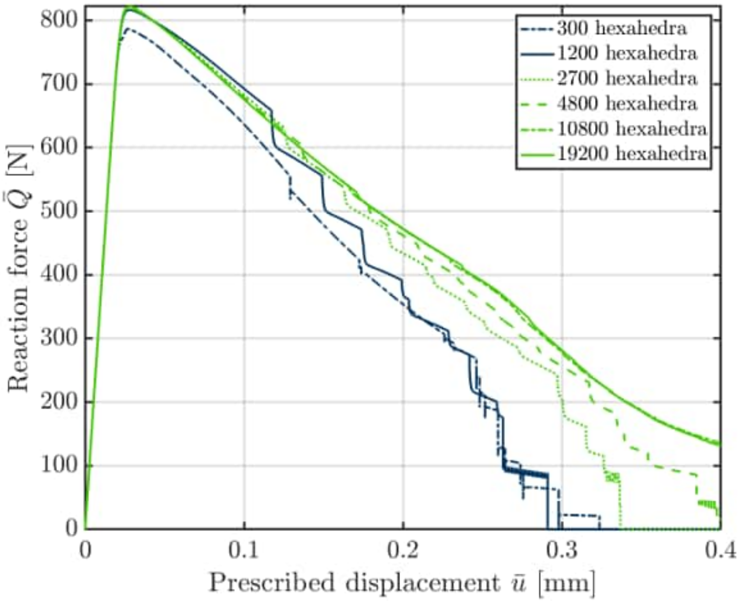

Figure 4.14.: Force-displacement curve for the regularized elasto-plastic material formulation, taken from Wingender and Balzani [150]. The converging response indicates mesh-independence.

distribution of the equivalent plastic strains α over the specimen are shown in the figures 4.15 and 4.16 for a prescribed displacement of $\bar{u} = 0.15$ mm. The higher the viscosity η is set, the more are the plastic deformations delayed. This enables the neighboring elements to deform plastically as well so that the shear bands are smeared out. In the specimen with the viscosity $\eta = 3000$ MPa, the plastic deformation is spread over the whole body. On other side, if the viscosity is chosen small, here 30 MPa and 100 MPa, the plastic deformation speed and thus, the localizations are high. As a result, the plastic field looses its symmetry and in extreme cases, only one shear band forms. However, the viscosity η is not sufficient for the adjustment of the shear bands because it delocalizes too heavily even if it is set small enough to form shear bands. In that case, the crack develops straight through the material. To avoid this case, the application of the localization parameter δ is considered additionally. The higher this parameter is chosen, the more the shear bands localize. With this parameter, the thickness of the shear bands are adjusted. In figure 4.17, the effect of the viscosity η and the localization parameter δ on the reaction forces $\bar{Q}$ are visualized. The force-displacement curves for different values of the viscosity η and the localization parameter δ are shown in figure 4.17. With increasing values of η and decreasing values of δ, the reaction force $\bar{Q}$ increases because the plastic deformations develop slower. Vice versa, if, e.g., δ is chosen to a large value, here $\delta = 5$ and $\delta = 20$, the reaction force drops rapidly because of the fast reduction of the specimen's stiffness in the elements that deform plastically. Note, that the results depend on the velocity $\dot{\bar{u}}$ of the prescribed displacements and on the time step size Δt since the viscosity behaves rate-dependently.

4.2.4. Simulation with cyclic loading

As seen in the previous examples for ductile crack propagation, the crack does not necessarily propagate through the whole specimen instantly but advances subcritically step by step under increasing deformation. This subcritical propagation may also occur under cyclic loads, even though the critical load at which the specimen breaks into two parts has not been reached. Here, the crack length increases with increasing number of load cycles. This effect takes an important role in the context of fatigue. To demonstrate the capability of

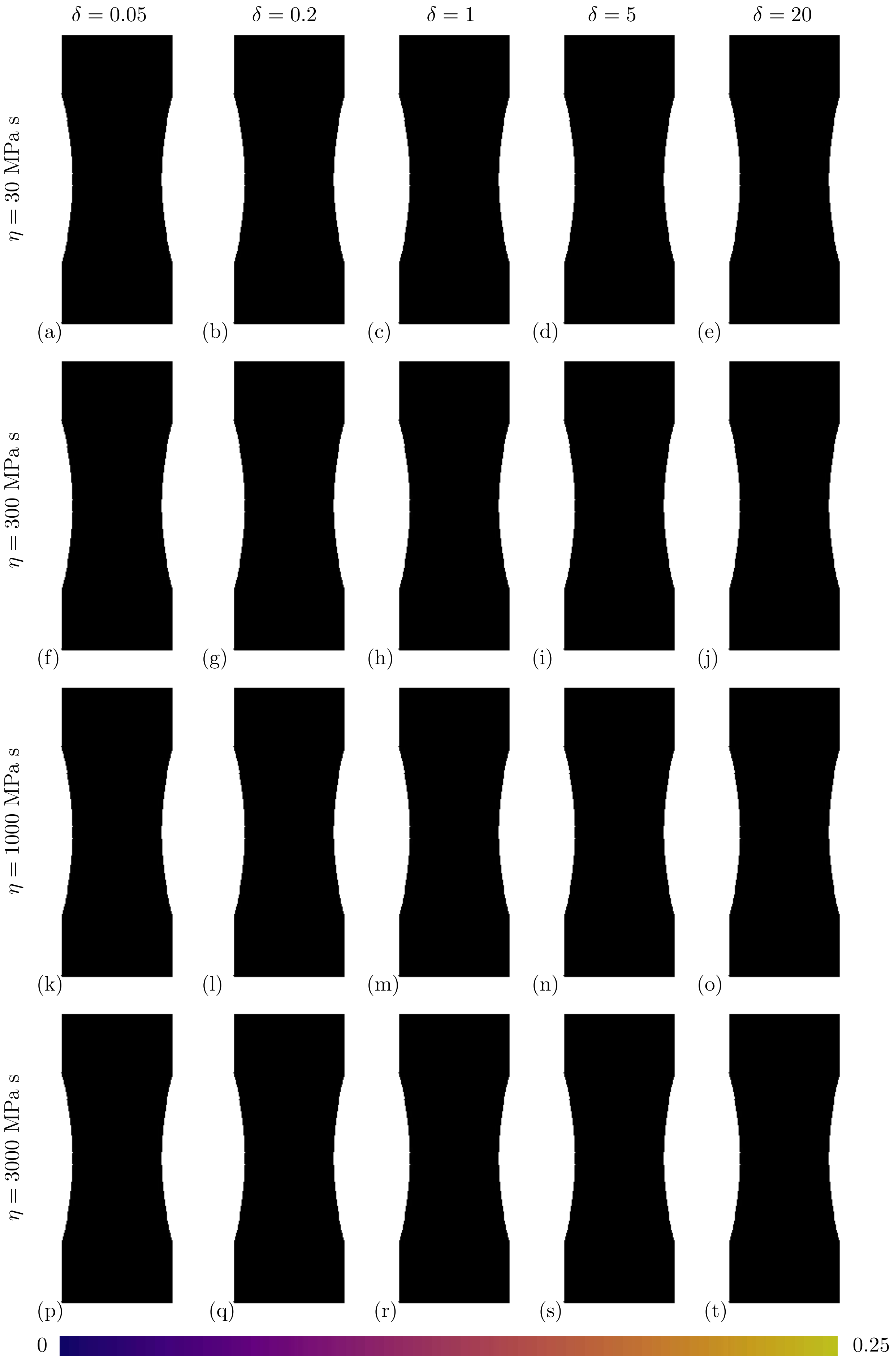
$\delta = 0.05$
$\delta = 0.2$
$\delta = 1$
$\delta = 5$
$\delta = 20$
$\eta = 30$ MPa s
$\eta = 300$ MPa s
$\eta = 1000$ MPa s
$\eta = 3000$ MPa s
(a)
(b)
(c)
(d)
(e)
(f)
(g)
(h)
(i)
(j)
(k)
(l)
(m)
(n)
(o)
(p)
(q)
(r)
(s)
(t)
0
0.25

Figure 4.15.: Distribution of equivalent plastic strain α in homogeneous specimen for different values of the viscosity η and the localization parameter δ at $\bar{u} = 0.15$ mm, taken from Wingender and Balzani [150].

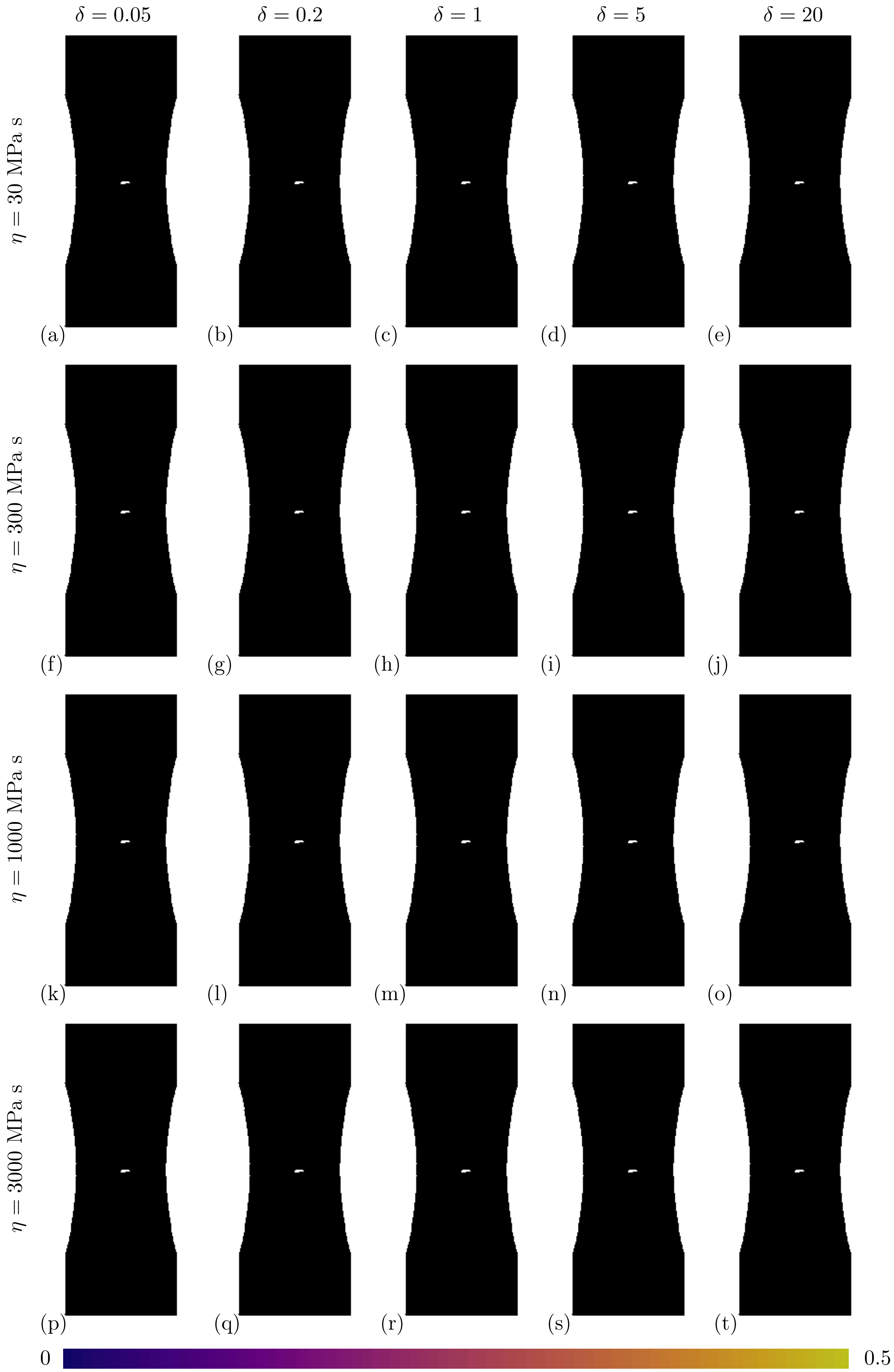

Figure 4.16.: Distribution of equivalent plastic strain α in weakened specimen for different values of the viscosity η and the localization parameter δ at $\bar{u} = 0.15$ mm, taken from Wingender and Balzani [150].

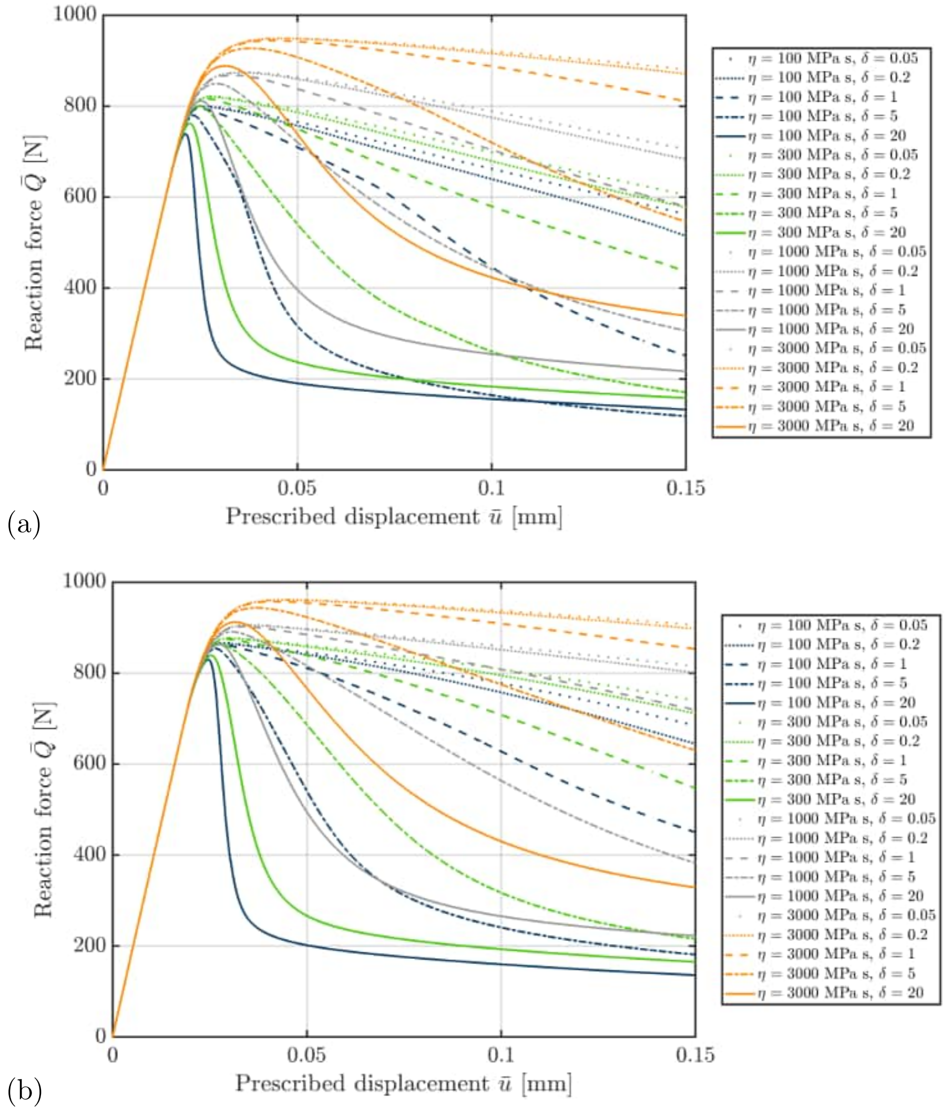

Figure 4.17.: Force-displacement curves for different values of regularization parameters for (a) homogeneous and (b) weakened specimen, taken from Wingender and Balzani [150].

the proposed framework to simulate fatigue solely based on macroscopic effects, in particular plasticity, the specimen in figure 4.18a is simulated under cyclic forces at the top edge. The force $F(t) = F_{\max} \sin(2\,\pi\,t)$ is sinusoidal with a frequency of 1 Hz. This frequency is so slow that inertia effects do not affect the results. In different simulations, the amplitudes $F_{\max}$ are varied so that the dependence of the crack propagation on the load is analyzed. To avoid bending of the plate when the load is negative, out-of-plane displacements at the backside of the specimen is prohibited. The specimen with the weakened area is considered with the previous geometry parameters from figure 4.9c and the material parameters from figure 4.8b. Here, the elasto-plastic material law is chosen. Even though no mesh convergence can be achieved with this assumption, qualitatively accurate results are expected because the same discretization is considered in all variations. However, the mesh-independent elasto-viscoplastic material formulation with fitted parameters should be applied in predictive calculations in order to obtain quantitatively accurate results. These simulations are carried out under the assumption of varied Griffith-type energy release rates $G_c = 3,\ 6,\ 11,\ 22$ N/mm. In contrast to the previous examples, in which the specimen is only loaded under tension and thus, the crack only opens, the crack closes under compression in physical experiments so that forces are transmitted from

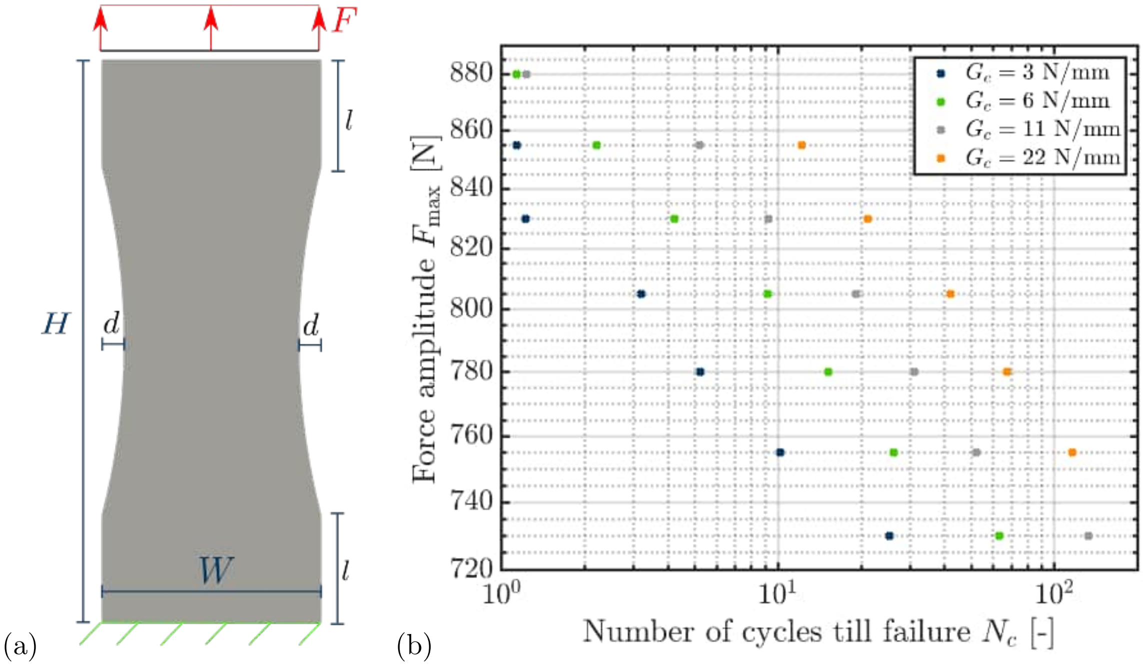

Figure 4.18.: (a) Geometry and boundary conditions of the simulations with cyclic loading $F_{\max}$, (b) resulting Wöhler curves for $G_c = 3, 6, 11, 22$ N/mm. The results show that qualitatively reasonable Wöhler curves can be obtained from the proposed algorithm, taken from Wingender and Balzani [150].

the two crack surfaces onto each other. Hence, the tension-compression split of the material formulation, which allows these forces under compression, in section 2.3.4 is applied. As a criterion to decide whether the specimen has failed or still is intact, the specimen is assumed to be failed if the specimen is broken into two parts. In figure 4.18, the resulting number of cycles N_c till failure until the specimen breaks is shown for each different investigated amplitude $F_{\max}$ and Griffith-type energy release rate G_c. This represents the technically important Wöhler curve. In the double-logarithmic space, the number of cycles till failure N_c linearly increases with decreasing amplitude $F_{\max}$. This shape coincides with data from laboratory experiments, cf., e.g., Susmel and Lazzarin [140]. If the force surpasses the maximum static force for the corresponding Griffith-type energy release rate G_c, the specimen fails in the first

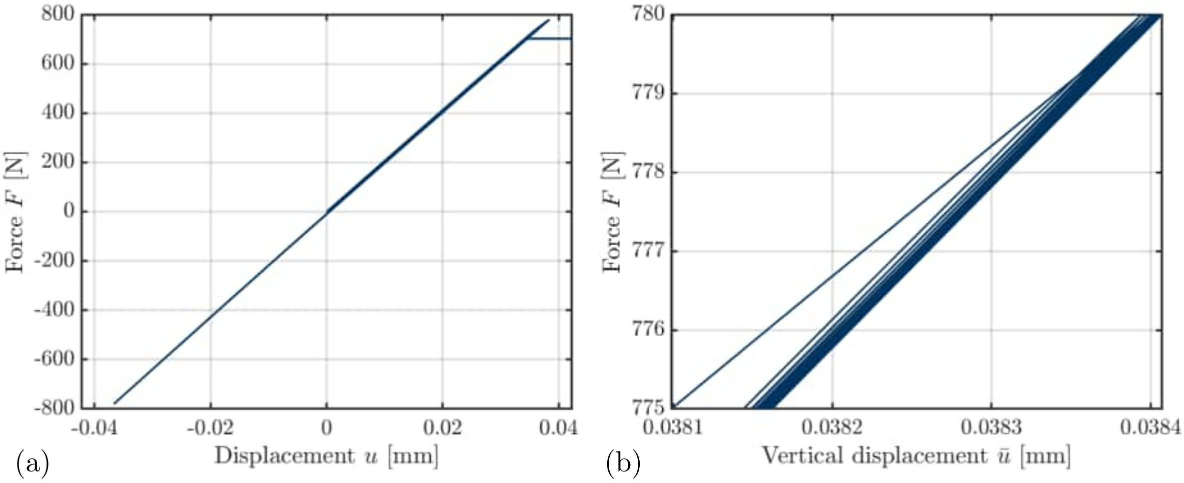

Figure 4.19.: (a) Force-displacement curve for simulation with cyclic loading and amplitude $F_{\max} = 780$ N and critical Griffith-type energy release rate $G_c = 6$ N/mm, and (b) zoomed-in illustration of the peak at the maximum of the implied force F, taken from Wingender and Balzani [150].

cycle. Furthermore, the lower the Griffith-type energy release rate G_c is set, the faster the specimen breaks into two parts. Note, that the slope of the Wöhler curves is not affected by G_c but shifted to the right with increasing values.

The force-displacement curve of the specimen with $G_c = 6$ N/mm and the amplitude F_{max} is given in figure 4.19a. Here, nothing seems to change during the cycles, whereas the zoomed figure 4.19b demonstrates that a small change occurs in every cycle. This results from plastic deformations that locally increase due to the cyclic load. The increase in the plastic deformation decreases exponentially with increasing load cycles. The elasto-plastic material law only considers isotropic hardening so that no change over the cycles would occur if a material point was loaded with a cyclic stress. However, the change in ever cycle on the specimen level is imposed by the property that the global hardening becomes slightly kinematic due to the structure. Due to hardening, the plastic potential ψ^{p} and thus, the imposed energy $-\Delta U_K$ is increased with every cycle until one element erodes. If the remaining cross-sectional of the specimen is large enough, hardening occurs over the next cycles until the next element erodes. In that case, the crack propagates subcritically. Otherwise, the crack becomes unstable so that it immediately propagates through the specimen until it breaks into two separate parts. The speed at which the plastic deformation grows depends on the applied amplitude F_{max}. It has be be chosen large enough to trigger plastic deformations in at least one material point of the specimen in order to cause crack propagation. Otherwise, the specimen behaves purely elastically so that no change in the plastic deformation occurs over the cycles and the crack cannot grow. Hence, fatigue can only be simulated with this framework if the load is chosen large enough to trigger macroscopic effects like plastic deformations. Because of this, only low cycle fatigue can be calculated with this setup. In laboratory experiments, crack propagation under lower loads appears due to microscopic effects, e.g., microscopic plastic deformations, void nucleation and microcracking. To incorporate these in simulations, multiple approaches are possible. For instance, simulations on the microscale enable the analysis of these effects and its influence on the macroscopic material behavior. As another approach, damage models, e.g., the Gurson-Tvergaard-Needlemen model, cf. Needleman and Tvergaard [100] enables the incorporation of the void, nucleation, void growth and void merging of the microscale on the macroscale.

5. Eigenerosion for heterogeneous structures

This chapter presents a way to efficiently simulate crack propagation through heterogeneous microstructures based on voxel data obtained from μCT-scans. A 2D example is demonstrated in figure 5.1a which shows a decomposition of a 48×48 pixels structure with a possible crack path. The naive approach for the discretization simply converts every pixel into a single quadrilateral (hexahedral in 3D) element. This approach leads to a high number of elements and therefore, enormous computational cost in the assembly as well as in the solving procedure. Alternatively, a somewhat parameterized geometric representation of the material boundaries can be computed, which is subsequently used for the generation of a FE mesh in terms of, e.g., tetrahedral finite elements. As seen in Schneider et al. [128], the meshing procedure becomes complicated because of fine morphological structures and again, high computational costs occur. To circumvent these problems, the **Finite Cell Method** (**FCM**), as introduced in Parvizian et al. [109], as an extension of the FEM is applied. Therein, the discretization of the microstructural displacement field is separated from the material boundary representation, as shown in Yang et al. [159]. Because of that, the discretization procedure is simplified. The second main advantage of this approach lies in the computational efficiency, because the number of equations in the global system of equations n_{eq} is kept low. If only subcells were eroded, the corresponding finite cell softens so that all remaining subcells in it erode as well. This approach leads to unrealistic wide crack paths, as shown in figure 5.1a. The microstructure would not be sufficiently incorporated. To circumvent this, a local split of finite cells is implemented, cf.Wingender and Balzani [149]. Thereby, hanging nodes occur. The conceptual numerical procedure in every time step consists of the following steps:

1. Solve the mechanical equilibrium
2. Evaluate the net energy gain $-\Delta F_{K/S}$ in every subcell S and element K
3. If any net energy gain $-\Delta F_{K/S}$ becomes larger than zero, the subcell/element with the largest net energy gains is eroded
4. If a subcell is eroded, switch all subcells in the corresponding finite cell to finite elements
5. If any subcell/element is eroded, repeat the previous steps until no erosion occurs

The standard FCM, the combination with the eigenerosion, the adaptive mesh refinement, the treatment of hanging nodes, as introduced in Demkowicz et al. [26], Oden et al. [103], Rachowicz et al. [113], the discretization scheme and a benchmark problem are described in this chapter.

5.1. The standard FCM

5.1.1. Basic concept

As an extension of the FEM, the FCM, as introduced in Parvizian et al. [109], allows the decomposition of the element domain $\mathcal{B}_K^{\mathrm{fc}}$ into n^{sc} subdomains $\mathcal{B}_1^{\mathrm{sc}} \cup \mathcal{B}_2^{\mathrm{sc}} \cup \ldots \cup \mathcal{B}_{n^{\mathrm{sc}}}^{\mathrm{sc}} = \mathcal{B}_K^{\mathrm{fc}}$ with different material properties. In this context, the element is called **finite cell**, whose corresponding variables are indicated with the superscript fc, and the subdomains are called

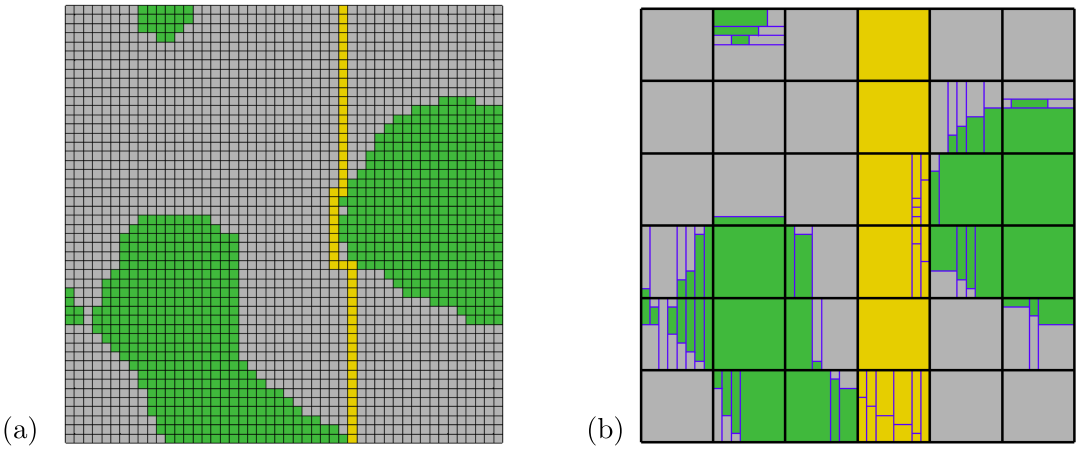

Figure 5.1.: Decomposition of (a) a binarized scan consisting of 48 × 48 pixel with two material phased (gray,green) and possible crack path (yellow) into (b) 6 × 6 finite cells simulated with FCM without transformation of the cells into elements, taken from Wingender and Balzani [149].

subcells, whose corresponding variables are indicated with the superscript sc. This permits the discretization of the domain of interest with a larger fictitious domain of simple shape, for instance hexahedra, without any restrictions regarding the material interfaces and boundaries. As shown in Düster et al. [33], the FCM was originally used to simulate complex shaped bodies like a plate with holes and bones consisting of only one material. Therein, a subcell either represents the material or void. However, in our case for the simulation of cubic microstructure RVEs based on voxel data, as seen in figure 5.2, the subcells represent different materials. The FCM leads to the advantage of not being forced to regard the material domains during the discretization of the domain of interest with finite cells. However, the finite cells have to be decomposed in such a way into subcells, that the material boundaries are represented by subcell boundaries. For the evaluation of the momentum balance in the FCM, the elemental volume integrals, that are necessary to calculate the elemental vectors and matrices of the standard FE framework, have to be modified. Therefore, they are calculated by summing up

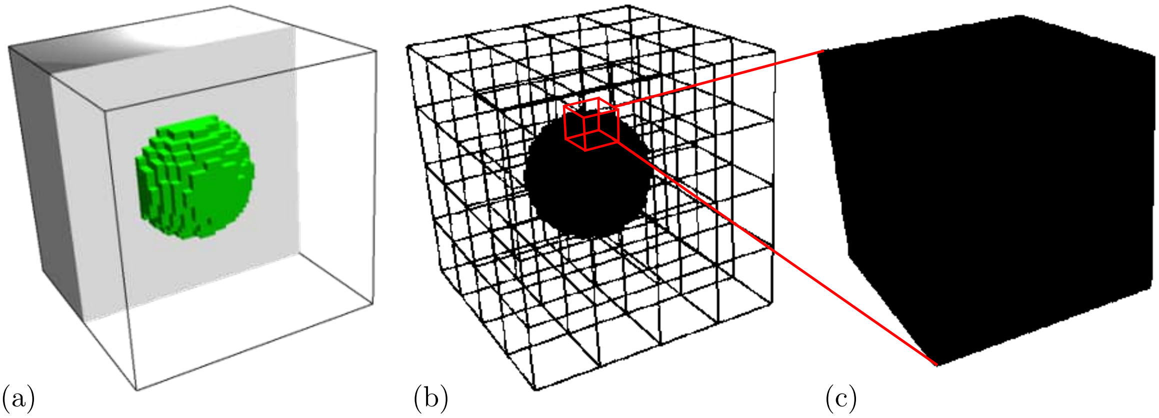

Figure 5.2.: (a) Cubic biphasic body $\mathcal{B}$ consisting of spherical inclusion (green) within matrix (gray), (b) structured mesh without regarding material interfaces and (c) one finite cell consisting of multiple subcells with different material properties as cutout of mesh, taken from Wingender and Balzani [149].

the partial vectors and matrices of the subcells S, indicated with the superscript sc. Hence,

$$\begin{aligned}
\boldsymbol{k}_K^{\mathrm{fc}} &= \sum_{S=1}^{n_K^{\mathrm{sc}}} \boldsymbol{k}_S^{\mathrm{sc}} &&= \sum_{S=1}^{n_K^{\mathrm{sc}}} \int_{\mathcal{B}_S^{\mathrm{sc}}} \underline{\boldsymbol{B}}^{\mathrm{T}} \cdot \underline{\mathbb{A}}_S \cdot \underline{\boldsymbol{B}} \,\mathrm{d}V_S \\
\boldsymbol{r}_K^{\mathrm{fc}} &= \sum_{S=1}^{n_K^{\mathrm{sc}}} \boldsymbol{r}_S^{\mathrm{sc}} &&= \sum_{S=1}^{n_K^{\mathrm{sc}}} \int_{\mathcal{B}_S^{\mathrm{sc}}} \underline{\boldsymbol{B}}^{\mathrm{T}} \cdot \underline{\boldsymbol{P}}_S \,\mathrm{d}V_S \\
\boldsymbol{m}_K^{\mathrm{fc}} &= \sum_{S=1}^{n_K^{\mathrm{sc}}} \boldsymbol{m}_S^{\mathrm{sc}} &&= \sum_{S=1}^{n_K^{\mathrm{sc}}} \int_{\mathcal{B}_S^{\mathrm{sc}}} \tfrac{\rho_{0,\,S}}{\beta\,\Delta t^2}\, \underline{\boldsymbol{N}}^{\mathrm{T}} \cdot \underline{\boldsymbol{N}} \,\mathrm{d}V_S \\
\boldsymbol{r}_K^{\mathrm{fc,m}} &= \sum_{S=1}^{n_K^{\mathrm{sc}}} \boldsymbol{r}_S^{\mathrm{sc,m}} &&= \sum_{S=1}^{n_K^{\mathrm{sc}}} \int_{\mathcal{B}_S^{\mathrm{sc}}} \rho_{0,S}\, \underline{\boldsymbol{N}}^{\mathrm{T}} \cdot \underline{\boldsymbol{N}} \\
& && \quad \cdot \left(\tfrac{1}{\beta\,\Delta t^2}\, (\boldsymbol{d}_K - \boldsymbol{d}_{K,n}) - \tfrac{1}{\beta\,\Delta t}\, \dot{\boldsymbol{d}}_{K,n} - \left(\tfrac{1}{2\,\beta} - 1\right) \ddot{\boldsymbol{d}}_{K,n} \right) \mathrm{d}V_S
\end{aligned} \tag{5.1}$$

with the subcell's material tangent $\mathbb{A}_S$, the subcell's first Piola-Kirchhoff stress $\boldsymbol{P}_S$ and the subcell density $\rho_{0,S}$ follows, cf., e.g., Wingender and Balzani [149]. Here, the mass matrix $\boldsymbol{m}_S^{\mathrm{sc}}$ of the subcells is always chosen as consistent mass matrix because if they erode, they are transformed into finite elements.

In the standard FCM, the vector of external forces $\boldsymbol{q}_K^{\mathrm{fc}}$ is modified as well, cf. Düster et al. [33], because the external tractions act on the Neumann boundaries $\partial\mathcal{B}_{\mathrm{N}}$ which may lie within a finite cell and not the finite cell's boundary. In this paper, the triangulated surfaces obtained from a CAD program are parameterized in the finite cell domain. Based on this parameterization, the force vector acting on the finite cell nodes are derived. The consideration of the subcell domains is obsolete because the external forces are only affected by the finite cell geometry and are independent from the internal discretization into subcells. Because the cuboid microstructure boundaries are represented by the finite cell boundaries exactly in our applications, the external forces $\boldsymbol{q}_K^{\mathrm{fc}} = \boldsymbol{q}_K$ are evaluated like the ones of the standard FEM. Analogously, the Dirichlet boundary conditions are directly applied on the corresponding nodes in our case, because the Dirichlet boundaries $\partial\mathcal{B}_{\mathrm{D}}$ coincide with finite cell boundaries. However, they have to be treated differently in cases, in which the Dirichlet boundaries cut finite cells. In the original FCM paper, cf. Parvizian et al. [109], the Dirichlet boundaries are approximated by assuming a "stiff strip" between the boundary of the body $\partial_{\mathrm{D}}\mathcal{B}$ and the Dirichlet boundary of the finite cells. The subcells in this strip are considered with an increased stiffness, e.g., by a factor of 10, so that the prescribed displacements are approximated. Following a second approach in Schillinger et al. [126], Ruess et al. [118], the Dirichlet boundary conditions are imposed by application of the Nitsche method. Therein, the weak form of the mechanical equilibrium equations is extended by a term, which includes the Dirichlet boundaries. The assembling procedure is executed analogously to the FEM, so that the global matrices and vectors

$$\boldsymbol{K} := \mathop{\mathsf{A}}_{K=1}^{n^{\mathrm{el}}} \boldsymbol{k}_K^{\mathrm{fc}},\ \ \boldsymbol{M} := \mathop{\mathsf{A}}_{K=1}^{n^{\mathrm{fc}}} \boldsymbol{m}_K^{\mathrm{fc}},\ \ \boldsymbol{R} := \mathop{\mathsf{A}}_{K=1}^{n^{\mathrm{fc}}} \boldsymbol{r}_K^{\mathrm{fc}},\ \ \boldsymbol{R}^{\mathrm{m}} := \mathop{\mathsf{A}}_{K=1}^{n^{\mathrm{fc}}} \boldsymbol{r}_K^{\mathrm{fc,\,m}} \ \text{and}\ \boldsymbol{Q} := \mathop{\mathsf{A}}_{K=1}^{n^{\mathrm{fc}}} \boldsymbol{q}_K^{\mathrm{fc}} \tag{5.2}$$

are calculated based on the values of the n^{fc} finite cells. With those, the global displacements $\boldsymbol{D}$ are iteratively approximated with the Newton-Raphson scheme.

5.1.2. Volume integration

In order to perform volume integration analogously to the FE framework, the integration is performed on each subcell S separately. Analogously to the FEM the Gauß quadrature is applied on the Gauß points, here in each subcell S. Therefore, the weight $w_{S,\,l}^{\mathrm{sc}}$ of the Gauß point l within the subcell S at the location $\boldsymbol{\xi}_l$ in the isoparametric space of the finite cell, as shown in figure 5.3 is considered. Furthermore, the vector $\boldsymbol{Q}_S(\boldsymbol{s})$ describes the location within the isoparametric finite cell based on the local coordinates $\boldsymbol{s} = (s_1, s_2, s_3)^{\mathrm{T}}$ of the subcell. In our case, cuboid finite cells and subcells with the dimensions h_x, h_y and h_z in the isoparametric space are assumed, so that this vector reads

$$\boldsymbol{Q}_S(\boldsymbol{s}) = \boldsymbol{\xi}_S^{\mathrm{A}} + \tfrac{1}{2}\begin{pmatrix}(1+s_1)h_x\\(1+s_2)h_y\\(1+s_3)h_z\end{pmatrix}. \tag{5.3}$$

$\boldsymbol{\xi}_S^{\mathrm{A}}$ denotes the anchor point in the middle of the subcell S. Based on this, the Jacobian

$$\boldsymbol{J}_S^{\mathrm{sc}} = \frac{\partial \boldsymbol{Q}_S(\boldsymbol{s})}{\partial \boldsymbol{s}} = \tfrac{1}{2}\begin{pmatrix}h_x & 0 & 0\\0 & h_y & 0\\0 & 0 & h_z\end{pmatrix}, \tag{5.4}$$

which maps from the isoparametric space of the finite cell to the isoparametric space of the subcell S, is derived. The Jacobian of the finite cell $\boldsymbol{J}^{\mathrm{fc}} = \boldsymbol{J}$ is evaluated analogously to the Jacobian $\boldsymbol{J}$ of the finite elements in the FEM. Due to the coordinate transformation, the matrices of the shape functions $\underline{\boldsymbol{N}}$ and their derivatives $\underline{\boldsymbol{B}}$ remain the ones from the FE framework. Considering the Gauß quadrature with n^{GP} Gauß points per subcell, the volume integrals of the subcell vectors and matrices result in

$$\begin{aligned}
\boldsymbol{k}_S^{\mathrm{sc}} &\approx \sum_{l=1}^{n^{\mathrm{GP}}} \det(\boldsymbol{J}_S^{\mathrm{sc}})\, w_{S,l}^{\mathrm{sc}}\, \det(\boldsymbol{J}^{\mathrm{fc}})\, \underline{\boldsymbol{B}}^{\mathrm{T}} \cdot \underline{\mathbb{A}}_S \cdot \underline{\boldsymbol{B}}\Big|_{\boldsymbol{\xi}_l}\\
\boldsymbol{r}_S^{\mathrm{sc}} &\approx \sum_{l=1}^{n^{\mathrm{GP}}} \det(\boldsymbol{J}_S^{\mathrm{sc}})\, w_{S,l}^{\mathrm{sc}}\, \det(\boldsymbol{J}^{\mathrm{fc}})\, \underline{\boldsymbol{B}}^{\mathrm{T}} \cdot \underline{\boldsymbol{P}}_S\Big|_{\boldsymbol{\xi}_l}\\
\boldsymbol{m}_S^{\mathrm{sc}} &\approx \sum_{l=1}^{n^{\mathrm{GP}}} \det(\boldsymbol{J}_S^{\mathrm{sc}})\, w_{S,l}^{\mathrm{sc}}\, \det(\boldsymbol{J}^{\mathrm{fc}})\, \tfrac{\rho_{0,S}}{\beta\,\Delta t^2}\, \underline{\boldsymbol{N}}^{\mathrm{T}} \cdot \underline{\boldsymbol{N}}\Big|_{\boldsymbol{\xi}_l}\\
\boldsymbol{r}_S^{\mathrm{sc,m}} &\approx \sum_{l=1}^{n^{\mathrm{GP}}} \det(\boldsymbol{J}_S^{\mathrm{sc}})\, w_{S,l}^{\mathrm{sc}}\, \det(\boldsymbol{J}^{\mathrm{fc}})\, \rho_{0,S}\, \underline{\boldsymbol{N}}^{\mathrm{T}} \cdot \underline{\boldsymbol{N}}\Big|_{\boldsymbol{\xi}_l}\\
&\quad \cdot \left(\tfrac{1}{\beta\,\Delta t^2}\,(\boldsymbol{d}_K - \boldsymbol{d}_{K,n}) - \tfrac{1}{\beta\,\Delta t}\,\dot{\boldsymbol{d}}_{K,n} - \left(\tfrac{1}{2\,\beta} - 1\right)\ddot{\boldsymbol{d}}_{K,n}\right).
\end{aligned} \tag{5.5}$$

In FCM calculations, a system of equations with a low number of degrees of freedom n_{eq} is solved in every iteration step of the Newton-Raphson scheme, even for a complex microstructure because the degrees of freedom only depend on the number of finite cells n^{fc} and their

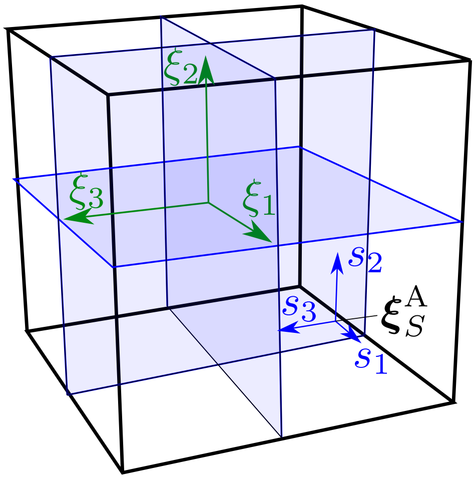

Figure 5.3.: One finite cell with its isoparametric coordinate system $\boldsymbol{\xi}$ and the coordinate system $\boldsymbol{s}$ of one of the eight subcells.

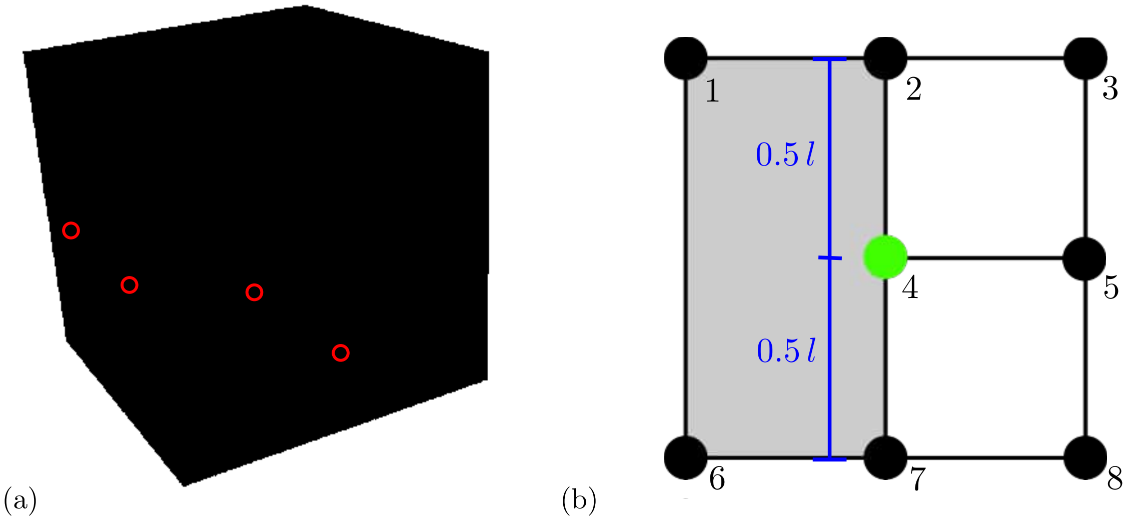

Figure 5.4.: (a) Three-dimensional semi-regular FE mesh with hanging nodes (marked with red circles), (b) two-dimensional mesh with one hanging node.

nodes, instead of the number of subcells. In opposite to that, the assembling effort depends on the number of subcells because the material law is evaluated for every Gauß point of every subcell to obtain the stress $\boldsymbol{P}_S$ and the material tangent $\mathbb{A}_S$. Additionally, the computer hardware memory is strongly influenced by the number of subcells because the history variables are also saved for every Gauß point. The FCM suffers from the disadvantage of not being able to handle strong discontinuities within the finite cells properly since continuity of the mechanical fields is required for the FEM and thus, for the FCM. This leads to the problem that crack propagation cannot simply be simulated by applying the eigenerosion approach on the FCM by eroding subcells. Another reason, why the eigenerosion cannot directly be applied, is that, even if a crack separates both sides of the finite cell, a connection between the nodes on both surfaces still exists because the stiffness matrices of the intact subcells still connect the nodes of the finite cell. An approach to tackle this kind of problem by changing the integration scheme is shown in Abedian et al. [1]. However, in our case for simulating crack propagation, we introduce a different scheme as demonstrated in section 5.3 in which hanging nodes occur.

5.2. Hanging node constraints

A second possibility to deal with hexahedral meshes based on voxel data is the generation of hexahedral meshes, e.g., by summation of voxels of the same material. Compared to the FCM, the computational effort in the assembling procedure remains but the number of equations n_{eq} which have to be solved in every iteration step of the Newton-Raphson scheme is increased tremendously due to the high number of nodes and additional constraint equations. In this approach, the mesh becomes semi-regular which leads to the occurrence of hanging nodes. These nodes do not coincide with the nodes of the neighboring elements and thus, are attached to these elements surfaces or edges, as seen in figure 5.4a. To ensure the C_0-continuity, the nodal displacements of the hanging nodes have to be constrained to the displacement of the elements they are attached to. Therefore, the concept of Demkowicz et al. [26], Oden et al. [103], Rachowicz et al. [113] for hanging node constraints is applied. The displacements $\boldsymbol{d}^H$ of the hanging node H are interpolated with

$$\boldsymbol{d}^H(\boldsymbol{X}^H) = \sum_i N_K^i(\boldsymbol{X}^H)\,\boldsymbol{d}_K^i \tag{5.6}$$

for the hanging node H at the location $\boldsymbol{X}^H$ and with the shape function N_K^i and the nodal displacements $\boldsymbol{d}_K^i$ of the nodes of constraining element K. Since all elements are subject to the same shape function, the displacement fields of two neighboring elements still match at the coinciding faces. This interpolation is rewritten to the linear constraint equation

$$d_m^H - \sum_i N_K^i(\boldsymbol{X}^H)\, d_{K,m}^i = 0 \tag{5.7}$$

for the degree of freedom m. For the implementation into the FE framework, the concept of Lagrange multipliers is applied. Therefore, the energy

$$\Pi_m^H = \lambda_m^H \left(d_m^H - \sum_i N_K^i(\boldsymbol{X}^H)\, d_{K,m}^i \right) = 0 \tag{5.8}$$

results from multiplication with the Lagrange multiplier λ_m^H, which can be interpreted as interaction force that is imposed on the hanging node in the direction m. The Lagrange multipliers are additional unknown variables, for which the global FE system of equations is solved. Vice versa, the interaction force $-\lambda_m^H N_K^i(\boldsymbol{X}^H)$ acts on the node i of the element K. Note, that the term $-N_K^i(\boldsymbol{X}^H)$ is solely nonzero for the nodes i, that lie on the surface, which the hanging node is attached on. If the hanging node lies on an edge, only the nodes on the same edge contribute to the energy. The sum of the interaction forces on all corresponding nodes vanishes due to the opposite sign of the forces at the nodes so that in total, no additional forces are imposed into the system. For the calculation of the reaction forces at Dirichlet boundaries, the interaction forces λ_m^H, in the case of the constrained node, or $-N_K^i(\boldsymbol{X}^H)\lambda_m^H$, in the case of the constraining nodes, are added to the reaction forces for the degree of freedom m. Analogously to the forces, the energy in equation (5.8) vanishes because the energy $\lambda_m^H d_m^H = \lambda_m^H \sum_i N_K^i(\boldsymbol{X}^H)\, d_{K,m}^i$ of the constrained node cancels out with the sum of the energy $-N_K^i(\boldsymbol{X}^H)\, d_{K,m}^i$ imposed at the constraining nodes. The sum of all energy terms due to hanging nodes is added to the total energy

$$\Pi^{\mathrm{H}} = \sum_H \sum_m \Pi_m^H. \tag{5.9}$$

For the implementation into the FE framework, this term is added to the potential Π of the momentum balance in equation (2.56). Because the terms of the potential Π^{H} are linear with respect to the Lagrange multipliers, the energy is rewritten into the form

$$\Pi^{\mathrm{H}} = \boldsymbol{\lambda} \cdot \boldsymbol{C}^{\mathrm{H}} \cdot \boldsymbol{D} = 0 \tag{5.10}$$

considering the global vector $\boldsymbol{\lambda} = [\lambda_1^1, \lambda_2^1, \lambda_3^1, \lambda_1^2, ...]^{\mathrm{T}}$ of Lagrange multipliers. The coefficient matrix $\boldsymbol{C}^{\mathrm{H}}$ contains the factor 1 and $-N_K^i(\boldsymbol{X}^H)$ of the equation (5.8) with respect to the global displacement vector $\boldsymbol{D}$. Hence, it consists of a line for each degree of freedom m for each hanging node H. Its width is the number of degrees of freedom n_{eq}. In each line there is a 1 in the column which corresponds to the constrained degree of freedom and the factor $-N_K^i(\boldsymbol{X}^H)$ in the columns of the degrees of freedom of the constraining nodes. In each constraint equation, the sum of the coefficients $\sum_i -N_K^i(\boldsymbol{X}^H) = -1$ results in minus one. All other entries are zero. Note, that the number of constraint equations $n_{\mathrm{eq}}^{\mathrm{C}}$ strongly depends on the number of nodes per element, and thus, on the chosen polynomial degree of the Lagrange polynomials. Because of that, the number of nonzero entries in the coefficient matrix is increased as well.

Under consideration of the coefficient matrix C^{H}, the first variation

$$\delta\Pi^{\mathrm{H}} = \delta\boldsymbol{D} \cdot \frac{\partial \Pi^{\mathrm{H}}}{\partial \boldsymbol{D}} + \delta\boldsymbol{\lambda} \cdot \frac{\partial \Pi^{\mathrm{H}}}{\partial \boldsymbol{\lambda}} = \delta\boldsymbol{D} \cdot \left(\boldsymbol{C}^{\mathrm{H}}\right)^{\mathrm{T}} \cdot \boldsymbol{\lambda} + \delta\boldsymbol{\lambda} \cdot \boldsymbol{C}^{\mathrm{H}} \cdot \boldsymbol{D} \tag{5.11}$$

of the potential Π^H results. By addition of this term to the variation $\delta\Pi$ of the momentum balance and by excluding $\delta\boldsymbol{D}$ afterwards, one obtains the extended global force vector

$$\boldsymbol{f} + \left(\boldsymbol{C}^{\mathrm{H}}\right)^{\mathrm{T}} \cdot \boldsymbol{\lambda} = \boldsymbol{R} + \boldsymbol{R}^{\mathrm{m}} + \boldsymbol{Q} + \left(\boldsymbol{C}^{\mathrm{H}}\right)^{\mathrm{T}} \cdot \boldsymbol{\lambda} \overset{!}{=} \boldsymbol{0} \tag{5.12}$$

which is solved for the global displacement vector $\boldsymbol{D}$ and the vector of Lagrange multipliers $\boldsymbol{\lambda}$ simultaneously. Additionally, the system of linear equations

$$\boldsymbol{C}^{\mathrm{H}} \cdot \boldsymbol{D} \overset{!}{=} \boldsymbol{0} \tag{5.13}$$

follows by assuming that the relation $\delta\boldsymbol{\lambda} \cdot \boldsymbol{C}^{\mathrm{H}} \cdot \boldsymbol{D} \overset{!}{=} \boldsymbol{0}$ holds for arbitrary $\delta\boldsymbol{\lambda}$. These two systems of equations are combined to

$$\bar{\boldsymbol{f}}(\bar{\boldsymbol{D}}) = \begin{pmatrix} \boldsymbol{R} + \boldsymbol{R}^{\mathrm{m}} + \boldsymbol{Q} + \left(\boldsymbol{C}^{\mathrm{H}}\right)^{\mathrm{T}} \cdot \boldsymbol{\lambda} \\ \boldsymbol{C}^{\mathrm{H}} \cdot \boldsymbol{D} \end{pmatrix} \overset{!}{=} \boldsymbol{0} \tag{5.14}$$

with the global vector of unknown variables $\bar{\boldsymbol{D}} := [\boldsymbol{D}^{\mathrm{T}},\ \boldsymbol{\lambda}^{\mathrm{T}}]^{\mathrm{T}}$. The solution of this nonlinear system of equations is approximated by application of the Newton-Raphson scheme

$$\frac{\partial \bar{\boldsymbol{f}}}{\partial \bar{\boldsymbol{D}}} \cdot \Delta\bar{\boldsymbol{D}} = -\bar{\boldsymbol{f}} \tag{5.15}$$

iteratively. By inserting the FE terms including the constraint equations, the linear system of equations

$$\underbrace{\begin{bmatrix} \boldsymbol{K} + \boldsymbol{M} & \left(\boldsymbol{C}^{\mathrm{H}}\right)^{\mathrm{T}} \\ \boldsymbol{C}^{\mathrm{H}} & \boldsymbol{0} \end{bmatrix}}_{:=\bar{\boldsymbol{K}}} \cdot \underbrace{\begin{bmatrix} \Delta\boldsymbol{D} \\ \Delta\boldsymbol{\lambda} \end{bmatrix}}_{:=\Delta\bar{\boldsymbol{D}}} = \underbrace{\begin{bmatrix} -\boldsymbol{R} - \boldsymbol{R}^{\mathrm{m}} - \boldsymbol{Q} - \left(\boldsymbol{C}^{\mathrm{H}}\right)^{\mathrm{T}} \cdot \boldsymbol{\lambda} \\ -\boldsymbol{C}^{\mathrm{H}} \cdot \boldsymbol{D} \end{bmatrix}}_{:=\bar{\boldsymbol{R}}} \tag{5.16}$$

with the extended global stiffness matrix $\bar{\boldsymbol{K}}$, the extended global residual vector $\bar{\boldsymbol{R}}$ and the increment vector $\Delta\bar{\boldsymbol{D}}$ are obtained. In every step of the Newton-Raphson scheme, the linear system of equations $\bar{\boldsymbol{K}} \cdot \Delta\bar{\boldsymbol{D}} = \bar{\boldsymbol{R}}$ is built and solved for the increment vector $\Delta\bar{\boldsymbol{D}}$. The extended global matrix of the new system of equations $\bar{\boldsymbol{K}}$ is still symmetric, but not positive definite anymore which restricts the choice of numerical solving algorithms. The chosen solver Pardiso [122] is able of handling this kind of linear equations. After solving for ΔD, the nodal displacement vector $\boldsymbol{D} \Leftarrow \boldsymbol{D} + \Delta\boldsymbol{D}$ and the vector of Lagrange multipliers $\boldsymbol{\lambda} \Leftarrow \boldsymbol{\lambda} + \Delta\boldsymbol{\lambda}$ are updated. This procedure is repeated until the unknowns are approximated accurately enough.

The desired accuracy of this method is determined by the definition of a termination criterion. Because the displacements and Lagrange multiplier are of different magnitudes, the corresponding values have to be weighted. For example, if the criterion $e = |\Delta\bar{\boldsymbol{D}}| < tol$ was applied, either the increment of displacements $\Delta\boldsymbol{D}$ or the increment of Lagrange multipliers $\Delta\boldsymbol{\lambda}$ would possibly be neglected because one of those might be so large that the other one does not affect the termination criterion anymore. To avoid this problem, the norms of the vectors of the different equilibriums $|\Delta\boldsymbol{D}|$ and $|\Delta\boldsymbol{\lambda}|$ are either weighted, so that $e = |\Delta\boldsymbol{D}| + w_\lambda|\Delta\boldsymbol{\lambda}| < tol$, or two separate tolerances $|\Delta\boldsymbol{D}| < tol_{\boldsymbol{D}}$ and $|\Delta\boldsymbol{\lambda}| < tol_{\boldsymbol{\lambda}}$ are chosen. Hence, two numerical parameters, namely either the tolerance tol and the weight w_λ or the two tolerances $tol_{\boldsymbol{D}}$ and $tol_{\boldsymbol{\lambda}}$, have to be set. The concept of the weights can be applied on different termination criteria. In the applied algorithm, the residual criterion $e = |\bar{\boldsymbol{R}}_{\boldsymbol{D}}| + w_\lambda|\bar{\boldsymbol{R}}_{\boldsymbol{\lambda}}| < tol$ with the partial residuals $\bar{\boldsymbol{R}}_{\boldsymbol{D}} = -\boldsymbol{R} - \boldsymbol{R}^{\mathrm{m}} - \boldsymbol{Q} - \left(\boldsymbol{C}^{\mathrm{H}}\right)^{\mathrm{T}} \cdot \boldsymbol{\lambda}$ and $\bar{\boldsymbol{R}}_{\boldsymbol{\lambda}} = -\boldsymbol{C}^{\mathrm{H}} \cdot \boldsymbol{D}$ has empirically been found to lead to convergence in the Newton-Raphson scheme. A problem, that may occur by using this criterion, is that the termination criterion might be fulfilled but the

Vector/matrix	$\boldsymbol{D}$	$\Delta\boldsymbol{D}$	$\boldsymbol{K}$	$\boldsymbol{M}$	$\boldsymbol{R}$	$\boldsymbol{R}^{\mathrm{m}}$	$\boldsymbol{Q}$
Size	$n_{\mathrm{eq}}^{\mathrm{FE}} \times 1$	$n_{\mathrm{eq}}^{\mathrm{FE}} \times 1$	$n_{\mathrm{eq}}^{\mathrm{FE}} \times n_{\mathrm{eq}}^{\mathrm{FE}}$	$n_{\mathrm{eq}}^{\mathrm{FE}} \times n_{\mathrm{eq}}^{\mathrm{FE}}$	$n_{\mathrm{eq}}^{\mathrm{FE}} \times 1$	$n_{\mathrm{eq}}^{\mathrm{FE}} \times 1$	$n_{\mathrm{eq}}^{\mathrm{FE}} \times 1$
Vector/matrix	$\boldsymbol{\lambda}$	$\Delta\boldsymbol{\lambda}$	$\boldsymbol{C}^{\mathrm{H}}$		$\bar{\boldsymbol{K}}$	$\Delta\bar{\boldsymbol{D}}$	$\bar{\boldsymbol{R}}$
Size	$n_{\mathrm{eq}}^{\mathrm{C}} \times 1$	$n_{\mathrm{eq}}^{\mathrm{C}} \times 1$	$n_{\mathrm{eq}}^{\mathrm{C}} \times n_{\mathrm{eq}}^{\mathrm{C}}$		$n_{\mathrm{eq}} \times n_{\mathrm{eq}}$	$n_{\mathrm{eq}} \times 1$	$n_{\mathrm{eq}} \times 1$

Table 5.1.: Sizes of the global vectors and matrices of the linearized system of equations that is solved in every Newton-Raphson step to iteratively approximate the solution of the mechanical equilibrium.

increment vector $\Delta\bar{\boldsymbol{D}}$ might still lie within the magnitude of the vector $\bar{\boldsymbol{D}}$. The energy criterion $e = |\Delta\boldsymbol{D} \cdot \bar{\boldsymbol{R}}_{\boldsymbol{D}}| + w_\lambda |\Delta\boldsymbol{\lambda} \cdot \bar{\boldsymbol{R}}_{\boldsymbol{\lambda}}| < tol$ circumvents this problem and has also been found to be reasonable for the proposed algorithm. However, the weight w_λ has to be chosen differently for different simulations because the magnitudes of the values of the two equilibriums varies. Even within one simulation, the ratio of these magnitudes may vary. For example in simulations with mesh refinement including hanging nodes, the number of degrees of freedom, that contribute to the two chosen norms, changes, because additional hanging nodes occur. For the description of the matrix sizes, the number of equations $n_{\mathrm{eq}} = n_{\mathrm{eq}}^{\mathrm{FE}} + n_{\mathrm{eq}}^{\mathrm{C}}$ is divided into two parts. $n_{\mathrm{eq}}^{\mathrm{FE}}$ describes the number of entries of the global displacement vector $\boldsymbol{D}$, whereas $n_{\mathrm{eq}}^{\mathrm{C}}$ denotes the number of constraint equations. The sizes of the global vectors and matrices are given in table 5.1.

As an example for the constraint equations, the hanging node constraint for a node attached to quadrilateral element with linear shape functions in figure 5.4b with a two-dimensional mesh is given in the form of the displacement

$$\boldsymbol{D}^4 = 0.5\,\boldsymbol{D}^2 + 0.5\,\boldsymbol{D}^7 \tag{5.17}$$

of the hanging node 4. This equation contains the coefficient 0.5 which is obtained from the shape functions of the nodes 2 and 7 at the corresponding edge. Note, that here already the global node numbers are used. By evaluating the constraint equation, one obtains the equations

$$\begin{aligned} \lambda_1^4 \left(D_1^4 - 0.5\,D_1^2 - 0.5\,D_1^7\right) &= 0 \\ \lambda_2^4 \left(D_2^4 - 0.5\,D_2^2 - 0.5\,D_2^7\right) &= 0 \end{aligned} \tag{5.18}$$

for the two degrees of freedom. This extends the global system of equations in the Newton-Raphson iteration by two additional equations. Combining the coefficients, one obtains the coefficient matrix

$$\boldsymbol{C}^{\mathrm{H}} = \begin{bmatrix} 0 & 0 & -0.5 & 0 & 0 & 0 & 1 & 0 & 0 & 0 & 0 & 0 & -0.5 & 0 & 0 & 0 \\ 0 & 0 & 0 & -0.5 & 0 & 0 & 0 & 1 & 0 & 0 & 0 & 0 & 0 & -0.5 & 0 & 0 \end{bmatrix} \tag{5.19}$$

with the coefficients in the columns of the corresponding degree of freedom of the $n_{\mathrm{eq}}^{\mathrm{FE}} = 16$ degrees of freedom for every equation. Here, the vector $\boldsymbol{\lambda} = (\lambda_1^4, \lambda_2^4)^{\mathrm{T}}$ containing the Lagrange multipliers λ_1^4 and λ_2^4 has to be solved additionally. Hence, with the $n_{\mathrm{eq}}^{\mathrm{C}} = 2$ additional constraint equations, the overall system of equations contains $n_{\mathrm{eq}} = n_{\mathrm{eq}}^{\mathrm{FE}} + n_{\mathrm{eq}}^{\mathrm{C}} = 18$ equations.

5.3. Adaptive mesh refinement

The basic concept of the proposed approach is demonstrated in figure 5.5. Therein, the application of the FCM including the eigenerosion approach is shown. The body is simulated as finite cell in areas, in which no crack occurs. This leads to a low size of the global vectors and matrices of the Newton-Raphson scheme and therefore, to a low computational effort for solving the linearized system of equations. Near the crack, finite elements are considered instead of the finite cells in order to accurately resolve the crack path. Figure 5.5a shows a crack through a microstructure, which is simulated with the proposed approach. In figure 5.5b, the next subcell is eroded and lies within a finite cell. Then, the subcells of the finite cell, which corresponds to the eroded subcell, are transformed into single finite elements, cf. figure 5.5c). Thereby, the hanging nodes occur.

The basic algorithm is given in figure 5.6. At first, the input data are read and the list of Gauß points for the eigenerosion are generated. Here, this list is generated based on the Gauß points of the subcells. This Gauß point list remains if subcells are transformed into single finite elements because the Gauß points of the subcells are located at the same position as in their corresponding finite element. Because no erosion has occurred yet in the beginning, the whole structure is simulated with the FCM, which consists of n^{fc} finite cells. Only their cell matrices and vectors contribute to the linearized global system of equations. Afterwards, the loop over all time steps begins. In each time step, the algorithm consists of two major steps. The first step deals with solving the nonlinear mechanical equilibrium. In the second step, the erosion procedure is executed. Herein, the transformation of subcells into finite cells might occur. This two steps are repeated until no erosion occurs anymore.

5.3.1. Mechanical equilibrium

In every time step, the mechanical equilibrium is solved firstly by application of the Newton-Raphson scheme. In every iteration step, the local vectors and matrices are calculated. In every finite cell K, the matrix $\boldsymbol{k}_K^{\mathrm{fc}}$, the stiffness matrix $\boldsymbol{m}_K^{\mathrm{fc}}$, the residual vector $\boldsymbol{r}_K^{\mathrm{fc}}$ and inertia residual vector $\boldsymbol{r}_K^{\mathrm{fc,\,m}}$ are evaluated by summing up the n_K^{sc} partial ones $\boldsymbol{k}_S^{\mathrm{sc}}$, $\boldsymbol{r}_S^{\mathrm{sc}}$, $\boldsymbol{m}_S^{\mathrm{sc}}$ and $\boldsymbol{r}_S^{\mathrm{fc,\,m}}$ of the subcell S. Additionally, the vector of external forces $\boldsymbol{q}_K^{\mathrm{fc}}$ that act on the finite cell is calculated. Furthermore, the elemental stiffness matrix $\boldsymbol{k}_K$, residual vector $\boldsymbol{r}_K$, mass matrix $\boldsymbol{m}_K$, inertia residual $\boldsymbol{r}_K^m$ and vector of external forces $\boldsymbol{q}_K$ of all elements n^{el} are calculated. These components are used to assemble the global vectors and matrices

$$\boldsymbol{K} := \underset{K=1}{\overset{n^{\mathrm{el}}}{\mathbf{A}}}{}_{\mathrm{fe}}\, \boldsymbol{k}_K + \underset{K=1}{\overset{n^{\mathrm{fc}}}{\mathbf{A}}}{}_{\mathrm{fc}}\, \boldsymbol{k}_K^{\mathrm{fc}}, \quad \boldsymbol{M} := \underset{K=1}{\overset{n^{\mathrm{el}}}{\mathbf{A}}}{}_{\mathrm{fe}}\, \boldsymbol{m}_K + \underset{K=1}{\overset{n^{\mathrm{fc}}}{\mathbf{A}}}{}_{\mathrm{fc}}\, \boldsymbol{m}_K^{\mathrm{fc}}, \quad \boldsymbol{R} := \underset{K=1}{\overset{n^{\mathrm{el}}}{\mathbf{A}}}{}_{\mathrm{fe}}\, \boldsymbol{r}_K + \underset{K=1}{\overset{n^{\mathrm{fc}}}{\mathbf{A}}}{}_{\mathrm{fc}}\, \boldsymbol{r}_K^{\mathrm{fc}},$$
$$\boldsymbol{R}^{\mathrm{m}} := \underset{K=1}{\overset{n^{\mathrm{el}}}{\mathbf{A}}}{}_{\mathrm{fe}}\, \boldsymbol{r}_K^{\mathrm{m}} + \underset{K=1}{\overset{n^{\mathrm{fc}}}{\mathbf{A}}}{}_{\mathrm{fc}}\, \boldsymbol{r}_K^{\mathrm{fc,\,m}} \quad \text{and} \quad \boldsymbol{Q} := \underset{K=1}{\overset{n^{\mathrm{el}}}{\mathbf{A}}}{}_{\mathrm{fe}}\, \boldsymbol{q}_K + \underset{K=1}{\overset{n^{\mathrm{fc}}}{\mathbf{A}}}{}_{\mathrm{fc}}\, \boldsymbol{q}_K^{\mathrm{fc}} \tag{5.20}$$

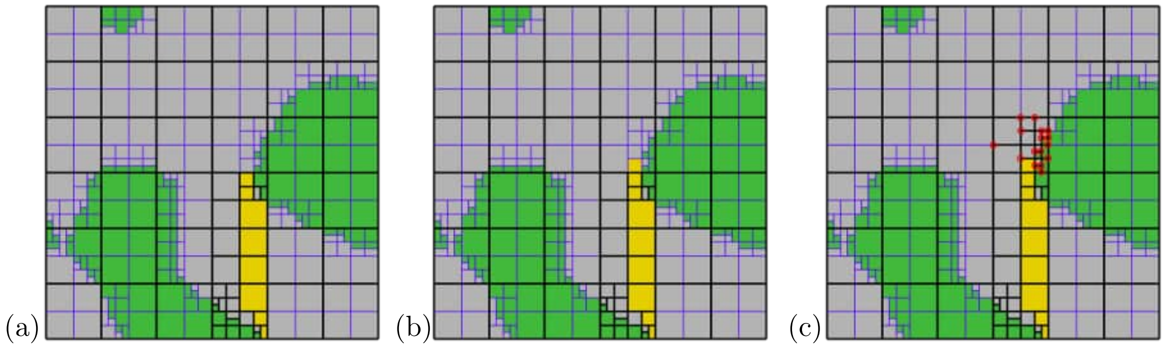

Figure 5.5.: (a) Crack (yellow) through biphasic microstructure (green, gray) with finite cell/element borders (black) and subcell borders (blue) before (b) crack propagates into the next finite cell so that (c) the subcells are transformed into single elements with new hanging nodes (red) assuming linear shape functions, taken from Wingender and Balzani [149].

```
1  Read input
2  Load lists of Gauß points in the neighborhood domain of each element
3  while time $t_k < t_{\mathrm{end}}$ do
4      while Termination criterion not fulfilled (FE/FCM not converged) do
5          for $K = 1$, number of finite cells $n^{\mathrm{fc}}$ do
6              for $S = 1$, $n_K^{\mathrm{sc}}$ do
7                  Calculation of $\boldsymbol{k}_S^{\mathrm{sc}}$, $\boldsymbol{r}_S^{\mathrm{sc}}$, $\boldsymbol{m}_S^{\mathrm{sc}}$ and $\boldsymbol{r}_S^{\mathrm{sc,m}}$
8              end
9              Calculation of $\boldsymbol{k}_K^{\mathrm{fc}} = \sum_{S=1}^{n_K^{\mathrm{sc}}} \boldsymbol{k}_S^{\mathrm{sc}}$, $\boldsymbol{r}_K^{\mathrm{fc}} = \sum_{S=1}^{n_K^{\mathrm{sc}}} \boldsymbol{r}_S^{\mathrm{sc}}$, $\boldsymbol{m}_K^{\mathrm{fc}} = \sum_{S=1}^{n_K^{\mathrm{sc}}} \boldsymbol{m}_S^{\mathrm{sc}}$, $\boldsymbol{r}_K^{\mathrm{fc,m}} = \sum_{S=1}^{n_K^{\mathrm{sc}}} \boldsymbol{r}_S^{\mathrm{sc,m}}$ and $\boldsymbol{q}_K^{\mathrm{fc}}$
10         end
11         for $K = 1$, number of finite cells $n^{\mathrm{el}}$ do
12             Calculation of $\boldsymbol{k}_K$, $\boldsymbol{r}_K$, $\boldsymbol{q}_K$, $\boldsymbol{m}_K$, $\boldsymbol{r}_K^{\mathrm{m}}$
13         end
14         Compute constraint equation matrix $\boldsymbol{C}^{\mathrm{H}}$ and assemble global system of
             equations $\bar{\boldsymbol{K}}\,\Delta\bar{\boldsymbol{D}} = \bar{\boldsymbol{R}}$
15         Solve system of equations and update vector of solution variables $\bar{\boldsymbol{D}} \Leftarrow \bar{\boldsymbol{D}} + \Delta\bar{\boldsymbol{D}}$
16     end
17     Compute net energy gain $-\Delta F_K$ and $-\Delta F_S$ for every element $K$ and subcell $S$
18     if any $-\Delta F_K > 0$ or $-\Delta F_S > 0$ then
19         Get element/subcell with $\max(-\Delta F_{K/S})$ and with $|-\Delta F_{K/S} - \max(-\Delta F_{K/S})| < tol_{\mathrm{NEG}}$
20         for elements/subcells to erode do
21             if subcell and not element then
22                 Transform finite cell into $n_K^{\mathrm{sc}}$ finite elements
23                 Change hanging node constraint matrix $\boldsymbol{C}^{\mathrm{H}}$
24             Change list of Gauß points
25         end
26         Go to 4 (solve for mechanical equilibrium)
27     else
28         $k \Leftarrow k + 1$
29     end
30 end
```

Figure 5.6.: Algorithm of the proposed strategy for the simulation of crack propagation including eigenerosion and FCM, taken from [149].

by summing up the assembled vectors and matrices of the n^{el} elements and the ones of the n^{fc} finite cells. The sizes of the global vectors and matrices remain the ones in table 5.1. Here, $\underset{K}{\mathbf{A}}_{\mathrm{fe}}$ denotes the assembly operator of the elemental matrices and vectors of the finite elements onto the global system matrices and vectors and, analogously, $\underset{K}{\mathbf{A}}_{\mathrm{fc}}$ of the ones of the finite cells. These assembly operators as well as the numbers of the finite elements n^{el} and of the finite cells n^{fc} change, if the transformation occurs. However, the sum of the number of elements and all subcells in the mesh remains over all time steps, i.e., $n^{\mathrm{el}} + \sum_K n_K^{\mathrm{sc}} = \text{const.}$, because every subcell either appears as a subcell itself or as a finite element. Hence, the computational effort for the assembly of the global system matrices and vectors is kept constant. Only the distribution of the partial matrices and vector changes due to transformation. Combined with the constraint coefficient matrix $\boldsymbol{C}^{\mathrm{H}}$, which is constructed in every time step, the global system of equations $\bar{\boldsymbol{K}}\,\Delta\bar{\boldsymbol{D}} = \bar{\boldsymbol{R}}$ is assembled. After solving this system of equations for $\Delta\bar{\boldsymbol{D}}$, the vector of nodal displacements $\boldsymbol{D} \Leftarrow \boldsymbol{D} + \Delta\boldsymbol{D}$ and the vector of Lagrange multipliers $\boldsymbol{\lambda} \Leftarrow \boldsymbol{\lambda} + \Delta\boldsymbol{\lambda}$ are updated. This process is repeated until the termination criterion, as discussed in section 5.2, is fulfilled, so that the solution of the mechanical equilibrium is approximated.

5.3.2. Element and subcell erosion

After the mechanical equilibrium is solved, the net energy gain $-\Delta F_K$ of every element K and the one $-\Delta F_S$ of every subcell S is evaluated. All elements and subcells with a net energy gain that is larger than zero are candidates for erosion. If there is no candidate, the algorithm continues with the next time step. Otherwise, the element or subcell with the largest net energy gain is eroded. Furthermore, elements or subcells, of which the net energy gain lies within a certain tolerance tol_{NEG} to the largest one, are eroded. Due to erosion, the static stiffness matrices $\boldsymbol{k}_K$ and residuals of the eroded elements and subcells are either set to zero or, in the case of material laws, which assume a tension-compression split, calculated under the assumption of the erosion variable $D = 1$. Additionally, their mass matrices $\boldsymbol{m}_K$ are switched from the consistent mass matrix to the lumped matrix. Analogously, the corresponding inertia residual vector $\boldsymbol{r}_K^{\mathrm{m}}$ is changed. If a subcell within a finite cell is eroded, the subcells of the corresponding finite cell are transformed into finite elements. Hence, the number of finite cells n^{fc} is reduced by one and the number of finite elements n^{el} is increased by the number of subcells n_K^{sc} of the finite cell. Due to the new finite elements, new nodes occur and the nodes of the former finite cell, that are not connected to any other finite cell or element, vanish. Because of that, the assembly operators $\underset{K}{\mathbf{A}}{}_{\mathrm{fe}}$ and $\underset{K}{\mathbf{A}}{}_{\mathrm{fc}}$ are adjusted during the transformation. The nodal displacements

$$\boldsymbol{d}_n = \sum_i N_K^i(\boldsymbol{X}_n)\,\boldsymbol{d}_K^i \tag{5.21}$$

of the new node n in the time step, in which the nodes exists for the first time, are calculated by interpolation based on the shape functions $N_K^i(\boldsymbol{X}_n)$ of the finite cell K at the location $\boldsymbol{X}_n$. In general, the number of nodes increases and thus, the global system matrices and vectors become larger with increasing number of eroded elements. Additionally, the number of nodes, that are hanging on the surfaces of finite elements or finite cells, increases. Because of that, the constraint coefficient matrix $\boldsymbol{C}^{\mathrm{H}}$ is enlarged vertically by the number of constrained degrees of freedom of the new hanging nodes, except by the ones that are Dirichlet bounded. In the beginning of the simulations, there is only the FCM mesh, which is regular. Hence, no hanging nodes occur and thus, the constraint coefficient matrix $\boldsymbol{C}^{\mathrm{H}}$ does not exist in the beginning. Horizontally, the constraint coefficient matrix is modified with respect to the new nodes, analogously to the assembly operators $\underset{K}{\mathbf{A}}{}_{\mathrm{fe}}$ and $\underset{K}{\mathbf{A}}{}_{\mathrm{fc}}$ during the erosion. If the constraining element is eroded, the corresponding hanging node constraints are removed, because otherwise, the nodes of the eroded element would still transfer unrealistic forces onto each other. This would contradict the assumption of traction free crack surfaces. Analogously, the hanging node constraints of constraining finite cells are removed if the finite cell is split. Although a node might be hanging on multiple elements, its constraint equations are only considered once. Otherwise, some of the constraint equations would become linearly dependent on each other so that more unknown variables λ_m^H than linearly independent equations exist. In that case, the system of equations does not have a unique solution. Thus, if a constraint equation is removed, it is checked whether the constrained node is a hanging node on another element or finite cell. If this is the case, these hanging node constraints are added to the constraint coefficient matrix $\boldsymbol{C}^{\mathrm{H}}$. In most cases, the size of this matrix is increased during the transformation of subcells into finite elements. For each line of the constraint coefficient matrix $\boldsymbol{C}^{\mathrm{H}}$, a Lagrange multiplier λ_m^H exists. Hence, the number of unknowns is changed if the constraint equations are changed. The values of the new Lagrange multiplier directly after the transformation are unknown and are not interpolated from previous values like the nodal displacements of the new nodes. Here, they are chosen to be zero, which has been found to lead to convergence of the Newton-Raphson scheme by empirical test simulations. However, the correct choice remains an open problem for future research.

The history variables at the Gauß points are not affected by the transformation process because they are located at the same place in the finite element as in the previous finite subcell. However, the inertia history variables, here the velocity $\dot{\boldsymbol{d}}_K$ and the acceleration $\ddot{\boldsymbol{d}}_K$ of the new elements, are adjusted. Therefore, these values are interpolated analogously to the interpolation of the displacements of the new nodes. Furthermore, the distribution of the mass changes because of the new distribution of the nodes due to the transformation process, whereas the total mass remains constant. Thus, an error in the inertia effects may occur. Because the dynamics is primarily applied for numerical stabilization of the simulation, this error does not change the results significantly. Only if high velocities, e.g., due to impact loading, occur, this might cause a problem because the inertia influences the crack propagation. Similar to this, the force vector of external loads $\boldsymbol{Q}$ is possibly changed because the nodes, that these forces act on, might be changed. Hereby, the sum of nodal external forces remains whereas its distribution on the nodes is changed. This also leads to a disturbance in the mechanical field, so that the Newton-Raphson scheme might fail to iteratively approximate the solution of the mechanical equilibrium, that is solved after the transformation. In a special case, some nodes might only be attached to eroded elements so that they move independently from the rest of the body. If external forces are applied on these, they accelerate constantly. This certainly leads to numerical problems. To avoid this case, the nodes, that are only attached to eroded elements, could be removed in the transformation. However, numerical problems also might occur in the case, that eroded elements underlie a material law, in which the tension-compression split is assumed. The reason for this is that the displacements of these nodes are then assumed to be fixed, so that their calculation under compression is necessary but restricted. Because of that, further work is necessary to circumvent this problem in simulations with external forces and the tension-compression split.

These two steps are repeated until the net energy gain of every element $-\Delta F_K$ and subcell $-\Delta F_S$ lies below zero. If this is the case, the crack path C as well as the vector of Lagrange multipliers $\boldsymbol{\lambda}$ and the nodal displacements $\boldsymbol{D}$ of the mechanical equilibrium are assumed to be converged in this time step. Then, the algorithm continues with the next time step until the final time step t_{end} is reached.

5.3.3. Technical remarks

As shown in section Energetic relations, initial cracks have to be imposed for mesh convergence. In this proposed approach, this is achieved by applying the same procedure as for subcell/element erosion, as shown above before the first time step. In some simulations, this procedure fails because the disturbance of the erosion of multiple elements, that are eroded at once, is so large that the Newton-Raphson scheme for the mechanical equilibrium does not converge anymore. Even in simulations considering very small time steps, this effect may occur. Especially in simulations considering the tension-compression split, the Newton-Raphson scheme has been found to be unstable if this technique for the initial crack is chosen. In another approach, the initial crack is imposed by assigning a small Griffith-type energy release rate G_c to the elements and subcells, that are supposed to be initially eroded. This leads to erosion of these elements and subcells within the first time step. In contrast to the first approach, the mechanical equilibrium is solved after the erosion of each element, so that the initial crack is imposed step by step so that the disturbance due to erosion is kept low for every time that the mechanical equilibrium is solved. This procedure stabilizes the simulation numerically. However, the computational effort is increased because for every initially eroded element or subcell, the mechanical equilibrium is solved.

The computational advantage of adaptive mesh refinement lies in the low number of global equations that are solved in every step in the Newton-Raphson iteration compared to other approaches. This results from the comparably low number of degrees of freedom in the global system of equations n_{eq}. This number depends on the sum $n^{\mathrm{el}}+n^{\mathrm{fc}}$ because only the nodes of the finite cells and elements instead of the subcells are considered. As an example for another approach, all subcells could be calculated as finite elements in the beginning of the simulation. Here, the number of finite elements $n^{\mathrm{el}} = n^{\mathrm{sc}}$ is larger than the number n^{fc} of the proposed approach. Hence, the number of equations $n_{\mathrm{eq}}^{\mathrm{FE}}$ is higher as well. Additionally, the number of constraint equations $n_{\mathrm{eq}}^{\mathrm{C}}$ is higher than in the proposed approach because a certain amount of hanging nodes are avoided in the proposed approach. Thus, the global number equations n_{eq} of the proposed approach is reduced. Far away from the crack, the global matrices and vectors are derived based on finite cells. Therefore, the computational effort for solving the linearized equations in every Newton-Raphson step is decreased. However, the computational effort for the assembly of these equations remains the same in both approaches because the number of elements and subcells is constant and equal.

For the computational memory management in the FE software FEAP, the finite cells including their subcells as well as their corresponding finite elements and the nodes that they are connected to are saved in the beginning of the simulation. The Gauß point history variables are only saved in the elements, whereas the history variables of the subcells are accessed from their corresponding finite elements. Each element or node is either considered as active, which means that they contribute to the global system of equations, or inactive, which means that they are excluded. In the beginning, only the finite cells and their nodes are assumed to be active, whereas the finite elements are assumed to be inactive. During the transformation, the finite cells are not active anymore. The elements, that have been the subcells of the finite cell before, and their nodes are activated. Furthermore, all possible hanging node constraints are calculated in a preprocessing step before the simulation starts by an external program. Therein, it is checked for each node if it lies on a surface of a finite element or finite cell, that the node is not connected to. If it does, the term $-N_K^i$ for every i node of the constraining element or cell is calculated. This process is computationally costful. The node numbers of the constrained node, the constraining nodes, their coefficients $-N_K^i$, and the finite element or finite cell number are saved into a list. Those are read as input in FEAP. In the beginning of the simulation, none of those are considered for the construction of the constraint coefficient matrix $\boldsymbol{C}^{\mathrm{H}}$. During the transformation process, the constraint equations of the new hanging nodes and their coefficients are extracted from the list. Based on these, the new constraint coefficient matrix $\boldsymbol{C}^{\mathrm{H}}$ is constructed. This avoids a computationally costly check if one of the nodes, that newly result from the transformation process, is a hanging node during the simulation because this work is shifted to the preprocessing step. As a drawback of this technique, additional memory is needed for the simulation.

5.4. Discretization of the voxel data

This section deals with the generation of voxel data by μCT-scanning and their subsequent decomposition for the simulation with the proposed framework. Figure 5.7 shows an example of the discretization. The cleaned and binarized voxel data in figure 5.7a are obtained from a μCT-scan. Afterwards, a representative cutout, cf. figure 5.7b is chosen and the proposed algorithm is applied on it so that the crack path as well as the von Mises stress in figure 5.7c results. In this section, the steps of processing the raw data obtained from the μCT-scan to obtain a binarized voxel image are described firstly. Secondly, different voxel decomposition techniques and their advantages and disadvantages as described in Fangye, Miska, and Balzani [36] are discussed. Finally, the discretization procedure for the FCM combined with the eigenerosion, as shown in Wingender and Balzani [149], is demonstrated by application on a numerical example.

5.4.1. Generation of voxel data from μCT-scan

Setup of the μCT-scan To obtain information about the morphology of MMCs, tomography methods are applied. In these methods, the structure is penetrated by an X-ray wave which is measured. For example, the electron backscatter diffraction (EBSD) is capable of providing microstructural information as for example crystallographic texture, as shown in Zaefferer et al. [162], Zaafarani et al. [161]. In our case, the computed tomography (CT), cf.Kalender [61] is applied. This technique is widely used in medicine for scanning human bodies or in industrial applications because it enables a high resolution, three-dimensional scan without destruction of the specimen. Because in our case, the CT-scan is applied on the microscopic level, which is the magnitude of the inclusions of the investigated MMC, it is referred as μCT-scan. In figure 5.8a, the scanning setup is presented. The specimen is polished and placed in front of the X-ray tube which emits X-rays. These penetrate the specimen and are measured with a sensor. The intensity of the X-ray passing the specimen depends on the density of the voxel's material. The lower the density, the more X-rays pass the specimen. In order to capture every point, the specimen is moved in discrete steps in such a way that the whole body or a chosen cutout is scanned. Afterwards, the 3D image representing the microstructure by assigning gray-scale values to voxels of a certain size is reconstructed computationally. Due to the high radiation, the setup is placed inside a chamber to reduce the radiation exposure on the laborands, cf. figure 5.8b. Note, that the μCT-scanning technique is only capable of scanning three-dimensional volume elements so that surfaces and interfaces cannot be represented because of their two-dimensional geometry. Hence, crack surfaces cannot be identified with this technique. Because the voxel boundaries do not match with the material boundaries in general, the voxels, that cut the material interfaces, will later be assigned to one of the phases the microstructure consists of so that the representation of the inner material surfaces is not accurate. To keep this effect small, a high resolution should be chosen high in order to reduce the voxel sizes. Some methods have been developed to reconstruct the surfaces for the meshing procedure. However, it is not guaranteed that the reconstructed surfaces coincide with the real surfaces of the specimen. Hence, the question whether the voxel data or the reconstructed surface represents the microstructure better is open for every scanned microstructure.

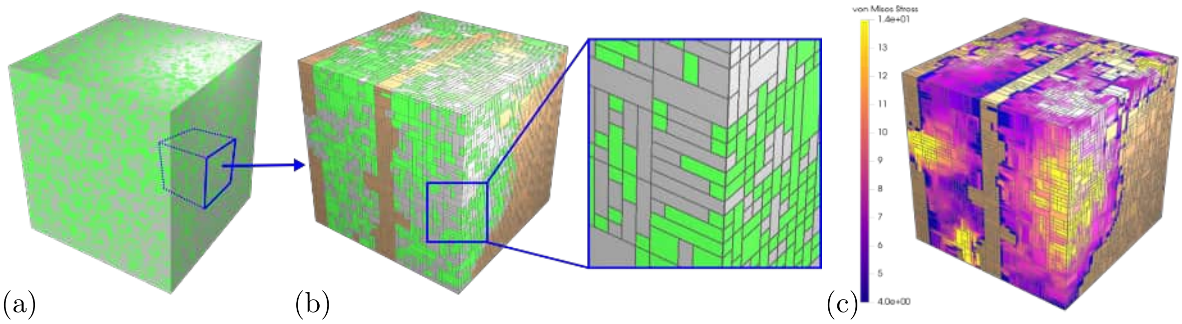

Figure 5.7.: (a) Binarized voxel image consisting of metal matrix inclusion (green) within metal matrix (silver), (b) decomposed extracted part of it with simulated crack (gold) and (c) von Mises stress, taken from Wingender and Balzani [148].

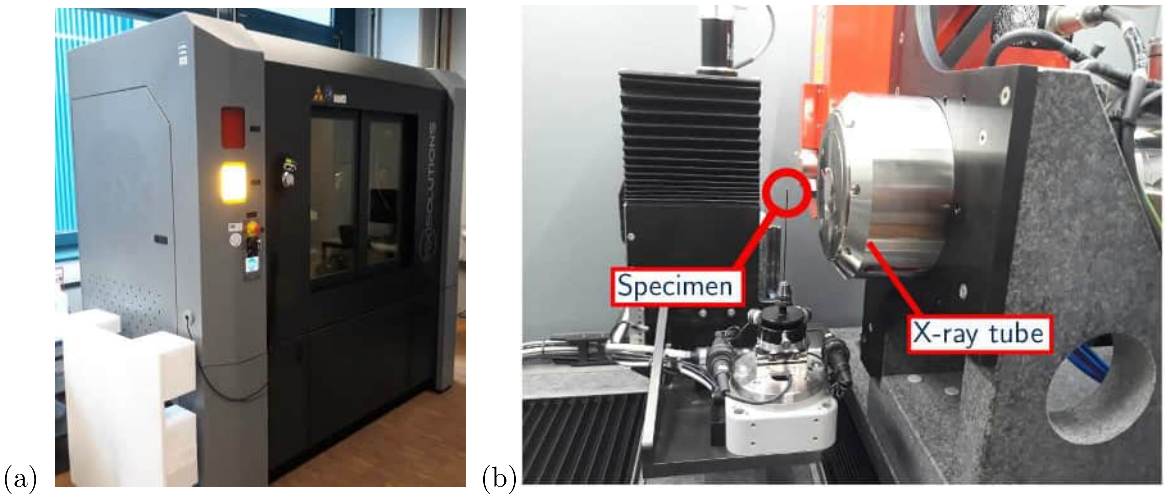

Figure 5.8.: (a) Scanning setup consisting of the X-ray tube emitting X-rays through the specimen inside the chamber in (b). The experiments were performed in the laboratories of the Zentrum für Grenzflächendominierte Höchstleistungswerkstoffe, ZGH (Ruhr-Universität Bochum, Germany).

Preparation of voxel data From the μCT-scan, a voxel data set consisting of $371 \times 359 \times 1043$ voxels containing gray scale values is obtained. Their gray-scale values represent the MMC microstructure Ferrotitanite, as shown in figure 5.9a. Here, the highest possible resolution of this setup $1\,\mu\mathrm{m} \times 1\,\mu\mathrm{m} \times 1\,\mu\mathrm{m}$ per voxel is chosen because it accurately represent the two phases of the microstructure which possesses inclusions with a size of a few voxels. This microstructure consists of titanium carbide inclusions surrounded by an iron matrix. Because the density of the titanium carbide is higher than the one of the iron matrix, brighter gray scale values represent the iron matrix. The voxel data contain more than two specific gray values for each phase because of artifacts due to the experimental setup and because of numerical noise. Additionally, the gray value of the voxels at the material interfaces contain a gray value between the gray scale values of the two phases. For FCM simulations for which the voxel data are decomposed into cells representing certain materials, each voxel has to be assigned to one of the two phases and the errors due to the measurements have to be filtered out. For the cleaning and binarizing process, the scheme in Fisher Scientific [37] is followed using the software Avizo. In the first step, the voxel data are binarized based on a known volume fraction of the two phases. Therefore, a threshold value is applied on the gray-scale values of all voxels in order to determine which voxel belongs to which phase. in the case of the Ferro-Titanit, the volume fraction of the inclusion as well as the matrix phase are $n_i = 0.5$,

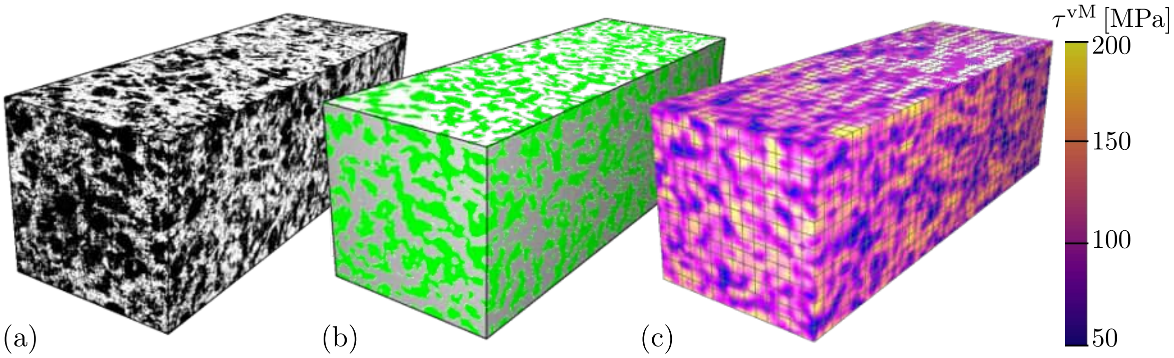

Figure 5.9.: (a) Voxel data as gray-scale values obtained from a μCT-scan, which is cleaned and binarized (b) into the inclusion (green) and iron matrix phase (silver), and (c) the contour plot of the von Mises stress τ^{vM} under one dimensional tension in axial direction at the macroscopic strain $\bar{\varepsilon} = 0.02$.

so that the threshold value is adjusted accordingly. Due to the artifacts, unphysical small islands of one phase within another appears. To erase those, a numerical method is applied which removes them if a cluster of those is smaller than a defined size. Applying this, the cleaned and binarized data in figure 5.9b result. Based on those, the structure is discretized and simulated, e.g., with the FCM or the proposed algorithm, cf. figure 5.9c.

5.4.2. Properties of discretizations

In order to choose proper techniques for the decomposition of the voxel data, knowledge about the properties of discretizations for the FEM, the FCM and the proposed approach is crucial. In the following, the different properties, that are considered for the proposed algorithm, are described.

- **Conformity**, which is fulfilled if the material borders coincide with element borders. In general, FE meshes are generated conformingly. In contrast to that, the finite cells of the FCM are constructed without regarding the inner material and body boundaries whereas the subcells are constructed conformingly. Hence, the discretization of the FCM and the proposed algorithm can also be called "semi-conforming" because on the one hand, the finite cells do not conform with the material boundaries and on the other hand, the subcells are conforming. Because the construction of conforming FE meshes might be challenging in some cases, especially when dealing with heterogeneous microstructures, cf. Schneider et al. [128], the application of the FCM simplifies the computational discretization.

- **Aspect ratio** which relates the edge lengths of the elements. Exemplary for hexahedral elements with the edge lengths l^{K}, w^{K} and h^{K}, the aspect ratio

  $$\mathrm{irr}[\mathrm{K}] = \frac{\max\left(l^{\mathrm{K}}, w^{\mathrm{K}}, h^{\mathrm{K}}\right)}{\min\left(l^{\mathrm{K}}, w^{\mathrm{K}}, h^{\mathrm{K}}\right)} \tag{5.22}$$

  of the element K is defined by dividing the maximal edge length by the minimal one. The larger the aspect ratio irr[K] becomes the worse becomes the representation of the mechanical fields over the elements and therefore, the accuracy of the FE simulation. Hence, the aspect ratio has to be kept small. However, Fangye, Miska, and Balzani [36] showed that the aspect ratio of the subcells within finite cells of the FCM does not affect the accuracy of the volume average. Nevertheless, the aspect ratio of the subcells of the proposed algorithm has to be kept small since the subcells might be transformed into finite elements.

- **Structured mesh**, which is obtained if the elements are ordered in such a way that the nodes, that are connected to it, can directly be calculated from the element number and number of elements in each direction. Because of that, the connectivity and other elemental variables are not saved additionally as it is the case for unstructured meshes. Therefore, less memory is necessary for simulations with structured meshes. Hence, structured meshes are computationally advantageous compared to unstructured ones if the applied FE software makes use of this property. In figure 5.10a, an unstructured mesh and in figure 5.10b, a structured mesh of the same geometry is shown. The location of an element and its node can directly derived from the element number in the structured mesh and vice versa with the formula $n = x + (y - 1) \cdot 8$ which calculates the element number n from the number x in horizontal direction and the number y in vertical direction for the shown mesh. The generation of structured meshes is mostly a challenging task for FE discretizations of complex structures. Hence, most FE meshes are unstructured. Structured FCM meshes can easily generated because the finite cells are not constructed conformingly. However, the management of the history

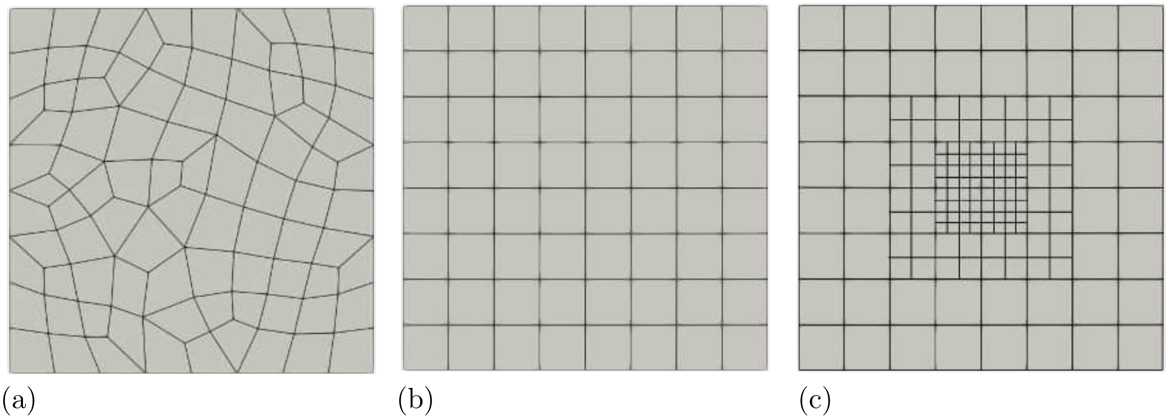

Figure 5.10.: (a) Unstructured, regular, quadrilateral mesh, (b) structured, regular, quadrilateral mesh with 8 × 8 elements and (c) semi-regular, quadrilateral mesh of a square.

variables of the subcells might be challenging. In the proposed algorithm, the meshes are unstructured due to the elements that have been subcells previously. Furthermore, the applied software FEAP does not take advantage of structured discretizations.

- **Regularity**, which is fulfilled if all nodes on the touching surfaces of neighboring elements coincide. Otherwise, hanging nodes occur. If some of the nodes of the touching surfaces of neighboring elements match and others don't, the mesh is called **semi-regular**. Figures 5.10a&b show regular meshes. In contrast to that, the mesh in figure 5.10c is semi-regular because the smaller elements inherit additional nodes on the edges that they have with the larger ones. Therefore, not all nodes on the touching edges coincide with each other. In the proposed algorithm, the FCM mesh is regular as long as no finite cells are split. If the subcells are transformed into finite elements, the mesh becomes usually semi-regular.

- **Consistency**, which is of importance in meshes including hanging nodes. For the examination of the consistency, the touching faces of neighboring elements are considered. If one of these faces geometrically matches with the other one or is a subset of the other one, the mesh is consistent in this part. Figure 5.11a shows that the edge of element 2 at the side at which the two elements touch, marked with green, is a subset of the edge of element 1 with red. In this case, the master-salve concept is applied. This states that the larger edge is the so-called master edge, at which the hanging nodes are constrained. The hanging nodes are nodes connected to the element at the so-called slave edge. In contrast to that, the corresponding edge of element 2 is not a subset figure 5.11b anymore. Here, the displacements of the hanging nodes are constraint with the hanging node constraints by each other. This often leads to numerical problems. Because the displacement field matches at the element boundaries, the shown structure leads to only one continuous function between the constraining node of element 1 and the constraining node of element 2. This leads to an overly stiff structure. Hence, inconsistency has to be avoided in order to avoid numerical problems. Furthermore, cyclic constraints of the hanging nodes onto each other may occur in more complex structures, as shown in figure 5.11c. Herein, four hanging nodes constrain each other. This problem can also occur in a more complex way in three dimensions which might be complicated to proof. Note, that all regular meshes are consistent because all touching faces of neighboring elements match with each other. In FCM simulations, the finite cells usually are arranged regularly and the arrangement of the subcells does not cause hanging nodes within the finite cell. Hence, consistency is not of importance for the discretization for the FCM.

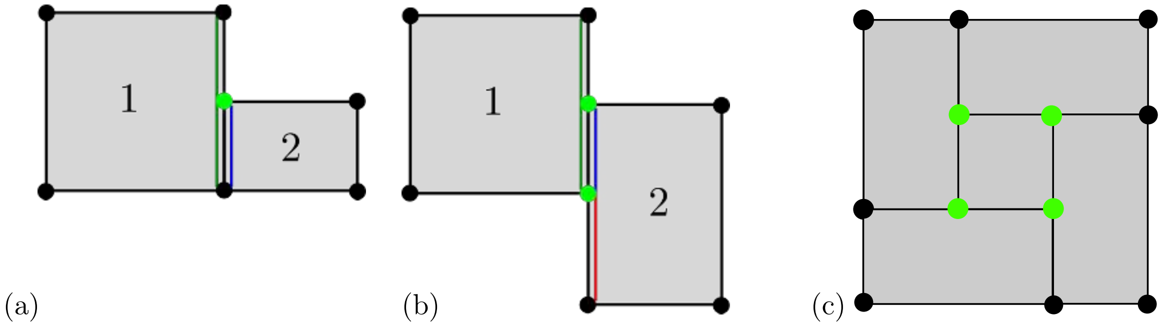

Figure 5.11.: (a) consistent and (b) inconsistent mesh containing two elements and (c) mesh containing five elements (example from Cerveny et al. [20]) with nodes (black) and hanging nodes (green).

> For the proposed algorithm, consistency of the mesh has to be ensured at any state during the simulation. Therefore, the subcells have to be arranged accordingly.

Conforming and regular meshes with hexahedral or with tetrahedral elements can be generated computationally by programs like GMSH in Geuzaine and Remacle [44]. These programs suffer from stability problems in the generation process and badly shaped elements, that have to be as equilateral as possible in order to ensure a proper derivation of the internal values of the elements. For example, cubic shapes are desired for hexahedral elements. These problems increase with increasing complexity of the body $\mathcal{B}$ for the discretization. Summing up, the subcells of the finite cells have to be arranged in such a way, that the mesh in every possible state is semi-regular, conforming to the inner material boundaries, consistent, inherit a small aspect ratio and are fine enough to accurately represent the crack for the simulation with the proposed approach.

5.4.3. Voxel decomposition techniques

In this subsection, the different techniques for decomposing voxel data into multiple finite cells containing subcells with different material properties are described as discussed in Fangye, Miska, and Balzani [36]. Therefore, a finite cell mesh is chosen and these cell are decomposed in such a way that they represent the morphology inside those as accurately as possible with a low number of subcells to keep the computational costs low. In addition to that, the aspect ratio has to be kept low to ensure a proper approximation of the mechanical fields within the elements that have previously been a subcell. Considering the proposed algorithm, the subcells are ought to be arranged consistently.

Quadtree/Octree The so-called **Octree** decomposition, here abbreviated with ‘T”, in three-dimensional applications and Quadtree in two-dimensional applications, as shown in Meagher [85] is the most common approach to decompose cells. Therein, the finite cells containing more than one material are split into $2 \times 2 \times 2$ subcells. In our case, the Octree split is applied equidistantly, which means that the former cell is cut in half in the middle. This procedure is applied into every dimension so that eight equally long, wide and deep new cells are produced. Afterwards, the subcells containing more than one material are split as well so that another level of fineness is imposed. This splitting process is repeated until the subcells only contain one material or a prescribed level of maximum splits $L_{\max}$ is reached. In the latter case, if the smallest subcells still contain more than one material, they are assigned with the material with the highest volume fraction V_i/V. In order to limit the number of subcells, the subcells are assigned with a material if its volume fraction V_i/V becomes higher than a threshold value $(V_i/V)_{\max}$. By application of the Octree decomposition, the aspect ratio $\mathrm{irr}[S]$ remains the same as the aspect ratio of the finite cell, so that in the case of cubic

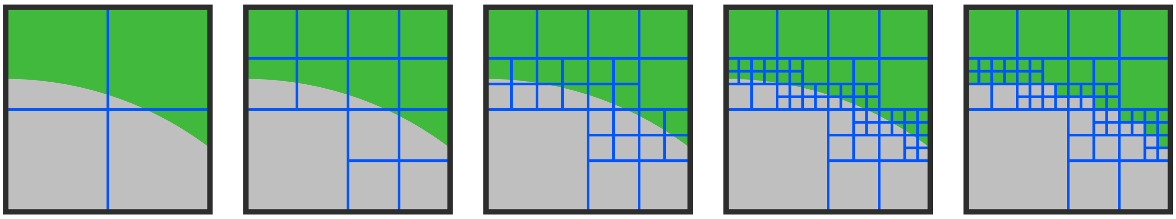

(a) (b) (c) (d) (e)

Figure 5.12.: Principle algorithm of the Octree/Quadtree decomposition (T) with a part of a circle shaped inclusion (gray) within a surrounding material (green) with firstly applied quadtree level 1 (a), secondly, quadtree level 2 (b), quadtree level 3 (c), quadtree level 4 (d) and final decomposition by unifying the sub areas of the subcells containing more than one material (e), taken from Fangye, Miska, and Balzani [36] .

finite cells, the aspect ratio irr[sc] = 1 becomes the best possible. As a drawback, the number of subcells may become large compared to the other approaches and thus, the computational costs of the mechanical simulations becomes large. Additionally, the geometrical accuracy of the Octree algorithm strongly depends on the chosen maximum level of splits. Furthermore, decompositions containing a number voxel that is not representable by 2^n cannot represent the location of the material boundaries perfectly, because some subcells may consist of more than one material after an arbitrary amount of Octree levels. Thus, an infinite number of Octree splits would be necessary to accurately represent the material borders perfectly. However, the subcells are always arranged consistently towards each other.

Optimal decomposition The second approach to decompose voxel data as presented in figure 5.13a, is the so-called **Optimal Decomposition** (OD), as introduced in Fangye, Miska, and Balzani [36], which decomposes the finite cells in such a way that the minimal amount of subcells is generated. Hence, this is seen as optimal regarding the computational costs in FCM simulations. In this approach, one corner voxel is identified and assigned as a prototype subcell with the size of one voxel. In a second step, the neighboring voxel in one specified direction is checked for compatibility with the with voxel, which means that they both exhibit the same material. If this is the case and if the merge of both leads to a cuboid subcell, they are combined to a new subcell, as seen in figure 5.13b. Otherwise, a second prototype subcell is generated and its neighbor in the same direction is checked for compatibility again. This process is repeated until the end of the finite cell is reached, as seen in 5.13c. This procedure is applied on the row next to the firstly investigated one in the same direction until all rows in this direction are decomposed, cf. figure 5.13d, e&f. In three-dimensional structures this process is also executed for each two-dimensional layer so that tube-like subcells are generated. To summarize those, the compatibility is checked in a second direction lateral to the first one. Again, these prototype subcells are merged, as seen in figure 5.13g&h, if their inherited materials match and if the resulting subcell becomes a plate-like cuboid. These are summed up in the third direction by applying the same scheme again so that the subcells now appear in the form of boxes and a three-dimensional decomposition of the finite cells has been found. This whole procedure does not necessarily find the optimal decomposition because the order of the directions in which the prototype subcells are merged strongly influences the resulting decomposition. Hence, all permutations of the order of the directions, as seen in figure 5.13i&j, have to examined in order to chose the optimal one by the means of the lowest number of subcells. In three-dimensional structures six permutations and in two-dimensional two permutations are considered. Nevertheless, the OD may lead to a high aspect ratio due to the tube-like structures that are combined. Furthermore, the subcells are in general arranged inconsistently. The inconsistency and high aspect ratios do not affect the results of the FCM calculations but the ones of the proposed algorithm. In order to improve

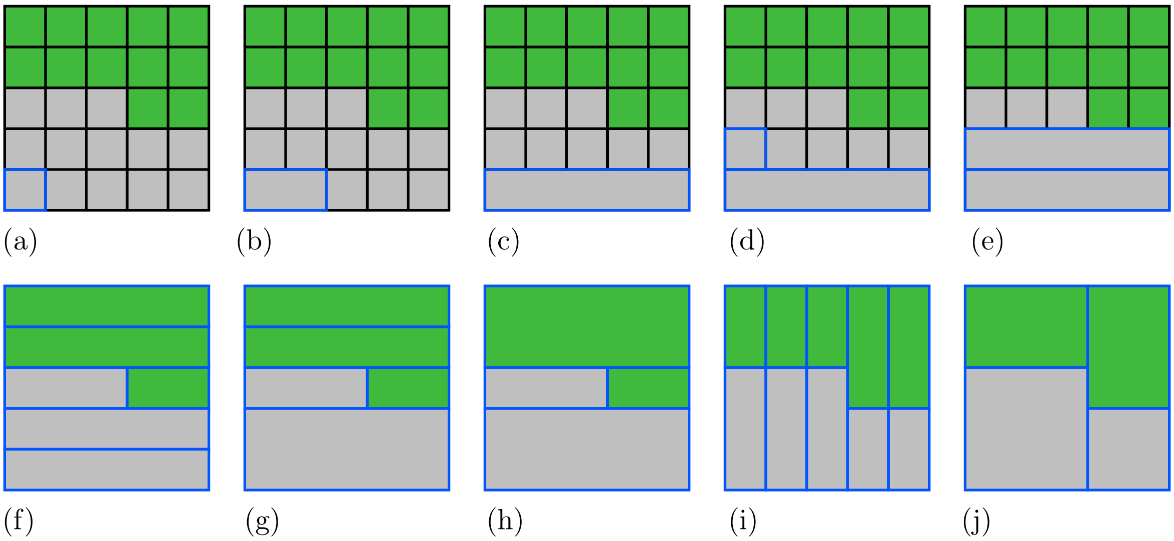

Figure 5.13.: Principle algorithm of the Optimal Decomposition (OD) for one single finite cell containing 5 by 5 pixels; (a) a prototype subcell, (b) extension in first search direction, (c) an entire joined row, (d) and (e) iterations on the next row, (f) the result of the extension in the first direction, (g) merge operation in second direction and (h) final decomposition result. In (i) and (j) the decomposition result for a permutation of the search direction is shown, taken from Fangye, Miska, and Balzani [36].

the current OD in such a way that consistency is achieved, the resulting arrangements from the tested permutations would have to be checked for consistency by checking whether one the neighboring faces of the subcells is a subset of the other one or matches the other one perfectly. This has to be checked for the subcells within the finite cell as well as the previously generated subcells of the neighboring finite cells. The checked permutations of the OD that do not meet this requirement are not considered for the final structure. This algorithm might fail in some cases because not in all finite cells, the construction of a consistent subcell arrangement is impossible for any OD permutation. Note, that in the case that the finite cell boundaries do not necessarily match the voxel boundaries so that only the part of the voxels lying inside of the finite cells are taken into account in the generation process. However, the subcells generated by the OD accurately represent the material boundaries independently from the number of voxels per edge.

Optimized Clustering As a third basic approach, the **Optimized Clustering** is introduced in Fangye, Miska, and Balzani [36] to circumvent the problem of the high number of subcells in the Octree algorithm and the narrow subcells obtained from the OD by solving an optimization problem for obtaining a decomposition with the least number of subcells. Herein, one random voxel is chosen as a starting point, as seen in figure 5.14a, for generating a subcell. This subcell grows in all directions as long as no abortion criterion in the form of a voxel containing a different material as the original one or a border of another finite cell or subcell is passed so that a cubic subcell develops. Afterwards, the subcell is extended into a randomly direction into positive or negative direction until the abortion criterion is met as well whereas the expansion into the other directions are stopped. Due to the differently chosen first growth directions, different decompositions may occur even though the same starting voxel has been chosen as demonstrated in figure 5.14b&c. Then, this growth process is executed as well for all the other directions after another until no growth is possible anymore. Here, the choice of the order of growth directions is of importance and the optimal growth direction might not be obvious beforehand, so that the optimal permutation of the growth directions is not necessarily found. Because of that, a certain randomness appears in the generation process of

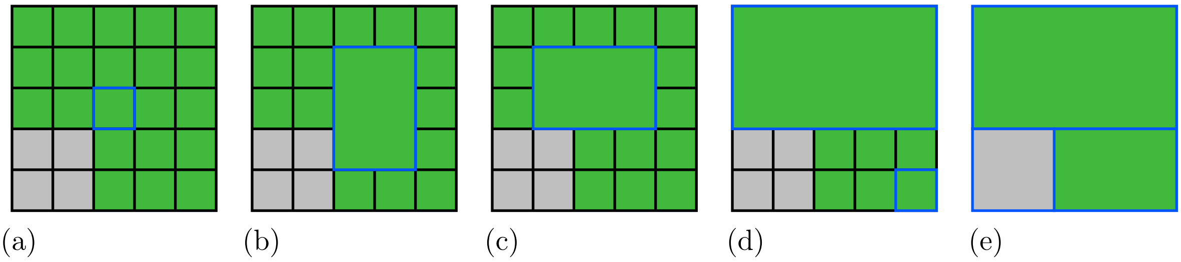
(a) (b) (c) (d) (e)

Figure 5.14.: Illustration of the Optimized Clustering algorithm (OC), (a) randomly chosen start pixel, (b) and (c) two possible restricted growth modes, (d) fully grown subcell and (e) resulting subcell decomposition, taken from Fangye, Miska, and Balzani [36].

the subcells. Afterwards, the growth process is repeated for another randomly chosen starting voxels, as shown in figure 5.14d, until all voxels belong to one subcell. Because of the randomness in the chosen starting points, the OC leads to different decompositions of the finite cell. In order to find the optimal one, the Monte Carlo optimization, cf. Metropolis and Ulam [87], Müller-Gronbach et al. [96] is used, which applies the given algorithm multiple times on every finite cell to obtain the one with the least number of subcells. Another advantage, lies in the comparably low aspect ratio compared to the OD. As a drawback, the computational costs become larger than the ones of the other algorithms due the multiple application of the algorithm on each finite cell. Nevertheless, these computational costs are way lower than the ones of the FCM calculations, so that the effort in the decomposition might be worthwhile. This decomposition technique leads in general to inconsistent decompositions and possible to narrow subcells. Hence, this method is not applicable for the proposed approach but for the FCM.

Combination of decomposition techniques To receive a voxel decomposition containing the advantages of multiple decomposition approaches, some of those are combined. Therefore, they are executed in sequence as exemplarily presented in figure 5.15 in Fangye, Miska, and Balzani [36]. As a first combination, the Octree algorithm is carried out, as shown in figure 5.15b, and afterwards, the resulting subcells are merged, so that the new Octree decomposition with subsequent cell merge (T-M) in figure 5.15c results. To find the decomposition with the lowest number of subcells, all permutations of directions for the merging procedure are tested and the best one regarding the number of subcells is chosen. Hence, a small number of subcells but with a possibly high aspect ratio occur. Additionally, the subcells are in general arranged inconsistently. As another disadvantage, the original structure might not be represented accurately due to the subcells generated by the Octree algorithm, which only ensures an accurate representation if the edges consist of 2^n voxels.
Secondly, to circumvent this problem, the Octree algorithm with subsequent Optimal decomposition on the lowest level (T-OD) as demonstrated in 5.15d is applied. Therein, the

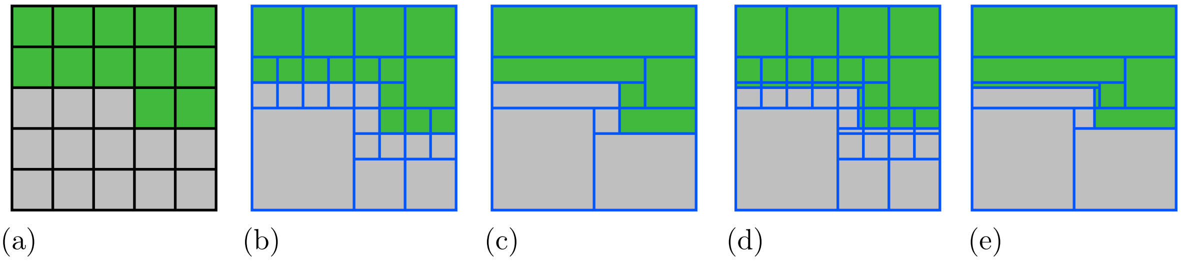
(a) (b) (c) (d) (e)

Figure 5.15.: Combinations of the Octree with the Optimal Decomposition; (a) base geometry, (b) Octree level 3, (c) the T-M , (d) the T-OD and (e) the T-OD-M algorithms Fangye, Miska, and Balzani [36].

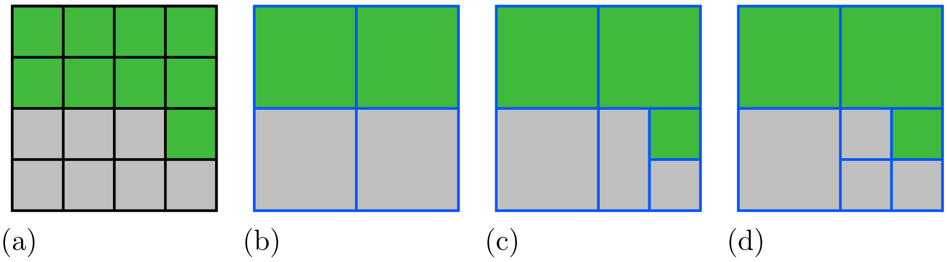

Figure 5.16.: (a) Voxel set consisting of $2^2 = 4$ voxels per edge, that are decomposed with (b) T1, (c) T1-MT and (d)T2 according to Fangye, Miska, and Balzani [36].

narrowness of the subcells is restricted by the previous Octree splits, but the number of subcells is larger than the one resulting from the OD. Nevertheless, the decomposition accurately represents the original structure.

The third combination in the form of the Octree with subsequent Optimal Decomposition and global merge (T-OD-M) is demonstrated in figure 5.15e. Herein, the number of subcells is kept low due to the merge. Additionally, material boundaries are represented accurately due to the Optimal Decomposition. However, the subcells are arranged inconsistently.

As a fourth approach, the Octree is applied with such a level, that only a maximum of $2\times2\times2$ voxels remain on the lowest level. Those are merged, which is abbreviated with **MT**. Technically, the OD is applied on the lowest level. This procedure is only possible, if the number of subcells is a power of 2 because otherwise the Octree split cannot leave over $2 \times 2 \times 2$ voxels for merging. Therefore, the number of finite cells of the edges of the simulated structure have to be chosen accordingly. Additionally, the total number of voxels has to be set in such a way that the split into finite cells containing 2^n voxels per edge length in every spatial direction is possible. Hence, the T-MT cannot be applied on the voxel set in figure 5.15a. In contrast to that the voxel set in figure 5.16a consists of $2^2 = 4$ voxels per edge so that it is decomposable by the application of the T1-MT=T1-OD, cf. figure 5.16c. The first Octree step is shown in figure 5.16b. The biggest advantage of the T-MT is that consistency of the subcell arrangement within the finite cell as well as between the subcells of different finite cells is a priori ensured. This results from the shape of the subcells which either are cubes with a aspect ratio of 1 or cuboids with a aspect ratio of 2 and from the location of the subcells towards each other. Compared to the standard Octree, this combination results in a lower number of subcells. As a comparison, the level 2 Octree split of the voxel set in figure 5.16a is shown in figure 5.16d. Herein, the number of subcells is increased by one compared to the T1-MT. In more complex, 3-dimensional structures, the T-MT highly reduces the number of subcells and therefore, the computational effort compared to the standard Octree algorithm.

5.4.4. Discretization of voxel data for the proposed approach

An example to demonstrate how the voxel data are discretized is shown in figure 5.17. Therefore, the voxel set in figure 5.17a consisting of 48×48 voxels with a possible crack path is considered. Here, the split of the structure into 6×6 finite cells chosen. In figure 5.17b, the structure is decomposed with the OD, but the transformation of the finite cells into finite elements is not applied, so that we see the motivation for this transformation step: The finite cells containing at least one eroded subcell undergo larger deformations compared them without eroded subcells due to the loss of stiffness of the finite cells. These larger deformations lead to an increase in the imposed work U_K in the remaining subcells so that they erode as well. Due to this, all subcells in the corresponding finite cell erode so that an artificially wide crack occurs and the structure within the finite cells is not incorporated. Hence, the transformation of the finite cells is reasonable. For example in figure 5.17c, shows the refined mesh near the crack. Here, the Optimal decomposition has been applied which leads to a low

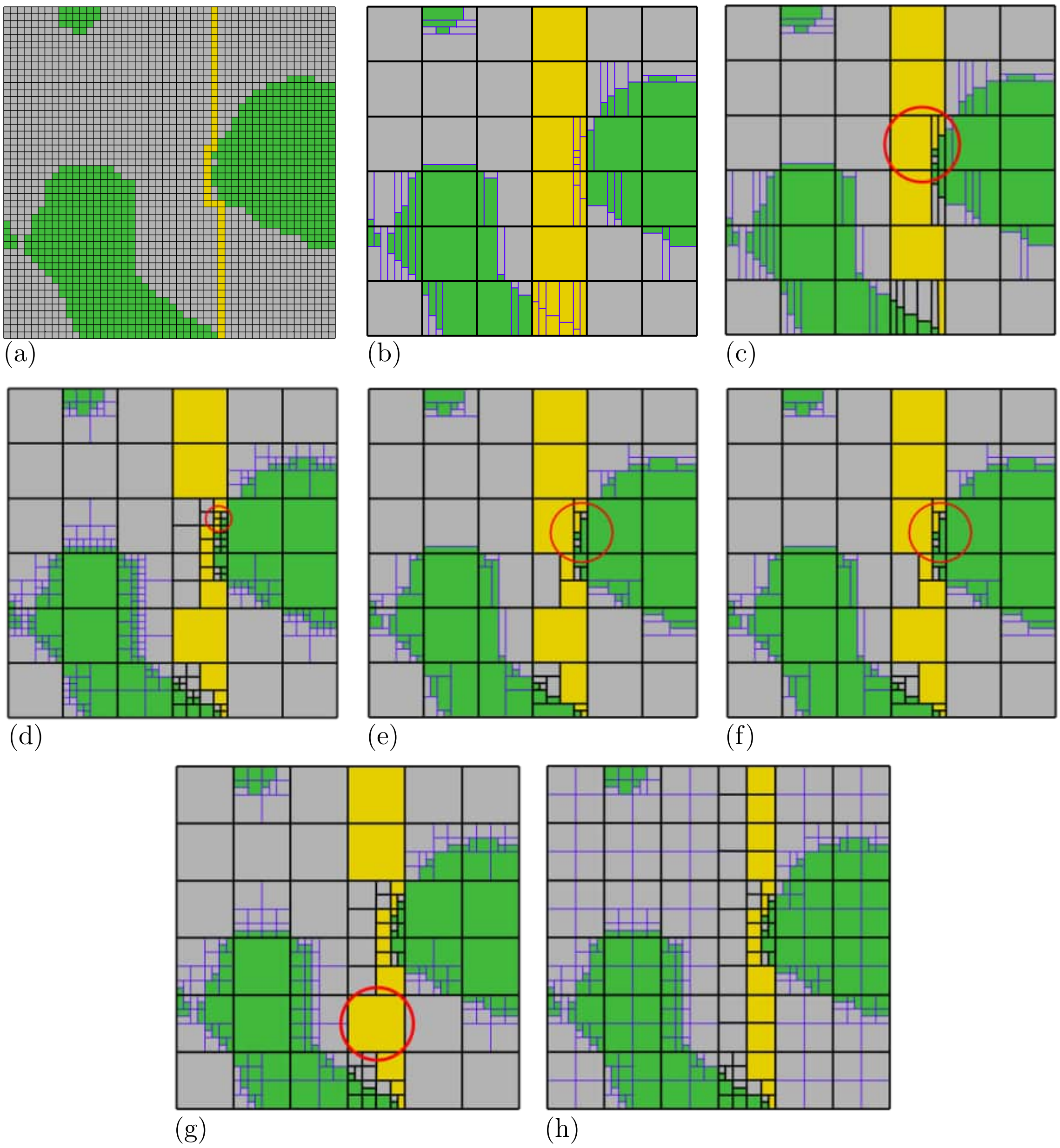

Figure 5.17.: Decomposition of (a) a binarized scan with possible crack path (yellow) consisting of 48×48 pixel into 6×6 finite cells simulated considering (b) FCM without transformation of the cells into elements decomposed with OD, (c) with transformation decomposed with OD, (d) T3, (e) T3-M , (f) T3-OD-M, (g) T3-OD and (h) T3-OD with additional minimum split, taken from Wingender and Balzani [149].

number of subcells and elements, but narrow ones, especially near material borders. However, a high number of hanging nodes occur due to the high number the different edge lengths of the subcells next to each other. Additionally, inconsistency of the mesh occurs. All in all, the Optimal Decomposition may lead to small assembling costs due to the low number of subcells but to high computational costs in the solving procedure of the linearized system of equations in the Newton-Raphson iteration due to the high number of hanging nodes and numerical instabilities due to linearly dependent equations resulting from the location of the hanging nodes. For the same reasons the T-M in figure 5.17e and T-OD-M in figure 5.17f may be disadvantageous for the application of the proposed algorithm. In contrast to that, the simple Octree level 3 in figure 5.17d leads to a high number of subcells, but a lower number

of hanging nodes due to the restriction that the subcell edges may only be cut in half. This discretization is consistent so that this one may be used for the simulations. Nevertheless, the T2-MT=T2-OD in figure 5.17g combines the advantages of the Octree and of the OD, namely the small number of hanging node constraints and subcells. Additionally, the subcells are arranged consistently. As a drawback of all above mentioned decomposition schemes above, finite cells far away from material boundaries and containing only one material are not decomposed and lead to artificially large crack widths. Hence, we introduce a minimum Octree split of every finite cell to ensure a reasonably small crack width. An increase in the minimum split increases the number of subcells which increases the computational effort. Figure 5.17h demonstrates the additional application of a minimum Octree level 1 split. This decomposition technique, namely T-MT with a minimum split, is applied for the following microstructures due its balance between an accurate representation of the crack, a small number of subcells with acceptable edge aspect ratios, a low number of hanging nodes and consistency of the subcell arrangement.
Note, that, for this approach, the number of hanging node constraints can be reduced by choosing an even polynomial degree for the shape function because the equidistant Octree split leads to nodes lying at the half, fourth, eighth,... of the edge which may coincide with the nodes the neighboring element and finite cells more often because the nodes of elements with even polynomial degrees of shape functions lie at the half, fourth, eighth,... of the edge as well.

5.4.5. Proof of concept with artificial microstructure

In order to proof the plausibility of the eigenerosion in combination of the FCM framework, a benchmark experiment on a simplified artificial hard metal microstructure, cf. figure 5.18 is investigated. This microstructure with an edge length of 70 μm consists of a spherical tungsten carbide inclusion with a diameter of 50 μm surrounded by a ductile nickel matrix. A brittle η-carbide layer with a thickness of 5 μm lies in-between these phases. Physically, this layer develops by diffusion of carbon from the tungsten carbide into the nickel matrix. This microstructure is simulated with different methods:

1. The classical FE in combination with the eigenerosion approach considering a regular and unstructured mesh with 10-node tetrahedra, cf. figure 5.19a is applied. Because of the simplified morphology, the meshing procedure is simple for this structure, but

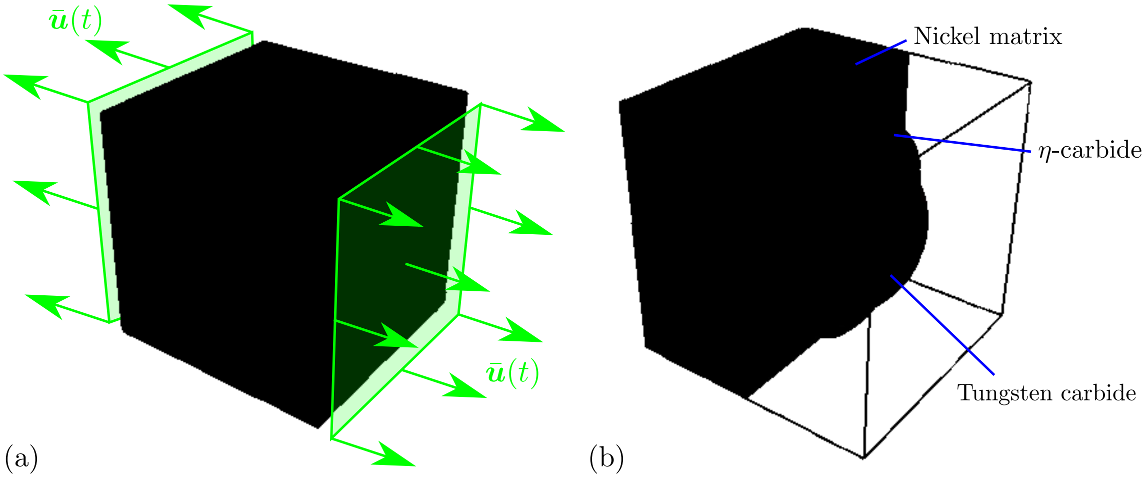

Figure 5.18.: (a) Boundary conditions of the simulation setup of the benchmark experiment and (b) its morphology consisting of a spherical tungsten carbide inclusion surrounded by a brittle η-carbide layer and a ductile nickel matrix, which is a typical hard metal, taken from Wingender and Balzani [149].

may become complicated in more complex structures. However, this microstructure morphology does not exactly represent the voxel data in figure 5.19b because the surfaces of the spheres are assumed to be smooth for this discretization type and not the brick-like structure of the voxel data consisting of 56 × 56 × 56 voxels as the basis for the other discretization types.

2. A regular and structured FE mesh, cf. figure 5.19 in which each voxel is simulated as one finite element is considered as a second reference. Note, that here only linear shape functions instead of quadratic shape functions as the other approaches are chosen because of the high computational costs.

3. A discretization for the proposed approach, cf. figure 5.19c. In the following, different realizations for the discretization of this approach are tested.

4. A semi-regular FE mesh with hexahedral finite elements, cf. figure 5.19d is assumed. Herein, hanging nodes occur. This discretization is constructed by considering the discretization of the microstructure under the assumption that every subcell from the proposed approach in figure 5.19c is a finite element from the beginning of the simulation.

In the next step, different decomposition methods for the proposed approach are tested in terms of efficiency, accuracy and consistency of the subcell arrangement. Afterwards, the crack path and the reaction forces of the different discretization types are compared.

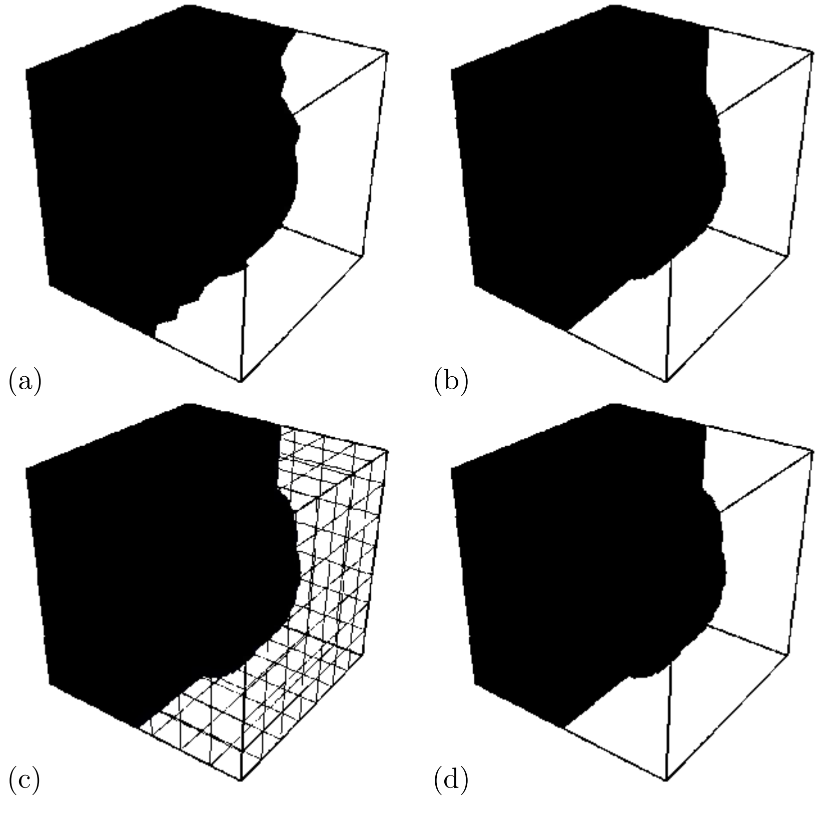
(a) (b) (c) (d)

Figure 5.19.: Different discretization types of the microstructure in figure 5.18: (a) discretization type 1, a regular tetrahedral FE mesh, (b) discretization type 2, a voxel set consisting of 56 × 56 × 56 voxels which serves as basis for the other discretizations and FE mesh with hexahedral elements, (c) discretization type 3, a finite cells (black) and subcells (blue) assuming 7 × 7 × 7 finite cells and the T2 min1-MT decomposition for the proposed algorithm and (d) discretization type 4, a semi-regular, hexahedral FE mesh generated by assuming each subcell of discretization type 3 to be a finite element.

Discretization for the proposed algorithm Here, the decomposition schemes for the proposed approach are applied in such a way, that the material boundaries are represented accurately in order to avoid inaccuracies in the mechanical behavior resulting from inaccuracies due to the discretization. Therefore, the $56 \times 56 \times 56$ voxels are split into $7 \times 7 \times 7$ finite cells so that there are $2^3 = 8$ voxels per edge in each direction. The properties of the resulting discretizations of some decomposition techniques considering quadratic shape functions are shown in figure 5.20a&b. As expected, the OD, T2-OD-M and T3-M result in the least numbers of subcells, while these discretizations contain subcells with the highest possible aspect ratio, which cause a loss in the accuracy of the simulations. Additionally, inconsistencies of the subcell arrangements occur in those. For instance, figure 5.22a shows a cross section through the arrangement that is obtained by the application of the OD. Therein, many inconsistencies of the subcell arrangement are visible. These can also been seen in figure 5.22c, in which the T3-M is applied. In contrast to that, the pure Octree decompositions T3, T3 min 1 and T3 min 2 lead to a consistent subcell arrangement, cf. figure 5.22b. Additionally, the element

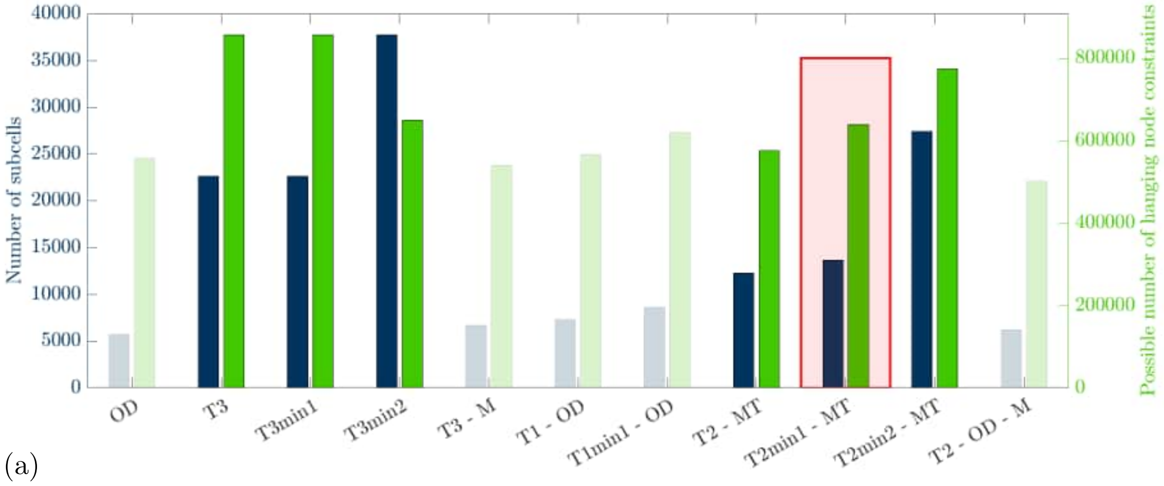

(a)

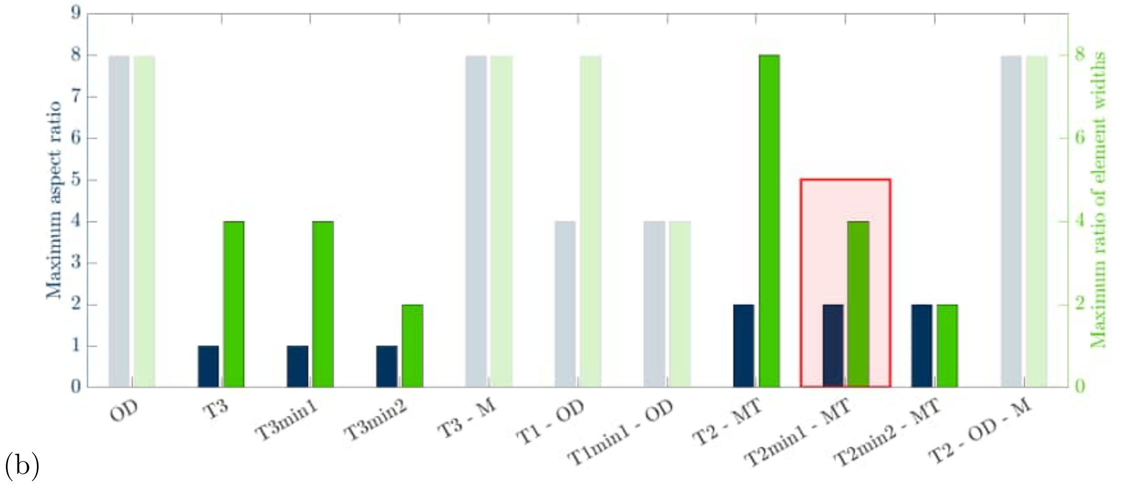

(b)

Figure 5.20.: Statistics of different decomposition schemes based on the voxel data of an artificial microstructure in the form of (a) number of subcells and possible hanging constraints and (b) the maximum aspect ratio of the elements' edge length and the maximum edge length of all subcells divided by the minimum edge length of all subcells assuming $7 \times 7 \times 7$ finite cells, taken from Wingender and Balzani [149]. The transparency indicates that the corresponding discretization contains inconsistencies if the discretization type 3 or 4 are applied. Because of that, these discretization cannot be used for the discretization types 3 or 4. For the numerical simulations, the discretization T2min1-MT is chosen.

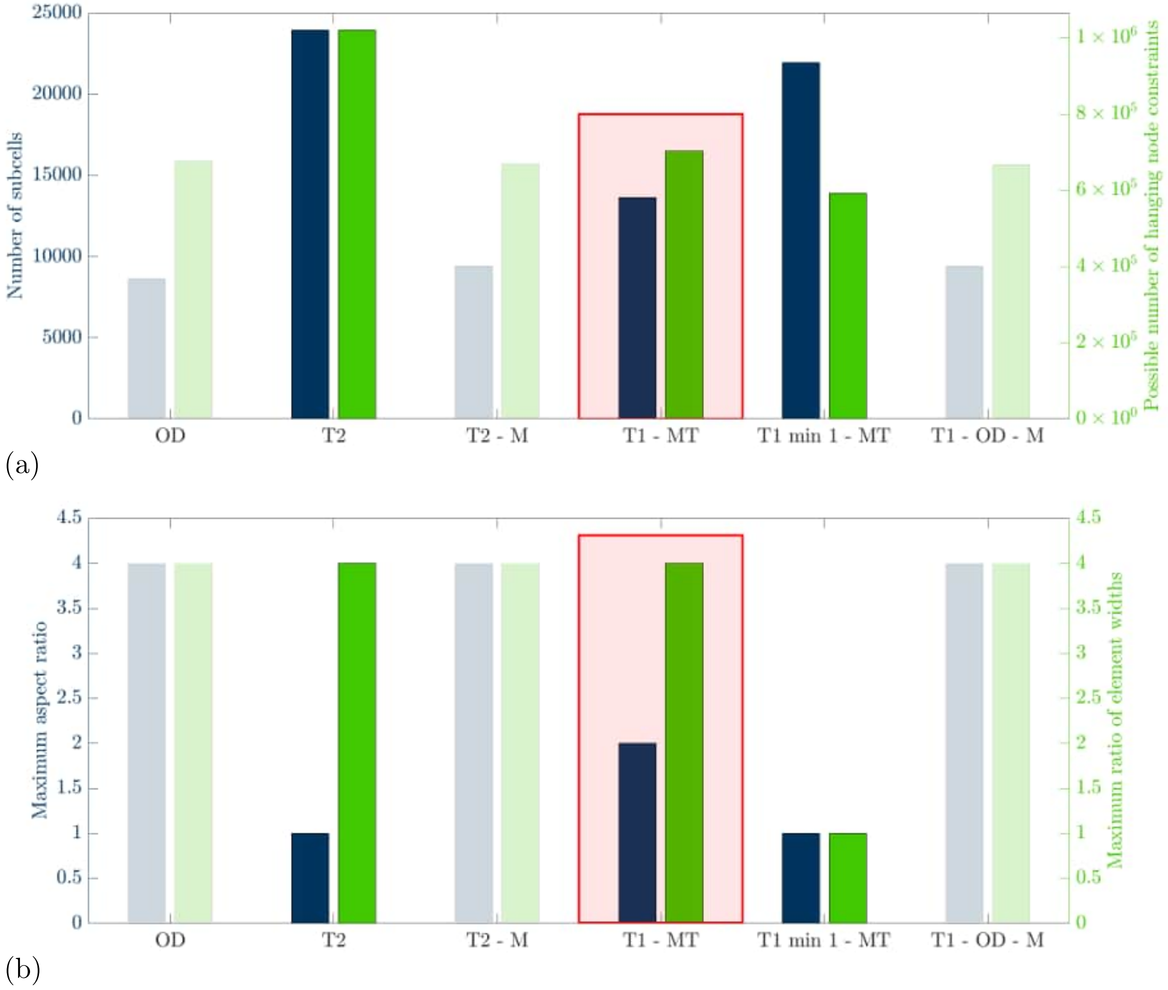

Figure 5.21.: Statistics of different decomposition schemes based on the voxel data of an artificial microstructure in the form of (a) number of subcells and possible hanging constraints and (b) the maximum aspect ratio of the elements' edge length and the maximum edge length of all subcells divided by the minimum edge length of all subcells assuming 14 × 14 × 14 finite cells. The transparency indicates that the corresponding discretization contains inconsistencies if the discretization type 3 or 4 are applied. For the numerical simulations, the discretization T1-MT is chosen.

aspect ratio is kept 1, as expected, and the maximum edge length divided by the minimum edge length of all subcells remains low. However, a high number of subcells and hanging nodes occurs, which increases the computational costs. The combination T2min1-MT=T2min1-OD enables a voxel decomposition that balances the number of subcells and hanging node constraints on the one hand, in contrast to the aspect ratios on the other hand. For instance, the computational advantage of the merge MT becomes clear by comparing the number of subcells with the ones of the alternative Octree T3min1 without the merge. The merging step MT reduces the number of subcells from $22,624$ to $13,648$ by a ratio of 39.67%. Additionally, the discretization T2min1-MT leads to a consistent subcell arrangement, cf. figure 5.22d. Because of that, this discretization scheme is considered for the mechanical simulations with the proposed approach. For the same reasons, this discretization is chosen for the simulations that consider the discretization type 4, namely a semi-regular, hexahedral mesh with hanging nodes, under the assumption that every subcell is a finite element.

Additionally, the same study is carried for the discretization of the volume element into $14 \times 14 \times 14$ finite cells which consist of $4 \times 4 \times 4$ voxels. Due to the lower number of voxels per finite

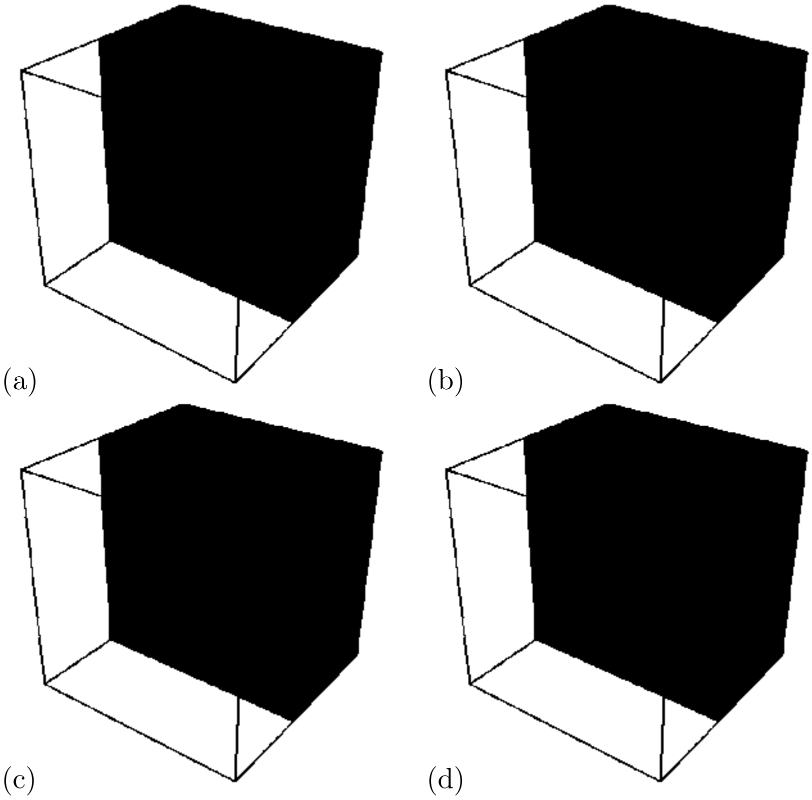

Figure 5.22.: Cross section through microstructure that is discretized by (a) OD, (b) T1min1, (c) T3-M and (d) T2min1-MT under the assumption of $7 \times 7 \times 7$ finite cells.

	K [GPa]	μ [GPa]	y_0 [GPa]	y_∞ [GPa]	h^{exp}	h^{lin} [GPa]	G_c [N/mm^2]
Tungsten carbide	308.12	288.71	10^{12}	10^{12}	0	0	0.0371
η-carbide	394.38	228.72	10^{12}	10^{12}	0	0	0.0065
Nickel	225.6	75.19	260	580	9	70	1.730

Table 5.2.: Material parameters of hard metal microstructure of the benchmark experiment, taken from Wingender and Balzani [149].

cell compared to the previous discretization, less different decompositions are possible. If the decomposition T1-MT=T1-OD is applied, the subcell appear in the identical arrangement as the one of the T2min1-MT of the microstructure which is divided into $7 \times 7 \times 7$ finite cells. This results from the reduction of the number of voxels per edge, Octree splits and minimum Octree splits by a factor of 2. Again the combination of the Octree decomposition and the subsequent merge leads to a discretization with a low number of subcells, possible hanging node constraints and aspect ratio.

Mechanical simulation For the mechanical simulations, the material parameters of the constituents in table 5.2 are considered. The elasto-plastic material model is used for the nickel matrix. In order to obtain the same elastic material model, namely the St. Venant Kirchhoff model, for the brittle phases, the initial yield stress y_0 is set to a high value, that is not reached in this simulation so that the plastic regime is not reached in this material. Here, displacement boundary conditions in figure 5.18a are applied. Therein, the displacements at the surface in x-direction are prescribed in x-direction. Because all other degrees of freedom are not bounded, the specimen is able to move freely in y- and z-direction. Because inertia effects are considered, this simulation setup does not lead to numerical problems due to missing statical bounds. If the displacements on other sides or the displacements in lateral directions

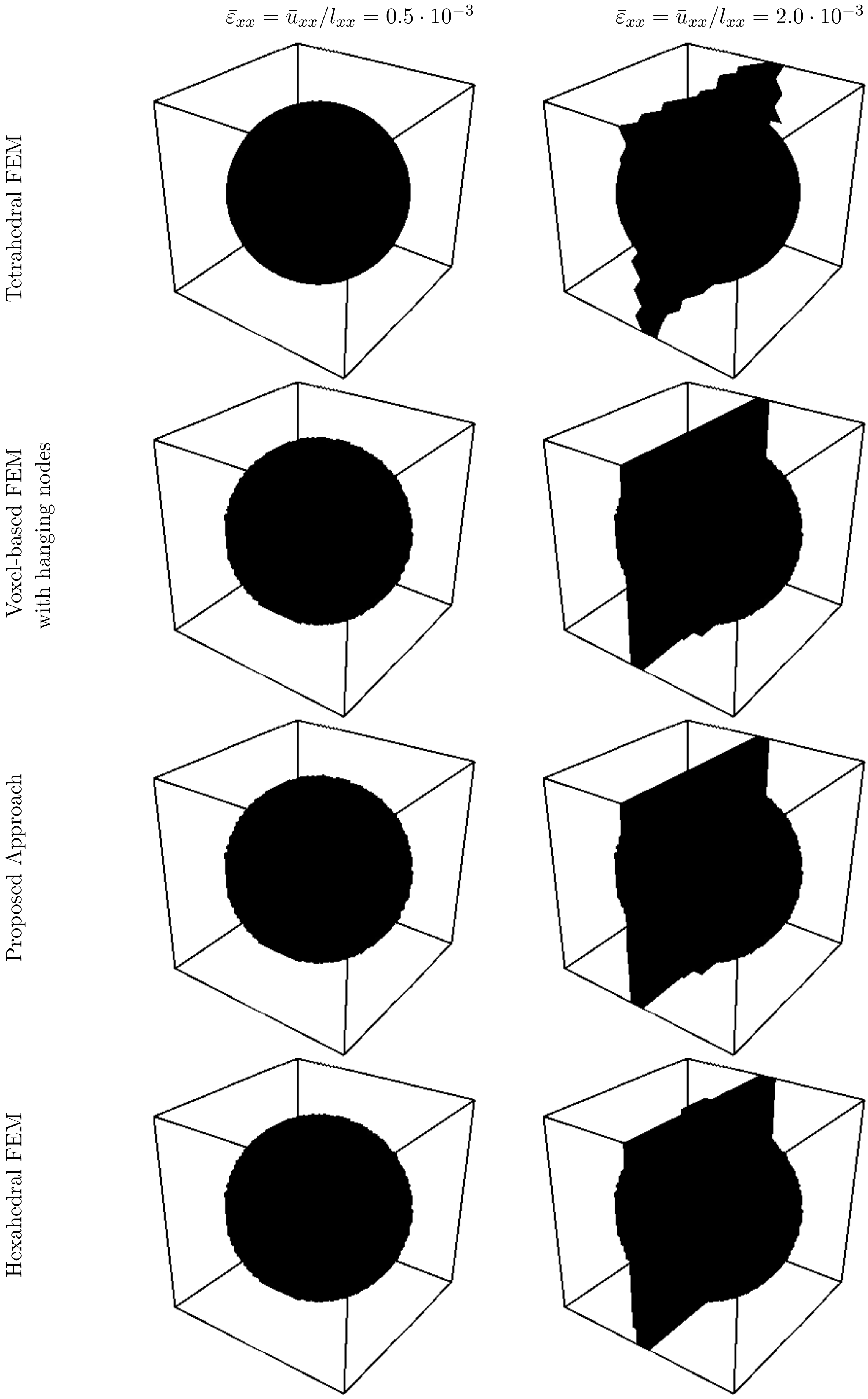
$\bar{\varepsilon}_{xx} = \bar{u}_{xx}/l_{xx} = 0.5 \cdot 10^{-3}$
$\bar{\varepsilon}_{xx} = \bar{u}_{xx}/l_{xx} = 2.0 \cdot 10^{-3}$
Tetrahedral FEM
Voxel-based FEM with hanging nodes
Proposed Approach
Hexahedral FEM

Figure 5.23.: Crack path through artificial hard metal microstructures at a macroscopic strain of $\bar{\varepsilon}_{xx} = 0.5 \cdot 10^{-3}$ and $\bar{\varepsilon}_{xx} = 2.0 \cdot 10^{-3}$, taken from Wingender and Balzani [149].

at the surfaces with normals in x-direction would be bounded additionally, the crack would occur at these boundaries because the additional restrictions impose additional stresses. The macroscopic displacements linearly increase over the time with the velocity $\dot{\bar{u}}_{xx} = 350\,\mathrm{mm/s}$ at the surfaces with normal in x-direction. The influence radius is chosen to $\epsilon = 0.5\,h$ in all simulations. Based on this, the influence radii $7.5 \cdot 10^{-4}$ mm for the discretization type 1, $6.25 \cdot 10^{-4}$ mm for the discretization type 2, $2.5 \cdot 10^{-3}$ mm for the discretization type 3 and 4 result. All of these values are of the same magnitude.
The resulting reaction force $\bar{Q}_{xx}$ at the boundaries, at which the displacements $\bar{u}$ are imposed, are shown in figure 5.24a. With increasing macroscopic strain $\bar{\varepsilon}_{xx} = \bar{u}_{xx}/l_{xx}$ with $l_{xx} = 70\,\mu\mathrm{m}$, the reaction force increases linearly until the η-carbide layer cracks at the a macroscopic strain $\bar{\varepsilon}_{xx} = 0.2 \cdot 10^{-3}$ and thus, the reaction forces drops rapidly. Afterwards, the structural response increases again. Thereby, the increase in the reaction force becomes nonlinear because of the occurrence of plastic deformations in the nickel matrix. Then, the nickel matrix breaks into two parts so that the reaction force slightly oscillates around zero due to the remaining inertia effects. Figure 5.23 shows the eroded elements of the discretization methods after the η-carbide layer is cracked and after the microstructure is broken into two parts. Similarities between the results of the crack paths are visible so that it can be assumed that the crack path is independent from the discretization method. Furthermore, it is shown that one constant C_h for determining the influence radius ϵ suffices even for different element and discretization types. However, small differences in the reaction forces are visible. The reaction forces of the proposed approach converge with increasing number of finite cells to the ones of the discretization type 4. The smaller the finite cells get, the more similar the spatial discretizations of type 3 and 4 become since the subcells and finite elements are arranged equally. Nevertheless, the number of equations n_{eq} in the beginning of the calculation increase with an increased number of subcells, as shown in figure 5.24b, because the lower number of finite cells leads to a lower number of nodes and therefore, degrees of freedom. To demonstrate this effect, the resultant reaction forces $\bar{Q}_{xx}$ of the discretization type 3 and 4 without crack propagation are shown in figure 5.25. With an increasing number of finite cells of the discretization type 3, the structural response becomes softer and converges to the one of discretization type 4. The reason for that is that smaller finite cells better represent the local properties at material borders. However, this effect only occurs in the plastic regime in this numerical example. For macroscopic strains lower than 0.001, when no plasticity becomes visible in the resultant reaction forces, all curves lie close to each other. Thus, the choice of the number of finite cells influences the development of the history variables but not the elastic properties. The reaction force of the simulation with the discretization type 1

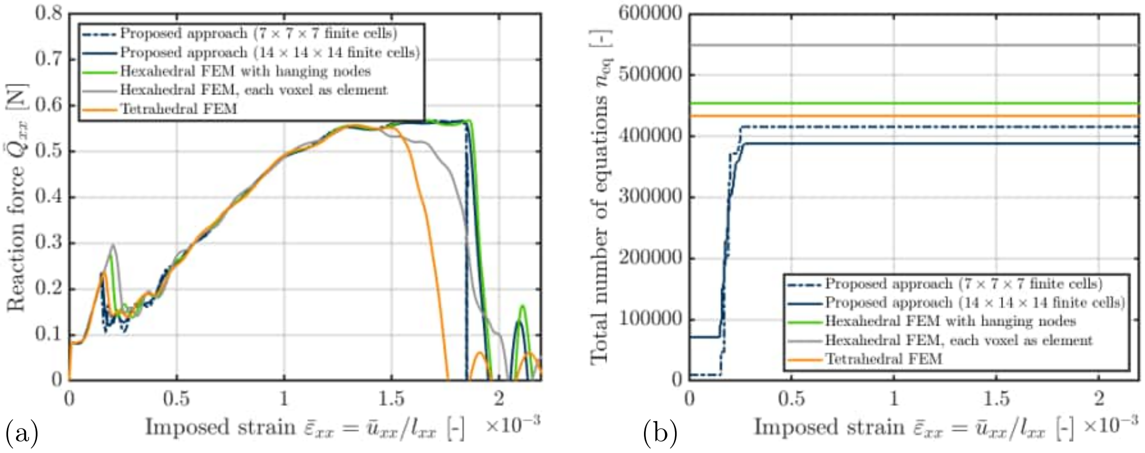

Figure 5.24.: (a) Reaction force and (b) number of equations in the Newton iteration of the proposed approach over the macroscopic strain $\bar{\varepsilon}_{xx}$ of the voxel based microstructure, taken from Wingender and Balzani [149].

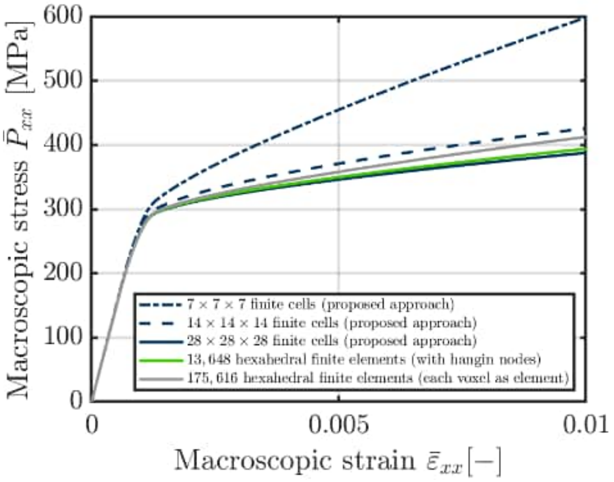

Figure 5.25.: Stress-strain curve for discretization type 3, 4 and 2 for tension test without crack propagation.

with the tetrahedral mesh including crack propagation, cf. figure 5.24a differs largely from the reaction forces of the discretization type 3 and 4 because its morphology is different. Therein, the surfaces of the spherical inclusions are interpolated smoothly from the voxel data. This interpolated surface does not necessarily represent the real microstructure that would be scanned in order to obtain the voxel data. In order to perform simulations with tetrahedral elements based on voxel data, each voxel would have to be split into tetrahedra. This would lead to high computational costs because of the high number of elements that would occur. Furthermore, the reaction force of the simulations with discretization type 2 differs from the ones of other discretization types because therein, only linear shape instead of quadratic shape functions are assumed. The resulting equivalent plastic strain α and the von Mises stress τ^{vM} of the simulation with discretization type 3 are shown in figure 5.26. Even if small macroscopic strains $\bar{\varepsilon}_{xx}$ are applied, plastic deformations occur due to microscopic strains larger than the macroscopic ones caused by the morphological heterogeneity.

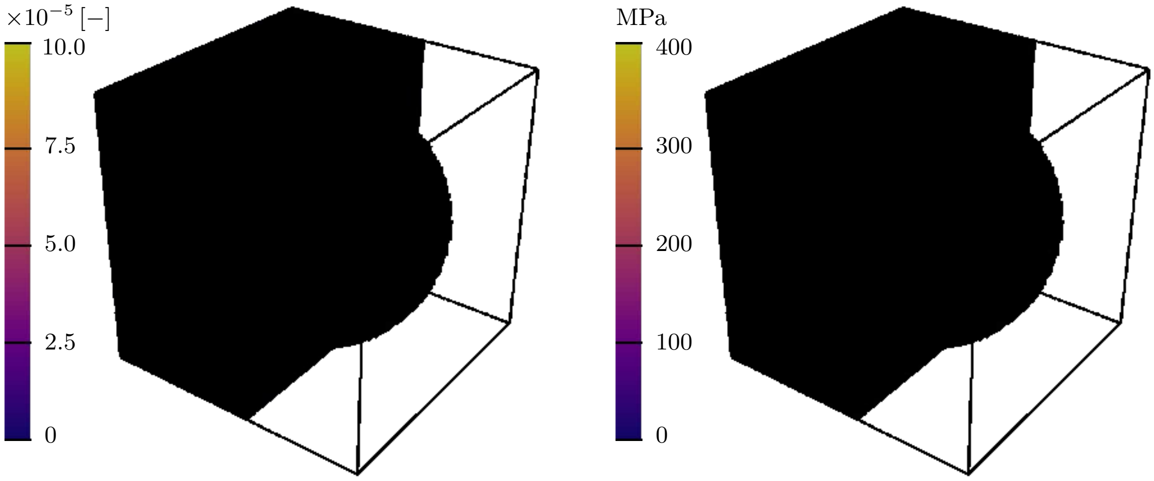

(a) (b)

Figure 5.26.: (a) Equivalent plastic strain α and (b) von Mises stress τ^{vM} over the specimen of the FCM simulation including the crack path (gold) at $\bar{\varepsilon}_{xx} = \bar{u}_{xx}/l_{xx} = 0.18\%$, taken from Wingender and Balzani [149]. Here, the boundaries (gray) indicate either the boundaries of the active finite cells or, if the corresponding finite cell is deactivated, the ones of the subcells transformed into finite elements.

The efficiency of the proposed algorithm is demonstrated by comparing the number of equations n_{eq} of the resulting system in figure 5.24b, which is solved in each Newton-Raphson iteration. In the beginning, when only finite cells and no elements including hanging nodes occur, the number of equations of the discretization type 3 is lower by a factor of 42.9 if $7 \times 7 \times 7$ finite cells considered, by a factor of 5.4 if $14 \times 14 \times 14$ finite cells considered, compared to the final state in which all finite cells at the material boundaries are transformed into single elements. Furthermore, the computational advantage of the proposed algorithm is indicated by comparison of the number of equations with the ones of semi-regular hexahedral mesh. Therein, $454,141$ equations occur in every time step, which is many times higher, especially in the beginning of the simulation. Later on, the number of equations become similar because here every finite cell, that contains multiple phases, is split. The computational gain will be even higher in simulations, in which not all finite cells, that contain multiple phases, are split. In these kind of simulations, the number of equations is reduced in all time steps. In the simulation in which each voxel is considered as a finite element, $549,081$ number of equations occur. If quadratic shape functions were considered, there would be $4,303,153$ equations and thus, an increase of factor 444.8 in the number of equations compared to the initial state of the simulation with the proposed approach with $7 \times 7 \times 7$ finite cells a factor of 11.1 considering $14 \times 14 \times 14$ finite cells. Furthermore, the number of elements for the assembling with $175,616$ elements is larger by a factor of 7.5 compared to the $23,360$ subcells/elements. Additionally, the number of eroded elements increases the computational effort because for every eroded element, the nonlinear system of FE equations has to be solved again. The final crack of the contains $4,046$ eroded elements in the proposed approach and $18,406$ eroded elements in the regular hexahedral FE mesh. Especially with respect to the number of $3,000$ time steps, this number strongly influences the number of solves and thus, the computational effort. Hence, the benchmark experiment demonstrates the efficiency of the proposed approach compared to the tetrahedral mesh, the hexahedral semi-regular and in particular to the regular hexahedral FE mesh.

6. Construction of artificial representative volume elements

To reduce the computational costs of simulations on the microstructure, the geometry is reduced by identification of smaller **representative volume elements** (**RVE**). Different definitions of RVEs are given in Zeman [163], Hill [51], Drugan and Willis [31]. RVEs are usually considered as a subsection of a material's microstructure whose material's morphology, properties and behavior resemble the ones of the full microstructure. This subsection can either be cut out of the original structure or artificially constructed. For the size of the RVE no unique definition exists. Following, e.g., Hashin [50], the RVEs have to be chosen large enough to contain sufficient information about the microstructure. However, it should be chosen as small as possible to reduce the computational effort, because the bigger and therefore, the more complex the structure becomes, the higher the number of degrees of freedom and thus, the computational effort get. In our case, the whole morphology of the μCT-scan is assumed to represent the microstructure. The meshing procedure of this microstructure and mechanical simulations are extremely computationally demanding. Thus, the microstructure morphology has to be reduced to a less complex structure. In figure 6.1a, an exemplary microstructure consisting of two phases is shown. The size of the whole microstructure is reduced to the size of the RVEs under the assumption of geometrical **periodicity** of the RVEs. Due to periodicity constraints, the RVEs can be multiplied and stuck together to the size of the original microstructure, cf. figure 6.1b. However, only one RVE is used for the simulations. Here, two different approaches to construct the RVEs are presented, namely the concept **Statistically Similar Representative Volume Elements** (**SSRVE**), cf. Schröder et al. [129], and the concept **Statistical Volume Elements** (**SVE**), cf., e.g., Yin et al. [160]. This chapter presents both approaches and its application on the MMC Ferro-Titanit and asphalt concrete. Afterwards, both approaches are compared.

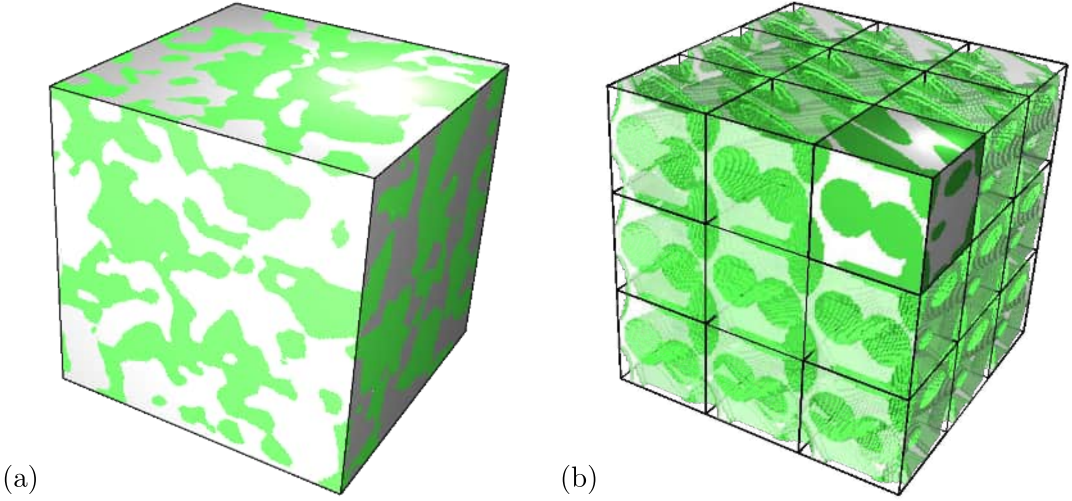

Figure 6.1.: (a) Exemplary microstructure consisting of inclusions (green) surrounded by matrix (gray) and (b) periodic microstructure consisting of periodic RVEs, that represent the original microstructure in (a).

6.1. SSRVE construction

The first approach for the construction of artificial RVEs is the concept for the construction of SSRVEs, as introduced in Schröder et al. [129], and extended to three dimensional applications in Balzani et al. [8], Scheunemann et al. [124], Scheunemann [123]. The SSRVEs are constructed based on parameterized inclusion shapes, e.g., spheres parameterized by their radii and center of masses. The parameters are determined by minimizing the mechanical error as well as the error of statistical descriptors of the artificially generated volume elements compared to the ones of the real microstructure. Different descriptors for the characterization of microstructures are exploited in Torquato [143], Lautensack and Sych [71], Zeman [163]. This section provides the basic approach, the statistical descriptors, the choice of morphological parameters and the application on the MMC Ferro-Titanit.

6.1.1. Basic approach

Here, the statistical similarity of artificially generated RVEs compared to the real microstructure is described by evaluating the error in morphological properties $\mathcal{E}$ as well as the error in mechanical properties $\tilde{r}_{\varnothing}$. These morphologies are obtained by placing simplified inclusions based on a set of parameters $\boldsymbol{\gamma}$ into a cubic specimen. For example, these inclusions may be spheres that are parameterized by their center points and radii. To find the best realization $\tilde{\boldsymbol{\gamma}}$ of the RVE regarding the similarity, the optimization problem

$$\tilde{\boldsymbol{\gamma}} = \arg\left\{\min_{\boldsymbol{\gamma}} \left[\mathcal{E}(\boldsymbol{\gamma}) + \tilde{r}_{\varnothing}(\boldsymbol{\gamma})\right]\right\} \tag{6.1}$$

as formulated in Balzani et al. [7] and applied in Balzani et al. [8] for three-dimensional microstructures is solved. Here, the objective function of the mechanical properties $\tilde{r}_{\varnothing}$ is evaluated by the least-square difference of considered macroscopic properties, for example the macroscopic stress-strain curve. These are derived by numerical simulations on the SSRVEs as well as on the target microstructure. The second objective function in the form of the error in the morphology

$$\mathcal{E}(\boldsymbol{\gamma}) := \sum_{L=1}^{n_{\text{sm}}} \omega_{(L)}\, \mathcal{L}_{(L)}(\boldsymbol{\gamma}) \tag{6.2}$$

consists of the sum of the n_{sm} functionals $\mathcal{L}_{(L)}$ multiplied with chosen weighting factors $\omega_{(L)}$. These functionals are evaluated for different statistical descriptors $\mathcal{P}_{(L)}$ by

$$\mathcal{L}_{(L)}(\boldsymbol{\gamma}) = \left(\mathcal{P}_{(L)}^{\text{target}}(\boldsymbol{\gamma}) - \mathcal{P}_{(L)}^{\text{SSRVE}}(\boldsymbol{\gamma})\right)^2 \tag{6.3}$$

with the descriptor $\mathcal{P}_{(L)}^{\text{target}}(\boldsymbol{\gamma})$ of the target structure, given in the form of the voxel data of the scan, and the descriptor $\mathcal{P}_{(L)}^{\text{SSRVE}}(\boldsymbol{\gamma})$ of the SSRVEs. Note, that the SSRVEs are voxelized in order to obtain comparable results. According to this formulation of the minimization problem, the analysis of the statistical descriptors and numerical simulations have to be carried out on each RVE, which is investigated in the optimization process. Mechanical simulations are computationally costly compared to the examination of the statistical descriptors. Hence, the number of necessary numerical simulations has to be reduced. Therefore, the original optimization problem in equation 6.1 is reformulated to the staggered scheme

$$\tilde{\boldsymbol{\gamma}} = \arg\underbrace{\left\{\min_{i}\left[\tilde{r}_{\varnothing}\left(\tilde{\boldsymbol{\gamma}}_i = \arg\underbrace{\left\{\min_{\boldsymbol{\gamma}_i}\left[\mathcal{E}(\boldsymbol{\gamma}_i)\right]\right\}}_{\text{inner problem}}\right)\right]\right\}}_{\text{outer problem}}. \tag{6.4}$$

Here, the optimization is split into two parts. Firstly, the inner problem minimizes the morphological objective function $\mathcal{E}(\boldsymbol{\gamma}_i)$ with respect to a parameterization $\boldsymbol{\gamma}_i$. The index i indicates the parametrization type for instance the parameters of $1, 2, 3$ and 5 ellipsoidal inclusions or even different inclusion types. The general shape of the inclusions, e.g., spheres, ellipsoids, tubes, cuboids etc., has to be chosen according to the shape of the inclusions in the target microstructure but may also serve as further parameterizations. In theory, an almost infinite number of parameterizations has to be evaluated for the morphological objective function $\mathcal{E}$ to perfectly characterize the microstructure. In practice, only a few chosen parameterizations are evaluated which suitably characterize the microstructure. Therefore, an optimization algorithm is applied. It calculates the parameterization $\tilde{\boldsymbol{\gamma}}_i$ for each parameterization type i by minimization of the objective function of the inner optimization problem. The inner optimization problem can be solved automatedly and in a highly parallelized manner. The objective function is highly nonlinear and non-convex with respect to the parameters $\boldsymbol{\gamma}_i$ in most cases which makes the optimization difficult because schemes like the Newton method may not necessarily find the global minimum. Hence, special numerical algorithms capable of optimizing this type of objective function, e.g., evolution methods or line search methods, have to be applied. Secondly, in the outer problem, the overall best parametrization $\tilde{\boldsymbol{\gamma}}$ is found by minimizing the objective function of the mechanical properties $\tilde{r}_{\varnothing}$ by only executing numerical simulations on the RVEs that are constructed based on the solution parameter sets $\tilde{\boldsymbol{\gamma}}_i$ of the inner problem. The reformulation of the optimization in equation 6.1 highly reduces the number of numerical simulations and thus, the computational costs. Note, that the staggered optimization in equation (6.4) may not necessarily result in the same best parameterization $\tilde{\boldsymbol{\gamma}}$ as the original one in equation (6.1) because the staggered scheme only considers the mechanical error $\tilde{r}_{\varnothing}$ of a few RVEs, namely the resulting ones of the inner optimization. However, it may be considered that reducing the morphological error $\mathcal{E}$ also leads to the reduction of the error in the mechanical error $\tilde{r}_{\varnothing}$, so that this approach is justified.

6.1.2. Statistical descriptors

The choice of the statistical descriptors $\mathcal{P}_{(L)}$ and their weighting factors $\omega_{(L)}$ strongly influence the morphology of the SSRVEs. Here, the concept of n-point probability function, one of the most important measures to characterize microstructures, is considered. Therein, the indicator function

$$\chi^{(P)}(\boldsymbol{x}) = \begin{cases} 1, & \text{if } \boldsymbol{x} \in D^{(P)} \\ 0, & \text{otherwise} \end{cases} \tag{6.5}$$

is taken into account which indicates if a material point with the position vector $\boldsymbol{x}$ lies within the domain $D^{(P)}$ of the microscopic phase P . It has the property $\sum_P \chi^{(P)}(\boldsymbol{x}) = 1$, which states that exactly one phase is assigned to each investigated point $\boldsymbol{x}$. Considering this, the n-point probability function

$$S_n^{(P)}(\boldsymbol{x}_1, \boldsymbol{x}_2, ..., \boldsymbol{x}_n) = \mathcal{P}\left[\chi^{(P)}(\boldsymbol{x}_1) = 1, \chi^{(P)}(\boldsymbol{x}_2) = 1, ..., \chi^{(P)}(\boldsymbol{x}_n) = 1\right] \tag{6.6}$$

supplies the probability that the n points at the location $\boldsymbol{x}_1, \boldsymbol{x}_2, ..., \boldsymbol{x}_n$ are part of the phase P. **Statistical homogeneity** of the microstructures is assumed, which means that the applied probability functions are invariant under a translational shift $\boldsymbol{y}$. Hence,

$$S_n^{(P)}(\boldsymbol{x}_1, \boldsymbol{x}_2, ..., \boldsymbol{x}_n) = S_n^{(P)}(\boldsymbol{x}_1 + \boldsymbol{y}, \boldsymbol{x}_2 + \boldsymbol{y}, ..., \boldsymbol{x}_n + \boldsymbol{y}) \tag{6.7}$$

holds. Therefore, the n-point probability function only depends on the relative position of the points $\boldsymbol{x}_1, \boldsymbol{x}_2, ..., \boldsymbol{x}_n$ towards each other but not on the absolute positions. This enables the reformulation into the form

$$S_n^{(P)}(\boldsymbol{x}_1, \boldsymbol{x}_2, ..., \boldsymbol{x}_n) = S_n^{(P)}(\boldsymbol{y}, \boldsymbol{x}_{12} + \boldsymbol{y}, ..., \boldsymbol{x}_{1n} + \boldsymbol{y}) \tag{6.8}$$

with the relative position vectors $\boldsymbol{x}_{1i} = \boldsymbol{x}_i - \boldsymbol{x}_1$. If the n-point probability function is invariant regarding rotation of the relative position vectors $\boldsymbol{x}_{12}, ..., \boldsymbol{x}_{1n}$, the structure is said to be **statistically isotropic**. Otherwise, it is characterized statistically anisotropic. Furthermore, **ergodicity** of the microstructures is assumed. A structure is considered as ergodic if the average over all realizations of an ensemble, e.g., the average of the mechanical stress over the microstructure, is equivalent to the volume average, if the volume $V_{\mathcal{B}}$ tends to infinity. Under consideration of this assumption, the form

$$\begin{aligned} S_n^{(P)}(\boldsymbol{x}_1, \boldsymbol{x}_2, ..., \boldsymbol{x}_n) &= \lim_{V_{\mathcal{B}} \to \infty} \frac{1}{V_{\mathcal{B}}} \int\limits_{\mathcal{B}} S_n^{(P)}(\boldsymbol{x}_1, \boldsymbol{x}_2, ..., \boldsymbol{x}_n) \, \mathrm{d}\boldsymbol{y} \\ &= \lim_{V_{\mathcal{B}} \to \infty} \frac{1}{V_{\mathcal{B}}} \int\limits_{\mathcal{B}} S_n^{(P)}(\boldsymbol{y}, \boldsymbol{x}_{12} + \boldsymbol{y}, ..., \boldsymbol{x}_{1n} + \boldsymbol{y}) \, \mathrm{d}\boldsymbol{y} \\ &= \lim_{V_{\mathcal{B}} \to \infty} \frac{1}{V_{\mathcal{B}}} \int\limits_{\mathcal{B}} \chi^{(P)}(\boldsymbol{y}) \, \chi^{(P)}(\boldsymbol{y} + \boldsymbol{x}_{12}) \, \chi^{(P)}(\boldsymbol{y} + \boldsymbol{x}_{13}), ..., \, \chi^{(P)}(\boldsymbol{y} + \boldsymbol{x}_{1n}) \, \mathrm{d}\boldsymbol{y} \end{aligned} \tag{6.9}$$

is obtained. In computational application on microstructures, a sufficiently large microstructure can be assumed instead of the infinite one, especially, if periodicity of the microstructure is assumed. Furthermore, n-point probability functions with $n > 2$ the computational effort becomes large so that they are only evaluated for $n = 1$ and $n = 2$. Firstly, the 1-point probability function is derived by

$$S_1^{(P)}(\boldsymbol{x}) = \lim_{V_{\mathcal{B}} \to \infty} \frac{1}{V_{\mathcal{B}}} \int\limits_{\mathcal{B}} \chi^{(P)}(\boldsymbol{y} + \boldsymbol{x}) \, \mathrm{d}\boldsymbol{y} \tag{6.10}$$

and is equivalent to the volume fraction

$$\mathcal{P}_{\mathrm{V}}^{(P)} := \frac{V(\mathcal{B}_{(P)})}{V(\mathcal{B})} \tag{6.11}$$

because it describes the probability that a certain point $\boldsymbol{x}$ lies within the phase P. For voxel data, the volume fraction $\mathcal{P}_{\mathrm{V}}^{(P)}$ is evaluated by summing up all voxels of the phase P and dividing by the total number of voxels. Secondly, the 2-point probability function, which is evaluated by

$$S_2^{(P)}(\boldsymbol{x}_1, \boldsymbol{x}_2) = \lim_{V_{\mathcal{B}} \to \infty} \frac{1}{V_{\mathcal{B}}} \int\limits_{\mathcal{B}} \chi^{(P)}(\boldsymbol{y} + \boldsymbol{x}_1) \, \chi^{(P)}(\boldsymbol{y} + \boldsymbol{x}_2) \, \mathrm{d}\boldsymbol{y}, \tag{6.12}$$

is also known as two-point correlation function or autocorrelation function. This value can be seen as the probability that the two points $\boldsymbol{x}_1$ and $\boldsymbol{x}_2$ are both located in the phase P. The Wiener-Khintchine theorem, cf. Wiener [147], Khintchine [62] states that the two-point correlation function is strongly related to the spectral density. This spectral density is equivalent to the Fourier transformation $\mathcal{F}$ of the two-point correlation function $S_2^{(P)}(\boldsymbol{x}_1, \boldsymbol{x}_2)$. Vice versa, the two point correlation can be derived as the inverse Fourier transformation $\mathcal{F}^\star$ of the spectral density. For the application on voxel data, the discrete Fourier transformation is applied. This transformation and its inverse are computationally enormously efficient. Here, the Fourier transform in the form of the FFTW ("Fastest Fourier Transform in the West", as seen in Frigo and Johnson [40]) is implemented because of its low computational costs. The spectral density descriptor

$$\mathcal{P}_{\mathrm{SD}} = \frac{|\mathcal{F}_{(P)}|}{2\pi N_x N_y N_z} = \frac{(\mathcal{F}^{(P)})^\star \, \mathcal{F}_{(P)}(i, j, k)}{2\pi N_x N_y N_z} \tag{6.13}$$

of the phase P is derived for each voxel by the application of the Fourier transform $\mathcal{F}^{(P)}$ of the phase P and its conjugate complex $(\mathcal{F}^{(P)})^{\star}$. The Fourier transform maps from the discrete spatial data set to the frequency domain and the inverse Fourier transform does the opposite. The discrete Fourier transform and its inverse are calculated by

$$\mathcal{F}^{(P)}(i,j,k) := \sum_{m=1}^{N_x}\sum_{n=1}^{N_y}\sum_{o=1}^{N_z} \exp\left(-2\,\pi\,\sqrt{-1}\left(\frac{i\,m}{N_x}+\frac{j\,n}{N_y}+\frac{l\,o}{N_z}\right)\right)\chi^{(P)}(m,n,o) \tag{6.14}$$

and

$$\chi^{(P)}(i,j,k) := \frac{1}{N_x N_y N_z}\sum_{m=1}^{N_x}\sum_{n=1}^{N_y}\sum_{o=1}^{N_z} \exp\left(2\,\pi\,\sqrt{-1}\left(\frac{i\,m}{N_x}+\frac{j\,n}{N_y}+\frac{l\,o}{N_z}\right)\right)\mathcal{F}^{(P)}(m,n,o). \tag{6.15}$$

This value is normalized by the number of voxels N_x in x-direction, N_y in y-direction and N_z in z-direction. For the reduction of the computational costs, all values of the resulting spectral density descriptor $\mathcal{P}_{\mathrm{SD}}$ below a chosen threshold value p_{SD}^{thres} are removed. The resulting field $\mathcal{P}_{\mathrm{SD}}$ is reduced to the space of nonzero values that contains $\tilde{N}_{\mathrm{SD}}$ voxels. This descriptor captures periodic properties of the microstructure morphology.

As the third and final statistical descriptor, the lineal-path function, cf. Lu and Torquato [77] is considered for the description of the microstructure morphology. Here, the indicator function is modified to

$$\overline{\chi^{(P)}_{\mathrm{LP}}(\overrightarrow{\boldsymbol{z}})} = \begin{cases} 1, & \text{if } \overrightarrow{\boldsymbol{z}} \in D^{(P)} \\ 0, & \text{otherwise} \end{cases} \tag{6.16}$$

that indicates whether the line segment $\vec{\boldsymbol{z}} := \overrightarrow{\boldsymbol{x}_1\boldsymbol{x}_2}$ lies completely in the phase P or not. The corresponding descriptor

$$\mathcal{P}_{\mathrm{LD}}(\vec{\boldsymbol{z}}) := \lim_{V\to\infty}\int_{\mathcal{B}} \chi^{(P)}_{\mathrm{LP}}(\boldsymbol{y}+\vec{\boldsymbol{z}})\,\mathrm{d}\boldsymbol{y} \tag{6.17}$$

is obtained by again assuming ergodicity of the microstructure. For its application on voxel data with $N_x \times N_y \times N_z$ voxels in x-, y- and z-direction, this descriptor is rewritten into the form

$$\mathcal{P}_{\mathrm{LD}}(i,j,k) = \frac{\sum\limits_{l}^{N_x}\sum\limits_{m}^{N_y}\sum\limits_{n}^{N_z}\chi^{(P)}_{\mathrm{LP}}(\boldsymbol{y}+\vec{\boldsymbol{z}})}{N_x N_y N_z}, \tag{6.18}$$

where i, j and k denote the indices of the voxel. To computationally evaluate this function, a template with $T_x = 2\,N_x - 1$ in x-, $T_y = 2\,N_y - 1$ in y- and $T_z = N_z$ in z-direction of the target microstructure is generated. Therein, data for characterizing the lineal-path properties are saved. Because of the invariance with respect to reflections of the line segments, the number of voxels in z-direction is not doubled to save computational costs. The template only contains zeros in the beginning. Then the center point of the template is shifted into every voxel of the microstructure. These voxels serve as starting point for the following algorithm. Starting from this voxel, line segments into different directions are checked whether all voxels, this line segments enters, are part of the phase $\chi^{(P)}$. If they are, the value of the end point of the line segment within the template is increased by one. This procedure is repeated for all investigated line segments for every voxel. To determine which voxels are passed by the line, the Bresenham algorithm, cf. Bresenham [18] is applied. The directions of the lines, in which the lineal path function is evaluated, are defined by the angle α_{LP} towards each other. Note, that in general two angles could by applied but for technical simplicity only one is used. To reduce the computational costs, all entries of the final template of the target microstructure below the threshold p_{LP}^{thres} are removed. The size of the template is reduced to the space in which nonzero values occur with $\tilde{N}_{\mathrm{LP}}$ voxels. If this scheme is applied on the artificially constructed microstructures, their periodicity has to be considered. To take this into account, the line segments that leave the periodic microstructure enter it on the opposite side and are continued from there on. With this technique, the shape of the inclusions and their orientation are taken into account for the statistical description of the microstructure.

6.1.3. Applications of the objective functions

For the construction of the SSRVEs, the definition of the specific optimization problem is crucial. This includes the statistical description and their influence on the objective function. In our case, the form

$$\mathcal{E}(\boldsymbol{\gamma}) = \omega_{\mathrm{V}}\, \mathcal{L}_{\mathrm{V}}(\boldsymbol{\gamma}) + \omega_{\mathrm{SD}}\, \mathcal{L}_{\mathrm{SD}}(\boldsymbol{\gamma}) + \omega_{\mathrm{LD}}\, \mathcal{L}_{\mathrm{LD}}(\boldsymbol{\gamma}) \tag{6.19}$$

is applied, which sums up the objective functions of the volume fraction $\mathcal{L}_{\mathrm{V}}(\boldsymbol{\gamma})$, of the spectral density $\mathcal{L}_{\mathrm{SD}}(\boldsymbol{\gamma})$ and of the lineal path functions $\mathcal{L}_{\mathrm{LP}}(\boldsymbol{\gamma})$. They measure the error of the statistical descriptors of the SSRVE compared to the ones of the target microstructure, namely the binarized voxel data of the μCT-scan. Because the magnitude of these objective functions varies, all of them are weighted with the corresponding weights ω_{V}, ω_{SD} and ω_{LP}. The choice of this weights strongly influences the overall objective function $\mathcal{E}(\boldsymbol{\gamma})$, because if one of those is chosen too large or too small, some of the partial objective functions and therefore, their statistical descriptors may be falsely neglected or overestimated.
For the one-point probability function, the objective function reads

$$\mathcal{L}_{V}(\boldsymbol{\gamma}) := \left(1 - \frac{\mathcal{P}_{\mathrm{V}}^{\mathrm{SSRVE}}}{\mathcal{P}_{\mathrm{V}}^{\mathrm{target}}}\right)^{2} . \tag{6.20}$$

The closer the statistical descriptor of the one-point probability function of the SSRVE $\mathcal{P}_{\mathrm{V}}^{\mathrm{SSRVE}}$ gets to the one of the target structure $\mathcal{P}_{\mathrm{V}}^{\mathrm{target}}$, the smaller becomes its objective function $\mathcal{L}_{V}(\boldsymbol{\gamma})$. For the comparison of the multidimensional descriptors $\mathcal{P}_{\mathrm{SD}}(\boldsymbol{y}_m, \boldsymbol{\gamma})$ and $\mathcal{P}_{\mathrm{LP}}(\boldsymbol{y}_m, \boldsymbol{\gamma})$ with a discrete set of voxels $\boldsymbol{y}_m$, the least-square functional is applied. They are evaluated by

$$\mathcal{L}_{\mathrm{SD}}(\boldsymbol{\gamma}) := \frac{1}{\tilde{N}^{\mathrm{SD}}} \sum_{m=1}^{\tilde{N}^{\mathrm{SD}}} \Big(\mathcal{P}_{\mathrm{SD}}^{\mathrm{target}}(\boldsymbol{y}_m) - \mathcal{P}_{\mathrm{SD}}^{\mathrm{SSRVE}}(\boldsymbol{y}_m, \boldsymbol{\gamma})\Big)^{2} \tag{6.21}$$

for the spectral density and

$$\mathcal{L}_{\mathrm{LP}}(\boldsymbol{\gamma}) := \frac{1}{\tilde{N}^{\mathrm{LP}}} \sum_{m=1}^{\tilde{N}^{\mathrm{LP}}} \Big(\mathcal{P}_{\mathrm{LP}}^{\mathrm{target}}(\boldsymbol{y}_m) - \mathcal{P}_{\mathrm{LP}}^{\mathrm{SSRVE}}(\boldsymbol{y}_m, \boldsymbol{\gamma})\Big)^{2} \tag{6.22}$$

for the lineal path function respectively. Here, the objective functions are normalized by the number of compared voxels of the spectral density $\tilde{N}^{\mathrm{SD}}$ and of the lineal path function $\tilde{N}^{\mathrm{LP}}$. In the original approach in Balzani et al. [8], these numbers of voxels are obtained by binning the target microstructure so that its resolution its reduced. Thereby, voxels are summarized to larger ones to reduce the computational effort. The choice of binning strongly influences the statistical descriptors, as shown in Povirk [111]. To avoid this effect, another technique is applied here. The voxel set of the SSRVE is multiplied in all spatial directions until the resulting voxel set is of the size of the target microstructure. The part of the SSRVEs that lie outside the target microstructure's space are cut off. By comparison of this new voxel set to the target microstructure, this approach is more accurate than the one that includes binning. Combining all those partial objective functions to the total inner optimization problem in equation (6.19), the parameters of the different parameterizations of the inclusions $\tilde{\boldsymbol{\gamma}}_i$ are obtained by optimization. Here, the Covariant Matrix Adaption Evolution Strategy (CMA-ES)

implementation in Python, cf. Auger and Hansen [5] is applied to obtain the desired parameters. Therein, multiple SSRVEs are constructed in a Monte-Carlo simulation and their corresponding objective values $\mathcal{E}(\boldsymbol{\gamma}_i)$ are evaluated. This process is executed in a parallelized manner so that the total computational time is kept low. The CMA-ES chooses the parameters partially randomized and partially on the basis of the previously examined SSRVEs.
The size of the SSRVE $V^{\mathrm{SSRVE}} = n_{\mathrm{incl}}\,\tilde{V}^{\mathrm{target}}_{\mathrm{incl}}/\mathcal{P}^{\mathrm{target}}_{\mathrm{V}}$ is determined based on the average inclusion size $\tilde{V}^{\mathrm{target}}_{\mathrm{incl}}$ of the target microstructure and the number of inclusions n_{incl} of the SSRVE. The average inclusion size $\tilde{V}^{\mathrm{target}}_{\mathrm{incl}}$ is identified by considering of the lineal path template because this descriptor captures the inclusion shape. The volume is calculated as the sum of the volumes of the remaining nonzero voxels. In our case, cubic SSRVEs are assumed so that the edge length results in

$$L^{\mathrm{SSRVE}} = \sqrt[3]{\frac{n_{\mathrm{incl}}\,\tilde{V}^{\mathrm{target}}}{\mathcal{P}^{\mathrm{target}}_{\mathrm{V}}}}. \tag{6.23}$$

Because the voxel size remains constant, the number of voxels in the SSRVE depends on the edge length and thus, on the number of inclusions.

Lastly, the outer optimization problem is solved by carrying out mechanical simulations for example with one dimensional strain or shear deformation on the microstructures of the different parameterizations $\bar{\boldsymbol{\gamma}}_i$ and the target microstructure. Afterwards, the structural response of the SSRVEs is compared to the one of the target microstructure. Here, the error

$$r_{e,j} = \frac{\bar{P}^{\mathrm{target}}_{e,j}(\bar{F}_{e,j}) - \bar{P}^{\mathrm{SSRVE}}_{e,j}(\bar{F}_{e,j})}{\bar{P}^{\mathrm{target}}_{e,j}(\bar{F}_{e,j})} \tag{6.24}$$

is derived in the macroscopic first Piola-Kirchhoff stress response for every evaluation point $j = 1, ..., n_{\mathrm{ep}}$ in every chosen experiment e with the macroscopic deformation gradient $\bar{F}_{e,j}$, which here is ramped linearly $\bar{F}_{e,j} = j\,\bar{F}^{\mathrm{max}}_{e}/n_{\mathrm{ep}}$ to the maximum deformation gradient $\bar{F}^{\mathrm{max}}_{e}$. To summarize these errors of all evaluation points of the experiment e to one objective function, the least-square functional

$$\tilde{r}_e = \sqrt{\frac{1}{n_{\mathrm{ep}}}\sum_{j=1}^{n_{\mathrm{ep}}}\left[r_{e,j}\right]^2} \tag{6.25}$$

is evaluated. The overall average error

$$\tilde{r}_{\varnothing} = \sqrt{\frac{1}{n_{\mathrm{exp}}}\sum_{j=1}^{n_{\mathrm{exp}}}\left[\tilde{r}_e\right]^2} \tag{6.26}$$

of the mechanical response of the n_{exp} is again derived with a least-square functional. Based on this, the outer optimization problem is solved by choosing the parameterization $\tilde{\boldsymbol{\gamma}}_i$ with the lowest objective function $\tilde{r}_{\varnothing}$. With this scheme, the SSRVEs are optimized regarding morphology and mechanical properties in a staggered manner.

6.1.4. Parameterizations of the inclusions

For the construction of three-dimensional SSRVEs, the shapes of the inclusions have to be chosen and parameterized for example as cylinders, spheres or cubes. In our case, we consider those as superellipsoids generated with the inequality

$$\sum_{i=1}^{3}\left|\frac{X_i - X^{\mathrm{C}}_i}{r_i}\right|^{p_i} \leq 1 \tag{6.27}$$

by taking into account the components X_i of the position vector $\boldsymbol{X}$, the radii of the orthogonal semi-axes r_i, the center coordinates x_i^{C} of the inclusion and the exponent p_i for each direction that influences the overall shape. All points $\boldsymbol{X}$, for which the inequality holds, are assumed to lie within or on the surface of the superellipsoid. Otherwise, they lie outside of it. Note, that the concept of the SSRVEs has only been exploited for ellipsoids which are equivalent to superellipoids with the exponent $p_i = 2$ in Schröder et al. [129], so that the superellipsoids for the generation of SSRVEs are firstly introduced here. The advantage of this shape lies in the variety of obtainable shapes as demonstrates in figure 6.2. This extension enables the construction of, e.g., star-like, diamond-shaped and cuboid structures additionally to the ellipsoids and spheres of the original implementation. As a constraint, the exponents are restricted to $p_i > 0$ to avoid inclusions with zero thickness at $\boldsymbol{X} = \boldsymbol{X}^{\mathrm{C}}$. Based on the assumption of superellipsoids, the parameterization vector for one inclusion becomes

$$\boldsymbol{\gamma}_{\mathrm{se3}}^{j} := [X_1^{\mathrm{C}},\, X_2^{\mathrm{C}},\, X_3^{\mathrm{C}},\, \theta_1,\, \theta_2,\, \theta_3,\, r_1,\, r_2,\, r_3,\, p_x,\, p_y,\, p_z]^{\mathrm{T}}. \tag{6.28}$$

Here, the semi-axes of the inclusions are rotated by the Euler angles θ_1, θ_2 and θ_3. In some applications, only one exponent $p_i = p$ per inclusion is optimized. Here, the parameterization is simplified to

$$\boldsymbol{\gamma}_{\mathrm{se1}}^{j} := [X_1^{\mathrm{C}},\, X_2^{\mathrm{C}},\, X_3^{\mathrm{C}},\, \theta_1,\, \theta_2,\, \theta_3,\, r_1,\, r_2,\, r_3,\, p]^{\mathrm{T}}. \tag{6.29}$$

This restricts the possible shapes, but leads to a lower number of parameters, which reduces the computational costs for the optimization. As a further approach, one global parameter for the exponent p can be considered. If $p = 2$ is set for all inclusions, ellipsoidal inclusion shapes with the parameterization

$$\boldsymbol{\gamma}_{\mathrm{el}}^{j} := [X_1^{\mathrm{C}},\, X_2^{\mathrm{C}},\, X_3^{\mathrm{C}},\, \theta_1,\, \theta_2,\, \theta_3,\, r_1,\, r_2,\, r_3]^{\mathrm{T}} \tag{6.30}$$

as in the original implementation in Schröder et al. [129] are obtained. The vectors of the parameterizations $\boldsymbol{\gamma}_{\bullet}^{j}$ for each inclusion j are summarized to the global vector

$$\boldsymbol{\gamma}_i = [\boldsymbol{\gamma}_{\bullet}^{1}, \boldsymbol{\gamma}_{\bullet}^{2}, ..., \boldsymbol{\gamma}_{\bullet}^{n_{\mathrm{incl}}}]^{\mathrm{T}} \tag{6.31}$$

of all n_{incl} inclusions. Here, the index i indicates the different realizations of the SSRVE. As an exception, the center coordinates $\boldsymbol{X}^{\mathrm{C}}$ of the first inclusion are fixed. This avoids numerical problems because otherwise an infinite amount of center points for the whole structure are possible due to the periodicity of the SSRVE. Note, that in this implementation, the inclusions may overlap, which may result in even more abstract inclusion shapes than superellipsoids. As an alternative for the parameterization of the microstructure with the supperellipsoidal inclusions, not one exponent for each inclusion but one global exponent may be assumed. Here, the parameterization results to

$$\boldsymbol{\gamma}_i = [\boldsymbol{\gamma}_{\mathrm{el}}^{1}, \boldsymbol{\gamma}_{\mathrm{el}}^{2}, ..., \boldsymbol{\gamma}_{\mathrm{el}}^{n_{\mathrm{incl}}}, p]^{\mathrm{T}} \tag{6.32}$$

with the global exponent p.

6.1.5. Application on Ferro-Titanit

The material of interest is the MMC named Ferro-Titanit. It consists of stiff and brittle tungsten carbide inclusions, that are surrounded by a ductile nickel martensite. The SSRVEs are constructed based on the voxel data in figure 5.9b from the μCT-scan in figure 5.9a. The weighting factors $\omega_{\mathrm{V}} = 1$, $\omega_{\mathrm{SD}} = 0.0001$ and $\omega_{\mathrm{LP}} = 1000$ of the objective function $\mathcal{E}$ have been found to lead to values of the partial objective functions $\mathcal{L}_{\mathrm{V}}$, $\mathcal{L}_{\mathrm{SD}}$ and $\mathcal{L}_{\mathrm{LP}}$ which lie in comparable magnitudes. Here, the parameterizations of $1, ..., 6$ ellipsoids and $1, ..., 6$ superellipsoids under the assumption of one exponent $p_x = p_y = p_z = p$ are considered inclusion shapes. The

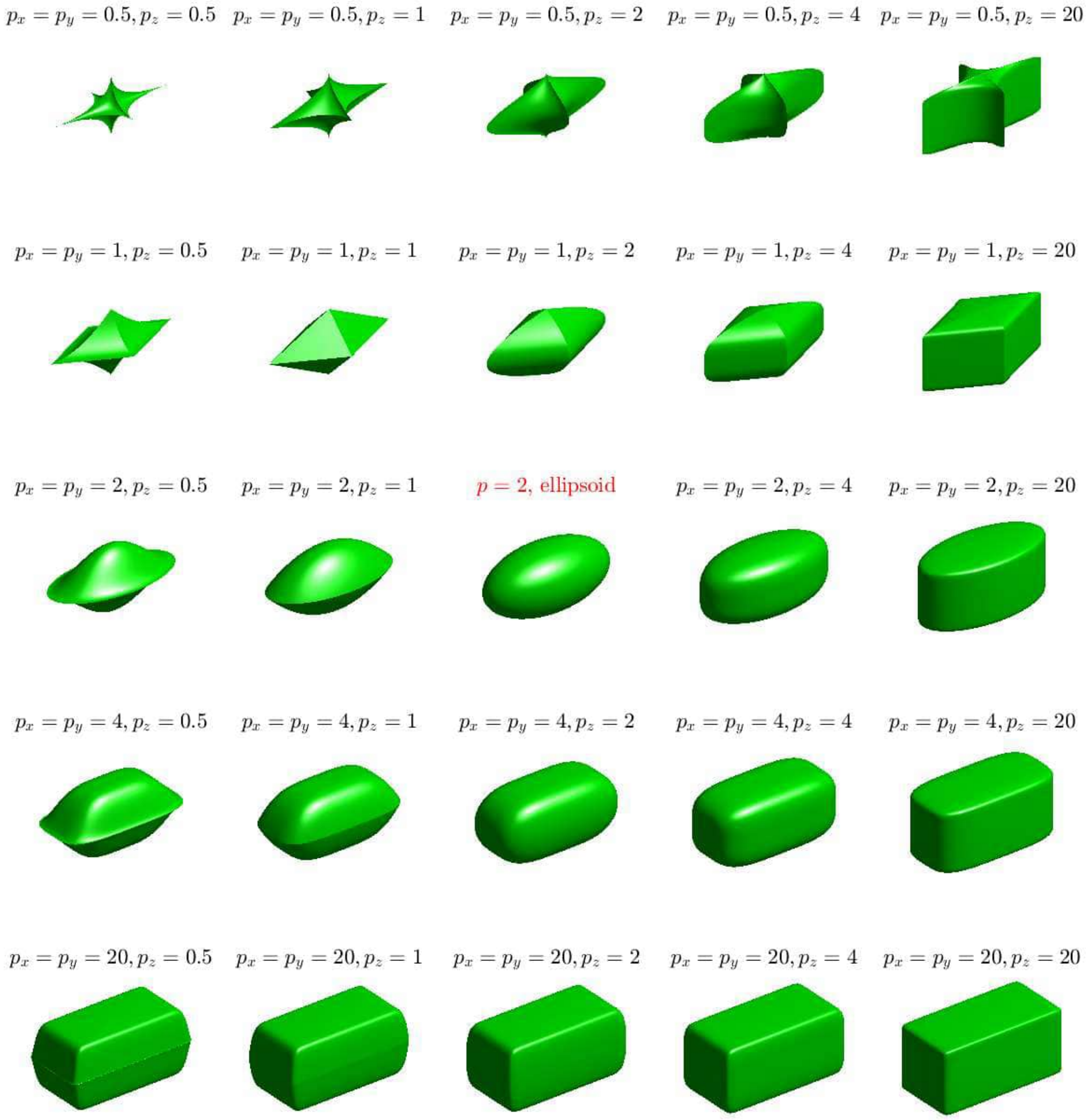
$p_x = p_y = 0.5, p_z = 0.5$
$p_x = p_y = 0.5, p_z = 1$
$p_x = p_y = 0.5, p_z = 2$
$p_x = p_y = 0.5, p_z = 4$
$p_x = p_y = 0.5, p_z = 20$
$p_x = p_y = 1, p_z = 0.5$
$p_x = p_y = 1, p_z = 1$
$p_x = p_y = 1, p_z = 2$
$p_x = p_y = 1, p_z = 4$
$p_x = p_y = 1, p_z = 20$
$p_x = p_y = 2, p_z = 0.5$
$p_x = p_y = 2, p_z = 1$
$p = 2$, ellipsoid
$p_x = p_y = 2, p_z = 4$
$p_x = p_y = 2, p_z = 20$
$p_x = p_y = 4, p_z = 0.5$
$p_x = p_y = 4, p_z = 1$
$p_x = p_y = 4, p_z = 2$
$p_x = p_y = 4, p_z = 4$
$p_x = p_y = 4, p_z = 20$
$p_x = p_y = 20, p_z = 0.5$
$p_x = p_y = 20, p_z = 1$
$p_x = p_y = 20, p_z = 2$
$p_x = p_y = 20, p_z = 4$
$p_x = p_y = 20, p_z = 20$

Figure 6.2.: Example shapes of inclusions formed by superellipsoids with the semi-axis radii $r_x = r_z = 1$ and $r_y = 2$ and different exponents p_x, p_y and p_z without any rotation

resulting SSRVEs are shown in figures 6.3 and 6.4, and the corresponding parameterizations in Appendix B. The morphology of the SSRVEs that are constructed under the assumption of ellipsoidal inclusions becomes complex with increasing number of inclusions. Especially due to the overlap of inclusions, a higher complexity is achieved. Additionally, some inclusions are distorted in such a way that they leave and enter the periodic unit cell multiple times. In contrast to the ellipsoidal inclusions, the superellipsoids' exponent p is with values larger than 8 so huge that the inclusions take a cuboid-like shapes. The roundness of the edges cannot be properly represented anymore by the voxelized geometry due to these high exponents. Hence, if a certain value of the exponent p is surpassed, it does not affect the voxelized morphology.

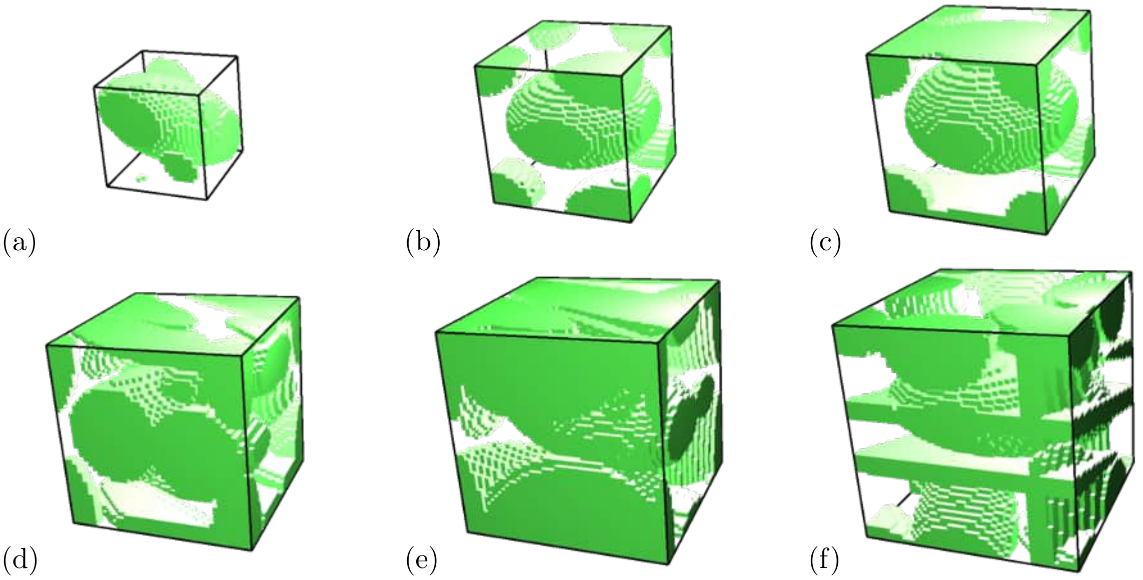

Figure 6.3.: SSRVEs of Ferro-Titanit with $1, ..., 6$ ellipsoidal inclusions that are optimized regarding their statistical measures of the morphology, taken from Wingender and Balzani [151]. For the parameterizations, see Appendix B.

For the objective function $\mathcal{E}(\tilde{\gamma}_i)$ of the parameterizations $\tilde{\gamma}_i$resulting from the inner optimization problem, it is expected that it decreases with increasing inclusion number n^{incl} since the additional number of parameters enable a wider range of possible morphologies and thus, a more accurate representation of the target microstructure. However, the plot objective function over the number of inclusions in figure 6.5a shows that this assumption only holds until an inclusion number of $n^{\text{incl}} = 5$ for ellipsoids and $n^{\text{incl}} = 3$ for the superellipsoids. For larger number of inclusions, the objective function is increased. This might be a numerical artifact, that may occur because the optimizer might not have found the global minimum of $\mathcal{E}(\gamma)$ with respect to the parameters of the SSRVEs with many inclusions due to their high variety of possible morphologies. This effect is additionally empathized by the fact that the objective

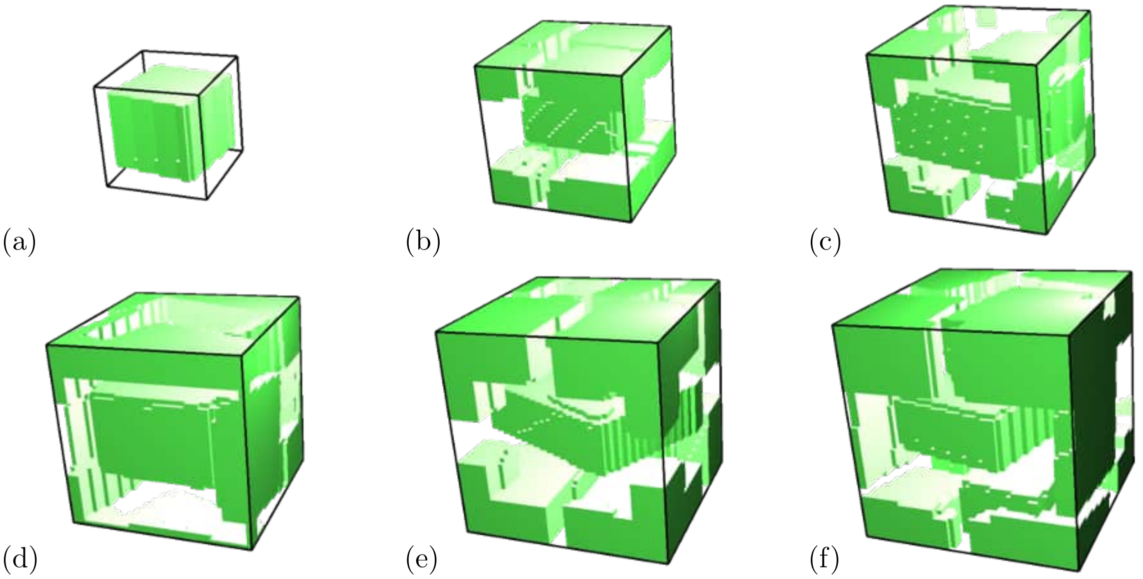

Figure 6.4.: SSRVEs of Ferro-Titanit with $1, ..., 6$ superellipsoidal inclusions that are optimized regarding their statistical measures of the morphology. For the parameterizations, see Appendix B.

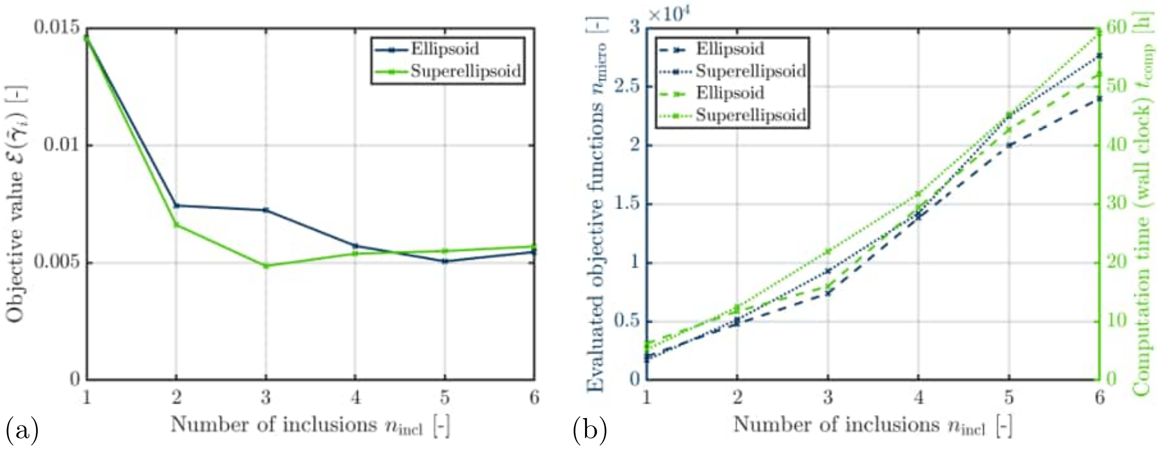

Figure 6.5.: (a) Objective values $\mathcal{E}(\tilde{\gamma}_i)$ of the statistical measures of the morphology and (b) number of evaluated microstructures n_{micro} and computation time t_{comp} over the number of inclusions n_{incl}.

function $\mathcal{E}$ of the superellipsoids surpasses the one of the ellipsoids for $n_{\text{incl}} \geq 5$. Because all possible parameterization of the ellipsoids are a subset of the parameterizations of the superellipsoids, the objective function of the superellipsoids is expected to be equal or lower. To circumvent this effect, the optimization scheme could be applied multiple times to find the parameterization of the SSRVE with the lowest objective function $\mathcal{E}(\tilde{\gamma}_i)$. In figure 6.5b, it is shown that the number of evaluated objective functions n_{micro} for each parameterization increases with increasing number of inclusions n_{incl} as expected. Resulting from this, the computational time t_{comp}, here the wall clock time, is increases as well. Note, that the microstructures are evaluated in a parallel manner on 39 threads, so that the computation time is highly reduced compared to the evaluation in series. The additional parameter of the superellipsoids increases the number of necessary evaluations n_{micro} of the objective function by around 15%.

For the optimization regarding the mechanical properties, the mechanical response of the target microstructure as well as the SSRVEs with the parameterizations $\tilde{\gamma}_i$ to chosen tests are compared. Here, tensile tests with symmetry boundary conditions in figure 6.6a are executed with the increasing deformation in each spatial direction. The material parameters from figure 7.1 under the assumption of the elasto-plastic material formulation are applied. The calibration of these parameters is presented in section 7.1. Since it is known from the simulations in section 5.4.5 that the size of the finite cells influences the structural response, the edge length of the finite cells $h_{\text{fc}} = 4\,\mu\text{m}$ is defined for all microstructures, to obtain comparable results. Note, that the number of finite cells varies with the number of inclusions because the size of the unit cell is adjusted to n_{incl}. Because the computational effort to simulate the target microstructure with the chosen resolution h_{fc} would be high, a representative cutout from the target microstructure is simulated to obtain its mechanical response. Because no crack propagation and thus, no split of the finite cells are considered in these simulations, the finite cells of the cutout as well as the SSRVEs are decomposed with the OD because of its computational efficiency. In figure 6.6b, the mechanical response of the cutout for the three different edge lengths 96, 144 and 192 is compared. While the mechanical response of the cutout consisting of 96^3 voxels is low compared to the one with the largest number of voxels, the values of the cutout with 144^3 voxels lie close. Hence, convergence with increasing number of voxels is shown, so that the cutout consisting of 192^3 voxels is considered as representative for the whole target microstructure since statistical homogeneity is assumed. The values of this microstructure is assumed as reference values. Additionally, the isotropy of the mechanical properties of the target microstructure is demonstrated. In figure 6.5c, the

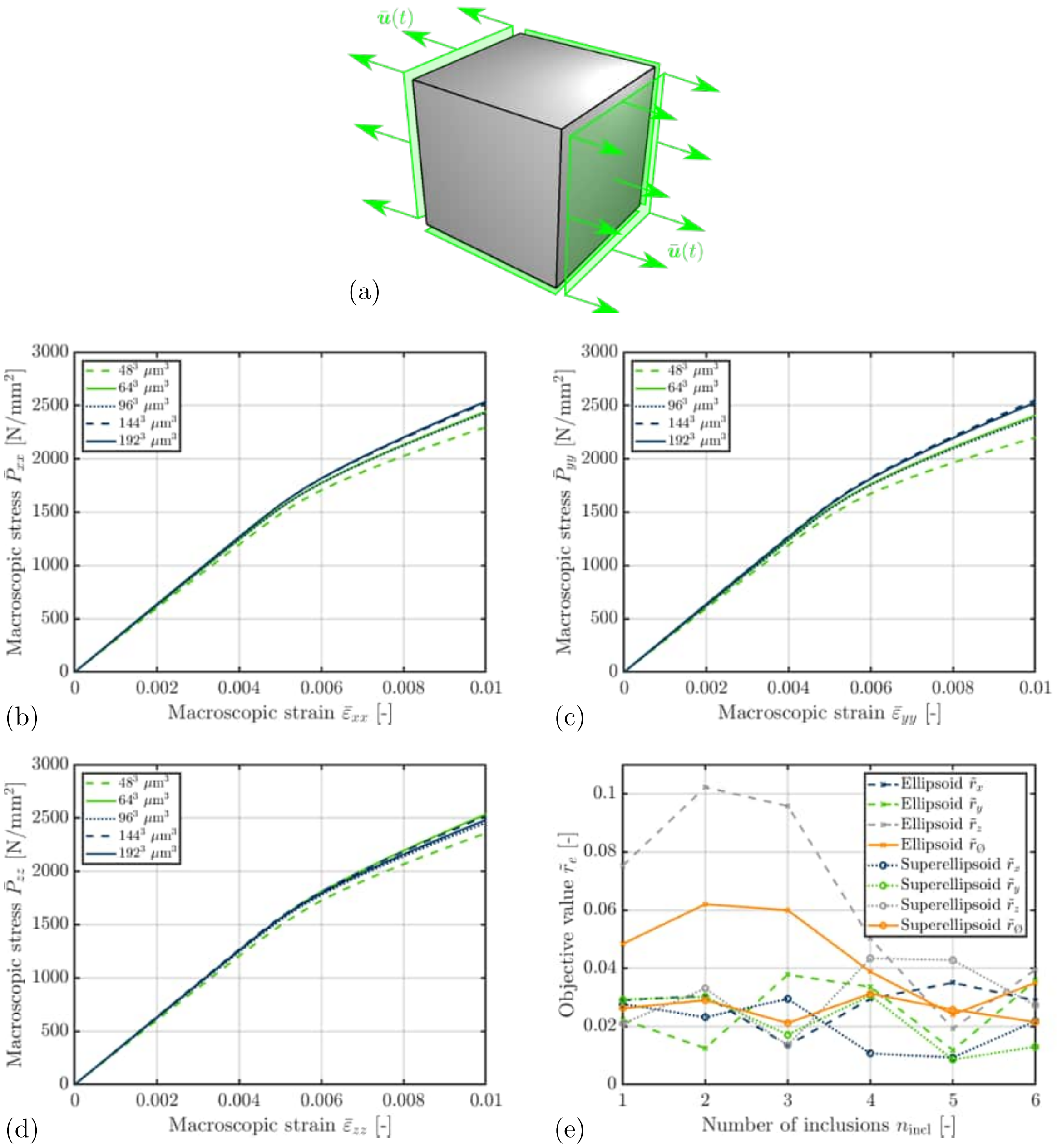

Figure 6.6.: (a)Dirichlet boundary conditions for the tensile test for the evaluation of the convergence of the mechanical response in (b)-(d) with increasing size of the cutout from the μCT-scan, taken from Wingender and Balzani [151], and of (e) the error in the mechanical response $r_{e,j}$ of the SSRVEs compared to the cutout of 192^3 voxels over the number of inclusions n_{incl}.

least-square errors $\tilde{r}_{\text{e}}$ and $\tilde{r}_\varnothing$ of the mechanical simulations of the SSRVEs compared to the cutout of target microstructure are presented. For all number of inclusions n_{incl}, the overall least-square error $\tilde{r}_\varnothing$ is lower for the SSRVEs with the superellipsoidal inclusions even though the morphological least-square error $\mathcal{E}$ of the SSRVEs with the superellipsoids surpasses the one of the SSRVE with the ellipsoids for 5 and 6 inclusions. Because the only parameter that additionally is adjusted is the exponent of the superellipsoids, it can be assumed that the resulting cuboid shape of the superellipsoids better represents the mechanical properties of the target microstructure. Because the least-square error $\tilde{r}_\varnothing = 2.15\%$ of the SSRVE with the six superellipsoidal inclusions is the lowest, this SSRVE is identified as the result of the optimization in both, the morphological as well as the mechanical properties.

6.2. Statistical volume elements

This section presents a second method to construct artificial microstructures and the application on a specific type of asphalt concrete, the PA8, see figure 6.7. This material consists of stiff, elastic mineral aggregate inclusions surrounded by a viscous binding agent. Here, the core idea is to generate the artificial microstructure bottom up based on the same parameters that are used for producing the asphalt concrete on the construction site so that no further information, for example voxel data obtained from a μCT-scan of the microstructure, is necessary. The investigations presented in this section have been carried out in cooperation with Prof. Ralf Jänicke. This makes this generation process easier applicable for civil engineering problems. Because this generation procedure includes a certain randomness, the artificial microstructures are called **Stochastic Volume Elements SVE**, as introduced in Yin et al. [160], because their characteristic morphological properties fluctuate with a certain stochastic variance around a mean value. Hence, an ensemble of multiple SVEs has to be considered that altogether represent the physical microstructure properly. The SVEs may also be understood as a specific class of the SSRVEs since the inner optimization problem of the basic equation 6.4 for the SSRVEs is solved by hand for the construction of the SVEs. The outer optimization problem is circumvented by considering multiple SVEs which altogether, resemble the mechanical properties of the sought material. However, both construction approaches are viewed as separate approaches in this work. To demonstrate this, the statistical measures are examined in the generated asphalt concrete SVEs.

6.2.1. Properties of asphalt concrete

The mechanical properties of asphalt concrete are influenced by its constituents' properties and its morphology on multiple scales, see figure 6.8. The macroscopic homogeneous properties of the asphalt concrete depend on the properties of its mixture on the heterogeneous mesoscale, cf. figure 6.8c. On this mesoscale, the asphalt concrete is a biphasic material consisting of stiff elastic mineral aggregate inclusions, usually rock particles, surrounded by a viscoelastic binding agent, the so-called mastic or bituminous binder. Asphalt concrete also appears as triphasic material containing voids additionally. The inclusions inherit an equivalent diameter $d_{\text{eq}} = \sqrt[3]{\frac{6\,V_{\text{incl}}}{\pi}}$ of 1 mm up to 8 mm, so that the edge length l of the structure on the mesoscale takes some centimeters. In our case, we investigate an asphalt concrete with the particle size distribution of PA8. The morphology of the inclusions is characterized by the volume fractions of the mineral aggregates n_{ma} and of the bituminous binder $n_{\text{b}} = 1 - n_{\text{ma}}$ and by the particle size distribution, the so-called **sieve curve**. In physical applications, the desired properties

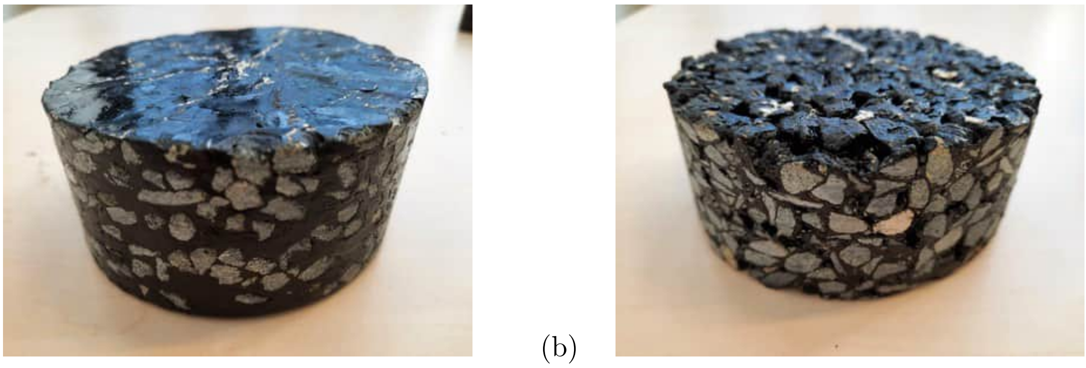
(a) (b)

Figure 6.7.: Cylindrical asphalt concrete specimen as (a) biphasic material consisting of mineral aggregates (gray) and mastic (black) and as (b) triphasic material containing voids additionally.

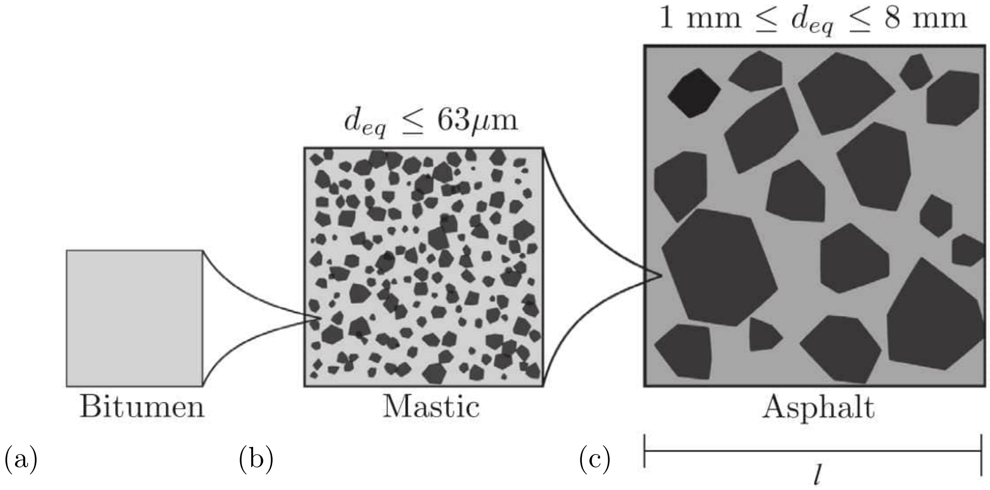
$1\text{ mm} \leq d_{eq} \leq 8\text{ mm}$
$d_{eq} \leq 63\mu\text{m}$
Bitumen
Mastic
Asphalt
(a)
(b)
(c)
l

Figure 6.8.: (a) Bitumen as part of the (b) microscale morphology of the mastic which is one of the constituents of the (c) asphalt concrete on the mesoscale, taken from Schüler et al. [130].

of the asphalt concrete are adjusted by these parameters. A sieve curve shows the cumulative volume fraction of the mineral aggregates compared to the overall volume fraction n_{ma} over the equivalent sphere diameter of the aggregates. In construction science, the equivalent sphere diameters d_{eq} are obtained by filtering the grains with sieves of different standardized mesh sizes that are assumed to equal the equivalent diameter d_{eq}. All mineral aggregates with equivalent diameters $d_{\text{eq}} \leq 63\,\mu m$ are assumed as filler material for the bituminous binding agent and thus, are only regarded on the microscale and not on the mesoscale. The sieve curve of PA8 only contains mineral aggregates that, on the one hand, are small enough to pass the sieve with a mesh size of 8 mm but on the other hand, large enough to be stopped by the next smaller sieve with a mesh size of 5.6 mm. Hence, all particles inherit a similar size which makes this grain size distribution monodisperse. in the case of the triphasic material, voids additionally occur. Their morphological properties cannot be obtained before the mixing process. They can be examined by evaluating μCT-scans, as shown in Schüler et al. [130]. On the microscale, the mastic consists of bitumen which contains rock particle inclusion with an equivalent diameter of $d_{\text{eq}} \leq 63\,\mu\text{m}$, cf. figure 6.8b. These particles influence the mechanical properties of the mastic. This material is described with a viscoelastic material model, namely the generalized Maxwell model, cf. Wiechert [146]. Its properties strongly depend on the temperature and on the load frequency. Here, we investigate the effects of the mesoscale on the biphasic asphalt concrete under the consideration of the mastic as one homogeneous material with homogeneous material properties.

6.2.2. Computational generation of SVEs

For the construction of the biphasic asphalt concrete SVEs on the mesoscale as presented in Schüler et al. [130], we apply a work flow, as shown in figure 6.9. Therein, several steps to obtain the volumes of the mineral aggregates and of the binder phase are described. Therefore, the generation parameters are set in a way that a sought particle size distribution and volume fraction of the mineral aggregates n_{ma} and of the bituminous binder n_{b} are achieved.

Dense sphere packing In the first step of the work flow, a dense sphere packing with S spheres is derived with the implementation of Donev et al. [29, 30], Lavergne et al. [73] of the Lubachevsky-Stillinger algorithm Lubachevsky and Stillinger [78], Lubachevsky et al. [79] which is illustrated in figure 6.10. This algorithm requires the different constant growth rates g_i of the spheres and the number of spheres S_g under the growth rate g_i as input

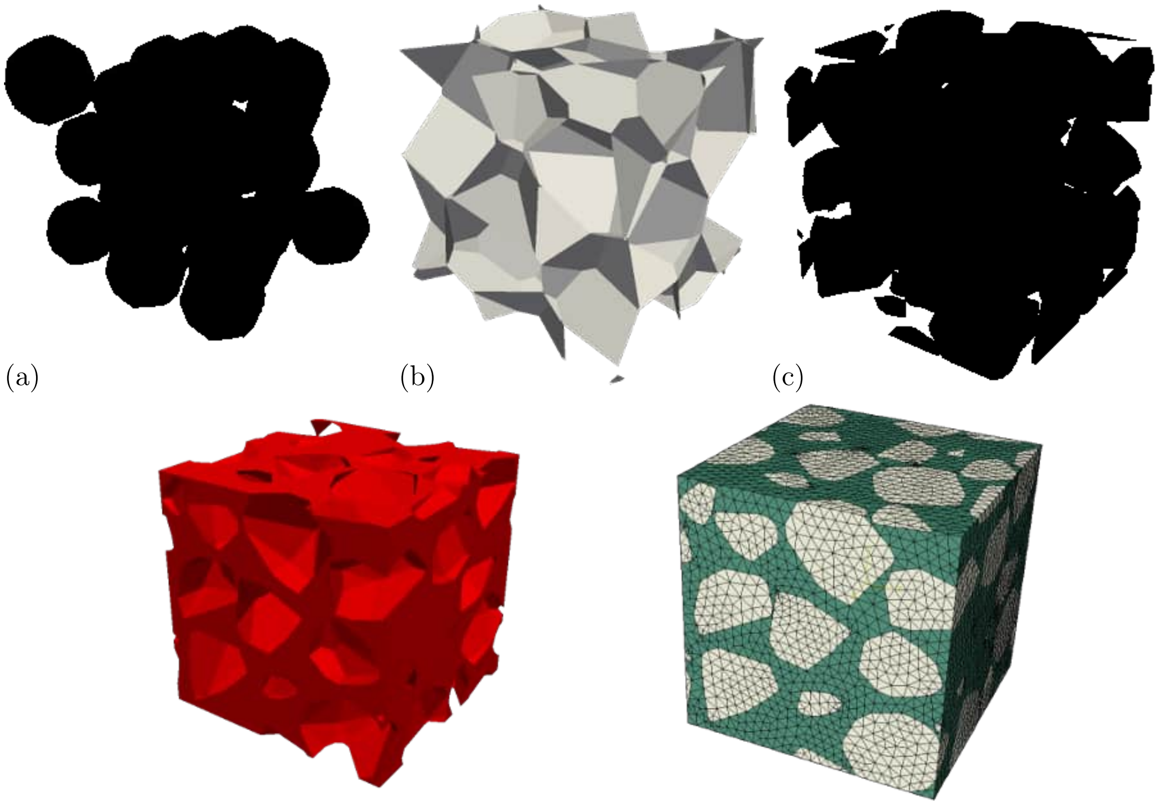

(a) (b) (c)

(d) (e)

Figure 6.9.: Work flow of the artificial asphalt concrete generation starting from (a) the Lubachevsky-Stillinger algorithm, continuing with (b) the Voronoi tesselation, (c) the statistical shrinking, (d) application of volume operations to obtain the bituminous binding agent and finally (e) meshing the volume element, taken from Wingender et al. [153].

parameters. Note, that the ratio of the growth rates towards each other represents the ratio of the final sphere radii r_i to each other due to the evolution

$$r_i(t) = g_i\, t \tag{6.33}$$

with the time t so that the particle size distribution of the mineral aggregates is controlled. The spheres are seeded at random initial positions $\mathbf{r}_{i,0}$ with random initial velocities $\mathbf{v}_{i,0}$ and infinite small radii in a periodic unit cube $\mathcal{V}_\Box$ at the time $t = 0$. As an event-driven algorithm, the Lubachevsky-Stillinger algorithm calculates from event to event, in our case from particle collision at the time t_n to particle collision at the time t_{n+1}. Therefore, it derives the difference in the times steps $\Delta t_{ij} = t_{n+1} - t_n$ at which each particle i collides with every other particle j under the assumption of constant velocities. Hereby, every sphere occurs 3 times with a distance of 1 in each direction from the one in the unit cube, so that each sphere occurs 27 times in order to maintain the periodicity of the dense sphere packing. The time difference Δt_{ij} between the collisions is derived by solving the equation

$$|\mathbf{x}_{i,n} - \mathbf{x}_{j,n} + (\mathbf{v}_{i,n} - \mathbf{v}_{j,n})\,\Delta t_{ij}| = r_{i,n} + r_{j,n} + (g_i + g_j)\,(t_n + \Delta t_{ij}). \tag{6.34}$$

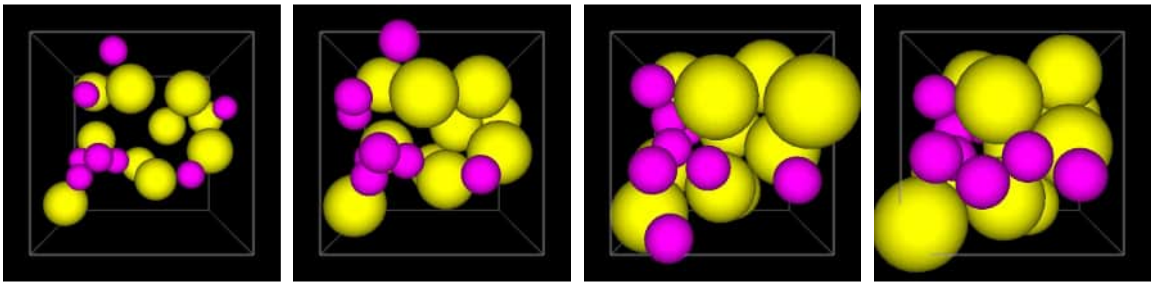
(a) (b) (c) (d)

Figure 6.10.: Visualization of the Lubachevsky-Stillinger algorithm with 8 spheres with the growth rate $g = 1$ (purple) and 10 spheres with the growth rate $g = 1.5$ (yellow) within a unit cube at different times (a)-(c) and the final state (d).

It states that the distance of the two centers of mass at t_{n+1} equals the sum of the current radii of these two spheres. By building the square on both sides, one obtains the form

$$\begin{aligned}&\underbrace{\left[|(\mathbf{v}_{i,n}-\mathbf{v}_{j,n})|-(g_i+g_j)\right]}_{=a}\Delta t_{ij}^2\\ &+2\,\underbrace{\left[(\mathbf{x}_{i,n}-\mathbf{x}_{j,n})\cdot(\mathbf{v}_{i,n}-\mathbf{v}_{j,n}-(r_{i,n}+r_{j,n})\cdot(g_i+g_j)\right]}_{=b}\Delta t_{ij}\\ &+\underbrace{\left[|\mathbf{x}_{i,n}-\mathbf{x}_{j,n}|^2+(r_{i,n}+r_{j,n})^2\right]}_{=c}=0\end{aligned} \tag{6.35}$$

which is solved by

$$\Delta t_{ij} = \frac{-b \pm \sqrt{b^2 - 4\,a\,c}}{2\,a}. \tag{6.36}$$

To possibilities for Δt_{ij} occur if the two spheres hit each other twice, one solution if the two spheres hit each other once and no solution if they never collide. The collision with the smallest positive Δt_{ij} occurring first is assumed to be effective and the velocities $\mathbf{v}_{i,n+1}$ and $\mathbf{v}_{j,n+1}$ of the participating spheres is changed assuming fully elastic impacts. Based on this assumption, the velocities after the impacts $\boldsymbol{v}_i^\star$ and $\boldsymbol{v}_j^\star$ of the particles i and j are derived by

$$\begin{aligned}\boldsymbol{v}_i^\star &= \boldsymbol{v}_j^{\mathrm{p}} + \boldsymbol{v}_i^{\mathrm{t}}\\ \boldsymbol{v}_j^\star &= \boldsymbol{v}_i^{\mathrm{p}} + \boldsymbol{v}_j^{\mathrm{t}}\end{aligned} \tag{6.37}$$

considering the split of the velocities

$$\begin{aligned}\boldsymbol{v}_i &= \boldsymbol{v}_i^{\mathrm{p}} + \boldsymbol{v}_i^{\mathrm{t}}\\ \boldsymbol{v}_j &= \boldsymbol{v}_j^{\mathrm{p}} + \boldsymbol{v}_j^{\mathrm{t}}\end{aligned} \tag{6.38}$$

directly before the collision into a part $\boldsymbol{v}_i^{\mathrm{p}}$ parallel to the connection line between both center of masses and into a part $\boldsymbol{v}_i^{\mathrm{t}}$ tangential to it see figure 6.11. After that, the next event is evaluated until the time between two events Δt falls below a certain limit Δt_{lim} so that it is assumed that the positions of the spheres towards each other will not change anymore because they occur in a state in which they touch each other continuously. Assuming this termination criterion, some particles may become so-called rattlers if different growth rates are assumed. Their size is small compared to other particles which leads to a free movement of these particles in the final state. Hence, their are arbitrarily positioned when the simulation stops. Because the initial positions and velocities of the particles are chosen randomly, the final positions vary statistically every time, the algorithm is executed. The final positions $\mathbf{x}_{i,\mathrm{end}}$ and the final radii $r_{i,\mathrm{end}}$ are used as the basis for the next step in the artificial microstructure generation process.

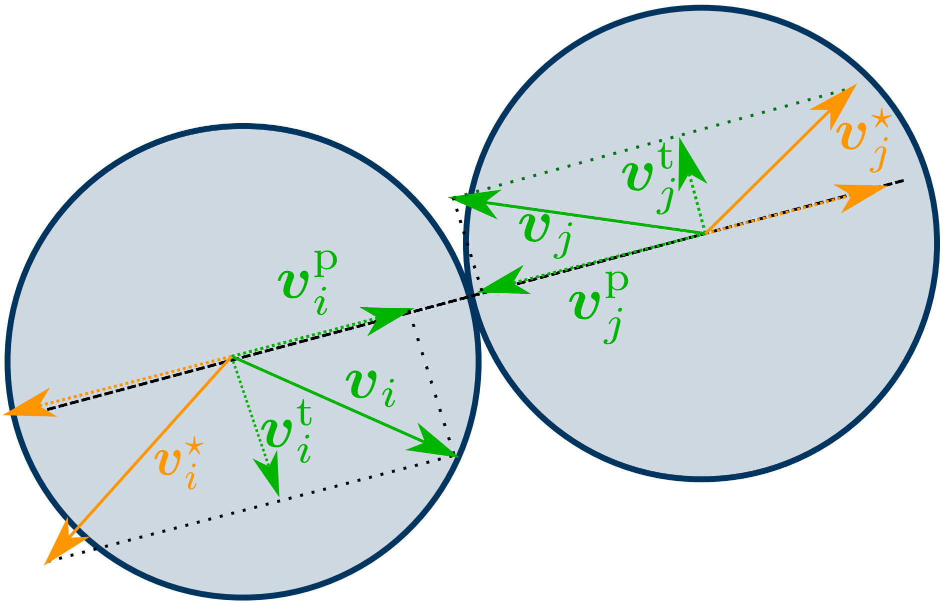
$\boldsymbol{v}_i^{\mathrm{p}}$
$\boldsymbol{v}_i$
$\boldsymbol{v}_i^{\mathrm{t}}$
$\boldsymbol{v}_i^{\star}$
$\boldsymbol{v}_j^{\mathrm{t}}$
$\boldsymbol{v}_j^{\star}$
$\boldsymbol{v}_j$
$\boldsymbol{v}_j^{\mathrm{p}}$

Figure 6.11.: Two colliding spheres and their velocities directly before the collision (green) and directly after the collision (orange).

Voronoi tessellation In the next step, the surfaces of the mineral aggregates are generated by applying the weighted Voronoi tessellation Rycroft [119], cf. figure 6.12a with the routine voro++. This technique is commonly used to generate crystalline structures as for example shown in Fritzen and Böhlke [41], Fritzen et al. [42] as well as random concrete microstructures, as shown in Ghossein and Lévesque [45], Wriggers and Moftah [155]. Note, that the Voronoi tessellation based on random starting points does not provide a possibility to control the later grain sizes. Hence, the previous step is necessary to adjust the later grain sizes as proposed in Lavergne et al. [72]. The Voronoi tessellation divides the periodic cube $\mathcal{V}_\square$ into S cells in the shape of convex polygons. Therefore, the condition

$$V_i = \left\{ \mathbf{y} \in \mathcal{V}_\square \;\middle|\; |\mathbf{y} - \mathbf{z}_i|^2 - w_i^2 \leq |\mathbf{y} - \mathbf{z}_j|^2 - w_j^2 \quad \forall \quad i \neq j \right\} \tag{6.39}$$

for each cell i with the weight w_i and w_j and the generation points $\mathbf{z}_i$ and $\mathbf{z}_j$ is evaluated. This condition states that all points $\mathbf{y}$ belong to the volume V_i if their Euclidian distance to the

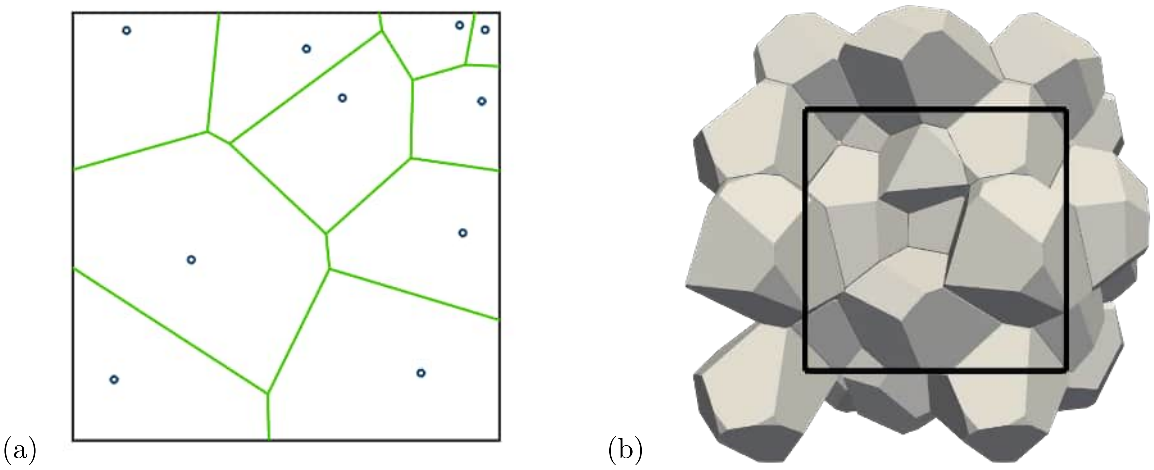
(a) (b)

Figure 6.12.: (a) Two-dimensional illustration of Voronoi tessellation with starting points (blue) and borders of their Voronoi cells (green) and (b) mineral aggregate cells generated by Voronoi tessellation which fully or partly intersect unit cube.

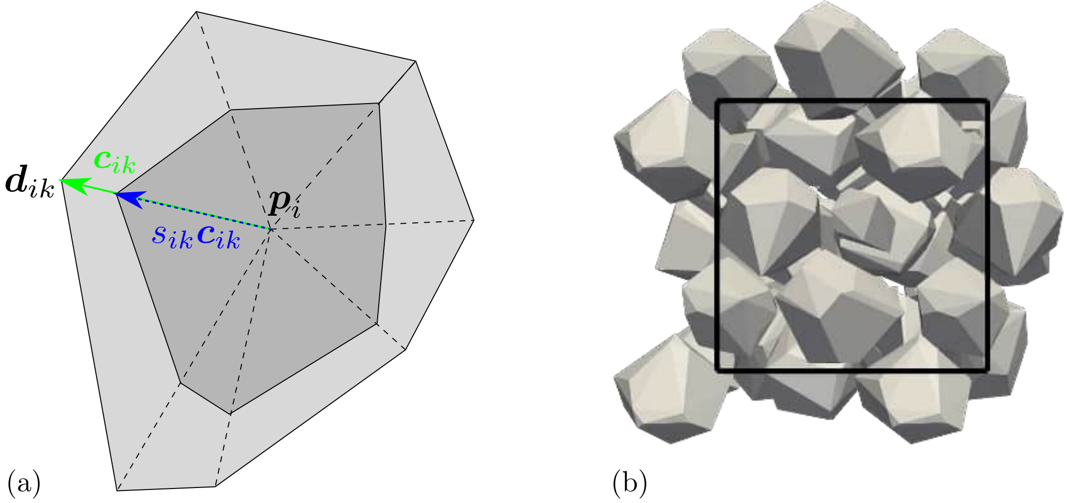

Figure 6.13.: (a) Statistical shrinking of the vector $\boldsymbol{c}_{ik}$ corner point k of cell i at the location $\boldsymbol{d}_{ik}$ towards the center of mass $\boldsymbol{p}_i$ with the shrinking factor s_{ik} and (b) cutout of cells lying in or on the border of unit cube in order to obtain periodic microstructure.

generation point $\mathbf{z}_i$ subtracted by the square of their weight w_i^2 is the lower than the one of all other volumes V_j. To apply this algorithm for the asphalt SVEs, the weights $w_i = r_{i,\text{end}}$ and $w_j = r_{j,\text{end}}$ are chosen as the final radii and the generation points $\mathbf{z}_i = \mathbf{x}_{i,\text{end}}$ and $\mathbf{z}_j = \mathbf{x}_{j,\text{end}}$ of the Lubachevsky-Stillinger algorithm of the previous step. Here, the periodicity is obtained by multiplying the initial unit cube with its generation points and weights 3 times in each spatial direction so that a cube of the size $3 \times 3 \times 3$ results, cf. figure 6.12b. The Voronoi tessellation is applied on this enlarged cube so that the geometry of the cells of middle unit cube becomes periodic. Afterwards, all cells with its center of mass outside the middle unit cube are deleted. As output of this algorithm, the corner points of the remaining cell are obtained. Since the Voronoi tessellation algorithm is deterministic and does not underly statistical variance, the statistical variance of the cell geometries in this state are only influenced by the statistical variance of the Lubachevsky-Stillinger algorithm.

Statistical shrinking By application of the Voronoi tessellation, S convex cells are generated, that fill the complete volume of the middle unit cube, as seen in figure 6.9b, so that the mineral aggregate volume fraction n_{ma} of the asphalt concrete would be 1 which wouldn't be reasonable. Hence, the cells are shrunk statistically by applying a statistical shrinking factor s_k on the vectors $\mathbf{c}_{ik} = \mathbf{d}_{ik} - \mathbf{p}_i$ from the corner points $\mathbf{d}_k$ of the cells to its center of mass $\mathbf{p}_i$, cf. 6.13a. The shrinking factor is calculated by

$$s_{ik} = \gamma_{ik}(u - v) + v, \tag{6.40}$$

where $0 \leq \gamma_{ik} \leq 1$ is a uniformly distributed random number for each corner point k of cell i. Here, $0 < u < 1$ and $0 < v \leq u$ are the upper and the lower limit of the shrinking factor. Those have to be chosen as input parameters for the construction of the SVEs. Note, that the statistical variance of the particle shapes depends on the difference in these two parameters and that their quantity highly influences the overall volume fraction of the mineral aggregates n_{ma}. The volumes of the mineral aggregate particles are generated by building a convex hull around the shrunk vertices of the Voronoi cells. Hereby, some cells are generated in a way that they are not completely allocated in the periodic cube $\mathcal{V}_\square$. To ensure that our final geometry of the SVE is periodic, we arrange this set of particles 27 times into a $3 \times 3 \times 3$-sized cube $\mathcal{V}_{27}$. Afterwards, this structure is intersected with a unit cube in the center of it so that periodic mineral aggregate phase $\mathcal{V}_{\text{ma}} = \mathcal{V}_{27} \cap \mathcal{V}_\square$ is obtained, cf. 6.13b. Furthermore, the volume of the bituminous binding agent phase is derived by $\mathcal{V}_\text{b} = \mathcal{V}_\square \setminus \mathcal{V}_\text{ma}$ in order to obtain the complete 3-dimensional microstructure. In order to obtain the correct size of the SVE, the unit cube is scaled in a such way, that the largest particle's equivalent diameter $\max(d_{i,\text{eq}})$ equals the largest sieve size $d_\text{max sieve}$ of the sieve curve. Therefore, the unit cube's edge length is multiplied by the factor $d_\text{max sieve} / \max(d_{i,\text{eq}})$. With this algorithm, the structure on the mesoscale of the asphalt concrete can be constructed with the real sieve curve.

Modifications and extensions to other materials The given algorithm enables the structure generation of other morphologies than the one of the biphasic asphalt concrete. For example, first ideas for the generation of the triphasic asphalt concrete morphology have been tested. In one version, a temperature field is solved on the FE mesh of the biphasic asphalt concrete. Here, the mineral aggregates are assumed to inherit initially a high temperature and the binding agent a low temperature so that a heterogeneous temperature field develops over the SVE. Afterwards, the binding agents below a threshold temperature are deleted which represent the voids, as shown in figure 6.14. Similarities between the microstructures and a μCT-scan of the asphalt concrete are observable. However, statistical measures to describe the void phase or the binging agent phase still have to be examined. Additionally, the new parameters for adjusting the temperature field and the threshold temperature have to be adjusted according to these statistical measures. Because these measures are derived on the basis of μCT-scans, the generation of triphasic asphalt concrete specimen becomes computationally expensive.

Furthermore, the presented algorithm is capable of the construction of artificial metallic microstructures that consist of grains, cf. figure 6.15a. Additionally, interface layers can be added be applying the statistical shrinking step setting both shrinking parameters u and v to the same value which is chosen close to 1, cf. figure 6.15b. If no interface between the grains are assumed, the shrinking of the cells is not executed so that the cells fill the whole unit cube. By distorting the microstructure in figure 6.15b into a certain direction, also rolled metal microstructures can be artificially generated, cf. figure 6.15c.

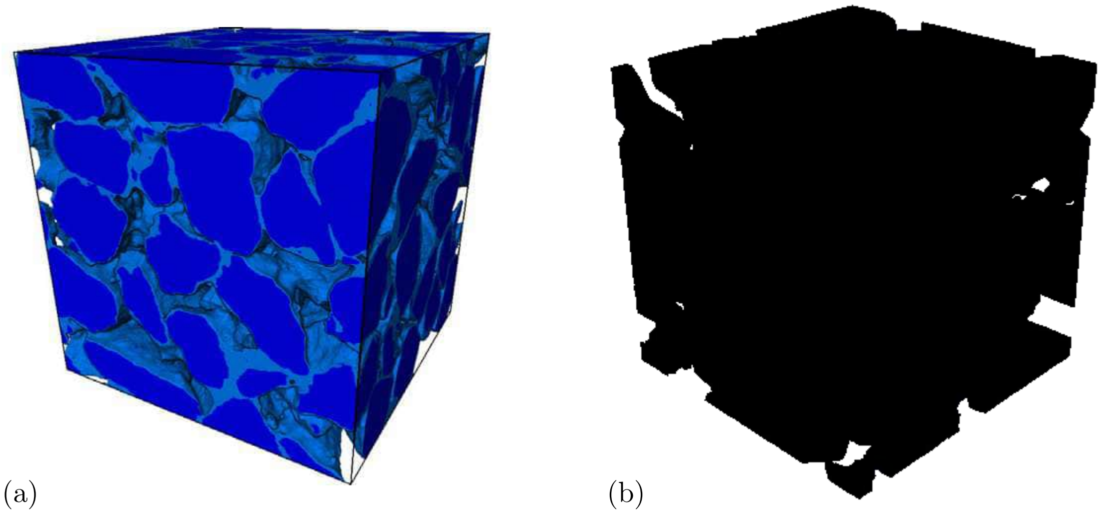

Figure 6.14.: (a) Binarized μCT-scan of triphasic asphalt concrete taken from Schüler et al. [130] which contains mineral aggregates (dark blue) surrounded by bituminous binging agent (bright blue) and voids and (b) artificially generated SVE with mineral aggregates (gray) surrounded by bituminous binging agent (rainbow colors) and voids.

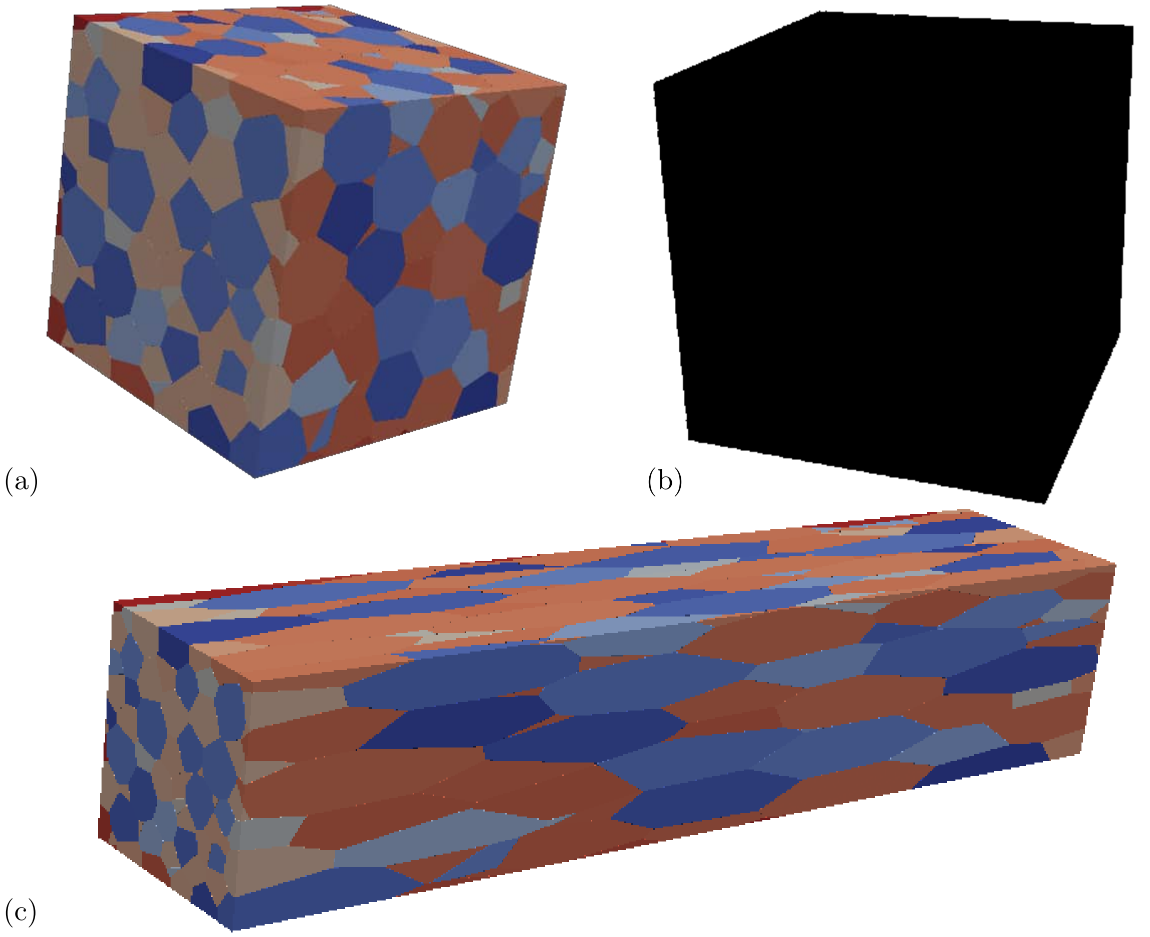

Figure 6.15.: (a) Metallic SVE containing grains, (b) containing an interface layer in-between and (c) distorted SVE representing rolled metal.

6.2.3. Numerical examples of SVEs

In this subsection, a numerical example of an ensemble of ten SVEs that represents the asphalt concrete PA8 is investigated. Due to the stochastic influences of the Lubachevsky-Stillinger algorithm and the shrinking process in the work flow of the structure generation, different geometries occur even though the same input parameters are considered, cf. figure 6.16. The allocations of the mineral aggregates differ strongly from structure to structure because of the different dense sphere packings of the Lubachevsky-Stillinger algorithm caused by the random initial positions and velocities. The shape of the mineral aggregates is strongly influenced by the choice of the upper and lower limit v and u of the statistical shrinking factor s_k. If these two are set to equal values, the mineral aggregates keep the form of the generated Voronoi cells because in this case, the shrinking is self-similar. With increasing difference between u and v, the shape of the mineral aggregates becomes more arbitrarily distorted from the shape of the Voronoi cells. Because of the arbitrary shape of the mineral aggregates within the asphalt concrete, these two parameters are set with a difference of at least 0.1 to a large difference between those. To obtain SVEs that fulfill certain statistical measures, these input parameters have to be set accordingly. These are found empirically by generating structures and comparing the resulting statistical measures of the SVEs. This process is repeated until the SVEs fulfill the statistical measures. Because of the statistical variance of the morphology, that occurs despite choosing the same set of input parameters, an ensemble of SVEs is generated for one parameter set. Nevertheless, the automatization of the structure generation enables the generation of many SVEs in a short time. Here, the desired abstracted geometrical properties are achieved with the parameters presented in table 6.1. The desired

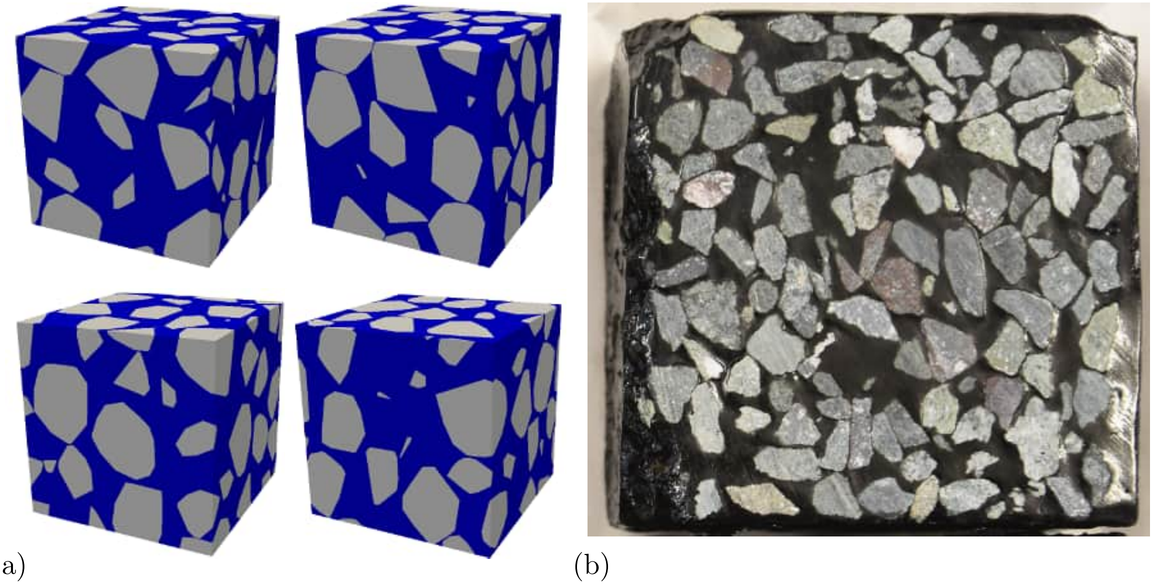
(a) (b)

Figure 6.16.: (a) Four different SVEs generated with the same parameters that represent the (b) mesoscale of the asphalt concrete PA8.

particle size distribution and volume fractions are achieved within a certain variance, as seen in the sieve curve in figure 6.17a for an ensemble of ten different structures. Hereby, we neglect mineral aggregates of the physical asphalt concrete below the sieve size of 5.6 mm to keep the SVEs simple. Another reason for that is that their influence on the whole structure is assumed to be small due to their low total volume compared to the volume of the generated particles. Furthermore, the total volume fraction of the bituminous binding agent n_b varies within a maximum deviation of 0.0085 around the mean value of 0.5015, as seen in figure 6.17b. This mean value is close to the desired volume fraction $n_b = 0.5$. Hence, the choice of parameters for PA8 is justified. For further studies of the statistical properties of the morphologies, other geometrical properties of the mineral aggregates, that are not regarded in the production of the asphalt concrete, are investigated. Thereby, the cells, that are generated in the statistical shrinking step, are considered in order to avoid inaccuracies due to cells that are split into multiple cells if they lie outside the unit cube. As an indicator for the magnitude of the distortion of the mineral aggregates, we focus on the maximum distance of the corner points within each particle d_{max} with respect to its equivalent diameter d_{eq}, that a sphere of the same volume has. The resulting distribution of all particles of the ensemble of the 10 SVEs is shown in figure 6.18a. The values lie within 1.72 and 1.84 for over 90% of the mineral aggregates while some particles only inherit values of around 1.45 which makes the structures look natural. The same can be seen in the particle surface distribution in figure 6.18b. It shows that the mineral aggregate surfaces vary between $273\,\text{mm}^2$ and $2097\,\text{mm}^2$, so by a factor of 7.7, although a monodisperse sieve curve is achieved. Due to the statistical variance in the geometry, the overall material behavior of the SVEs varies within a certain variance as well. Hence, an ensemble of SVEs have to be investigated to obtain the macroscopic material response.

Lubachevsky-Stillinger algorithm	Growth rate g_1	Growth rate g_2	Sphere number S_1	Sphere number S_2
	1	0.8	17	13
Statistical shrinking	Lower limit for shrinking factor v		Upper limit for shrinking factor u	
	0.45		0.99	

Table 6.1.: Parameters for the generation of an ensemble of artificial SVEs representing the asphalt concrete PA8.

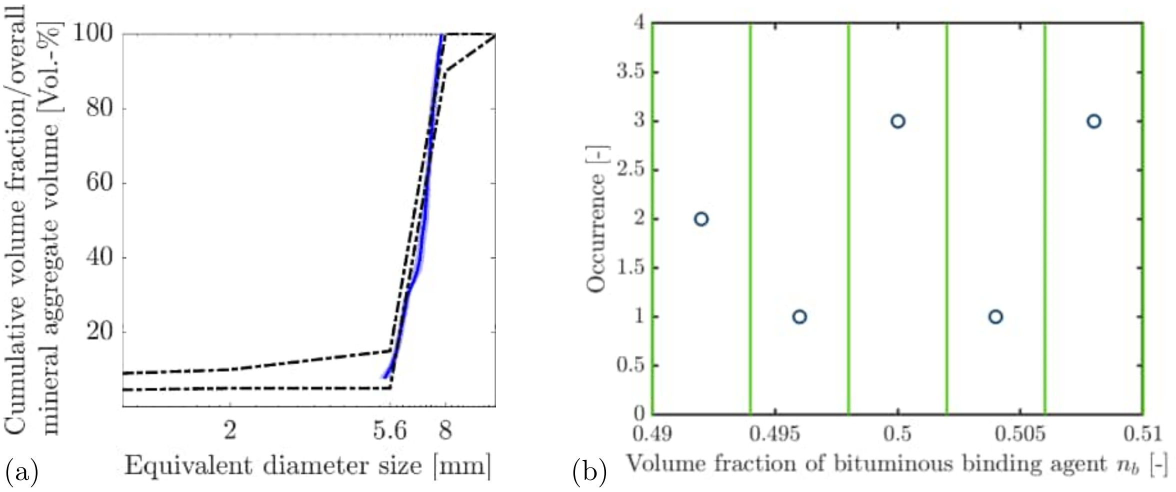

Figure 6.17.: (a) Average sieve curve (dark blue) and its standard deviation (bright blue) of an ensemble consisting of 10 microstructures with prescribed borders (black) and (b) distribution of the volume fraction of the bituminous binding agent n_b of the 10 SVEs.

6.2.4. Generalized Maxwell model

Because numerical examples of numerical simulations of asphalt concrete are carried out under the assumption of the momentum balance, the viscoelastic material model for the bituminous binding agent is presented. Here, the generalized Maxwell model, cf. Wiechert [146] is applied. In figure 6.19, a schematic illustration of this constitutive law is given. One linear spring, that represents the purely elastic part of the material model, is connected parallelly to multiple Maxwell chains, that consist of a linear spring and a dash pot in series. The compression modulus K_0 and shear modulus G_0 are the parameters of the purely elastic part whereas the viscous part consists of properties of multiple so-called “Maxwell chains”. Here, M Maxwell chains are assumed that contain the shear modulus G_m and viscous strain $\boldsymbol{\varepsilon}^{\mathrm{v}}_m$ for each Maxwell chain m. If no Maxwell chain is assumed, this material coincides with the linear elastic Hooke’s law. The free Helmholtz energy density

$$\psi = \frac{1}{2}\left[3\,K_0\,(\boldsymbol{\varepsilon}_{\mathrm{s}}^{\mathrm{vol}})^2 + 2\,G_0(\boldsymbol{\varepsilon}_{\mathrm{s}}^{\mathrm{dev}})^2 + \sum_{m=1}^{M} 2\,G_m(\boldsymbol{\varepsilon}_{\mathrm{s}}^{\mathrm{dev}} - \boldsymbol{\varepsilon}^{\mathrm{v}}_{m})^2\right] \tag{6.41}$$

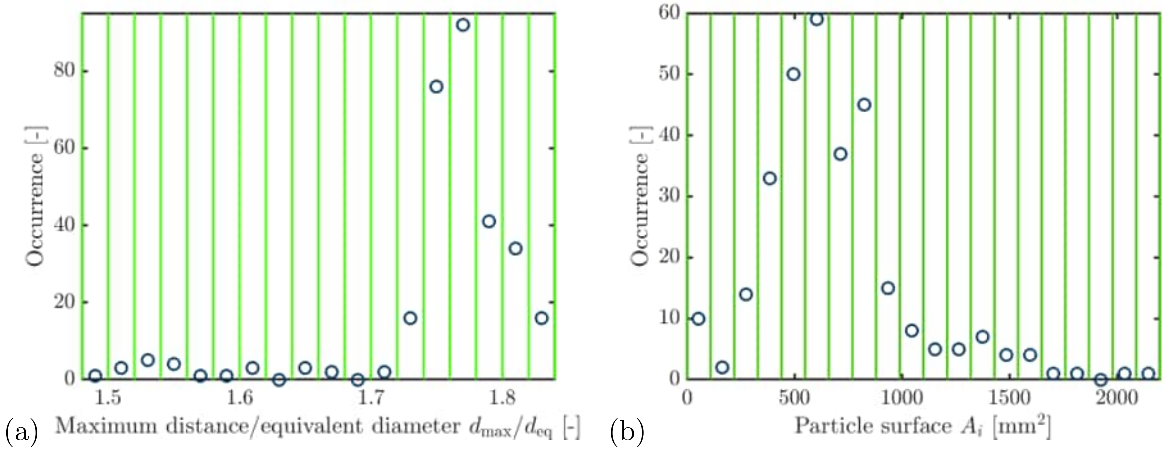

Figure 6.18.: (a) Ratio of maximum distance of corner points within one particle $d_{\max}$ to the equivalent diameter d_{eq} and (b) distribution of the particle surfaces in the ensemble of the 10 artificial asphalt concrete structures.

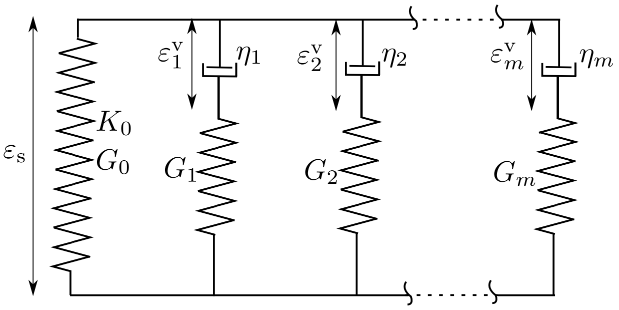
ε_s
K_0
G_0
ε_1^v
η_1
G_1
ε_2^v
η_2
G_2
ε_m^v
η_m
G_m

Figure 6.19.: Schematic illustration of the Maxwell-Zener model in which the viscous parts are represented as dash pots and the elastic parts as springs.

with the linearized strain tensor $\varepsilon_\mathrm{s} = 1/2\left(\mathrm{Grad}(\boldsymbol{u}) + \mathrm{Grad}^\mathrm{T}(\boldsymbol{u})\right)$ for small strains describes the behavior of this material law. The strain is split into a volumetric part $\boldsymbol{\varepsilon}_\mathrm{s}^\mathrm{vol} = 1/3\,\mathrm{tr}(\boldsymbol{\varepsilon}_\mathrm{s})\,\boldsymbol{I}$ and a deviatoric part $\boldsymbol{\varepsilon}_\mathrm{s}^\mathrm{dev} = \boldsymbol{\varepsilon}_\mathrm{s} - \boldsymbol{\varepsilon}_\mathrm{s}^\mathrm{vol}$. The viscous strain $\boldsymbol{\varepsilon}_m^\mathrm{v}$ evolves with

$$\dot{\boldsymbol{\varepsilon}}_m^\mathrm{v} = \frac{2}{\tau_m}(\boldsymbol{\varepsilon}_\mathrm{s}^\mathrm{dev} - \boldsymbol{\varepsilon}_m^\mathrm{v}) \tag{6.42}$$

with the relaxation time $\tau_m = \eta_m / G_m$ which depends on the viscosity η_m. The viscous strains in every time step are implicitly derived based on the discretized form $\boldsymbol{\varepsilon}_{m,n+1}^\mathrm{v} = \boldsymbol{\varepsilon}_{m,n}^\mathrm{v} + \Delta t\,\dot{\boldsymbol{\varepsilon}}_{m,n+1}^\mathrm{v}$. From this, the update of the viscous strains

$$\boldsymbol{\varepsilon}_{m,n+1}^\mathrm{v} = \frac{1}{\tau_m + 2\,\Delta t}\,\left(\tau_m\,\boldsymbol{\varepsilon}_{m,n}^\mathrm{v} + 2\,\Delta t\,\boldsymbol{\varepsilon}_{\mathrm{s},n+1}^\mathrm{dev}\right) \tag{6.43}$$

follows. The Clausius-Duhem inequality

$$\begin{aligned}
\mathcal{D} = \boldsymbol{\sigma} : \dot{\boldsymbol{\varepsilon}}_\mathrm{s} - \dot{\psi} &= \boldsymbol{\sigma} : \dot{\boldsymbol{\varepsilon}}_\mathrm{s} - \frac{\partial \psi}{\partial \boldsymbol{\varepsilon}_\mathrm{s}} : \dot{\boldsymbol{\varepsilon}}_\mathrm{s} - \sum_{m=1}^{M} \frac{\partial \psi}{\partial \boldsymbol{\varepsilon}_v^\mathrm{v}} : \dot{\boldsymbol{\varepsilon}}_m^\mathrm{v} \\
&= \underbrace{\left(\boldsymbol{\sigma} - \frac{\partial \psi}{\partial \boldsymbol{\varepsilon}_\mathrm{s}}\right)}_{=\boldsymbol{0}} : \dot{\boldsymbol{\varepsilon}}_\mathrm{s} + \sum_{m=1}^{M} 2\,G_m\left(\boldsymbol{\varepsilon}_\mathrm{s}^\mathrm{dev} - \boldsymbol{\varepsilon}_m^\mathrm{v}\right) : \dot{\boldsymbol{\varepsilon}}_m^\mathrm{v} \\
&= \sum_{m=1}^{M} \eta_m\,\dot{\boldsymbol{\varepsilon}}_m^\mathrm{v} : \dot{\boldsymbol{\varepsilon}}_m^\mathrm{v} > 0
\end{aligned} \tag{6.44}$$

demonstrates the thermodynamical consistency under the assumption of $\eta_m > 0$. Additionally, the stress tensor $\boldsymbol{\sigma}_\mathrm{s}$ for small strains is derived by the derivative

$$\boldsymbol{\sigma}_\mathrm{s} = \frac{\partial \sigma}{\partial \boldsymbol{\varepsilon}_\mathrm{s}} = 3\,K_0\,\boldsymbol{\varepsilon}_\mathrm{s}^\mathrm{vol} + 2\,G_0 \boldsymbol{\varepsilon}_\mathrm{s}^\mathrm{dev} + \sum_{m=1}^{\mathrm{v}} 2\,G_m(\boldsymbol{\varepsilon}_\mathrm{s}^\mathrm{dev} - \boldsymbol{\varepsilon}_m^\mathrm{v}) \tag{6.45}$$

that is obtained from the Clausius-Duhem inequality. Additionally, the material tangent for small strains

$$\begin{aligned}
\mathbb{C} = \frac{\mathrm{d}\boldsymbol{\sigma}_{n+1}}{\mathrm{d}\boldsymbol{\varepsilon}_{\mathrm{s},n+1}} &= \frac{\partial \boldsymbol{\sigma}_{\mathrm{s},n+1}}{\partial \boldsymbol{\varepsilon}_{\mathrm{s},n+1}} + \sum_{m=1}^{M} \frac{\partial \boldsymbol{\sigma}_{\mathrm{s},n+1}}{\partial \boldsymbol{\varepsilon}_{m,n+1}^\mathrm{v}} : \frac{\partial \boldsymbol{\varepsilon}_{m,n+1}^\mathrm{v}}{\partial \boldsymbol{\varepsilon}_{\mathrm{s},n+1}} \\
&= K_0\,\boldsymbol{I} \otimes \boldsymbol{I} + 2\,G_0\left(\mathbb{I} - \tfrac{1}{3}\,\boldsymbol{I} \otimes \boldsymbol{I}\right) + \sum_{m=1}^{M} 2\,G_m\left(1 - \frac{2\,\Delta t}{\tau_m + 2\Delta t}\right)\left(\mathbb{I} - \tfrac{1}{3}\,\boldsymbol{I} \otimes \boldsymbol{I}\right)
\end{aligned} \tag{6.46}$$

results by derivation for the stress $\boldsymbol{\sigma}_\mathrm{s}$.

6.2.5. Mechanical test on SVEs

In order to investigate the statistical variance in the macroscopic material response, a quasi-static stress relaxation test is applied on the previously investigated ensemble consisting of 10 SVEs. Therefore, a simple shear deformation $\bar{\varepsilon}_{12}$ is prescribed, as shown in figure 6.20a. At first the deformation is ramped up linearly over the time t in the double logarithmic space until a strain of $\bar{\varepsilon}_{12} = 0.01/\sqrt{2}$ is reached. Afterwards, it is held at a constant value. Here, the shear test instead of a tension test is chosen because viscosity only occurs in the deviatoric part of the strains which is triggered by shear. Periodic boundary conditions are applied by imposing the additional constraint

$$\boldsymbol{u}(\boldsymbol{X}^+) = \boldsymbol{u}(\boldsymbol{X}^-) + \bar{\boldsymbol{F}} \cdot \boldsymbol{X} \tag{6.47}$$

which states that the displacements $\boldsymbol{u}(\boldsymbol{X}^+)$ at the location $\boldsymbol{X}^+$ on the boundary of the cube $\partial\mathcal{B}^+$ on one side equals the displacement $\boldsymbol{u}(\boldsymbol{X}^-)$ location $\boldsymbol{X}^-$ on the opposite $\partial\mathcal{B}^-$ side of the cube. Additionally, the macroscopic deformation gradient $\bar{\boldsymbol{F}}$ that prescribes the macroscopic deformation is imposed in this equation. Here, it takes the form

$$\bar{\boldsymbol{F}} = \begin{pmatrix} 1 & \bar{\varepsilon}_{12} & 0 \\ \bar{\varepsilon}_{12} & 1 & 0 \\ 0 & 0 & 1 \end{pmatrix} . \tag{6.48}$$

To impose those boundary conditions in FE applications, the surface mesh, in particular, the nodes on the opposite sides of the cubic specimen have to match. For the nodal displacements at these sides, additional constraint equations are applied. Technically, those are handled the same way as the constraint equations of the hanging nodes. Here, the FE software Abaqus is used and the 10-node tetrahedral elements “C3D10” with quadratic shape functions are chosen. The material parameters in figure 6.21 are determined from the results of dynamic shear rheometer (DSR) tests with our bituminous binding agent. Therefore, the mastercurve concept, as seen in Dickinson and Witt [27], is applied on the experimental data. The compression modulus K^0 cannot be obtained from DSR tests but set to a large value compared to the shear modulus G^0 because the bituminous binding agent is assumed to be incompressible. The mineral aggregates are considered as linear elastic. In figure 6.20b the resulting macroscopic stress $\bar{\sigma}_{12}$ is presented. The results show that the shear stress $\bar{\sigma}_{12}$ of the 10 SVEs varies within a tiny variance but the overall shape of the stress curves behave similarly. This indicates that the specific forms of the particles barely influence the overall macroscopic material response as long as the sieve curve and volume fractions remain almost constant. However, multiple SVEs have to be taken into account for the description of the macroscopic

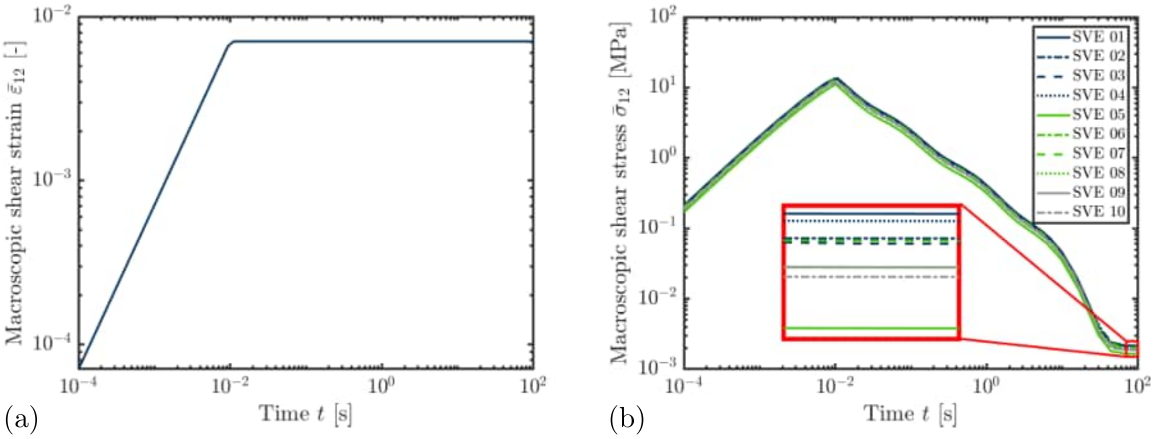

Figure 6.20.: (a) Prescribed macroscopic strain $\bar{\varepsilon}_{12}$ over the time t and (b) resulting macroscopic shear stress $\bar{\sigma}_{12}$ of an ensemble of 10 SVEs over the time t.

Maxwell chain m	0	1	2	3	4	Mineral aggregates
Compression modulus K_m [MPa]	17321					56032
Shear modulus G_m [MPa]	0.0282	2.822	17.98	77.76	222.9	32019
Relaxation time τ_m [s]	—	6.341	0.6341	0.06341	0.006341	

Figure 6.21.: Mechanical properties of the asphalt concrete PA8 under the assumption of small strain Maxwell viscoelasticity with 4 Maxwell chains for the bituminous binding agent and small strain elasticity for the mineral aggregates.

material behavior because of the small variances in the material response. When the strain $\bar{\varepsilon}_{12}$ is ramped up, the shear stress $\bar{\sigma}_{12}$ grows as well. Afterwards, the shear stress decreases due to relaxation of the viscous part of the Maxwell chains until it converges to a lower limit. In this final state only the purely elastic part of the generalized Maxell model remains active. The waves in the part of the macroscopic stress $\bar{\sigma}_{12}$, in which the strain is held constant, occur due to the different relaxation times τ^m of the Maxwell chains. Figure 6.22a demonstrates the deformation of one SVE in the fully relaxed state at $t = 100\,\mathrm{s}$. Here, the inclusions do not deform largely but rather move and turn because of their high stiffness compared to the soft binding agent. In the binding agent, most of the deformation takes place. In figure 6.22b, it is demonstrated that the von Mises stress τ^{vM} is low in the bituminous binding agent in the relaxed state at $t = 100\,\mathrm{s}$ compared to the von Mises stress τ^{vM} of the mineral aggregates. This results from the higher stiffness of the mineral aggregates compared to the binging agent.

6.3. Comparison of SSRVE for MMCs with SVEs for asphalt concrete

Two different types of the computational generation of artificial RVEs have been presented, namely the concept of SSRVEs for MMCs and SVEs for asphalt concrete. The main advantage of the SSRVEs over the SVEs is that it solely from the concept of the algorithm finds the best representation of the physical microstructure regarding chosen morphological and mechanical properties simultaneously. In contrast to that, the SVEs are only obtained on the basis of morphological properties. Therefore, the SSRVEs may construct more reasonable microstructures in general. However, it is assumed that a reasonable morphology leads to a proper representation of the mechanical properties as well. Therefore, the SVEs as an ensem-

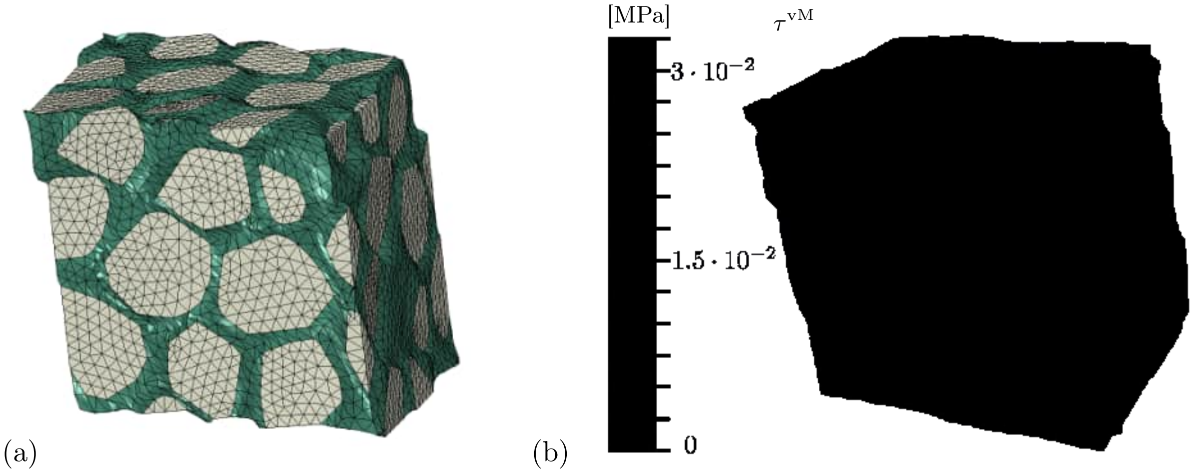

Figure 6.22.: (a) SVE consisting of mineral aggregate (gray) and bituminous binding agent (green) deformed with a scaling factor of 100 at $t = 100\,\mathrm{s}$ of the relaxation test and (b) the von Mises τ^{vM} of another SVE in the almost relaxed state at $t = 100\,\mathrm{s}$.

ble may also supply a proper representation in the mechanical properties. Nevertheless, the morphological similarity of the artificial microstructures to the target microstructures may be more accurate in the concept of SSRVEs because more accurate statistical measures are chosen. For the construction of the SSRVEs, an image of the structure morphology, e.g., in the form of a μCT-scan is mandatory. These images require costly laboratory equipment and experienced personnel. The concept of SVEs as presented here enables the generation without the evaluation of an image of the microstructure, because their inclusions are generated on the basis of characteristic morphological properties that are used for manufacturing the asphalt concrete on construction sites. Therefore, they are easier applicable on engineering problems. As a drawback of the SVEs, adjusting the parameters for the generation requires experience and multiple attempts for obtaining certain morphological properties, for example in the form of the sieve curves, because here, the optimization is executed “by hand”. Nevertheless, the computational costs stay low compared to the generation of SSRVEs due to the lower number of constructed microstructures. However, for the calculation of macroscopic mechanical material response based on the microstructures, an ensemble of SVEs has to be simulated in order to obtain average values and their variance, which increases the computational costs in the FE simulations. Furthermore, the FE simulations of the SVEs for the asphalt concrete become larger because more inclusions have to be taken into account to obtain a reasonable sieve curve. Summing up, the choice of the two presented generation procedures depends on the available structural data, desired morphological accuracy, the shape of the inclusions and the other points mentioned above.

7. Calibrated simulations of crack propagation on microstructures

In this chapter, various calculations of cracks through microstructures are presented. At first, it is demonstrated how the numerical parameters for the eigenerosion are identified by comparison with macroscopic experimental tensile tests. Afterwards, the parameters are validated by consideration of a three-point bending test in comparison to experimental results. Therefore, the stress tensor at a chosen Gauß points is extracted from a macroscopic experiment and applied as boundary conditions on the microscale with cyclic loads so that the crack lengths over time are compared. Based on these calibrated and validated parameters, the crack propagation through the Ferro-Titanit and through its SSRVEs is calculated. In the last investigation, we perform simulations of the crack propagation through a microstructure with varied morphology are simulated. The results are compared to experimental data and the resistance against crack propagation is examined. All data from laboratory experiments are obtained from the group of Arne Röttger and Lukas Brackmann.

7.1. Parameter identification

Some material parameters like the Young's modulus E, the Poisson ratio μ or the yield stress y_0 of the inspected materials are available from literature. But for the identification all parameters, the data from literature are not sufficient for reproducing the plastic flow curve, e.g., in the stress-strain diagram, accurately in numerical simulations. Additionally, the Griffith-type energy release rate G_c necessary for the calculation of crack propagation does not coincide with the values obtained from the literature because this parameter serves as a numerical parameter which depends on the size of the structure and on the influence radius ϵ. Hence, the necessary material parameters have to be found by numerical simulations according to laboratory experiments. Here, tensile tests are executed to fit material parameters by comparing the resulting structural response. Figures 7.1a&b show the setup of the laboratory experiments compared to the simulation with the specimen and its boundary conditions in figure 7.2a. The cylindrical specimen with the length $l_0 = 20\,\text{mm}$ and the radius 2.5 mm is deformed with a prescribed axial strain $\bar{\varepsilon}_{xx} = 0.01\,t/\text{min}$ until it breaks into two parts. Here, the material parameters of the simulation are fitted by comparing the resulting stress-strain curve with the macroscopic strains derived by $\bar{\varepsilon}_{xx} = \bar{u}_{xx}/l_0$ and the macroscopic technical stress $\bar{P}_{xx} = \bar{f}_{xx}/(\pi\, r^2)$ with the axial reaction force $\bar{f}_{xx}$ at the upper and lower boundary. Because the fitted Griffith-type energy release rate G_c depends on the specimen size as demonstrated in subsection 4.1.3, this value has to be scaled to the microscopic level for simulations on the microscale. If the length of a structure is increased by a factor, the Griffith-type energy release rate G_c is increased by this factor as well. For brittle inclusions, the elastic parameters are obtained from experts, since they coincide with the ones of the simulations, whereas the Griffith-type energy release rate is fitted by simulating the tensile test as well. Here, the tensile strength $\bar{P}_{xx}^{\max} = 258\,\text{MPa}$ at which the specimen breaks is considered based on information expert material scientists. In figure 7.2, the resulting stress-strain curves using the fitted material parameters from table 7.1 are presented. Herein, the elasto-plastic as well

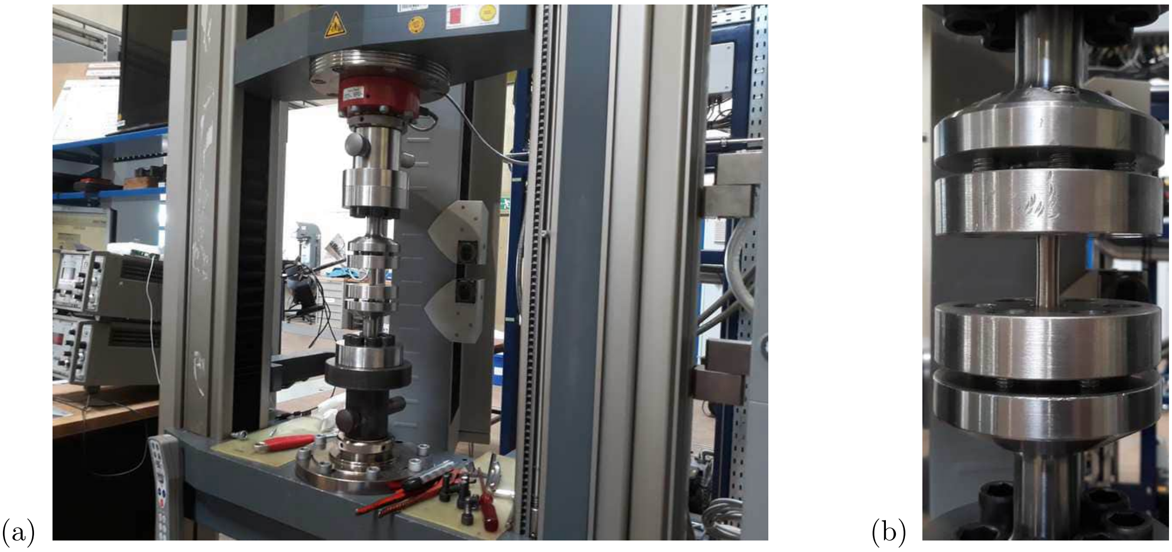

Figure 7.1.: (a) Experimental tensile test and (b) zoom into the holding device in which a cylindrical specimen is clamped.

as the elasto-viscoplastic versions of the material laws under the consideration of the tension-compression split are applied. Note, that multiple combinations of material parameters for the plastic regime are possible to obtain similar results in a tensile test with linearly increasing deformation. However, these parameters of the plastic flow curve influence the behavior under cyclic loads because the choice of the parameters influences the development of the plastic deformations. E.g., the initial yield stress y_0 determines at which stress plasticity is triggered. Under linearly increasing deformation, the other parameters can be adjusted in such a way, that the desired stress-strain curve is achieved under consideration of a fixed initial yield stress y_0. The lower initial yield stress is chosen, the lower are the necessary loads under which crack propagation under cyclic loads occurs because plastic deformations occur earlier.

7.2. Validation with three-point bending test

7.2.1. Macroscopic experiment

For the validation of the simulation setup including the material parameters, the three-point bending test as presented in figure 7.3a is investigated. The specimen with the width $l_x = 50$ mm, height $l_y = 10$ mm and thickness 5 mm is loaded with a cyclic load imposed by a horizontal cylinder in the middle of the upper side. The load takes the form

$$F = (0.6 + 0.4 \sin(2\pi\, f\, t))\, F_A \tag{7.1}$$

	K [GPa]	μ [GPa]	y_0 [GPa]	y_∞ [GPa]	h^{exp} [−]	h^{lin} [GPa]	$\eta\, [GPa\, s]$	G_c [N/mm]
Titanium carbide	235.42	191.53	10^{12}	10^{12}	0	0	0	0.0114
NiBSi matrix (ep)	167.56	77.33	0.92	1.21	1803.49	2.00	0	0.0268
Nikro-128 martensite matrix (ep)	161.09	74.35	1.08	1.29	1335	0.04	0	0.0268
Nikro-128 martensite matrix (evp)	167.56	77.33	1.30	1.50	300	5	1	0.0268

Table 7.1.: Material parameters of MMC Ferro-Titanit constituents fitted to tensile tests under the assumtion of the elasto-plastic formulation (ep) or the elasto-viscoplastic material formulation (evp).

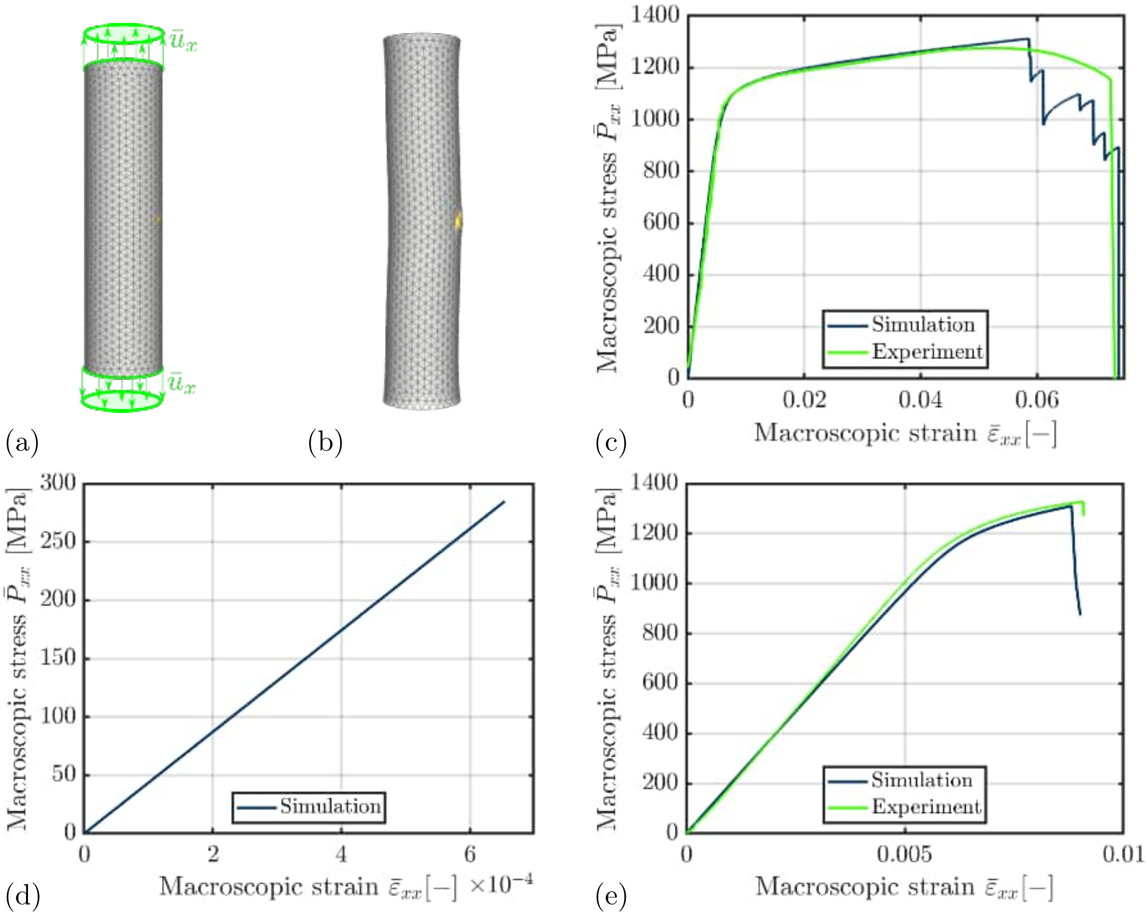

(a) (b) (c) (d) (e)

Figure 7.2.: (a) Cylindrical specimen, which is meshed with a tetrahedral mesh, for tensile test with boundary conditions and weakened area (yellow) and (b) the deformed state of the specimen at the strain $\bar{\varepsilon}_x = 0.01$ (deformation scaled with a factor of 20), taken from [17]. Exemplarily, the resulting stress-strain curves of (c) the ductile nickel matrix material of the Ferro-Titanit NiBSi, (e) the slightly ductile nickel matrix of the Ferro-Titanit Nikro-128 and (d) the brittle titanium carbide under the assumption of the elasto-plastic material formulation are presented.

with the maximum force F_A and the frequency $f = 10\,\text{Hz}$ which ensures that the specimen is always loaded with a minimum load of $0.2\,F_A$ so that contact between the specimen and the supports is given at any time. This load results in the technically important force ratio $R = \min(F)/\max(F) = 0.2$, cf., e.g., Bathias and Pineau [12]. Multiple experiments are carried out, each considering a different maximum force F_A. This ratio influences the crack propagation. Near the edges, the specimen is held loosely by cylindrical supports. On the bottom side in the middle at $l_x/2$, the specimen is sledged with a defined shape to enforce that crack propagation occurs in the middle. Prior to the experiment, the specimen is loaded until the crack becomes visible at the side of it because only crack propagation and not crack initiation is examined in this experiment. Especially for brittle MMC, this procedure is difficult in laboratory experiments as well as in simulations because low differences in the crack length may be enough for the crack to become unstable and propagate through the complete structure immediately. In the laboratory experiment, the crack length is measured on the microscopic level at the side with a microscope repeatedly after a certain amount of load cycles have passed. In the cross section of the specimen, the crack takes a parabolic form with its maximum in the middle and its lowest points on the outside at which the crack is tracked. This experiment is carried out under different force amplitudes F_A with specimens

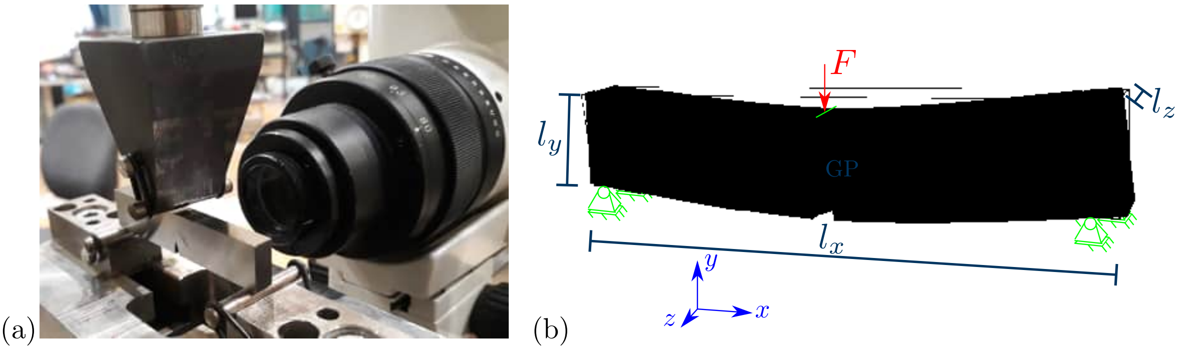

Figure 7.3.: (a) Experimental setup of the three-point bending test with microscope and (b) analogous macroscopic simulation of it for the extraction of the stress tensors as boundary conditions for microscopic simulations.

consisting of the investigated MMCs as well as on the homogeneous matrix material in order to validate the proposed simulation framework for crack propagation under cyclic loading with fitted material parameters.

7.2.2. Extraction of boundary conditions of the microscale simulations

For simulations on the microscale, the stress tensor has to be extracted from the macroscopic experiment to apply it as the Neumann boundary conditions on the microscopic scale. Therefore, the macroscopic three-point bending test is simulated considering 12, 126 tetrahedral elements with quadratic shape functions, cf. figure 7.3b. Here, the boundary conditions are chosen in line with the experimental boundary conditions. At the top in the middle of the beam, the nodal movements in vertical direction are linked to each other. Additionally, the vertical force is applied on one of these nodes in order to represent the top cylinder of the experiments. For the representation of the supports, displacement of the nodes are restricted at the supports' location. The initial crack is imposed according to the geometry of the physical specimen. In order to impose an initial crack, the specimen is loaded with an linearly increasing force until the first element on the outer side erodes. This ensures the initial conditions similar to the ones of the experiment. Note, that this initial crack is generated under the assumption of the ductile matrix material. Since the crack propagates through the whole structure of the brittle composite immediately, the initial crack of the matrix material is also considered for the MMC. After the initial crack is imposed, the maximum load F_A is applied. Using this state, the Cauchy stress $\boldsymbol{\sigma}_{\mathrm{GP}}$ is extracted from the highest Gauß point at the side of the element directly above the highest eroded element on the specimen's side cf. figure 7.3b. This Cauchy stress tensor $\boldsymbol{\sigma}_{\mathrm{GP}}$ is considered to be close to the one near the crack tip of the side of the physical specimen at the maximum load. In this macroscopic simulation, the material parameters of the metal matrix are assumed as the macroscopic material parameters for this simulation, whereas the estimated homogenized material parameters, namely the Young's modulus $E = 292$ GPa and the shear modulus $G = 117$ GPa, are assumed for the macroscopic material parameters based on estimation by experts from the field of material science. In simulations considering the largest maximum load $F_A = 1000$ N, the Cauchy stresses

$$\boldsymbol{\sigma}_{\mathrm{GP}}^{\mathrm{matrix}} = \begin{pmatrix} 989.85 & -45.97 & -14.42 \\ -45.97 & 85.81 & -39.60 \\ -14.42 & -39.60 & 19.26 \end{pmatrix} \text{ MPa} \tag{7.2}$$

of the homogeneous matrix material simulations and

$$\boldsymbol{\sigma}_{\mathrm{GP}}^{\mathrm{composite}} = \begin{pmatrix} 284.48 & 13.52 & 13.75 \\ 13.52 & 88.19 & -1.68 \\ 13.75 & -1.68 & 10.87 \end{pmatrix} \text{ MPa} \tag{7.3}$$

of the MMC simulations are extracted. Because only small deformations occur in these simulations and thus, the stress tensors remain even after transformation into other continuum mechanical configurations, these are directly applied as Neumann boundary conditions on the microscopic RVEs as technical stress. Thereby, the nodal forces are obtained by multiplying the stress with the corresponding surface in the reference configuration. The direct assumptions of these forces might cause problems in the boundary conditions at the microscale due to their complexity. Hence, their are decomposed into the principal stresses, so that only one traction vector at each side of the cubic RVE is applied. Therefore, the eigenvalues and eigenvectors are derived by the spectral decomposition. Here, the principal stresses $\hat{\boldsymbol{\sigma}}_{\mathrm{GP}}^{\mathrm{matrix}} = [992.34; 102.85; -0.26]^{\mathrm{T}}$ MPa for the matrix material and $\hat{\boldsymbol{\sigma}}_{\mathrm{GP}}^{\mathrm{MMC}} = [232.20; 67.05; -0.05]^{\mathrm{T}}$ MPa for the MMC are obtained. In the microscopic simulations, they are multiplied by the area l_{RVE}^2 resulting from the edge length l_{RVE} of the corresponding side of the cubic RVE in order to obtain the forces that are applied as nodal forces. These are ramped up in the beginning of the simulation and afterwards, imposed cyclically by multiplying them with the time-dependent factor $c_f(t) = 0.6 + 0.4 \sin(2\pi\, f\, t)$ The corresponding eigenvectors of the matrix

$$\boldsymbol{n}_1^{\mathrm{matrix}} = \begin{pmatrix} -0.9979 \\ 0.0501 \\ 0.0128 \end{pmatrix}, \qquad \boldsymbol{n}_2^{\mathrm{matrix}} = \begin{pmatrix} 0.0396 \\ 0.9003 \\ -0.4334 \end{pmatrix}, \qquad \boldsymbol{n}_3^{\mathrm{matrix}} = \begin{pmatrix} 0.0332 \\ 0.4323 \\ 0.9011 \end{pmatrix} \tag{7.4}$$

and of the MMC

$$\boldsymbol{n}_1^{\mathrm{MMC}} = \begin{pmatrix} -0.9971 \\ -0.0754 \\ -0.0117 \end{pmatrix}, \qquad \boldsymbol{n}_2^{\mathrm{MMC}} = \begin{pmatrix} -0.0751 \\ 0.9968 \\ -0.0259 \end{pmatrix}, \qquad \boldsymbol{n}_3^{\mathrm{MMC}} = \begin{pmatrix} -0.0163 \\ 0.0250 \\ 0.9996 \end{pmatrix} \tag{7.5}$$

indicate that the largest principal stresses occur in the x-direction as expected for the three-point bending test. The two smaller principal stresses lie in lateral directions, close to the y- and z-direction.

7.2.3. Validation of the numerical and material parameters with homogeneous microstructure

For the validation of the material and numerical parameters and of the algorithm under cyclic loading, results of the simulations of the RVE considering the homogeneous matrix material of Nikro-128 are compared to the experimental results. Here, the crack length over the cycle number is compared. Because the highest load occurs in the x-direction, the crack is expected to develop in the yz-plane. Here, the crack is initialized in y-direction at $x = l_{\mathrm{RVE}}/2$ with an initial crack length of $a = l_{\mathrm{RVE}}/5$ in y-direction. The cubic specimen with the edge length of $l_{\mathrm{RVE}} = 100\,\mu$m discretized by 7×100 elements in the xy-plane. In z-direction, there is only one layer of elements in order to reduce the computational costs. Furthermore, the elasto-plastic material law is chosen instead of the elasto-viscoplastic one because the load velocities of this experiment is higher compared to the tension test from which the material parameters were extracted. Since the effect of the viscosity η strongly depends on the load speed, the elasto-viscoplastic material law would lead to inaccurate results. Figure 7.4 shows that the resulting curves of the crack length a over the cycle number N take the similar exponential shapes. The slope of the crack length increases with the cycle number N until the crack becomes unstable and the specimen breaks immediately. This effect occurs due to the decreasing remaining cross sectional area. in the case of the higher maximum loads F_A, the crack length increases faster. These are well known phenomena that are described in standard books about fracture mechanics cf., e.g., Gross and Seelig [47]. Furthermore, the crack propagation in the simulations lies with $\mathrm{d}a/\mathrm{N} = 6.8{\cdot}10^{-6}$ mm per cycle for the maximum

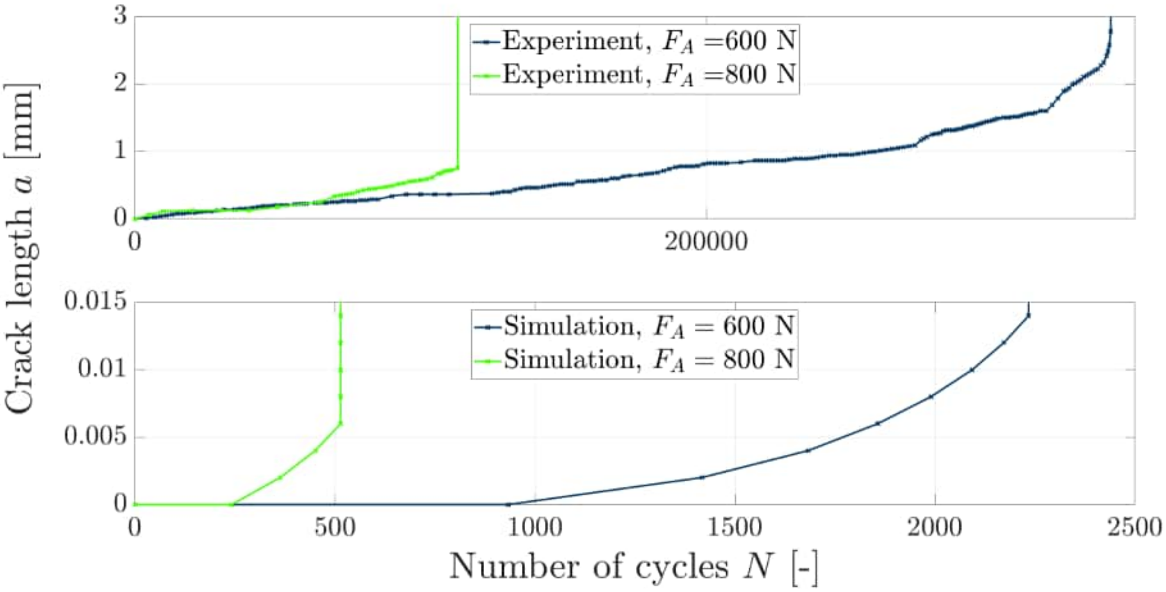

Figure 7.4.: Crack length a over number of load cycles N of (a) data from laboratory experiments and (b) simulated crack propagation at the side of a three-point bending test under cyclic loading with maximum load F_A, taken from Wingender et al. [154].

load $F_A = 600$ N and da/N $= 2.0 \cdot 10^{-5}$ mm per cycle for the maximum load $F_A = 800$ N in the same magnitude as the experimental data with da/N $= 4.5 \cdot 10^{-6}$ mm per cycle for the maximum load $F_A = 600$ N and da/N $= 7.9 \cdot 10^{-5}$ mm per cycle for the maximum load $F_A = 800$ N. Hence, the chosen adjusted material parameters for the metal matrix are justified for the simulations under cyclic load. Simulations under cyclic Neumann loads pose a numerically more difficult challenge due to the higher complexity of the microstructure and still have to be performed.

7.3. Crack propagation through Ferro-Titanit

7.3.1. Voxel data from scan

For simulations of the crack propagation through the MMC, a cutout from the scan of the size $l^3_{\text{RVE}} = 96 \times 96 \times 96\,\mu\text{m}^3$, as shown in figure 7.5a, is considered. Originally, each voxel is of the size $1 \times 1 \times 1$ μm^3. To reduce the computational effort the voxels of the cutout are summarized to $48 \times 48 \times 48$ voxels in figure 7.6b which is discretized into $12 \times 12 \times 12$ finite cells by the decomposition strategy T1min1-MT cf. figure 7.5b. On this discretization, symmetry boundary conditions are applied as Dirichlet boundary conditions with an imposed linearly increasing macroscopic strain $\bar{\varepsilon}_{ii} = \frac{\bar{u}_i}{96\,\mu\text{m}} = \frac{0.01\,t}{60\,\text{s}}$ macroscopic strain with the placeholder i for either the x-, y- and z-direction in figure 7.6. This strain rate and the time increment $\Delta t = 0.1\,\text{s}$ are chosen in line with the simulations on tensile test for the parameter identification because of the dependence of the viscous deformations on the load rate and the time step size Δt. In different simulations, the crack is initialized in different zones with a length of $l_{\text{RVE}}/24$ to trigger the crack propagation into different directions. The initial cracks are located at in the middle of the sides that are lateral to the load direction. The different scenarios of boundary conditions and initial cracks are shown in figure 7.6. The boundary conditions and initial cracks are permuted in order to check whether the crack propagation through the microstructure behaves isotropic or anisotropic. Since the constitutive laws do not include anisotropy and since the microstructure morphology is assumed to be isotropic in average, the isotropy of the crack propagation is expected. The simulation

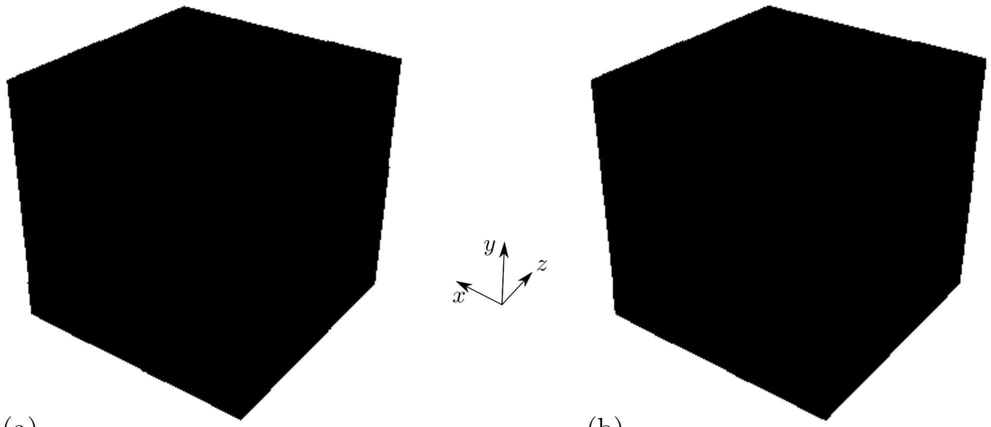

(a) (b)

Figure 7.5.: (a) Ferro-Titanit microstructure which is given as 48 × 48 × 48 voxels each the size $2 \times 2 \times 2\,\mu\text{m}^3$ in (a); (c) its discretization with the discretization scheme T1min1-MT into 12 × 12 × 12 finite cells. Voxels that represent the chromium carbide inclusions are marked with the color green whereas the martensite matrix is shown in silver.

under force boundary conditions under cyclic loads still stays a challenging task because of Newton-Raphson scheme fails for the complex microstructure under the application of the proposed approach. For the same reason, the elasto-viscoplastic material formulation with the material parameters in figure 7.1 is considered since simulations with the elasto-plastic material formulation have been proven difficult. One of the reasons for this is the too strong localization of the plastic zones that occur in calculations with the elasto-plastic material law, as shown in section 4.2.1. In figure 7.7a, the resulting von Mises stress τ^{vM} at the macroscopic strain $\bar{\varepsilon}_{xx} = \bar{u}/l_{\text{RVE}} = 0.0025$ over the specimen of the scenarios “xy” “xz” is shown. As expected, the von Mises stress is higher near the crack tip than in the surrounding areas due to the stress concentration that the crack induces. Additionally, the stress is higher in the inclusions than in the ductile matrix because their stiffness is larger than the one of the soft matrix. This shows, that mainly the inclusions carry the load. As shown in figure 7.8, the crack propagates primarily straightly through the microstructure but accepts small bypasses around the inclusions for the different scenarios. Hence, it is energetically more favorable for the crack to shortly bypass the inclusions than splitting those. Additionally, the resulting macroscopic stress $\bar{P}_{ii} = \bar{Q}_i/l^2_{\text{RVE}}$ in figure 7.9a behaves quiet similar over the induced strain $\bar{\varepsilon}_{ii}$ for all different scenarios. Together with the similar crack paths, this confirms isotropy of the microstructure which is expected because neither anisotropy of the morphology nor the anisotropy of the material law is assumed. Because the reaction force increases and then drops in discrete steps, the overall microstructure is assumed to be brit-

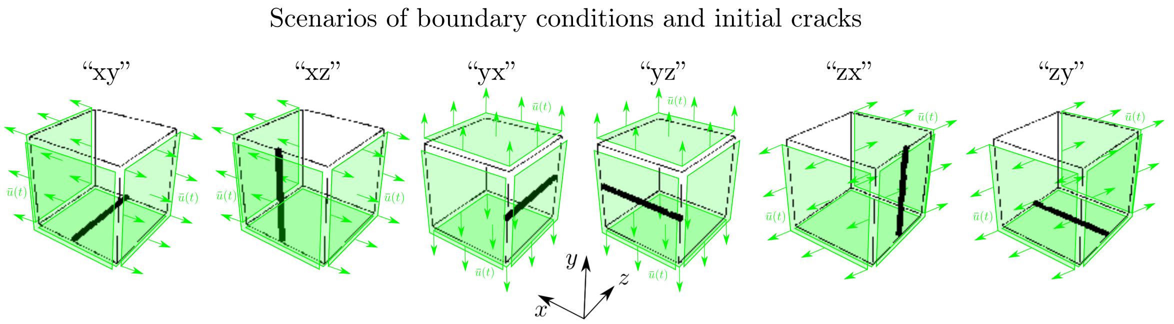

Figure 7.6.: Different scenarios of Dirichlet boundary conditions and initial cracks for the investigation of isotropy of the crack propagation through the Ferro-Titanit microstructure, taken from Wingender and Balzani [151]

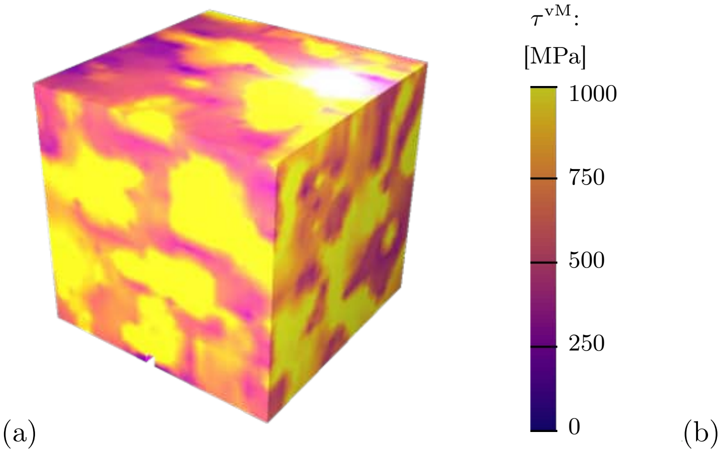

Figure 7.7.: Contour plot of the von Mises stress τ^{vM} over the Ferro-Titanit microstructure of scenario (a) “xy” and (b) “xz” at a macroscopic strain of $\bar{\varepsilon}_{xx} = \bar{u}/96\,\mu\mathrm{m} = 0.025$.

tle even though the matrix is ductile. As a further remark, the macroscopic strain $\bar{\varepsilon}_{ii}$, at which the Ferro-Titanit microstructure fails, is with a value between 0.45% and 0.65% lower than the one of the tensile test on the nickel martensite in figure 7.2e with a value of 0.9% even though the crack primarily propagates through the martensite matrix. This results from the increased stresses and thus, deformations in the matrix near the inclusions. Because the deformation is primarily carried by the martensite matrix, the brittle inclusions mainly stay crack-free even though the macroscopic strain $\bar{\varepsilon}_{ii}$ surpasses the one at which the specimen in the tensile test on the tungsten carbide in figure 7.2d fractures.

To further demonstrate the efficiency of the proposed approach, the number of linearized equations n_{eq} that are solved in every Newton-Raphson step is plotted over the macroscopic strain $\bar{\varepsilon}_{ii}$ in figure 7.9b. In the initial state when only the initial crack is present and most of the structure is simulated with finite cells, the number of equations is with around $50,000$ ($52,388$ for scenario “xy”) lower by a factor of $2-3$ (2.24 for scenario “xy”) compared to the number of equations in the final state when more finite cells have been split and additional hanging nodes occur. This high factor can be explained by the large number of subcells that erode ($3,994$ out of $19,880$ subcells for scenario “xy”). About $1/5$ of all subcells are eroded in the final state. As a comparison, the number of equations of a FE simulation, in which

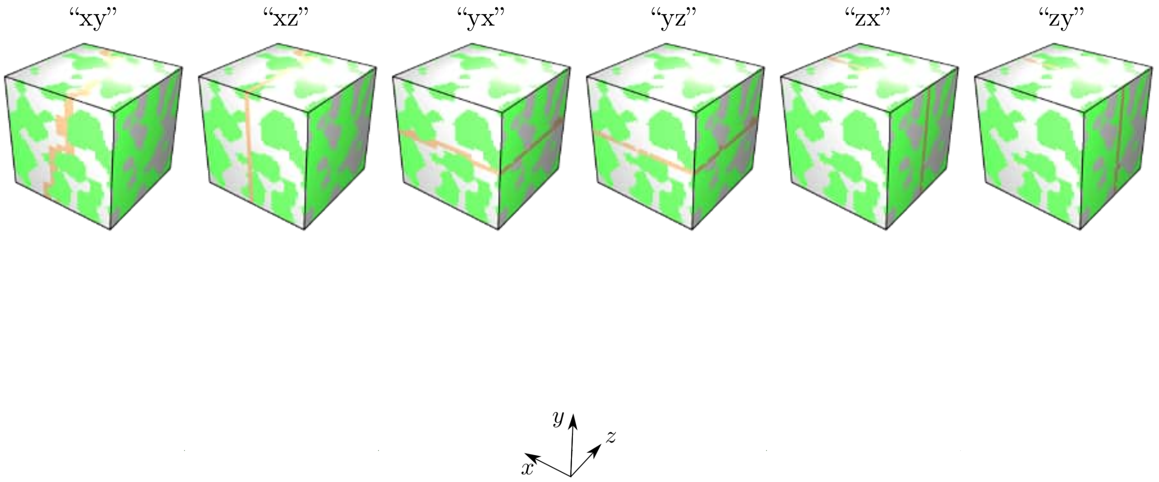

Figure 7.8.: Final crack path with and without surrounding material through Ferro-Titanit microstructure in figure 7.5a for the six different scenarios in figure 7.6, taken from Wingender and Balzani [151].

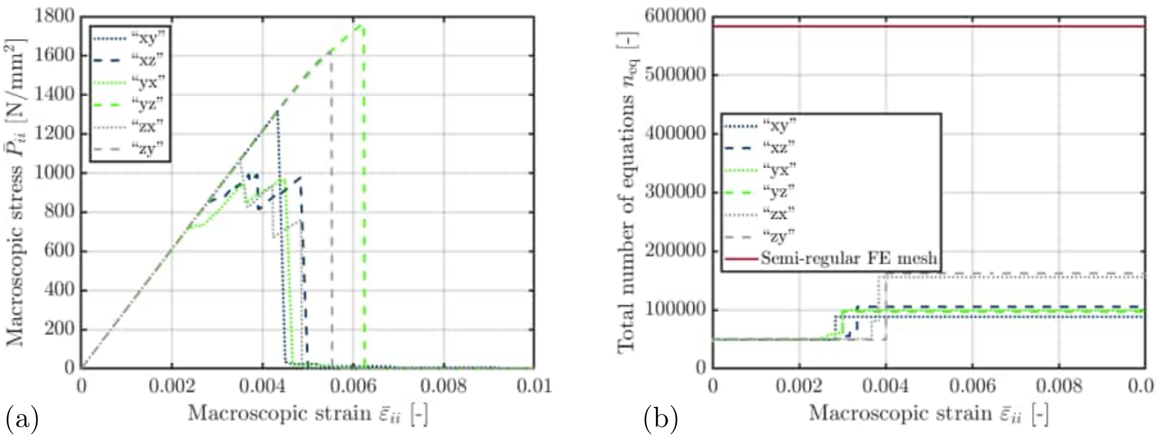

Figure 7.9.: (a) Resultant macroscopic first Piola-Kirchhoff stress $\bar{P}_{ii} = \bar{Q}_i / l_{\mathrm{RVE}}^2$ at the Dirichlet boundary in direction $i = x,\, y,\, z$ of the prescribed load, taken from Wingender and Balzani [151], and (b) number of equations in the linearized system within each Newton-Raphson iteration versus the macroscopic strain $\bar{\varepsilon}$.

all subcells are calculated as finite elements with hanging nodes from the beginning of the simulations, are presented for scenario "xy". With $n_{\mathrm{eq}} = 845,530$, the number of equations is increased by a factor of 16.1 compared to the proposed approach. This empathizes the efficiency of the FCM with the split of the finite cells including the eroded elements. However, the cost for the assembly of the linearized system of equations is equal in both cases since the number of subcells of the proposed approach equals the number of finite elements of the semi-regular FE mesh. Therefore, the number integration points, which highly influences the computational costs, is equal. If every voxel was simulated as a single hexahedral finite element, $96^3 = 884,736$ finite elements would be necessary, which surpasses the number of subcells of the two previous approaches by a factor of 44.5, so that the costs in the assembly of the global linearized system of equations would be high. Furthermore, around $21,500,000$ linearized equations would be solved, which surpasses the number of the proposed approach by a factor of 411 in the initial state and 183 in the final state of the scenario "xy". Summing up, this numerical example demonstrates the efficiency of the proposed approach and its capability to perform simulations including crack propagation directly on voxel data.

7.3.2. SSRVE

In this section, the crack propagation through an SSRVE is presented. Here, we consider the SSRVE with 6 ellipsoidal inclusions because of its acceptable objective values in the morphology as well as in the mechanical error. Additionally, the $48 \times 48 \times 48$ voxels supply a the possibility to decompose the chosen $12 \times 12 \times 12$ finite cells accurately and efficiently. The same material parameters and scenarios for the different boundary conditions and initial cracks as for the cutout of the μCT scan in figure 7.6 with an linearly increasing macroscopic strain $\bar{\varepsilon}_{ii} = \frac{\bar{u}_i}{l_i} = \frac{0.01\,t}{60\,\mathrm{s}}$ are applied. Since this simulation setup is equivalent to the one of the cutout of the Ferro-Titanit in the previous section, similar results are expected because the SSRVE's morphology is constructed in such a way that it represents the Ferro-Titanit microstructure with respect to the morphological as well as mechanical properties. The resulting distribution of the von Mises at a macroscopic strain of $\bar{\varepsilon}_{xx} = 0.025$ in figure 7.10 resembles the one of the cutout in figure 7.7. E.g., the load is primarily carried by the inclusions again. Hence, it is assumed that the mechanical fields of the SSRVE represent the mechanical fields of the Ferro-Titanit properly. However, the crack does not propagate straightly from the initial crack through the microstructure of the scenarios "xy", "xz" and "yx", cf. figure 7.11, because

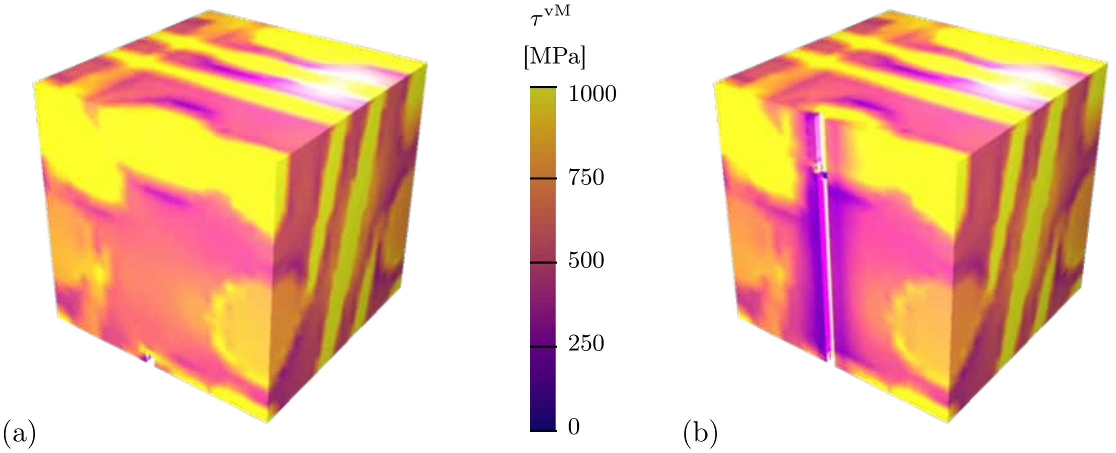

Figure 7.10.: Contour plot of the von Mises stress τ^{vM} over the SSRVE with six ellipsoidal inclusions in figure 6.3f of scenario (a) "xy" and (b) "xz" at a macroscopic strain of $\bar{\varepsilon}_{xx} = \bar{u}/96\,\mu\mathrm{m} = 0.025$.

the crack is deflected by the clusters of inclusions. In the other microstructures the final crack paths are primarily straight as expected. Thus, the crack propagation behaves anisotropically in this SSRVE. The same effect occurs in the resultant macroscopic stress at the Dirichlet boundaries in figure 7.12. The SSRVE of scenario "xz" finally breaks into two parts at a strain of $\bar{\varepsilon} = 0.0083$ whereas the final crack path of the SSRVEs of the other scenarios occurs in the same range as the one of the cutout of the μCT-scan. Because the SSRVE is smaller, its inclusions appear larger compared to the size of the microstructure than the ones in the cutout of the μCT-scan although the inclusions take the same volume fraction in both cases. As a result, the crack is deflected further from the straight way in the SSRVEs. Because of this, some information can be extracted from the simulation of the crack propagation through the SSRVEs but an accurate representation of the crack might not be given. However, the chosen SSRVE size is sufficient for simulations without crack propagation. To circumvent the problem of the erroneous representation of the SSRVE for crack propagation, larger SSRVEs have to be considered to properly represent the crack propagation of the Ferro-Titanit which leads to increased computational costs. As an alternative to larger SSRVEs, the crack propa-

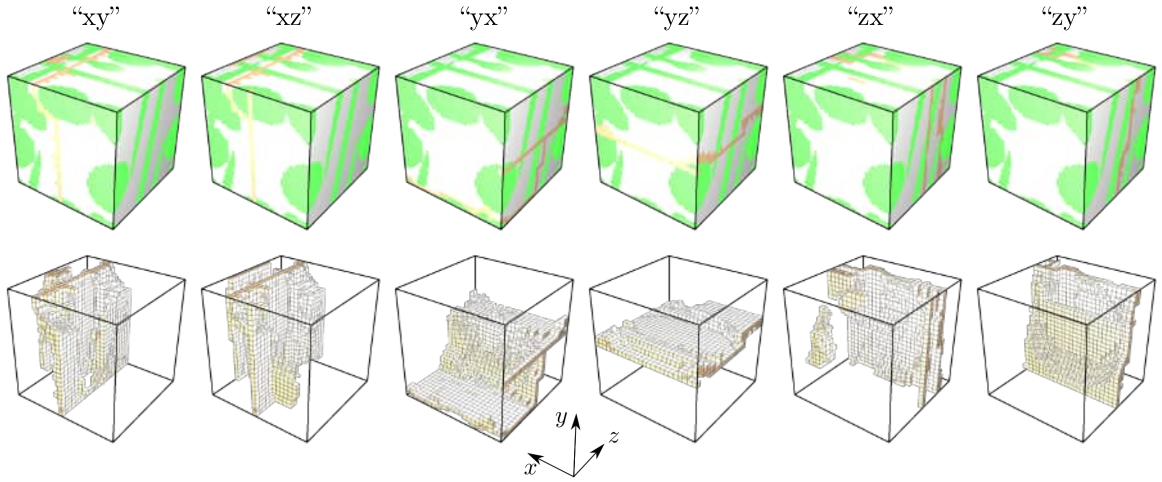

Figure 7.11.: Final crack path through the SSRVE with six ellipsoidal inclusions in figure 6.3f, which is discretized by 12 × 12 × 12 finite cell with T1-min1-MT, for the different scenarios in figure 7.6, taken from Wingender and Balzani [151]. The SSRVE is constructed in section 6.1 based on the minimization of th error regarding morphological and mechanical properties compared to the Ferro-Titanit microstructure.

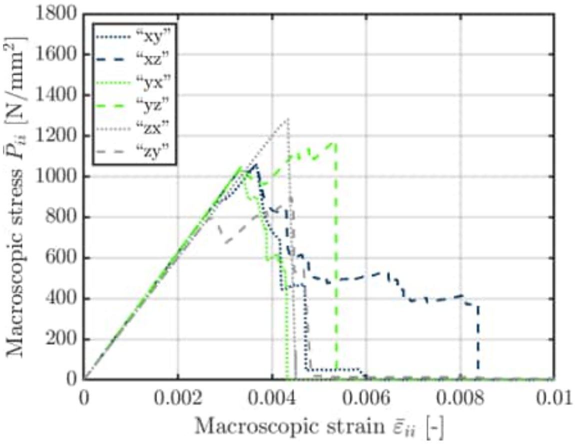

Figure 7.12.: Resultant macroscopic first Piola-Kirchhoff stress $\bar{P}_{ii} = \bar{Q}_i/l_{\mathrm{RVE}}^2$ at the Dirichlet boundary in direction of the prescribed load versus the macroscopic strain $\bar{\varepsilon}$, taken from Wingender and Balzani [151].

gation could be incorporated in the optimization scheme for the construction of the SSRVEs. Therein, simulations including crack propagation could be carried out on the RVEs and on a representative cutout of the scan in the outer optimization in which the mechanical error $\tilde{r}_{\varnothing}$ is minimized. This leads to additional computational costs in the construction of the SSRVEs since the computational costs of the simulations including crack propagation are higher. Nevertheless, the computational costs of SSRVE simulations are lower compared to simulations on real microstructures which reduces the computation time in mechanical simulations which is computationally advantageous if many evaluations are needed, e.g., for investigations of uncertainty quantification, cf. Miska and Balzani [95].

7.4. Influence of microstructure morphology of cold work tool steel

In the next simulations, the microstructure morphology of the cold work tool steel AISI D2 (DIN 1.2379) is varied in order to identify the one with the best resistance against crack propagation and thus, against surface spalling. Here, five different inclusion shapes are chosen, which result from different manufacturing processes, cf. [17]. The different manufacturing processes and their corresponding morphologies are the following:

I By sintering with hot isostatic pressing (HIP), spherical inclusions with a diameter of 10 μm develop, cf. figure 7.13a. The cubic RVE's edge length is of the size $l_{\mathrm{RVE}}^{\mathrm{I}} = 50\,\mu$m.

II If the material in I is rolled after sinterng, the spherical inclusions are stretched into one direction so that the inclusions become ellipsoidal with the semi-axis lengths $r_1 = 16.66$ μm, $r_2 = 13$ μm and $r_3 = 5$ μm, cf. figure 7.13b. This induces a strong anisotropy into the microstructure morphology which still has an edge length is of the size $l_{\mathrm{RVE}}^{\mathrm{II}} = 50\,\mu$m.

III HIP allows the adjustment of the inclusion sizes. In contrast to the morphology I, spherical inclusions with two different diameters of 57.5 μm and 2 μm cf. figure 7.13c are produced. Here, the microstructure's edge is of the length $l_{\mathrm{RVE}}^{\mathrm{III}} = 200\mu$m.

IV If the cold work tool steel is produced by casting, the inclusions form a framework with ellipsoidal holes, cf. figure 7.13d because the inclusions diffuse away from the centers

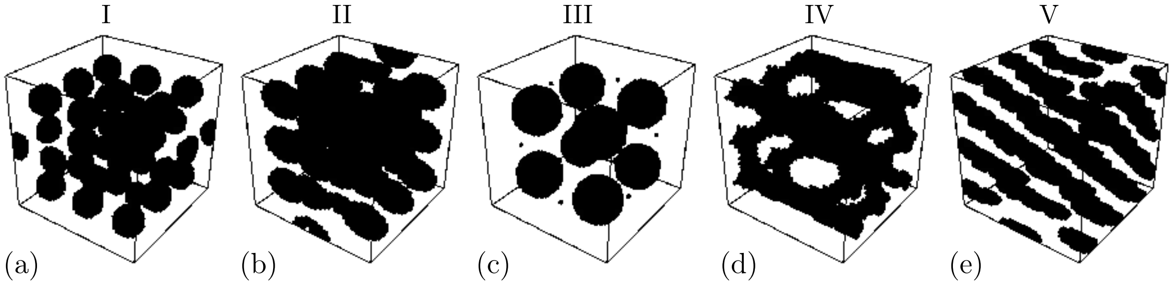

Figure 7.13.: Different cold work tool steel morphologies, that result from different manufacturing processes: (a) spherical inclusions, (b) ellipsoidal inclusions, (c) spherical inclusions with different sizes, (d) ellipsoidal framework and (e) clustering of the framework in (d), taken from [17].

of cooling during the cooling phase. These ellipsoids have semi-axes of the approximated size $r_1 = 50\ \mu$m, $r_2 = 20\ \mu$m and $r_3 = 20\ \mu$m within the microstructure of the size $(l^{\mathrm{IV}}_{\mathrm{RVE}})^3 = 75 \times 75 \times 75\,\mu\mathrm{m}^3$. Computationally, this artificial microstructure is constructed by assuming every voxel in the cube as inclusion first. Afterwards, 9 ellipsoids with the semi-axes ratios towards each other as mentioned above are increased and the voxels in those are considered as the matrix. This process is executed until the wanted volume fraction is achieved.

V After casting, the microstructure in IV is rolled so that the framework breaks and the inclusions cluster, as shown in figure 7.13e. For the simulations, the inclusions are artificially constructed by taking into account the microstructure morphology IV with ellipsoids that are shrunk by a factor of 0.8 as a basis. Afterwards, only the inclusion voxels are kept, which lie within a certain distance towards the center points of the lengthy horizontal bars. All other voxels are assumed as the matrix material. Because the volume fraction of the inclusions is shrunk with this procedure, the sizes of the ellipsoids for the first construction step are decreased. Here, the edge length is of the size $l^{\mathrm{V}}_{\mathrm{RVE}} = 150\,\mu$m which is double the size of the microstructure IV to obtain a sufficient number of inclusions.

Each of these microstructures is discretized into $48 \times 48 \times 48$ voxel since it is known from the previous examples that reasonable results with $12 \times 12 \times 12$ finite cells are achieved. Again, the decomposition scheme T1-min1-MT is applied. For comparable results, the all microstructures contain the same constituents, namely chromium inclusions in a martensite matrix with the material parameters in table 7.2, and the same volume fractions of the different phases. Here, the volume fraction $n_{\mathrm{chromium}} \approx 11.3\%$ is chosen in line with the physical material. The material parameters in table 7.2 are fitted to experimental data, as shown in section 7.1.

7.4.1. Linearly increasing load

Multiple boundary conditions and initial cracks with a crack length of 1/24 of the microstructure edge length in figure 7.6 are applied because the microstructure morphology is anisotropic in all cases. Therefore, the scenarios in figure 7.6 are considered. Since some microstructure morphologies equal into some directions, some of the scenarios are neglected. Again, linearly

	K [GPa]	μ [GPa]	y_0 [GPa]	y_∞ [GPa]	h^{exp} [$-$]	h^{lin} [GPa]	η [GPa s]	G_c [N/mm]
Martensite	167.56	77.33	0.92	1.20	1803.49	4.00	10	0.18
Chromium carbides	224.63	122.05	10^{12}	10^{13}	0	0	0	0.153

Table 7.2.: Material parameters of the constituents of the cold work tool steel fitted to tensile tests, taken from [17].

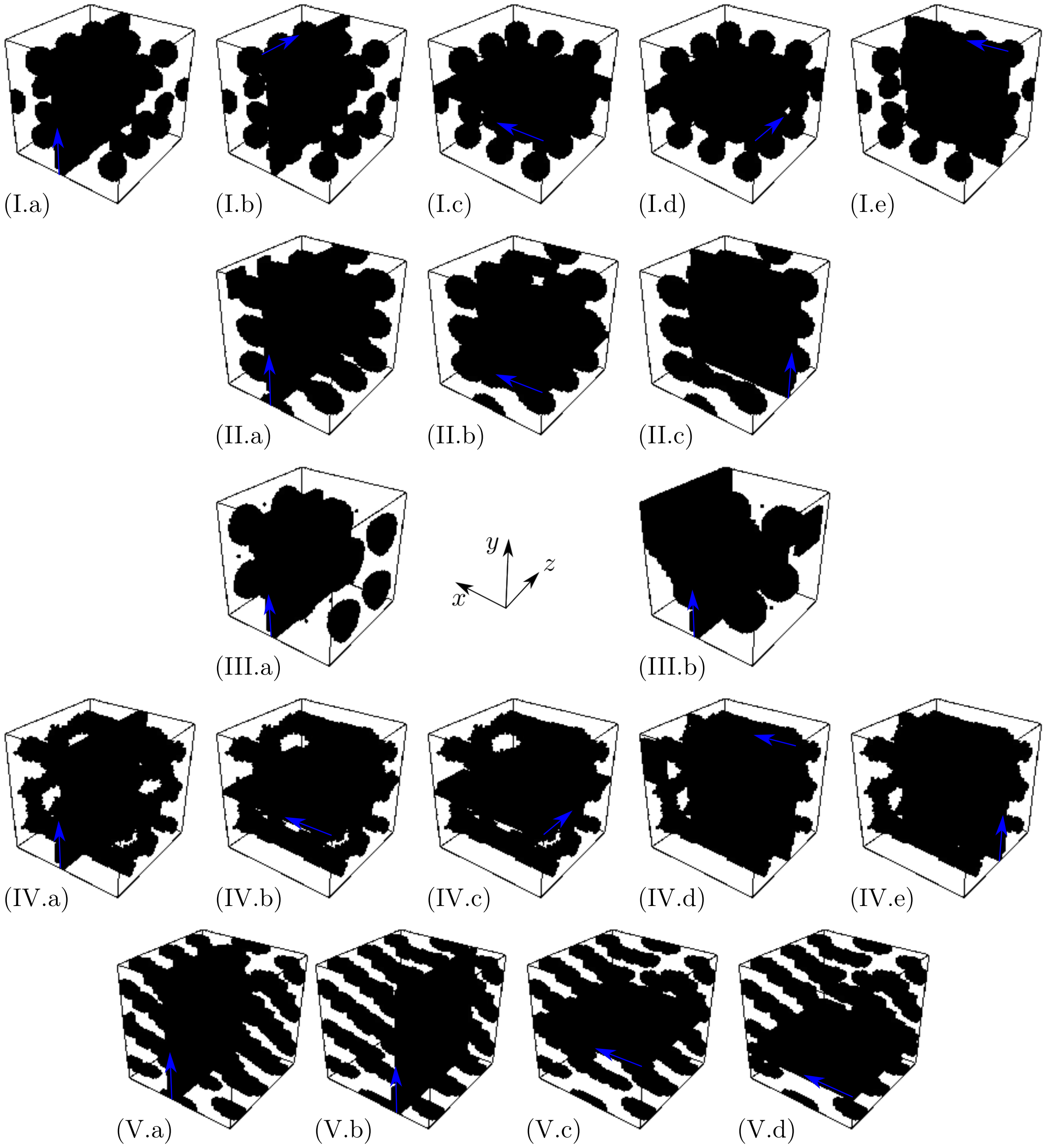

Figure 7.14.: Crack path through microstructures I-V from figure 7.13 under linearly increasing tension of the microstructure lateral to crack surface, taken from [17]. The blue arrow starts at the edge with the initial crack and points into the principal direction in which the crack propagates.

increasing macroscopic strains $\bar{\varepsilon}_{ii} = \frac{\bar{u}_i}{l_i} = \frac{0.01\,t}{60\,\mathrm{s}}$ are assumed at the Dirichlet boundary. In figure 7.14, the resulting final crack paths are shown. In microstructure I, the crack propagates straight but surrounds the spherical inclusions. This effect even occurs if the crack is initiated in the inclusions in figure 7.14I.c-d so that the crack propagation occurs isotropically in this microstructure. It can be followed that it is energetically more favorable for the crack to propagate around the spherical inclusions than directly through those, even though the fracture toughness of the chromium carbide is lower. Because the inclusions are stiff compared to the matrix, the ductile matrix primarily captures the deformation so that plastic deformation occurs around the inclusions. Therefore, energy is dissipated into plasticity which is captured in the energetic fracture criterion. The contour plot of the equivalent plastic strains α at a prescribed macroscopic deformation of $\bar{\varepsilon}_{xx} = 1\%$ for scenario "xy" in figure 7.16a demon-

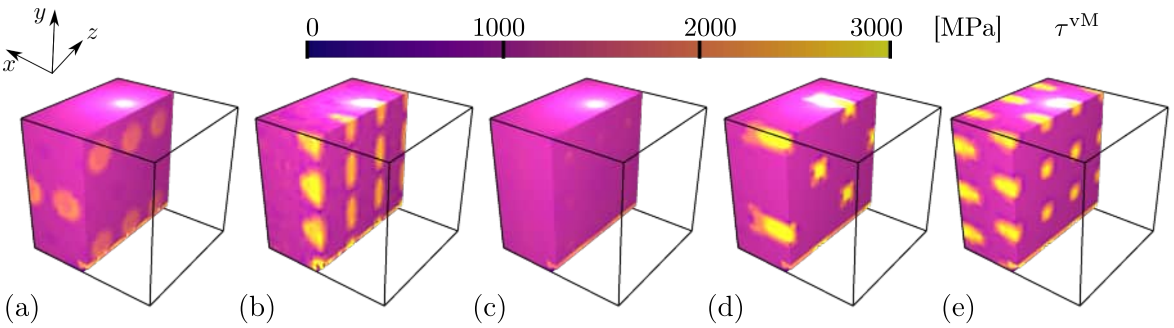

Figure 7.15.: Contour plot of the von Mises stress τ^{vM} over the cold work tool steel microstructures of the simulations corresponding to the simulations of figure 7.14I-V.a at a prescribed macroscopic strain of $\bar{\varepsilon}_{xx} = 1\%$, taken from [17].

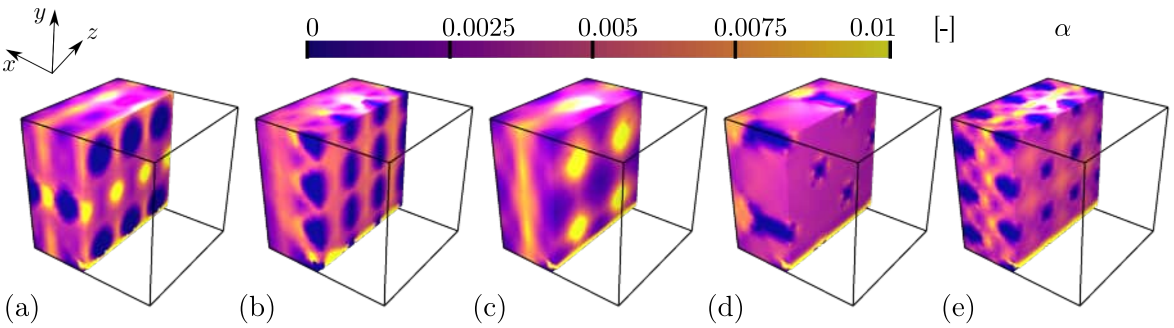

Figure 7.16.: Contour plot of the equivalent plastic strain α over the cold work tool steel microstructures of the simulations corresponding to the simulations of figure 7.14I-V.a at a prescribed macroscopic strain of $\bar{\varepsilon}_{xx} = 1\%$, taken from [17].

strates that the plastic deformations reach their maximum between the spheres in x-direction and near the initial crack at the bottom. This contributes to the development of the crack path. The specific energy $\psi^{\mathrm{e}}_{+} + \psi^{\mathrm{p}} + \int_t \mathcal{D}^{\mathrm{vis}}\,\mathrm{d}t$ which is evaluated for the fracture criterion in figure 7.17 concentrate near the crack tip as well, while it remains low in the inclusions. This results from the increased stresses at the crack tip and from the plastic deformations in the matrix which strongly influence the specific energy for the fracture criterion.

In contrast to the crack through microstructure I, the crack propagates straight through the inclusions in microstructure II cf. figure 7.14II.a-b. This results from the smaller area of the

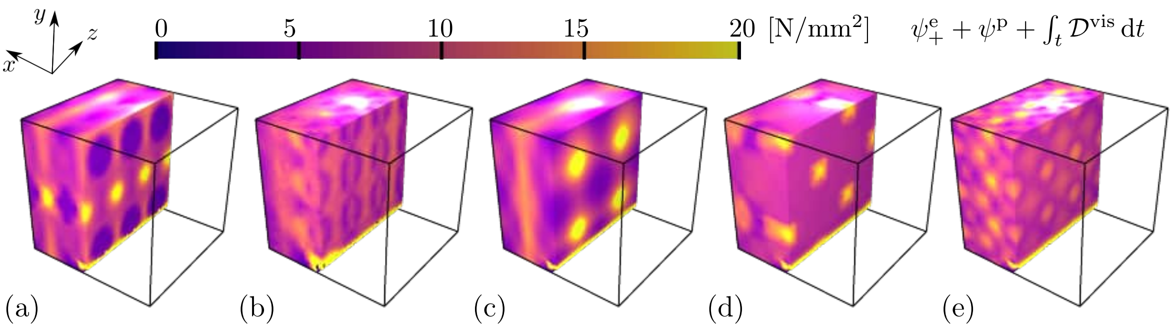
y
z
x
0
5
10
15
20
[N/mm²]
$\psi^{\mathrm{e}}_{+} + \psi^{\mathrm{p}} + \int_t \mathcal{D}^{\mathrm{vis}}\,\mathrm{d}t$
(a)
(b)
(c)
(d)
(e)

Figure 7.17.: Contour plot of the specific energy for fracture criterion $\psi^{\mathrm{e}}_{+} + \psi^{\mathrm{p}} + \int_t \mathcal{D}^{\mathrm{vis}}\,\mathrm{d}t$ over the cold work tool steel microstructures of the simulations corresponding to the simulations of figure 7.14I-V.a at a prescribed macroscopic strain of $\bar{\varepsilon}_{xx} = 1\%$, taken from [17].

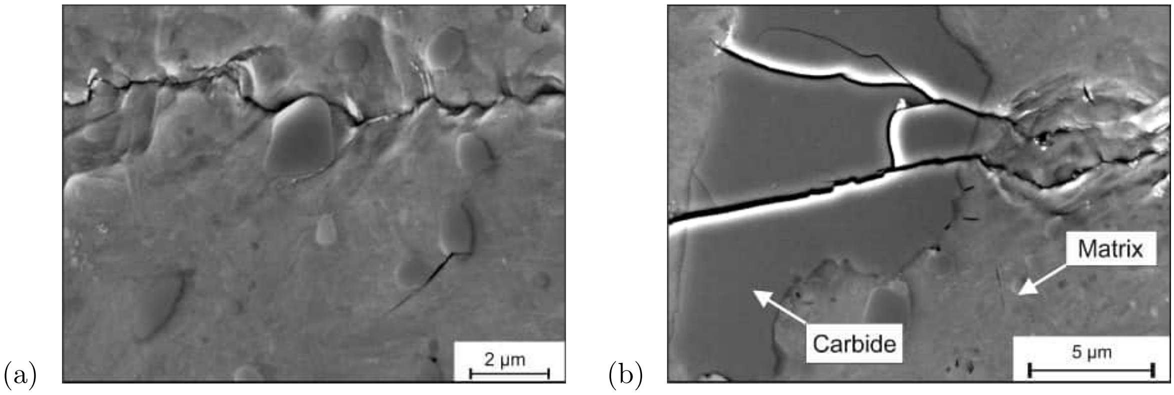

Figure 7.18.: Microscopic image of crack through cold work tool steel that was produced with HIP (a) without being hot rolled (comparable to the simulations of microstructure I) (b) with hot rolling (comparable to the simulations of microstructure II), taken from Brackmann et al. [16].

narrow inclusions through that the crack has to propagate if it develops straight through the microstructure. As an exception, the crack bypasses the inclusions if its principal direction lies within the plane of the largest ellipsoidal area in figure 7.14II.c. Hereby, the crack path is only slightly elongated and simultaneously avoids the crack through the inclusions. Similar results are achieved with the casted and hot rolled microstructures in figure 7.14V.a-d. If the principal crack direction is lateral to the long axis of the inclusions, the crack straightly propagates through those cf. figure 7.14V.a-b. However, if the crack propagates along the long axis, it avoids cutting the inclusions, as seen in figure 7.14V.c-d. The difference in the imposed work in figure 7.17b between the inclusion phase and the matrix is small compared to the difference in microstructure I. That the crack bypasses the spherical inclusions in structure I and primarily propagates through the inclusions is confirmed by microscopic images of the crack path in figure 7.18 obtained from experiments by the group of Arne Röttger and Lukas Brackmann. Hence, the plausibility of the results is demonstrated. The resulting crack paths of the microstructure III show that the crack path is influenced by the size of the inclusions because the inclusion diameter of the large inclusions are increased by a factor of 5.75 compared to the ones of microstructure I whereas the spherical shape stays constant. Herein, the final crack

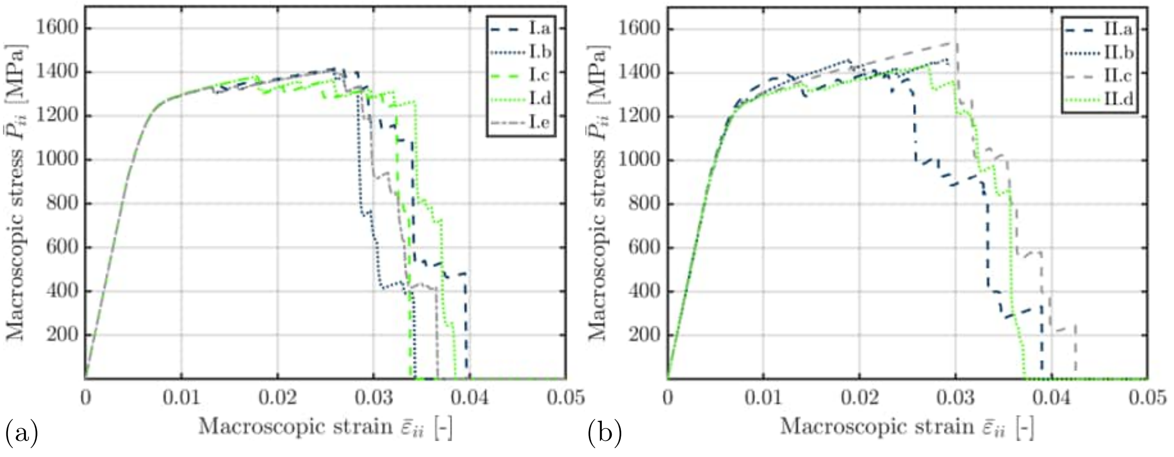

Figure 7.19.: Resultant macroscopic first Piola-Kirchhoff stress $\bar{P}_{ii} = \bar{Q}_i / l^2_{\mathrm{RVE}}$ of a one-dimensional tension test with prescribed displacements $\bar{u}_i$ in i direction, in which i denotes one of the three directions x, y or z on the microstructure (a) I and (b) II, taken from [17].

plane is straight but surrounds the inclusions in figure 7.14III.a. However, the crack starts propagating straightly upto the middle of the microstructure and then diagonally to the side until it reaches the boundary. This effect occurs because the crack would propagate diagonally in a microstructure which purely consists of the ductile matrix. The large space between the spheres allow the propagation into this direction. In the as-cast microstructure IV the crack path is primarily straight as well and breaks the network with small exceptions near the thick parts of the inclusion in figure 7.14IV.c-e. The resulting macroscopic first Piola-Kirchhoff stress $\bar{P}_{ii} = \bar{Q}_i/l_{\text{RVE}}^2$ in figure 7.19 and 7.20 behaves similar for all microstructures, even though the crack paths vary. It linearly increases with increasing prescribed displacement $\bar{u}$ until a stress around 1000 MPa is reached. From there on, the typical stress-strain curve for elasto-viscoplastic materials occurs until the stress drops with discrete jumps to zero due to the crack propagation. Hence, ductile material behavior is observable. All microstructures break into two parts at macroscopic strains between $\bar{\varepsilon}_{ii} = 0.026$ and 0.048 although the crack path in some microstructures is elongated in some which leads to an increased energy that dissipates into crack propagation. Thus, the microstructures with elongated crack paths do not provide a better resistance against crack propagation of the material under linear load.

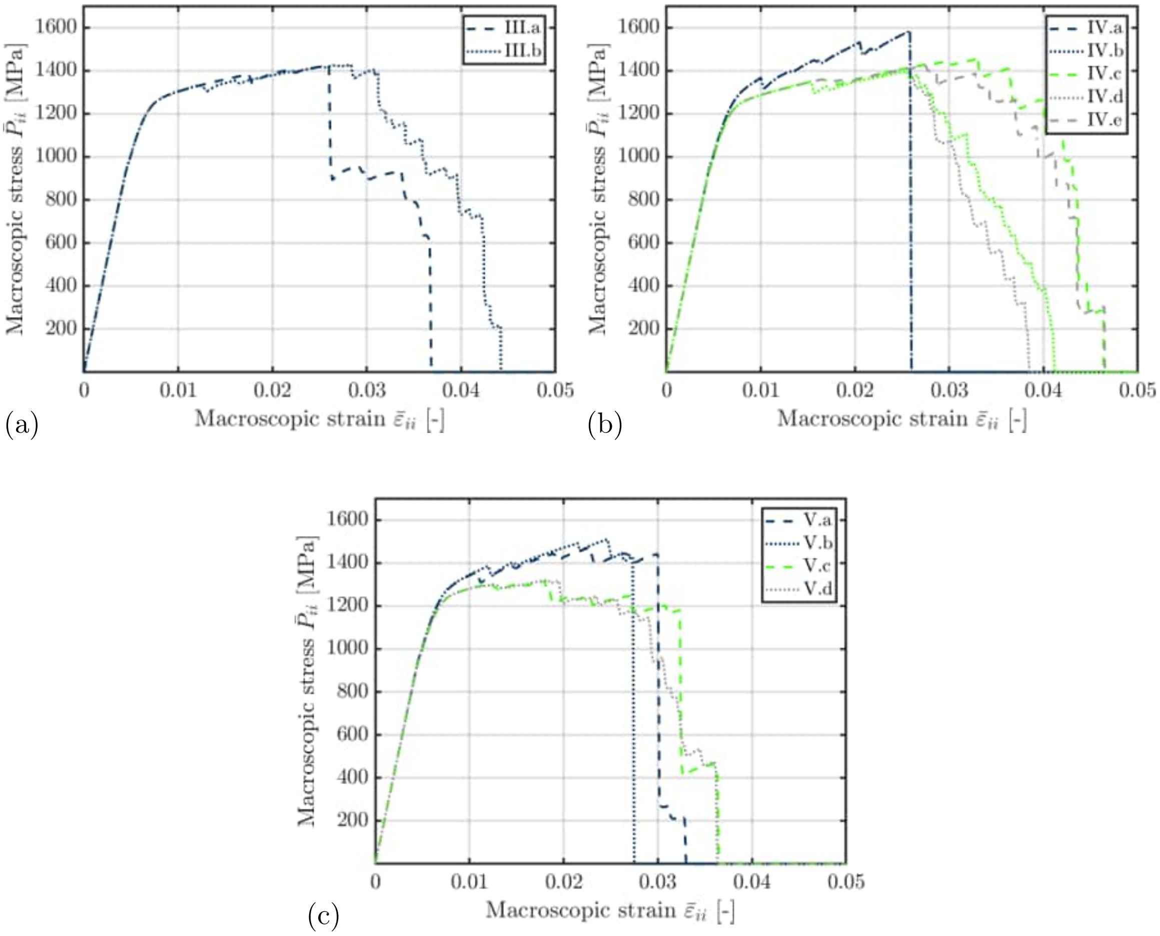

Figure 7.20.: Resultant macroscopic first Piola-Kirchhoff stress $\bar{P}_{ii} = \bar{Q}_i/l_{\text{RVE}}^2$ of a one-dimensional tension test with prescribed displacements $\bar{u}_i$ in i direction, in which i denotes one of the three directions x, y or z on the microstructure (a) III, (b) IV and (c) V, taken from [17].

7.4.2. Cyclic load

To investigate which of the manufacturing process leads to the microstructure with the best resistance against wear, simulations under cyclic loads are performed on all five microstructures with the loading scenario “xy” which coincides with the cases I.a-V.a. The macroscopic strain is imposed cyclically between the maximum of $\bar{\varepsilon}_{xx}^{\max} = 2/3\,\%$ and the minimum of $\bar{\varepsilon}_{xx}^{\min} = -2/3\,\%$ by considering an alternating strain rate of $\dot{\bar{\varepsilon}}_{xx} = \pm 1/60\,\mathrm{s}$ cf. figure 7.21a. The load is applied linearly and not sinusoidal in order to keep the velocity constant which is necessary because the development of the history variables in the elasto-viscoplastic material model depend on the loading speed. For the comparison of the crack length through the microstructure of different sizes over the number of cycles, the volumes of the eroded elements are scaled by the volume of the eroded elements at the time at which the crack has fully developed. Even though the different morphologies barely affect the resulting stress-strain curve under linear loads, differences become visible in the crack propagation under cyclic loads cf. figure 7.21b. The crack propagates fastest through morphology II, in which the crack is primarily straight, and slowest through morphology III, in which the crack path is elongated around the inclusions. Hence, it can be concluded that the crack path influences the crack propagation under cyclic loads. Furthermore, the results show that morphology III exhibits the highest resistance against wear because it endures the highest number of cycles until the microstructure is split into two parts. Additionally, it is shown that hot rolling the material of morphology I to morphology II weakens the materials resistance against surface spalling. Note, that these results only hold for the five investigated scenarios with their boundary conditions and initial cracks. For a full investigation, the cyclic simulations have to be repeated for all scenarios for all morphologies. Even though number of cycles is low, it can be assumed that these conclusions hold for higher number of cycles in engineering applications since the underlying effects are the same. Altogether, it is demonstrated that the proposed algorithm is capable of simulating crack propagation under cyclic loads through metallic microstructures to investigate surface spalling and to make predictions for the wear resistance.

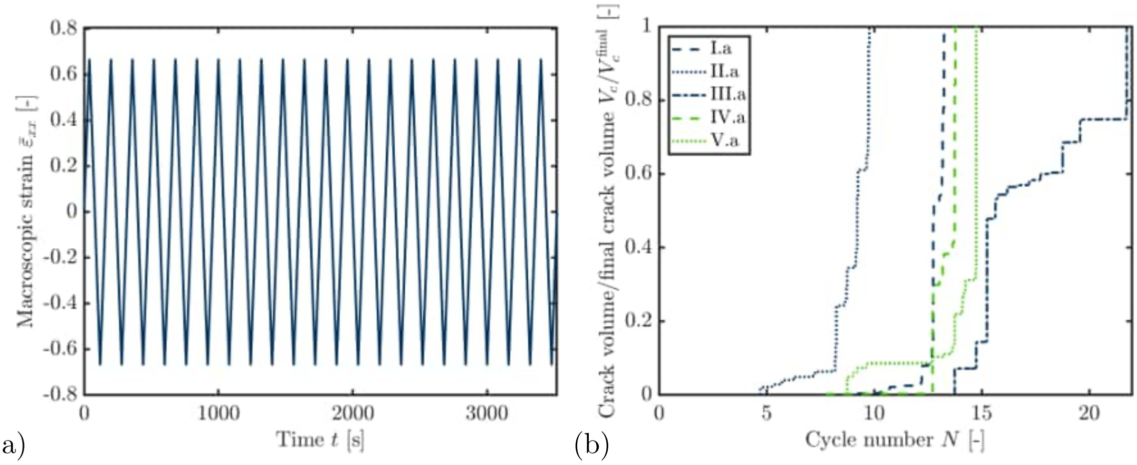

(a) (b)

Figure 7.21.: (a) Imposed macroscopic strain $\bar{\varepsilon}$ and (b) the resulting volume of the cracked elements divided by the volume of the finally cracked elements over time, taken from [17].

8. Conclusion and outlook

The aim of this work was the development of an efficient, robust and mesh-independent framework for the simulation of subcritical crack propagation through metallic microstructures based on voxel data obtained from μCT-scans. This was motivated by the field of mechanized tunneling. The framework was required to simulate the wear in the form of surface spalling acting on the metal matrix composite layers of the mining tools used for the tunneling.

For the simulations of surface spalling, the requirement for the numerical framework to simulate brittle as well as ductile crack propagation through complex three-dimensional structures along paths, that are not known a priori, had to be fulfilled independently from the discretization. In this work, a framework, which met all of these requirements, was developed. The simulations were based on the FE framework for solids including the inertia effects that were imposed with the Newmark scheme. Because the metallic microstructures consisted of brittle inclusions surrounded by a ductile metal matrix, the Neo-Hookean hyperelastic material law was assumed for the brittle phases and the finite strain J_2-elasto-plastic material law and its extension to elasto-viscoplasticity for the ductile phases. These material laws were extended by a tension-compression split which allowed the cracked material to transmit forces under compression but ensured traction-free crack surfaces under tension. For the extension of the FE framework to crack propagation, the eigenerosion scheme was applied because of its robustness and mesh independence. This approach assumed element erosion based on the Griffith criterion which compared the total imposed energy with a constant, namely the Griffith-type energy release rate, multiplied with a crack area. This crack area was regularized to avoid mesh dependency. The basic approach had only considered brittle materials under small strains. In this work, the eigenerosion was extended to ductile crack propagation at finite strains. Therefore, material laws for metal plasticity were applied and the total imposed energy was evaluated based on those for application of the Griffith-type criterion. As another enhancement of the basic approach, the regularized area was evaluated based on the Gauß points instead of the center of masses of the elements.

Numerical studies with the extended eigenerosion framework were carried out on a dogbone-shaped specimen. The mesh convergence of the crack path as well as of the reaction forces of a plate under a given deformation rate was shown for brittle materials. Herein, it was additionally demonstrated that both ways, namely sledging the specimen or imposing a weakness by reducing the Griffith-type energy release rate, were possible to circumvent the problem that the eigenerosion is only capable of simulating crack propagation and not initiation. Assuming the elasto-plastic material law, mesh convergence was observed in the crack path but not in the reaction force due to too strong localization of the plastic shear bands. Hence, the elasto-plastic material model was extended by viscosity, which smears out the shear bands. Additionally, the hardening function was modified to control the thickness of the shear bands. The influence of the two new parameters was shown. Assuming these modifications, mesh convergence of the reaction force for ductile materials was also achieved. In other simulations, the specimen was loaded cyclically with a force. Under a certain amount of cycles, a crack developed and later, the plate broke into two parts. This showed that the simulation setup is capable of simulating subcritical crack propagation under cyclic loads and of reproducing the technically important Wöhler curves.

For efficient simulations based on voxel data obtained from μCT-scans, the Finite Cell Method was additionally applied. This method extended the FEM by assuming that each finite element, now called finite cell, may contain multiple subcells with different properties. If simply the subcells were eroded, unphysically large crack widths would occur because all subcells within the finite cells. To avoid this, the finite cells that contained at least one eroded subcell were split into multiple finite elements that represent the previous subcells. This could be conceptually seen as adaptive mesh refinement near the crack tip. During the transformation process, hanging nodes occurred and the mass was kept constant but spread onto the subcells. Additionally, the integration scheme was kept so that no projection of the history variables was necessary. For the decomposition of the finite cells into subcells the following requirements have to be fulfilled. The number of subcells, the aspect ratio and the maximum subcell size should be kept low simultaneously. Additionally, not all arrangements of subcells are possible because some lead to numerical problems due to possible combinations of hanging node constraints. Therefore, a combination of multiple decomposition techniques was applied for a reasonable balance between computational efficiency and the other aspects. This combination consisted of the Octree decomposition with a certain minimum split and a subsequent merge on the lowest level. In a numerical example of an artificial microstructure consisting of a brittle spherical inclusion surrounded by a ductile metal matrix, it was shown that this combination lead to the desired properties of the discretization. In tensile tests considering different numerical approaches, the resulting crack paths and reaction forces were similar, yet different, especially in the softening phase. The results from the proposed algorithm considering the FCM converged with increasing number of finite cells towards the results of the semi-regular hexahedral mesh. The elements of this mesh were chosen in line with the subcells of the proposed approach, so that it represented the mesh of the proposed approach if all finite cells were split. Hence, the proposed approach lead to qualitatively and quantitatively comparable results, but the computational costs were reduced.

In order to further reduce the computational costs of microstructures based on μCT scans, smaller simplified artificial representative volume elements were constructed, namely the statistically similar representative volume elements (SSRVE). They were obtained by optimization of parameterized inclusion shapes regarding morphological as well as mechanical properties compared to the original microstructure. Thereby, a new inclusion shape, namely the superellipsoids, was introduced and its advantages and disadvantages were examined. Additionally, statistical volume elements (SVE) were constructed for asphalt concrete and the two construction concepts were compared.

Numerical results by application of the proposed algorithm were shown in comparison to laboratory experiments. Therefore, the calibration of material and numerical parameters based on experimental tensile test was demonstrated. In comparison to results from a three-point bending test, the simulation setup was validated. In an exemplary simulation of a real microstructure based on a μCT scan, the efficiency of the proposed approach was shown. Therein, the number of linearized equations of the Newton-Raphson scheme were reduced by a factor of 3 compared to the FE approach with the semi-regular hexahedral mesh. Additionally, it was shown, that differently located initial cracks resulted into a similar crack path and macroscopic material response. This demonstrates isotropy of the microstructure. Furthermore, simulations on SSRVEs were carried out and slightly different crack paths as in the cutout of the real microstructure was obtained. The difference resulted from the smaller sizes of the SSRVEs so that the SSRVEs represented the mechanical properties accurately in simulations without crack propagation but slightly erroneous results if crack propagation was considered. However, qualitative conclusion can be extracted by simulations on the SSRVEs. In order to improve the microstructure of cold work tool steel regarding surface spalling, different microstructures that resulted from different manufacturing processes were compared.

Under linearly increasing load, the crack paths developed similarly to results from laboratory tests because the crack either breaks the inclusions or wanders around them, depending on the morphology. Hence, the plausibility of the simulation setup including material parameters and numerical parameters was demonstrated. In simulations under cyclic loads, it was shown that the microstructure that was produced by sintering with large inclusions had the highest resistance against crack propagation because the crack propagated around the inclusions which elongated the crack path. Summing up, it was demonstrated that the proposed algorithm was capable to simulate subcritical crack propagation under cyclic loads through metallic microstructures based on voxel data. Hence, the aim of this work was fulfilled. By supplying a method to investigate the surface spalling on the microscopic level to improve the mining tools' material regarding wear, this work contributed to increase the efficiency of mechanized tunneling.

However, open tasks in this field remain. As one example, some metals, e.g., titanium, undergo phase transformation under a certain load. During the phase transformation, material properties change so that the mechanical fields and thus, the crack propagation are influenced as well. This effect has already been investigated in laboratoy experiments. However, simulations on this have not been carried out yet to the author's knowledge. The phase transformation can be implemented easily into the existing framework by extending the material law. When a certain load is locally reached, the set of material parameters is exchanged. Based on this, its influence and the influence of the microstructure morphology on the crack propagation can be investigated.

In a second task, the microstructures will be homogenized by application of the mean-field homogenization. With this approach, the macroscopic properties of the microstructure are captured. Therein, the crack propagation softens the macroscopic material, so that damage occurs macroscopically. In numerical studies, the connection from the microscopic crack to a macroscopic damage variable will be examined. In order to improve the mining tools regarding the surface spalling as well as the abrasion, the results from the homogenization are combined with a numerical simulation setup, in which the abrasion is simulated on the macroscopic tool level. This enables the investigation on the influence of the microstructure on both wear mechanisms. Based on the results, lifetime predictions and suggestions for the overall improvements of the mining tools will be made.

In general, the core idea of applying the FCM with refinement in certain areas can be used in a wide field of applications, e.g., for the simulation of tissue microstructures. In this example, the subcells are simulated as elements in the areas in which two fibers have contact with each other. In the contact zones, friction occurs between the fibers. Elsewhere, the FCM is applied in order to reduce the computational effort.

A. Voigt notation

The Voigt notation simplifies and reduces second order tensors to vectors and fourth oder tensors to matrices. This leads to a better readability of the tensors and simplifies the implementation into to FE-softwares like FEAP. In 3D, second order tensors contain 3 × 3 components and are rewritten into vectors containing 9 components. If a tensor is given in Voigt notation, it is underlined $\underline{\bullet}$. For example, the Voigt notation of the deformation gradient $\boldsymbol{F}$ and the first Piola-Kirchhoff stress $\boldsymbol{P}$ result in

$$\underline{\boldsymbol{F}} = \begin{bmatrix} F_{11} \\ F_{22} \\ F_{33} \\ F_{12} \\ F_{23} \\ F_{13} \\ F_{21} \\ F_{32} \\ F_{31} \end{bmatrix} \qquad \text{and} \qquad \underline{\boldsymbol{P}} = \begin{bmatrix} P_{11} \\ P_{22} \\ P_{33} \\ P_{12} \\ P_{23} \\ P_{13} \\ P_{21} \\ P_{32} \\ P_{31} \end{bmatrix}. \tag{A.1}$$

Diagonal components are located in the top rows whereas all other components lie on the middle and lower rows. In terms of stresses and strains, the normal components occupy the upper rows and the shear components the other rows. Symmetric tensors are additionally simplified by neglecting the last three components with the indices 21, 32 and 31 in Voigt notation which are equal to the components with the indices 12, 23 and 13. Exemplarily, the symmetric Green-Lagrange tensor $\boldsymbol{E}$ and the second Piola-Kirchhoff tensor are rewritten to

$$\underline{\boldsymbol{E}} = \begin{bmatrix} E_{11} \\ E_{22} \\ E_{33} \\ E_{12} \\ E_{23} \\ E_{13} \end{bmatrix} \qquad \text{and} \qquad \underline{\boldsymbol{S}} = \begin{bmatrix} S_{11} \\ S_{22} \\ S_{33} \\ S_{12} \\ S_{23} \\ S_{13} \end{bmatrix}. \tag{A.2}$$

The same scheme for the Voigt notation is applied on fourth order tensors. The Voigt notation of the nominal material tangent $\mathbb{A} = \frac{\partial \boldsymbol{P}}{\partial \boldsymbol{F}}$ reads

$$\underline{\mathbb{A}} = \begin{bmatrix}
\mathbb{A}_{1111} & \mathbb{A}_{1122} & \mathbb{A}_{1133} & \mathbb{A}_{1112} & \mathbb{A}_{1123} & \mathbb{A}_{1113} & \mathbb{A}_{1121} & \mathbb{A}_{1132} & \mathbb{A}_{1131} \\
\mathbb{A}_{2211} & \mathbb{A}_{2222} & \mathbb{A}_{2233} & \mathbb{A}_{2212} & \mathbb{A}_{2223} & \mathbb{A}_{2213} & \mathbb{A}_{2221} & \mathbb{A}_{2232} & \mathbb{A}_{2231} \\
\mathbb{A}_{3311} & \mathbb{A}_{3322} & \mathbb{A}_{3333} & \mathbb{A}_{3312} & \mathbb{A}_{3323} & \mathbb{A}_{3313} & \mathbb{A}_{3321} & \mathbb{A}_{3332} & \mathbb{A}_{3331} \\
\mathbb{A}_{1211} & \mathbb{A}_{1222} & \mathbb{A}_{1233} & \mathbb{A}_{1212} & \mathbb{A}_{1223} & \mathbb{A}_{1213} & \mathbb{A}_{1221} & \mathbb{A}_{1232} & \mathbb{A}_{1231} \\
\mathbb{A}_{2311} & \mathbb{A}_{2322} & \mathbb{A}_{2333} & \mathbb{A}_{2312} & \mathbb{A}_{2323} & \mathbb{A}_{2313} & \mathbb{A}_{2321} & \mathbb{A}_{2332} & \mathbb{A}_{2331} \\
\mathbb{A}_{1311} & \mathbb{A}_{1322} & \mathbb{A}_{1333} & \mathbb{A}_{1312} & \mathbb{A}_{1323} & \mathbb{A}_{1313} & \mathbb{A}_{1321} & \mathbb{A}_{1332} & \mathbb{A}_{1331} \\
\mathbb{A}_{2111} & \mathbb{A}_{2122} & \mathbb{A}_{2133} & \mathbb{A}_{2112} & \mathbb{A}_{2123} & \mathbb{A}_{2113} & \mathbb{A}_{2121} & \mathbb{A}_{2132} & \mathbb{A}_{2131} \\
\mathbb{A}_{3211} & \mathbb{A}_{3222} & \mathbb{A}_{3233} & \mathbb{A}_{3212} & \mathbb{A}_{3223} & \mathbb{A}_{3213} & \mathbb{A}_{3221} & \mathbb{A}_{3232} & \mathbb{A}_{3231} \\
\mathbb{A}_{3111} & \mathbb{A}_{3122} & \mathbb{A}_{3133} & \mathbb{A}_{3112} & \mathbb{A}_{3123} & \mathbb{A}_{3113} & \mathbb{A}_{3121} & \mathbb{A}_{3132} & \mathbb{A}_{3131}
\end{bmatrix}. \tag{A.3}$$

In this notation, the original 3 × 3 × 3 × 3 sized fourth order tensor becomes a 9 × 9 matrix in Voigt notation. The Voigt notation of the spatial material tangent $\mathfrak{c}_{\boldsymbol{\tau}} = 2\,\boldsymbol{b} \cdot \frac{\partial \boldsymbol{\tau}}{\partial \boldsymbol{b}}$ takes advantage of the symmetry of the Kirchhoff stress $\boldsymbol{\tau}$ and the left Cauchy stretch tensor $\boldsymbol{b}$. The relation $[\mathfrak{c}_{\boldsymbol{\tau}}]_{ijkl} = [\mathfrak{c}_{\boldsymbol{\tau}}]_{jikl}$ and $[\mathfrak{c}_{\boldsymbol{\tau}}]_{ijkl} = [\mathfrak{c}_{\boldsymbol{\tau}}]_{ijlk}$ hold, so that the spatial material tangent in Voigt notation becomes

$$\underline{\mathfrak{c}}_{\boldsymbol{\tau}} = \begin{bmatrix} \mathfrak{c}_{1111} & \mathfrak{c}_{1122} & \mathfrak{c}_{1133} & 2\mathfrak{c}_{1112} & 2\mathfrak{c}_{1123} & 2\mathfrak{c}_{1113} \\ \mathfrak{c}_{2211} & \mathfrak{c}_{2222} & \mathfrak{c}_{2233} & 2\mathfrak{c}_{2212} & 2\mathfrak{c}_{2223} & 2\mathfrak{c}_{2213} \\ \mathfrak{c}_{3311} & \mathfrak{c}_{3322} & \mathfrak{c}_{3333} & 2\mathfrak{c}_{3312} & 2\mathfrak{c}_{3323} & 2\mathfrak{c}_{3313} \\ \mathfrak{c}_{1211} & \mathfrak{c}_{1222} & \mathfrak{c}_{1233} & 2\mathfrak{c}_{1212} & 2\mathfrak{c}_{1223} & 2\mathfrak{c}_{1213} \\ \mathfrak{c}_{2311} & \mathfrak{c}_{2322} & \mathfrak{c}_{2333} & 2\mathfrak{c}_{2312} & 2\mathfrak{c}_{2323} & 2\mathfrak{c}_{2313} \\ \mathfrak{c}_{1311} & \mathfrak{c}_{1322} & \mathfrak{c}_{1333} & 2\mathfrak{c}_{1312} & 2\mathfrak{c}_{1323} & 2\mathfrak{c}_{1313} \end{bmatrix}. \tag{A.4}$$

In this form, the number of components of the fourth order tensor is reduced from $3 \times 3 \times 3 \times 3 = 81$ to $6 \times 6 = 36$.

B. SSRVE data

In this appendix, the applied numerical parameters, the optimized parameterizations and objective values of the SSRVEs are presented. For the evaluation of the statistical descriptors of the target microstructure, the threshold values $p_{\mathrm{SD}}^{\mathrm{thresh}} = 1\%$ for the spectral density and $p_{\mathrm{LP}}^{\mathrm{thresh}} = 4\%$ for the lineal path function are applied. The corresponding template for the lineal path function is presented in figure B.1. Based on this, the volume of the average inclusion size results to $9,216\,\mu\mathrm{m}^3$. This leads to the edge lengths of the SSRVEs $L^{\mathrm{SSRVE}} = 26\,\mu\mathrm{m}$ for $n_{\mathrm{incl}} = 1$ inclusions, $L^{\mathrm{SSRVE}} = 34\,\mu\mathrm{m}$ for $n_{\mathrm{incl}} = 2$ inclusions, $L^{\mathrm{SSRVE}} = 38\,\mu\mathrm{m}$ for $n_{\mathrm{incl}} = 3$ inclusions, $L^{\mathrm{SSRVE}} = 42\,\mu\mathrm{m}$ for $n_{\mathrm{incl}} = 4$ inclusions, $L^{\mathrm{SSRVE}} = 46\,\mu\mathrm{m}$ for $n_{\mathrm{incl}} = 5$ inclusions and $L^{\mathrm{SSRVE}} = 48\,\mu\mathrm{m}$ for $n_{\mathrm{incl}} = 6$ inclusions. In table B.1, the data of the SSRVEs including ellipsoidal inclusions and in figure B.2 the data of the SSRVEs with the superellipsoidal inclusions are shown.

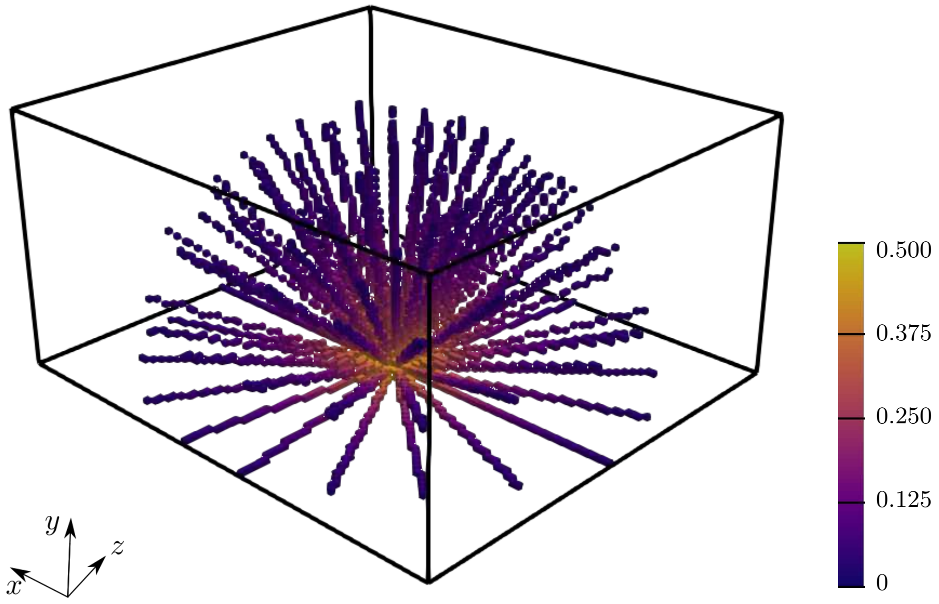

Figure B.1.: Template of the target microstructure thresholded by $p_{\mathrm{LP}}^{\mathrm{thresh}} = 4\%$ consisting of $85 \times 48 \times 95$ voxels.

i	Incl.	X_1^{C} [μm]	X_2^{C} [μm]	X_3^{C} [μm]	r_1 [μm]	r_2 [μm]	r_3 [μm]	θ_1 [°]	θ_2 [°]	θ_3 [°]	$\mathcal{L}_{\mathrm{V}}$	$\mathcal{L}_{\mathrm{SD}}$	$\mathcal{L}_{\mathrm{LP}}$	$\mathcal{E}(\boldsymbol{\gamma}_\rangle)$	$\tilde{r}_x$ [%]	$\tilde{r}_y$ [%]	$\tilde{r}_z$ [%]	$\tilde{r}_\varnothing$ [%]
I	1	13.00	13.00	13.00	19.76	11.00	9.73	0.49	30.38	43.58	$1.13 \cdot 10^{-6}$	$1.24 \cdot 10^{2}$	$2.14 \cdot 10^{-6}$	$1.46 \cdot 10^{-2}$	4.4	2.9	13.9	8.6
II	1	17.00	17.00	17.00	18.44	17.51	10.82	3.83	0.14	5.08	$3.35 \cdot 10^{-7}$	$5.31 \cdot 10^{1}$	$2.13 \cdot 10^{-6}$	$7.44 \cdot 10^{-3}$	4.6	1.0	18.2	10.8
	2	30.74	30.81	33.98	11.94	13.18	8.10	3.10	1.39	2.38								
III	1	19.00	19.00	19.00	17.23	16.91	5.54	0.99	0.01	0.99	$1.31 \cdot 10^{-5}$	$5.10 \cdot 10^{1}$	$2.13 \cdot 10^{-6}$	$7.24 \cdot 10^{-3}$	3.2	8.0	17.7	11.3
	2	36.17	36.94	36.66	9.41	18.87	9.96	4.31	3.79	3.86								
	3	35.82	36.99	35.58	18.50	19.66	13.76	6.07	0.25	7.53								
IV	1	21.00	21.00	21.00	43.34	10.73	12.15	8.93	3.83	16.06	$7.09 \cdot 10^{-7}$	$3.62 \cdot 10^{1}$	$2.11 \cdot 10^{-6}$	$5.72 \cdot 10^{-3}$	5.3	7.3	8.3	7.1
	2	23.16	35.08	32.53	18.65	9.27	5.83	19.56	0.00	19.09								
	3	41.85	40.19	41.99	7.49	7.55	16.24	2.21	2.60	16.53								
	4	41.98	27.54	42.00	9.17	47.16	3.66	0.36	9.80	31.56								
V	1	23.00	23.00	23.00	17.89	29.57	11.05	13.44	6.15	22.26	$1.32 \cdot 10^{-7}$	$2.94 \cdot 10^{1}$	$2.12 \cdot 10^{-6}$	$5.06 \cdot 10^{-3}$	7.6	2.2	1.8	4.7
	2	45.79	45.66	45.56	30.19	3.82	19.45	12.72	0.00	21.70								
	3	21.10	31.35	44.00	9.40	44.97	4.30	14.95	2.09	8.97								
	4	45.96	25.32	43.47	3.34	23.81	22.76	1.22	6.02	2.50								
	5	36.34	31.27	45.68	1.49	18.68	19.42	24.44	14.14	7.24								
VI	1	24.00	24.00	24.00	25.45	23.70	10.86	7.91	16.03	7.31	$2.93 \cdot 10^{-6}$	$3.35 \cdot 10^{1}$	$2.11 \cdot 10^{-6}$	$5.46 \cdot 10^{-3}$	6.7	7.9	5.4	6.7
	2	17.07	47.99	46.61	13.22	10.01	9.44	43.95	32.75	3.48								
	3	38.30	42.03	44.75	8.32	20.79	5.67	18.40	14.81	16.07								
	4	43.80	20.89	47.85	5.63	11.83	19.24	0.62	32.94	0.74								
	5	19.53	47.44	22.61	58.53	36.72	2.34	15.13	14.05	4.74								
	6	45.60	40.14	47.88	23.94	2.40	23.51	6.75	2.47	9.36								

Table B.1.: Parameters of the SSRVEs with $1, \ldots, 6$ ellipsoidal inclusions and their corresponding objective values $\mathcal{L}$ and $\mathcal{E}$ of the morphology and $\tilde{r}_{e,j}$ of the mechanical properties.

i	Incl.	X_1^{C} [μm]	X_2^{C} [μm]	X_3^{C} [μm]	r_1 [μm]	r_2 [μm]	r_3 [μm]	θ_1 [°]	θ_2 [°]	θ_3 [°]	p	$\mathcal{L}_{\mathrm{V}}$	$\mathcal{L}_{\mathrm{SD}}$	$\mathcal{L}_{\mathrm{LP}}$	$\mathcal{E}(\boldsymbol{\gamma}_\rangle)$	$\tilde{r}_x$ [%]	$\tilde{r}_y$ [%]	$\tilde{r}_z$ [%]	$\tilde{r}_\varnothing$ [%]
I	1	13.00	13.00	13.00	10.82	10.82	9.84	0.94	0.26	8.56	21.87	$8.29 \cdot 10^{-6}$	$1.24 \cdot 10^{2}$	$2.14 \cdot 10^{-6}$	$1.45 \cdot 10^{-2}$	6.2	6.2	2.9	5.3
II	1	17.00	17.00	17.00	9.19	12.25	6.27	3.27	7.26	3.96	8.92	$6.13 \cdot 10^{-7}$	$4.48 \cdot 10^{1}$	$2.13 \cdot 10^{-6}$	$6.62 \cdot 10^{-3}$	2.9	7.4	3.8	5.1
	2	33.92	28.64	34.00	15.91	14.6	8.04	9.11	0.00	0.000									
III	1	19.00	19.00	19.00	11.85	15.75	10.02	1.96	30.07	$6.3e-05$	16.8977	$6.72 \cdot 10^{-6}$	$2.72 \cdot 10^{1}$	$2.14 \cdot 10^{-6}$	$4.84 \cdot 10^{-3}$	6.6	1.2	1.8	4.0
	2	26.40	37.64	35.26	23.70	14.11	1.86	19.32	5.29	6.08									
	3	35.41	13.61	27.39	2.34	18.82	25.08	6.23	16.07	0.20									
IV	1	21.00	21.00	21.00	18.38	17.22	8.97	13.73	0.77	2.13	16.79	$3.76 \cdot 10^{-8}$	$3.29 \cdot 10^{1}$	$2.11 \cdot 10^{-6}$	$5.39 \cdot 10^{-3}$	2.2	7.1	6.6	5.7
	2	41.58	41.74	41.87	28.84	5.67	3.73	0.75	18.49	0.60									
	3	31.60	35.98	40.98	6.03	27.59	3.72	3.76	12.96	14.69									
	4	39.85	40.08	41.98	8.12	7.23	18.03	20.68	20.57	2.21									
V	1	23.00	23.00	23.00	16.11	19.57	5.82	13.49	0.85	13.57	17.66	$1.97 \cdot 10^{-5}$	$3.36 \cdot 10^{1}$	$2.12 \cdot 10^{-6}$	$5.50 \cdot 10^{-3}$	1.0	1.2	7.3	4.3
	2	45.98	45.44	44.87	13.00	6.76	18.09	1.35	3.96	6.72									
	3	45.98	29.29	44.79	16.66	5.40	10.63	6.35	9.40	7.54									
	4	45.41	45.90	39.88	12.52	13.11	1.90	3.72	2.64	0.93									
	5	32.57	45.60	45.17	14.20	20.40	9.64	0.06	0.45	1.27									
VI	1	24.00	24.00	24.00	17.93	11.33	7.42	6.41	9.09	0.16	24.50	$1.2 \cdot 10^{-6}$	$3.98 \cdot 10^{1}$	$2.10 \cdot 10^{-6}$	$6.08 \cdot 10^{-3}$	4.1	2.3	4.0	3.6
	2	35.41	46.61	48.00	14.56	14.90	12.65	0.64	8.93	12.17									
	3	47.99	43.96	47.94	5.36	16.91	4.75	0.285	11.84	21.93									
	4	42.52	42.04	46.92	20.79	21.26	9.78	0.05	0.49	2.63									
	5	46.91	46.00	29.44	23.81	2.12	14.17	2.00	0.06	3.94									
	6	29.49	32.78	39.20	14.06	5.47	2.44	4.07	10.45	5.27									

Table B.2.: Parameters of the SSRVEs with $1, \ldots, 6$ superellipsoidal inclusions and their corresponding objective values $\mathcal{L}$ and $\mathcal{E}$ of the morphology and $\tilde{r}_{e,j}$ of the mechanical properties.

List of Tables

5.1. Sizes of the global vectors and matrices of the linearized system of equations that is solved in every Newton-Raphson step to iteratively approximate the solution of the mechanical equilibrium. 70
5.2. Material parameters of hard metal microstructure of the benchmark experiment, taken from Wingender and Balzani [149]. 90

6.1. Parameters for the generation of an ensemble of artificial SVEs representing the asphalt concrete PA8. 115

7.1. Material parameters of MMC Ferro-Titanit constituents fitted to tensile tests under the assumtion of the elasto-plastic formulation (ep) or the elasto-viscoplastic material formulation (evp). 122
7.2. Material parameters of the constituents of the cold work tool steel fitted to tensile tests, taken from [17]. 132

B.1. Parameters of the SSRVEs with $1, ..., 6$ ellipsoidal inclusions and their corresponding objective values $\mathcal{L}$ and $\mathcal{E}$ of the morphology and $\tilde{r}_{e,j}$ of the mechanical properties. 145
B.2. Parameters of the SSRVEs with $1, ..., 6$ superellipsoidal inclusions and their corresponding objective values $\mathcal{L}$ and $\mathcal{E}$ of the morphology and $\tilde{r}_{e,j}$ of the mechanical properties. 145

List of Figures

1.1. (a) Overall number of tunnels and tunnel length in Germany from 1965 until 2017 [43], and (b) proportion of three excavation methods, namely NATM, Mechanized Tunneling and Cut-and-Cover method, for tunneling for underground, urban and rapid transit systems in Germany from 1999 until 2020 related to driven length [120]. 1
1.2. (a) Tunnel boring machine (TBM) in Madrid and (b) front view on its cutter head at the tunnel breakthrough by the company AG [2] 2
1.3. (a) Schematic structure of the tribological system of the TBM mining tool, (b) chisel subject to abrasive wear and (c) top-view on chisel subject to surface spalling, taken from Küpferle et al. [69] 3
1.4. (a) Schematic illustration of subcritical crack propagation under cyclic loading and (b) scanning electron micrograph of MMC Ferro-Titanit microstructure consisting of titanium carbides (TiC) within metal matrix including crack, taken from Küpferle [66] 5

2.1. Undeformed body $\mathcal{B}_0$ in the reference configuration at $t = t_0$ and deformed body $\mathcal{B}_t$ in the current configuration at $t > t_0$. 12
2.2. (a) Body $\mathcal{B}$ and (b) its discretization $\mathcal{B}^{\mathrm{FE}}$ into tetrahedral elements with their edges (black) and nodes (yellow) including the body $\mathcal{B}_K$ of the element K and its outer surface $\partial\mathcal{B}_K$. 19
2.3. (a) Quadrilateral element of a mesh in the reference configuration which is transformed into (b) the isoparametric space in order to evaluate the material response at the Gauß points $\boldsymbol{\xi}_l$. 20
2.4. Undeformed body $\mathcal{B}_0$ in the reference configuration at $t = t_0$, deformed body $\mathcal{B}_{\mathrm{i}}$ in the intermediate and $\mathcal{B}_t$ in the current configuration at $t > t_0$. 26
2.5. Yield surface in the principal stress space (τ_1,τ_2,τ_3) with a trial stress $\boldsymbol{\tau}^{\mathrm{tr}}$ for elasto-plasticity (a) without hardening and (b) with hardening. 27
2.6. Yield surface in the principal stress space (τ_1,τ_2,τ_3) with a trial stress $\boldsymbol{\tau}^{\mathrm{tr}}$ for elasto-viscoplasticity (a) without hardening and (b) with hardening. 31

3.1. (a) Body $\mathcal{B}_0$ with crack C and Dirichlet boundary conditions as well as Neumann boundary conditions. (b) crack plane within the body with previous crack plane $C(t)$ (green), of the crack area ΔC (blue) with the crack width s and the crack velocity v. 37
3.2. Mesh with eroded elements C (dark gray), their ϵ-neighborhood C_ϵ (dark blue) and additional crack area $(C \cup K)_\epsilon \backslash C_\epsilon$ for element domain K (green) based on (a) the center of masses and (b) the Gauß points, taken from Wingender and Balzani [150]. 41
3.3. (a) Banana-shaped triangular element with quadratic shape function with influence area (green) based on (a) barycenter and (b) Gauß points (black). . . 42
3.4. Schematic illustration of the considered eigenerosion algorithm within a finite element framework, taken from Wingender and Balzani [150]. 43
3.5. Mesh with intact elements (gray), eroded elements (blue) and elements that might erode simultaneously (green). 44

3.6. Mesh with its nodes (blue) and eroded elements (gray) with the nodes attached to these (green) in the case (a) and (b) of linear shape functions and (c) quadratic shape functions. Nodes that are connected to any element anymore are marked with a red circle. 45

4.1. (a) Specimen for tension test with initial crack at time t_0, (b) specimen for tension test without crack, and (c) considered geometric parameters; T denotes the thickness of the specimens, taken from Wingender and Balzani [150]. . . 48
4.2. Final crack through specimen in tension test with the initial crack length $a =$ 0.95 mm for the different element sizes (a) $h = 0.22$ mm, (b) $h = 0.11$ mm, (c) $h = 0.065$ mm, and (d) $h = 0.0325$ mm, taken from Wingender and Balzani [150]. The eroded elements are removed from these images. 49
4.3. Force-displacement curve for brittle material (a) with and (b) without prescribed initial crack, taken from Wingender and Balzani [150]. The converging response indicates mesh-independence. 50
4.4. Specimen with weakened area (red) for different mesh sizes (a) $h = 0.22$ mm, (b) $h = 0.11$ mm, (c) $h = 0.065$ mm and (d) $h = 0.0325$ mm, taken from Wingender and Balzani [150]. 50
4.5. Final crack through brittle specimen with weakened area in the tension test with the different element sizes (a) $h = 0.22$ mm, (b) $h = 0.11$ mm, (c) $h =$ 0.065 mm, and (d) $h = 0.0325$ mm, taken from Wingender and Balzani [150]. 51
4.6. (a)Reaction force $\bar{Q}$ over displacement $\bar{u}$ of brittle specimen for different Griffith-type energy release rates G_c, (b) different influence radii constants C_h that determine the influence radius $\epsilon = C_h\, h$ and (c) number of entries in Gauß point list over influence radius constant C_h. 52
4.7. Average energy $\bar{\psi}$ of the element that is going to be eroded first over (a) macroscopic displacement $\bar{u}$ and (c) critical average energy $\bar{\psi}$ at which this element erodes over the characteristic in-plane edge length h at the displacement $\bar{u} = 0.01$ mm, and incremental crack area $\mathrm{d}A_K$ over (b) the macroscopic displacement $\bar{u}$ and over (d) the characteristic in-plane edge length h at the displacement $\bar{u} = 0.01$ mm. 53
4.8. (a) Adjusted stress-strain curve of elasto-plastic material (iron alloy) and (b) material parameters, taken from Wingender and Balzani [150]. 53
4.9. Distribution of equivalent plastic strain α at $\bar{u} = 0.2$ mm using the unregularized elasto-plastic formulation for different element sizes (a) $h = 0.22$ mm, (b) $h = 0.11$ mm and (c) $h = 0.065$ mm, taken from Wingender and Balzani [150]. 54
4.10. Force-displacement curve for the unregularized elasto-plastic material formulation. Clearly, convergence cannot be observed, taken from Wingender and Balzani [150]. 54
4.11. Crack path and equivalent plastic strain α resulting from unregularized elasto-plastic formulation for different element sizes (a) $h = 0.22$ mm, (b) $h = 0.11$ mm and (c) $h = 0.065$ mm, taken from Wingender and Balzani [150]. 55
4.12. Distribution of equivalent plastic strain α at $\bar{u} = 0.25$ mm using the regularized elasto-viscoplastic formulation for different mesh sizes (a) $h = 0.22$ mm, (b) $h = 0.11$ mm and (c) $h = 0.065$ mm, taken from Wingender and Balzani [150]. 56
4.13. Crack path resulting from regularized elasto-plastic formulation for different element sizes (a) $h = 0.22$ mm, (b) $h = 0.11$ mm and (c) $h = 0.065$ mm, taken from Wingender and Balzani [150]. 56
4.14. Force-displacement curve for the regularized elasto-plastic material formulation, taken from Wingender and Balzani [150]. The converging response indicates mesh-independence. 57

4.15. Distribution of equivalent plastic strain α in homogeneous specimen for different values of the viscosity η and the localization parameter δ at $\bar{u} = 0.15$ mm, taken from Wingender and Balzani [150]. 58
4.16. Distribution of equivalent plastic strain α in weakened specimen for different values of the viscosity η and the localization parameter δ at $\bar{u} = 0.15$ mm, taken from Wingender and Balzani [150]. 59
4.17. Force-displacement curves for different values of regularization parameters for (a) homogeneous and (b) weakened specimen, taken from Wingender and Balzani [150]. 60
4.18. (a) Geometry and boundary conditions of the simulations with cyclic loading $F_{\max}$, (b) resulting Wöhler curves for $G_c = 3, 6, 11, 22$ N/mm. The results show that qualitatively reasonable Wöhler curves can be obtained from the proposed algorithm, taken from Wingender and Balzani [150]. 61
4.19. (a) Force-displacement curve for simulation with cyclic loading and amplitude $F_{\max} = 780$ N and critical Griffith-type energy release rate $G_c = 6$ N/mm, and (b) zoomed-in illustration of the peak at the maximum of the implied force F, taken from Wingender and Balzani [150]. 61

5.1. Decomposition of (a) a binarized scan consisting of 48×48 pixel with two material phased (gray,green) and possible crack path (yellow) into (b) 6×6 finite cells simulated with FCM without transformation of the cells into elements, taken from Wingender and Balzani [149]. 64
5.2. (a) Cubic biphasic body $\mathcal{B}$ consisting of spherical inclusion (green) within matrix (gray), (b) structured mesh without regarding material interfaces and (c) one finite cell consisting of multiple subcells with different material properties as cutout of mesh, taken from Wingender and Balzani [149]. 64
5.3. One finite cell with its isoparametric coordinate system $\boldsymbol{\xi}$ and the coordinate system $\boldsymbol{s}$ of one of the eight subcells. 66
5.4. (a) Three-dimensional semi-regular FE mesh with hanging nodes (marked with red circles), (b) two-dimensional mesh with one hanging node. 67
5.5. (a) Crack (yellow) through biphasic microstructure (green, gray) with finite cell/element borders (black) and subcell borders (blue) before (b) crack propagates into the next finite cell so that (c) the subcells are transformed into single elements with new hanging nodes (red) assuming linear shape functions, taken from Wingender and Balzani [149]. 71
5.6. Algorithm of the proposed strategy for the simulation of crack propagation including eigenerosion and FCM, taken from [149]. 72
5.7. (a) Binarized voxel image consisting of metal matrix inclusion (green) within metal matrix (silver), (b) decomposed extracted part of it with simulated crack (gold) and (c) von Mises stress, taken from Wingender and Balzani [148]. . . 76
5.8. (a) Scanning setup consisting of the X-ray tube emitting X-rays through the specimen inside the chamber in (b). The experiments were performed in the laboratories of the Zentrum für Grenzflächendominierte Höchstleistungswerkstoffe, ZGH (Ruhr-Universität Bochum, Germany). 77
5.9. (a) Voxel data as gray-scale values obtained from a μCT-scan, which is cleaned and binarized (b) into the inclusion (green) and iron matrix phase (silver), and (c) the contour plot of the von Mises stress τ^{vM} under one dimensional tension in axial direction at the macroscopic strain $\bar{\varepsilon} = 0.02$. 77
5.10. (a) Unstructured, regular, quadrilateral mesh, (b) structured, regular, quadrilateral mesh with 8×8 elements and (c) semi-regular, quadrilateral mesh of a square. 79

5.11. (a) consistent and (b) inconsistent mesh containing two elements and (c) mesh containing five elements (example from Cerveny et al. [20]) with nodes (black) and hanging nodes (green). 80

5.12. Principle algorithm of the Octree/Quadtree decomposition (T) with a part of a circle shaped inclusion (gray) within a surrounding material (green) with firstly applied quadtree level 1 (a), secondly, quadtree level 2 (b), quadtree level 3 (c), quadtree level 4 (d) and final decomposition by unifying the sub areas of the subcells containing more than one material (e), taken from Fangye, Miska, and Balzani [36] 81

5.13. Principle algorithm of the Optimal Decomposition (OD) for one single finite cell containing 5 by 5 pixels; (a) a prototype subcell, (b) extension in first search direction, (c) an entire joined row, (d) and (e) iterations on the next row, (f) the result of the extension in the first direction, (g) merge operation in second direction and (h) final decomposition result. In (i) and (j) the decomposition result for a permutation of the search direction is shown, taken from Fangye, Miska, and Balzani [36]. 82

5.14. Illustration of the Optimized Clustering algorithm (OC), (a) randomly chosen start pixel, (b) and (c) two possible restricted growth modes, (d) fully grown subcell and (e) resulting subcell decomposition, taken from Fangye, Miska, and Balzani [36]. 83

5.15. Combinations of the Octree with the Optimal Decomposition; (a) base geometry, (b) Octree level 3, (c) the T-M , (d) the T-OD and (e) the T-OD-M algorithms Fangye, Miska, and Balzani [36]. 83

5.16. (a) Voxel set consisting of $2^2 = 4$ voxels per edge, that are decomposed with (b) T1, (c) T1-MT and (d)T2 according to Fangye, Miska, and Balzani [36]. 84

5.17. Decomposition of (a) a binarized scan with possible crack path (yellow) consisting of 48×48 pixel into 6×6 finite cells simulated considering (b) FCM without transformation of the cells into elements decomposed with OD, (c) with transformation decomposed with OD, (d) T3, (e) T3-M , (f) T3-OD-M, (g) T3-OD and (h) T3-OD with additional minimum split, taken from Wingender and Balzani [149]. 85

5.18. (a) Boundary conditions of the simulation setup of the benchmark experiment and (b) its morphology consisting of a spherical tungsten carbide inclusion surrounded by a brittle η-carbide layer and a ductile nickel matrix, which is a typical hard metal, taken from Wingender and Balzani [149]. 86

5.19. Different discretization types of the microstructure in figure 5.18: (a) discretization type 1, a regular tetrahedral FE mesh, (b) discretization type 2, a voxel set consisting of $56 \times 56 \times 56$ voxels which serves as basis for the other discretizations and FE mesh with hexahedral elements, (c) discretization type 3, a finite cells (black) and subcells (blue) assuming $7 \times 7 \times 7$ finite cells and the T2 min1-MT decomposition for the proposed algorithm and (d) discretization type 4, a semi-regular, hexahedral FE mesh generated by assuming each subcell of discretization type 3 to be a finite element. 87

5.20. Statistics of different decomposition schemes based on the voxel data of an artificial microstructure in the form of (a) number of subcells and possible hanging constraints and (b) the maximum aspect ratio of the elements' edge length and the maximum edge length of all subcells divided by the minimum edge length of all subcells assuming $7 \times 7 \times 7$ finite cells, taken from Wingender and Balzani [149]. The transparency indicates that the corresponding discretization contains inconsistencies if the discretization type 3 or 4 are applied. Because of that, these discretization cannot be used for the discretization types 3 or 4. For the numerical simulations, the discretization T2min1-MT is chosen. . . . 88

5.21. Statistics of different decomposition schemes based on the voxel data of an artificial microstructure in the form of (a) number of subcells and possible hanging constraints and (b) the maximum aspect ratio of the elements' edge length and the maximum edge length of all subcells divided by the minimum edge length of all subcells assuming $14 \times 14 \times 14$ finite cells. The transparency indicates that the corresponding discretization contains inconsistencies if the discretization type 3 or 4 are applied. For the numerical simulations, the discretization T1-MT is chosen. 89

5.22. Cross section through microstructure that is discretized by (a) OD, (b) T1min1, (c) T3-M and (d) T2min1-MT under the assumption of $7 \times 7 \times 7$ finite cells. 90

5.23. Crack path through artificial hard metal microstructures at a macroscopic strain of $\bar{\varepsilon}_{xx} = 0.5 \cdot 10^{-3}$ and $\bar{\varepsilon}_{xx} = 2.0 \cdot 10^{-3}$, taken from Wingender and Balzani [149]. 91

5.24. (a) Reaction force and (b) number of equations in the Newton iteration of the proposed approach over the macroscopic strain $\bar{\varepsilon}_{xx}$ of the voxel based microstructure, taken from Wingender and Balzani [149]. 92

5.25. Stress-strain curve for discretization type 3, 4 and 2 for tension test without crack propagation. 93

5.26. (a) Equivalent plastic strain α and (b) von Mises stress τ^{vM} over the specimen of the FCM simulation including the crack path (gold) at $\bar{\varepsilon}_{xx} = \bar{u}_{xx}/l_{xx} = 0.18\%$, taken from Wingender and Balzani [149]. Here, the boundaries (gray) indicate either the boundaries of the active finite cells or, if the corresponding finite cell is deactivated, the ones of the subcells transformed into finite elements. 93

6.1. (a) Exemplary microstructure consisting of inclusions (green) surrounded by matrix (gray) and (b) periodic microstructure consisting of periodic RVEs, that represent the original microstructure in (a). 95

6.2. Example shapes of inclusions formed by superellipsoids with the semi-axis radii $r_x = r_z = 1$ and $r_y = 2$ and different exponents p_x, p_y and p_z without any rotation 103

6.3. SSRVEs of Ferro-Titanit with $1, ..., 6$ ellipsoidal inclusions that are optimized regarding their statistical measures of the morphology, taken from Wingender and Balzani [151]. For the parameterizations, see Appendix B. 104

6.4. SSRVEs of Ferro-Titanit with $1, ..., 6$ superellipsoidal inclusions that are optimized regarding their statistical measures of the morphology. For the parameterizations, see Appendix B. 104

6.5. (a) Objective values $\mathcal{E}(\tilde{\gamma}_i)$ of the statistical measures of the morphology and (b) number of evaluated microstructures n_{micro} and computation time t_{comp} over the number of inclusions n_{incl}. 105

6.6. (a)Dirichlet boundary conditions for the tensile test for the evaluation of the convergence of the mechanical response in (b)-(d) with increasing size of the cutout from the μCT-scan, taken from Wingender and Balzani [151], and of (e) the error in the mechanical response $r_{e,j}$ of the SSRVEs compared to the cutout of 192^3 voxels over the number of inclusions n_{incl}. 106

6.7. Cylindrical asphalt concrete specimen as (a) biphasic material consisting of mineral aggregates (gray) and mastic (black) and as (b) triphasic material containing voids additionally. 107

6.8. (a) Bitumen as part of the (b) microscale morphology of the mastic which is one of the constituents of the (c) asphalt concrete on the mesoscale, taken from Schüler et al. [130]. 108

6.9. Work flow of the artificial asphalt concrete generation starting from (a) the Lubachevsky-Stillinger algorithm, continuing with (b) the Voronoi tesselation, (c) the statistical shrinking, (d) application of volume operations to obtain the bituminous binding agent and finally (e) meshing the volume element, taken from Wingender et al. [153]. 109

6.10. Visualization of the Lubachevsky-Stillinger algorithm with 8 spheres with the growth rate $g = 1$ (purple) and 10 spheres with the growth rate $g = 1.5$ (yellow) within a unit cube at different times (a)-(c) and the final state (d). 110

6.11. Two colliding spheres and their velocities directly before the collision (green) and directly after the collision (orange). 111

6.12. (a) Two-dimensional illustration of Voronoi tessellation with starting points (blue) and borders of their Voronoi cells (green) and (b) mineral aggregate cells generated by Voronoi tessellation which fully or partly intersect unit cube. 111

6.13. (a) Statistical shrinking of the vector $\boldsymbol{c}_{ik}$ corner point k of cell i at the location $\boldsymbol{d}_{ik}$ towards the center of mass $\boldsymbol{p}_i$ with the shrinking factor s_{ik} and (b) cutout of cells lying in or on the border of unit cube in order to obtain periodic microstructure. 112

6.14. (a) Binarized μCT-scan of triphasic asphalt concrete taken from Schüler et al. [130] which contains mineral aggregates (dark blue) surrounded by bituminous binging agent (bright blue) and voids and (b) artificially generated SVE with mineral aggregates (gray) surrounded by bituminous binging agent (rainbow colors) and voids. 113

6.15. (a) Metallic SVE containing grains, (b) containing an interface layer in-between and (c) distorted SVE representing rolled metal. 114

6.16. (a) Four different SVEs generated with the same parameters that represent the (b) mesoscale of the asphalt concrete PA8. 115

6.17. (a) Average sieve curve (dark blue) and its standard deviation (bright blue) of an ensemble consisting of 10 microstructures with prescribed borders (black) and (b) distribution of the volume fraction of the bituminous binding agent n_b of the 10 SVEs. 116

6.18. (a) Ratio of maximum distance of corner points within one particle d_{max} to the equivalent diameter d_{eq} and (b) distribution of the particle surfaces in the ensemble of the 10 artificial asphalt concrete structures. 116

6.19. Schematic illustration of the Maxwell-Zener model in which the viscous parts are represented as dash pots and the elastic parts as springs. 117

6.20. (a) Prescribed macroscopic strain $\bar{\varepsilon}_{12}$ over the time t and (b) resulting macroscopic shear stress $\bar{\sigma}_{12}$ of an ensemble of 10 SVEs over the time t. 118

6.21. Mechanical properties of the asphalt concrete PA8 under the assumption of small strain Maxwell viscoelasticity with 4 Maxwell chains for the bituminous binding agent and small strain elasticity for the mineral aggregates. 119

6.22. (a) SVE consisting of mineral aggregate (gray) and bituminous binding agent (green) deformed with a scaling factor of 100 at $t = 100\,\mathrm{s}$ of the relaxation test and (b) the von Mises τ^{vM} of another SVE in the almost relaxed state at $t = 100\,\mathrm{s}$. 119

7.1. (a) Experimental tensile test and (b) zoom into the holding device in which a cylindrical specimen is clamped. 122

7.2. (a) Cylindrical specimen, which is meshed with a tetrahedral mesh, for tensile test with boundary conditions and weakened area (yellow) and (b) the deformed state of the specimen at the strain $\bar{\varepsilon}_x = 0.01$ (deformation scaled with a factor of 20). Exemplarily, the resulting stress-strain curves of (c) the ductile nickel matrix material of the Ferro-Titanit NiBSi, (e) the slightly ductile nickel matrix of the Ferro-Titanit Nikro-128 and (d) the brittle titanium carbide under the assumption of the elasto-plastic material formulation are presented. 123

7.3. (a) Experimental setup of the three-point bending test with microscope and (b) analogous macroscopic simulation of it for the extraction of the stress tensors as boundary conditions for microscopic simulations. 124

7.4. Crack length a over number of load cycles N of (a) data from laboratory experiments and (b) simulated crack propagation at the side of a three-point bending test under cyclic loading with maximum load F_A, taken from Wingender et al. [154]. 126

7.5. (a) Ferro-Titanit microstructure which is given as $48 \times 48 \times 48$ voxels each the size $2 \times 2 \times 2\,\mu\mathrm{m}^3$ in (a); (c) its discretization with the discretization scheme T1min1-MT into $12 \times 12 \times 12$ finite cells. Voxels that represent the chromium carbide inclusions are marked with the color green whereas the martensite matrix is shown in silver. 127

7.6. Different scenarios of Dirichlet boundary conditions and initial cracks for the investigation of isotropy of the crack propagation through the Ferro-Titanit microstructure, taken from Wingender and Balzani [151] 127

7.7. Contour plot of the von Mises stress τ^{vM} over the Ferro-Titanit microstructure of scenario (a) “xy” and (b) “xz” at a macroscopic strain of $\bar{\varepsilon}_{xx} = \bar{u}/96\,\mu\mathrm{m} = 0.025$. 128

7.8. Final crack path with and without surrounding material through Ferro-Titanit microstructure in figure 7.5a for the six different scenarios in figure 7.6, taken from Wingender and Balzani [151]. 128

7.9. (a) Resultant macroscopic first Piola-Kirchhoff stress $\bar{P}_{ii} = \bar{Q}_i/l^2_{\mathrm{RVE}}$ at the Dirichlet boundary in direction $i = x,\ y,\ z$ of the prescribed load, taken from Wingender and Balzani [151], and (b) number of equations in the linearized system within each Newton-Raphson iteration versus the macroscopic strain $\bar{\varepsilon}$. . . . 129

7.10. Contour plot of the von Mises stress τ^{vM} over the SSRVE with six ellipsoidal inclusions in figure 6.3f of scenario (a) “xy” and (b) “xz” at a macroscopic strain of $\bar{\varepsilon}_{xx} = \bar{u}/96\,\mu\mathrm{m} = 0.025$. 130

7.11. Final crack path through the SSRVE with six ellipsoidal inclusions in figure 6.3f, which is discretized by $12\times12\times12$ finite cell with T1-min1-MT, for the different scenarios in figure 7.6, taken from Wingender and Balzani [151]. The SSRVE is constructed in section 6.1 based on the minimization of th error regarding morphological and mechanical properties compared to the Ferro-Titanit microstructure. 130

7.12. Resultant macroscopic first Piola-Kirchhoff stress $\bar{P}_{ii} = \bar{Q}_i/l^2_{\mathrm{RVE}}$ at the Dirichlet boundary in direction of the prescribed load versus the macroscopic strain $\bar{\varepsilon}$, taken from Wingender and Balzani [151]. 131

7.13. Different cold work tool steel morphologies, that result from different manufacturing processes: (a) spherical inclusions, (b) ellipsoidal inclusions, (c) spherical inclusions with different sizes, (d) ellipsoidal framework and (e) clustering of the framework in (d), taken from [17]. 132

7.14. Crack path through microstructures I-V from figure 7.13 under linearly increasing tension of the microstructure lateral to crack surface, taken from [17]. The blue arrow starts at the edge with the initial crack and points into the principal direction in which the crack propagates. 133

7.15. Contour plot of the von Mises stress τ^{vM} over the cold work tool steel microstructures of the simulations corresponding to the simulations of figure 7.14I-V.a at a prescribed macroscopic strain of $\bar{\varepsilon}_{xx} = 1\%$, taken from [17]. 134

7.16. Contour plot of the equivalent plastic strain α over the cold work tool steel microstructures of the simulations corresponding to the simulations of figure 7.14I-V.a at a prescribed macroscopic strain of $\bar{\varepsilon}_{xx} = 1\%$, taken from [17]. 134

7.17. Contour plot of the specific energy for fracture criterion $\psi^{\mathrm{e}}_{+} + \psi^{\mathrm{p}} + \int_t \mathcal{D}^{\mathrm{vis}}\,\mathrm{d}t$ over the cold work tool steel microstructures of the simulations corresponding to the simulations of figure 7.14I-V.a at a prescribed macroscopic strain of $\bar{\varepsilon}_{xx} = 1\%$, taken from [17]. 134

7.18. Microscopic image of crack through cold work tool steel that was produced with HIP (a) without being hot rolled (comparable to the simulations of microstructure I) (b) with hot rolling (comparable to the simulations of microstructure II), taken from Brackmann et al. [16]. 135

7.19. Resultant macroscopic first Piola-Kirchhoff stress $\bar{P}_{ii} = \bar{Q}_i / l^2_{\mathrm{RVE}}$ of a one-dimensional tension test with prescribed displacements $\bar{u}_i$ in i direction, in which i denotes one of the three directions x, y or z on the microstructure (a) I and (b) II, taken from [17]. 135

7.20. Resultant macroscopic first Piola-Kirchhoff stress $\bar{P}_{ii} = \bar{Q}_i / l^2_{\mathrm{RVE}}$ of a one-dimensional tension test with prescribed displacements $\bar{u}_i$ in i direction, in which i denotes one of the three directions x, y or z on the microstructure (a) III, (b) IV and (c) V, taken from [17]. 136

7.21. (a) Imposed macroscopic strain $\bar{\varepsilon}$ and (b) the resulting volume of the cracked elements divided by the volume of the finally cracked elements over time, taken from [17]. 137

B.1. Template of the target microstructure thresholded by $p^{\mathrm{thresh}}_{\mathrm{LP}} = 4\%$ consisting of $85 \times 48 \times 95$ voxels. 144

Bibliography

[1] A. Abedian, J. Parvizian, A. Düster, H. Khademyzadeh, and E. Rank. Performance of different integration schemes in facing discontinuities in the finite cell method. *International Journal of Computational Methods*, 10(03):1350002, 2013.

[2] H. AG. M-30 By-Pass Sur Túnel Norte, 2021. URL `https://www.herrenknecht.com/de/referenzen/referenzendetail/m-30-by-pass-sur-tunel-norte/`. [Online; accessed October 05, 2021].

[3] F. Aldakheel. *Mechanics of Nonlocal Dissipative Solids: Gradient Plasticity and Phase Field Modeling of Ductile Fracture.* PhD thesis, Institut für Mechanik, Universität Stuttgart, 2016.

[4] H. Amor, J.-J. Marigo, and C. Maurini. Regularized formulation of the variational brittle fracture with unilateral contact: Numerical experiments. *Journal of the Mechanics and Physics of Solids*, 57(8):1209–1229, 2009. doi: 10.1016/j.jmps.2009.04.011.

[5] A. Auger and N. Hansen. A restart CMA evolution strategy with increasing population size. *2005 IEEE congress on evolutionary computation*, 2:1769–1776, 2005.

[6] J. M. Ball. Convexity conditions and existence theorems in nonlinear elasticity. *Archive for Rational Mechanics and Analysis*, 63(4):337–403, 1976.

[7] D. Balzani, J. Schröder, and D. Brands. FE 2-simulation of microheterogeneous steels based on statistically similar RVEs. *IUTAM Symposium on Variational Concepts with Applications to the Mechanics of Materials*, pages 15–28, 2010.

[8] D. Balzani, L. Scheunemann, D. Brands, and J. Schröder. Construction of two-and three-dimensional statistically similar RVEs for coupled micro-macro simulations. *Computational Mechanics*, 54(5):1269–1284, 2014. doi: 10.1007/s00466-014-1057-6.

[9] G. I. Barenblatt. The mathematical theory of equilibrium cracks in brittle fracture. *Advances in Applied Mechanics*, 7:55–129, 1962. doi: 10.1016/S0065-2156(08)70121-2.

[10] K.-J. Bathe. *Finite-Elemente-Methoden.* Springer, 1986.

[11] K.-J. Bathe, E. Ramm, and E. L. Wilson. Finite element formulations for large deformation dynamic analysis. *International Journal for Numerical Methods in Engineering*, 9(2):353–386, 1975.

[12] C. Bathias and A. Pineau. *Fatigue of Materials and Structures: Fundamentals.* John Wiley & Sons, 2013.

[13] S. Beese, S. Löhnert, and P. Wriggers. 3D ductile crack propagation within a polycrystalline microstructure using XFEM. *Computational Mechanics*, 61(1):71–88, 2018. doi: 10.1007/s00466-017-1427-y.

[14] T. Belytschko and T. Black. Elastic crack growth in finite elements with minimal remeshing. *International Journal for Numerical Methods in Engineering*, 45(5):601–620, 1999.

[15] L. Brackmann, A. Röttger, S. Weber, and W. Theisen. Subcritical crack growth in hard alloys under cyclic loading. *Fatigue & Fracture of Engineering Materials & Structures*, 44(2):349–365, 2021. doi: 10.1111/ffe.13363.

[16] L. Brackmann, A. Röttger, H. G. Bui, S. Butt, G. Hoormazdi, A. R. L. Bal, S. Priebe, D. Wingender, H. Yang, D. Balzani, K. Hackl, G. Meschke, I. Mueller, and J. Renner. *Excavation Simulations and Cutting Tool Wear.* Springer, 2023.

[17] L. Brackmann, D. Wingender, S. Weber, D. Balzani, and A. Röttger. Influence of hard phase morphology on the fatigue crack propagation in tool steels - Numerical simulation and experimental validation. *Ruhr-Universität Bochum, Universitätsbibliothek*, pages 1–30, 2023. doi: 10.13154/294-9580.

[18] J. E. Bresenham. Algorithm for computer control of a digital plotter. *IBM Systems Journal*, 4(1):25–30, 1965.

[19] S. Butt, L. Brackmann, H. Yang, G. Hoormazdi, D. Wingender, S. Priebe, G. Meschke, A. Vogel, A. Röttger, J. Renner, D. Balzani, K. Hackl, and I. Müller. Soil excavation and tool wear. *Tunnel*, 2:36–39, 2021.

[20] J. Cerveny, V. Dobrev, and T. Kolev. Nonconforming mesh refinement for high-order finite elements. *SIAM Journal on Scientific Computing*, 41(4):C367–C392, 2019. doi: 10.1137/18M1193992.

[21] J. Cheng, X. Tu, and S. Ghosh. Wavelet-enriched adaptive hierarchical FE model for coupled crystal plasticity-phase field modeling of crack propagation in polycrystalline microstructures. *Computer Methods in Applied Mechanics and Engineering*, 361:112757, 2020. doi: 10.1016/j.cma.2019.112757.

[22] C. Chu and A. Needleman. Void nucleation effects in biaxially stretched sheets. *Journal of Engineering Materials and Technology*, 1980. doi: 10.1115/1.3224807.

[23] A. Conrads. *Maintenance of cutting tools in mechanised tunnelling - Develpment of a Process Simulation Model for the Scheduling and Evaluation of Maintenance Strategies.* PhD thesis, Ruhr-Universität Bochum, 2020.

[24] H. Czichos and K.-H. Habig. *Tribologie-Handbuch: Tribometrie, Tribomaterialien, Tribotechnik.* Springer-Verlag, 2010.

[25] G. Dal Maso. An Introduction into γ-Convergence. *Progress in Nonlinear Differential Equations and their Applications*, 1993. doi: 10.1007/978-1-4612-0327-8.

[26] L. Demkowicz, J. T. Oden, W. Rachowicz, and O. Hardy. Toward a universal hp adaptive finite element strategy, part 1. Constrained approximation and data structure. *Computer Methods in Applied Mechanics and Engineering*, 77(1-2):79–112, 1989. doi: 10.1016/0045-7825(89)90129-1.

[27] E. Dickinson and H. Witt. The dynamic shear modulus of paving asphalts as a function of frequency. *Transactions of the Society of Rheology*, 18(4):591–606, 1974. doi: 10.1122/1.549349.

[28] DIN-50100. Schwingfestigkeitsversuch–Durchführung und Auswertung von zyklischen Versuchen mit konstanter Lastamplitude für metallische Werkstoffproben und Bauteile, 2016, G. Beuth-Verlag Berlin, editor.

[29] A. Donev, S. Torquato, and F. H. Stillinger. Neighbor list collision-driven molecular dynamics simulation for nonspherical hard particles. I. Algorithmic details. *Journal of Computational Physics*, 202(2):737 – 764, 2005. ISSN 0021-9991. doi: 10.1016/j.jcp.2004.08.014.

[30] A. Donev, S. Torquato, and F. H. Stillinger. Neighbor list collision-driven molecular dynamics simulation for nonspherical hard particles.: II. applications to ellipses and ellipsoids. *Journal of Computational Physics*, 202(2):765–793, 2005. doi: 10.1016/j.jcp.2004.08.025.

[31] W. J. Drugan and J. R. Willis. A micromechanics-based nonlocal constitutive equation and estimates of representative volume element size for elastic composites. *Journal of the Mechanics and Physics of Solids*, 44(4):497–524, 1996. doi: 10.1016/0022-5096(96)00007-5.

[32] D. S. Dugdale. Yielding of steel sheets containing slits. *Journal of the Mechanics and Physics of Solids*, 8(2):100–104, 1960. doi: 10.1016/0022-5096(60)90013-2.

[33] A. Düster, J. Parvizian, Z. Yang, and E. Rank. The finite cell method for three-dimensional problems of solid mechanics. *Computer Methods in Applied Mechanics and Engineering*, 197(45-48):3768–3782, 2008. doi: 10.1016/j.cma.2008.02.036.

[34] A. Düster, E. Rank, and B. Szabó. The p-version of the finite element and finite cell methods. *Encyclopedia of Computational Mechanics*, pages 1–35, 2017. doi: 10.1002/9781119176817.ecm2003g.

[35] N. Espallargas, P. Jakobsen, L. Langmaack, and F. Macias. Influence of corrosion on the abrasion of cutter steels used in tbm tunnelling. *Rock Mechanics and Rock Engineering*, 48(1):261–275, 2015. doi: 10.1007/s00603-014-0552-6.

[36] Y. F. Fangye, N. Miska, and D. Balzani. Automated simulation of voxel-based microstructures based on enhanced finite cell approach. *Archive of Applied Mechanics*, pages 1–19, 2020. doi: 10.1007/s00419-020-01719-x.

[37] T. Fisher Scientific. *User's Guide Avizo Software 2019.* Konrad-Zuse-Zentrum für Informationstechnik Berlin (ZIB), 2019.

[38] C. Frenzel, H. Käsling, and K. Thuro. Factors influencing disc cutter wear. *Geomechanik und Tunnelbau: Geomechanik und Tunnelbau*, 1(1):55–60, 2008. doi: 10.1016/j.tust.2017.05.013.

[39] T.-P. Fries, A. Byfut, A. Alizada, K. W. Cheng, and A. Schröder. Hanging nodes and XFEM. *International Journal for Numerical Methods in Engineering*, 86(4-5):404–430, 2011. doi: 10.1002/nme.3024.

[40] M. Frigo and S. G. Johnson. The design and implementation of FFTW3. *Proceedings of the IEEE*, 93(2):216–231, 2005. doi: 10.1109/JPROC.2004.840301. Special issue on "Program Generation, Optimization, and Platform Adaptation".

[41] F. Fritzen and T. Böhlke. Periodic three-dimensional mesh generation for particle reinforced composites with application to metal matrix composites. *International Journal of Solids and Structures*, 48(5):706 – 718, 2011. ISSN 0020-7683. doi: 10.1016/j.ijsolstr.2010.11.010.

[42] F. Fritzen, T. Böhlke, and E. Schnack. Periodic three-dimensional mesh generation for crystalline aggregates based on Voronoi tessellations. *Computational Mechanics*, 43(5):701–713, 2009. doi: 10.1007/s00466-008-0339-2.

[43] B. für Verkehr und digitale Infrastruktur. Tunnel: Zahlen, Daten, Fakten, 2021. URL `https://www.bmvi.de/SharedDocs/DE/Artikel/StB/tunnel-zahlen-daten-fakten.html`. [Online; accessed October 05, 2021].

[44] C. Geuzaine and J.-F. Remacle. Gmsh: A 3-D finite element mesh generator with built-in pre-and post-processing facilities. *International Journal for Numerical Methods in Engineering*, 79(11):1309–1331, 2009.

[45] E. Ghossein and M. Lévesque. A fully automated numerical tool for a comprehensive validation of homogenization models and its application to spherical particles reinforced composites. *International Journal of Solids and Structures*, 49(11-12):1387–1398, 2012. doi: 10.1016/j.ijsolstr.2012.02.021.

[46] A. A. Griffith. The phenomena of rupture and flow in solids. *Philosophical Transactions of the Royal Society A: Mathematical, Physical and Engineering Sciences*, 221(582-593): 163–198, 1921. doi: 10.1098/rsta.1921.0006.

[47] D. Gross and T. Seelig. *Bruchmechanik*, volume 2. Springer, 1996. ISBN 10 3-540-37113-3.

[48] A. L. Gurson. Continuum theory of ductile rupture by void nucleation and growth: Part i—yield criteria and flow rules for porous ductile media. *Journal of Engineering Materials and Technology*, 1977. doi: doi.org/10.1115/1.3443401.

[49] V. Guski, W. Verestek, E. Oterkus, and S. Schmauder. Microstructural investigation of plasma sprayed ceramic coatings using peridynamics. *Journal of Mechanics*, 36(2): 183–196, 2020. doi: doi.org/10.1017/jmech.2019.58.

[50] Z. Hashin. Analysis of composite materials—a survey. *Journal of Applied Mechanics*, 50(481), 1983.

[51] R. Hill. Elastic properties of reinforced solids: some theoretical principles. *Journal of the Mechanics and Physics of Solids*, 11(5):357–372, 1963.

[52] A. Hillerborg, M. Modéer, and P.-E. Petersson. Analysis of crack formation and crack growth in concrete by means of fracture mechanics and finite elements. *Cement and Concrete Research*, 6(6):773–781, 1976. doi: 10.1016/0008-8846(76)90007-7.

[53] G. Hoormazdi. *Modeling of soil-tool abrasive wear processes in mechanized tunneling.* PhD thesis, Lehrstuhl für Materialtheorie, Ruhr-Univertität Bochum, 2021.

[54] G. Hoormazdi, J. Küpferle, A. Röttger, W. Theisen, and K. Hackl. A concept for the estimation of soil-tool abrasive wear using astm-g65 test data. *International Journal of Civil Engineering*, 17(1):103–111, 2019. doi: 10.1007/s40999-018-0333-9.

[55] G. Hoormazdi, J. Küpferle, A. Röttger, W. Theisen, and K. Hackl. A concept for the estimation of soil-tool abrasive wear using ASTM-G65 test data. *International Journal of Civil Engineering*, 17(1):103–111, 2019. doi: doi.org/10.1007/s40999-018-0333-9.

[56] S. M. Hsu, J. Zhang, and Z. Yin. The nature and origin of tribochemistry. *Tribology Letters*, 13(2):131–139, 2002. doi: 10.1023/A:1020112901674.

[57] G. Irwin. Analysis of stresses and strains near the end of a crack traversing a plate. *Journal of Applied Mechanics*, 24:361–364, 1957.

[58] P. Junker, S. Schwarz, J. Makowski, and K. Hackl. A relaxation-based approach to damage modeling. *Continuum Mechanics and Therodynamics*, 29(1):291–310, 2017. doi: 10.1007/s00161-016-0528-8.

[59] P. Junker, D. Schwarz, S. Jantos, and K. Hackl. A fast and robust numerical treatment of a gradient-enhanced model for brittle damage. *International Journal for Multiscale Computational Engineering*, 17, 2019. doi: 10.1615/IntJMultCompEng.2018027813.

[60] P. Junker, J. Riesselmann, and D. Balzani. Efficient and robust numerical treatment of a gradient-enhanced damage model at large deformations. *International Journal for Numerical Methods in Engineering*, 123(3):774–793, 2022. doi: 10.1002/nme.6876.

[61] W. A. Kalender. *Computertomographie: Grundlagen, Gerätetechnologie, Bildqualität, Anwendungen;[mit Mehrschicht-Spiral-CT]*. Publicis-MCD-Verlag, 2000.

[62] A. Khintchine. Korrelationstheorie der stationären stochastischen Prozesse. *Mathematische Annalen*, 109(1):604–615, 1934.

[63] S. Klinkel. *Theorie und Numerik eines Volumen-Schalen-Elementes bei finiten elastischen und plastischen Verzerrungen*. PhD thesis, Institut für Baustatik, Universität Karlsruhe, 2000.

[64] M. Köhler, U. Maidl, and L. Martak. Abrasiveness and tool wear in shield tunneling in soil. *Geomechanics and Tunnelling*, 10:36–53, 2011. doi: 10.1002/geot.201100002.

[65] E. Kröner. Allgemeine Kontinuumstheorie der Versetzungen und Eigenspannungen. *Archive for Rational Mechanics and Analysis*, 4(1):273, 1959.

[66] J. Küpferle. *Skalenübergreifende materialkundliche Betrachtung des Werkzeugverschleißes für den maschinellen Tunnelvortrieb beim Einsatz in nichtbindigen Böden*. PhD thesis, Ruhr-Universität Bochum, 2017.

[67] J. Küpferle, A. Röttger, and W. Theisen. Excavation tool concepts for TBMs–understanding the material-dependent response to abrasive wear. *Tunnelling and Underground Space Technology*, 68:22–31, 2017. doi: 10.1016/j.tust.2017.05.013.

[68] J. Küpferle, A. Röttger, and W. Theisen. Fatigue and surface spalling of cemented carbides under cyclic impact loading–evaluation of the mechanical properties with respect to microstructural processes. *Wear*, 390:33–40, 2017. doi: 10.1016/j.wear.2017.07.002.

[69] J. Küpferle, A. Röttger, W. Theisen, and M. Alber. Tribological analysis of the TBM tool wear in soil from the view of material science: Tribologische Analyse des Abbauwerkzeugverschleißes von Tunnelvortriebsmaschinen in Lockergestein aus werkstofftechnischer Sicht. *Geomechanics and Tunnelling*, 11(2):131–141, 2018. doi: 10.1002/geot.201700066.

[70] G. Lancioni and G. Royer-Carfagni. The variational approach to fracture mechanics. A practical application to the French Panthéon in Paris. *Journal of Elasticity*, 95(1-2): 1–30, 2009. doi: 10.1007/s10659-009-9189-1.

[71] C. Lautensack and T. Sych. 3D image analysis of open foams using random tessellations. *Image Analysis & Stereology*, 25(2):87–93, 2006. doi: 10.5566/ias.v25.p87-93.

[72] F. Lavergne, R. Brenner, and K. Sab. Effects of grain size distribution and stress heterogeneity on yield stress of polycrystals: A numerical approach. *Computational Materials Science*, 77:387–398, 2013. doi: 10.1016/j.commatsci.2013.04.061.

[73] F. Lavergne, R. Brenner, and K. Sab. Effects of grain size distribution and stress heterogeneity on yield stress of polycrystals: A numerical approach. *Computational Materials Science*, 77:387–398, 2013. doi: 10.1016/j.commatsci.2013.04.061.

[74] E. H. Lee. Elastic-plastic deformation at finite strains. *Journal of Applied Mechanics*, 36(1):1–6, 1969. doi: 10.1115/1.3564580.

[75] B. Li, A. Pandolfi, and M. Ortiz. Material point erosion simulation of dynamic fragmentation of metals. *Mechanics of Materials*, 80:288–297, 2015. doi: 10.1007/Fs10704-012-9788-x.

[76] Y. Liang and P. Sofronis. Micromechanics and numerical modelling of the hydrogen–particle–matrix interactions in nickel-base alloys. *Modelling and Simulation in Materials Science and Engineering*, 11(4):523, 2003. doi: 10.1088/0965-0393/11/4/308.

[77] B. Lu and S. Torquato. Lineal-path function for random heterogeneous materials. *Physical Review A*, 45(2):922, 1992.

[78] B. D. Lubachevsky and F. H. Stillinger. Geometric properties of random disk packings. *Journal of Statistical Physics*, 60(5):561–583, 1990. doi: 10.1007/BF01025983.

[79] B. D. Lubachevsky, F. H. Stillinger, and E. N. Pinson. Disks vs. spheres: Contrasting properties of random packings. *Journal of Statistical Physics*, 64(3):501–524, 1991. doi: 10.1007/BF01048304.

[80] E. Madenci and E. Oterkus. *Peridynamic Theory and its Applications.* Springer, 2014.

[81] B. Maidl, M. Thewes, and U. Maidl. *Handbook of Tunnel Engineering: Volume I: Structures and Methods.* Wilhelm Ernst & Sohn, Verlag für Architektur und technische Wissenschaften GmbH & Co. KG, 2013.

[82] B. Maidl, M. Thewes, and U. Maidl. *Handbook of Tunnel Engineering II: Basics and Additional Services for Design and Construction.* Wilhelm Ernst & Sohn, Verlag für Architektur und technische Wissenschaften GmbH & Co. KG, 2014.

[83] J. E. Marsden and T. J. Hughes. *Mathematical Foundations of Elasticity.* Courier Corporation, 1994.

[84] G. E. Mase. *Schaum's Outline of Continuum Mechanics.* McGraw-Hill New York, 1970.

[85] D. Meagher. Geometric modeling using octree encoding. *Computer Graphics and Image Processing*, 19(2):129–147, 1982.

[86] Q. Meng and Z. Wang. Prediction of interfacial strength and failure mechanisms in particle-reinforced metal-matrix composites based on a micromechanical model. *Engineering Fracture Mechanics*, 142:170–183, 2015. doi: 10.1016/j.engfracmech.2015.06.001.

[87] N. Metropolis and S. Ulam. The monte carlo method. *Journal of the American Statistical Association*, 44(247):335–341, 1949.

[88] C. Miehe and M. Lambrecht. Algorithms for computation of stresses and elasticity moduli in terms of Seth–hill's family of generalized strain tensors. *Communication in Numerical Methods in Engineering*, 17:337–353, 2001. doi: 10.1002/cnm.404.

[89] C. Miehe, E. Stein, and W. Wagner. Associative multiplicative elasto-plasticity: formulation and aspects of the numerical implementation including stability analysis. *Computers & Structures*, 52(5):969–978, 1994. doi: 10.1016/0045-7949(94)0081-7.

[90] C. Miehe, M. Hofacker, and F. Welschinger. A phase field model for rate-independent crack propagation: Robust algorithmic implementation based on operator splits. *Computer Methods in Applied Mechanics and Engineering*, 199:2765–2778, 2010. doi: 10.1016/j.cma.2010.04.011.

[91] C. Miehe, F. Welschinger, and M. Hofacker. Thermodynamically consistent phase-field models of fracture: Variational principles and multi-field FE implementations. *International Journal for Numerical Methods in Engineering*, 83:1273–1311, 2010. doi: 10.1002/nme.2861.

[92] C. Miehe, F. Aldakheel, and A. Raina. Phase field modeling of ductile fracture at finite strains: A variational gradient-extended plasticity-damage theory. *International Journal of Plasticity*, 84:1–32, 2016. doi: 10.1016/j.ijplas.2016.04.011.

[93] C. Miehe, F. Aldakheel, and S. Teichtmeister. Phase-field modeling of ductile fracture at finite strains: A robust variational-based numerical implementation of a gradient-extended theory by micromorphic regularization. *International Journal for Numerical Methods in Engineering*, 111(9):816–863, 2017. doi: 10.1002/nme.5484.

[94] A. Mielke and M. Ortiz. A class of minimum principles for characterizing the trajectories and the relaxation of dissipative systems. *ESAIM: Control, Optimisation and Calculus of Variations*, 14(3):494–516, 2008. doi: 10.1051/cocv:2007064.

[95] N. Miska and D. Balzani. Quantification of uncertain macroscopic material properties resulting from variations of microstructure morphology based on statistically similar volume elements: application to dual-phase steel microstructures. *Computational Mechanics*, 64(6):1621–1637, 2019. doi: 10.1007/s00466-019-01738-8.

[96] T. Müller-Gronbach, E. Novak, and K. Ritter. *Monte Carlo-Algorithmen*. Springer-Verlag, 2012.

[97] S. Nagaraja, M. Elhaddad, M. Ambati, S. Kollmannsberger, L. De Lorenzis, and E. Rank. Phase-field modeling of brittle fracture with multi-level hp-FEM and the finite cell method. *Computational Mechanics*, 63(6):1283–1300, 2019. doi: 10.1007/s00466-018-1649-7.

[98] P. Navas, C. Y. Rena, B. Li, and G. Ruiz. Modeling the dynamic fracture in concrete: an eigensoftening meshfree approach. *International Journal of Impact Engineering*, 113: 9–20, 2018. doi: 10.1016/j.ijimpeng.2017.11.004.

[99] S. Nayak, R. Ravinder, N. A. Krishnan, and S. Das. A peridynamics-based micromechanical modeling approach for random heterogeneous structural materials. *Materials*, 13(6):1298, 2020. doi: 0.3390/ma13061298.

[100] A. Needleman and V. Tvergaard. An analysis of ductile rupture in notched bars. *Journal of the Mechanics and Physics of Solids*, 32(6):461–490, 1984. doi: 10.1016/0022-5096(84)90031-0.

[101] N. M. Newmark. A method of computation for structural dynamics. *Journal of the Engineering Mechanics Division*, 85(3):67–94, 1959. doi: 10.1061/JMCEA3.0000098.

[102] T.-T. Nguyen, J. Yvonnet, Q.-Z. Zhu, M. Bornert, and C. Chateau. A phase-field method for computational modeling of interfacial damage interacting with crack propagation in realistic microstructures obtained by microtomography. *Computer Methods in Applied Mechanics and Engineering*, 312:567–595, 2016. doi: 10.1016/j.cma.2015.10.007.

[103] J. T. Oden, L. Demkowicz, W. Rachowicz, and T. Westermann. Toward a universal hp adaptive finite element strategy, part 2. A posteriori error estimation. *Computer Methods in Applied Mechanics and Engineering*, 77(1-2):113–180, 1989. doi: 0.1016/0045-7825(89)90130-8.

[104] E. T. Onat and W. Prager. The necking of a tension specimen in plane plastic flow. *Journal of Applied Physics*, 25(4):491–493, 1954. doi: 10.1063/1.1721667.

[105] E. Orowan. Theory of the fatigue of metals. *Proceedings of the Royal Society of London. Series A. Mathematical and Physical Sciences*, 171(944):79–106, 1939. doi: 10.1098/rspa.1939.0055.

[106] A. Pandolfi and M. Ortiz. An eigenerosion approach to brittle fracture. *International Journal for Numerical Methods in Engineering*, 92(8):694–714, 2012. doi: 10.1002/nme.4352.

[107] A. Pandolfi, B. Li, and M. Ortiz. Modeling failure of brittle materials with eigenerosion. *Computational Modelling of Concrete Structures*, 1:9–21, 2013. doi: 10.1007/s10704-012-9788-x.

[108] A. Pandolfi, K. Weinberg, and M. Ortiz. A comparative accuracy and convergence study of eigenerosion and phase-field models of fracture. *Computer Methods in Applied Mechanics and Engineering*, 386:114078, 2021. doi: 10.1016/j.cma.2021.114078.

[109] J. Parvizian, A. Düster, and E. Rank. Finite cell method - h- and p-extension for embedded domain problems in solid mechanics. *Computational Mechanics*, 41:121 – 133, 2007. doi: 10.1007/s00466-007-0173-y.

[110] P. Perzyna. Fundamental problems in viscoplasticity. *Advances in Applied Mechanics*, 9:243–377, 1966. doi: 10.1016/S0065-2156(08)70009-7.

[111] G. Povirk. Incorporation of microstructural information into models of two-phase materials. *Acta Metallurgica et Materialia*, 43(8):3199–3206, 1995. doi: 10.1016/0956-7151(94)00487-3.

[112] A. Qinami, A. Pandolfi, and M. Kaliske. Variational eigenerosion for rate dependent plasticity in concrete modelling at small strain. *International Journal for Numerical Methods in Engineering*, 2019. doi: 10.1002/nme.6271.

[113] W. Rachowicz, J. T. Oden, and L. Demkowicz. Toward a universal hp adaptive finite element strategy part 3. Design of hp meshes. *Computer Methods in Applied Mechanics and Engineering*, 77(1-2):181–212, 1989. doi: 10.1016/0045-7825(89)90131-X.

[114] M. Ranjbar, M. Mashayekhi, J. Parvizian, A. Düster, and E. Rank. Using the finite cell method to predict crack initiation in ductile materials. *Computational Materials Science*, 82:427–434, 2014. doi: 10.1016/j.commatsci.2013.10.012.

[115] A. Raoult. Non-polyconvexity of the stored energy function of a Saint Venant-Kirchhoff material. *Aplikace matematiky*, 31(6):417–419, 1986.

[116] R. Rivlin. Large elastic deformations of isotropic materials. I. Fundamental concepts. *Philosophical Transactions of the Royal Society of London. Series A, Mathematical and Physical Sciences*, 240(822):459–490, 1948. doi: 10.1098/rsta.1948.0002.

[117] A. Röttger, J. Küpferle, S. Brust, A. Mohr, and W. Theisen. Abrasion in tunneling and mining. *International Conference on Stone and Concrete Machining (ICSCM)*, 3: 246–261, 2015.

[118] M. Ruess, D. Schillinger, Y. Bazilevs, V. Varduhn, and E. Rank. Weakly enforced essential boundary conditions for nurbs-embedded and trimmed nurbs geometries on the basis of the finite cell method. *International Journal for Numerical Methods in Engineering*, 95(10):811–846, 2013. doi: 10.1002/nme.4522.

[119] C. Rycroft. Voro++: A three-dimensional voronoi cell library in c++. *Lawrence Berkeley National Laboratory*, 2009.

[120] M. Schäfer. Tunnelbau in Deutschland: Statistik (2019/2020), Analyse und Ausblick, 2020. URL `https://www.stuva.de/?id=statistik`. [Online; accessed October 05, 2021].

[121] J. Schellekens and R. De Borst. On the numerical integration of interface elements. *International Journal for Numerical Methods in Engineering*, 36(1):43–66, 1993. doi: 10.1002/nme.1620360104.

[122] O. Schenk and K. Gärtner. Solving unsymmetric sparse systems of linear equations with pardiso. *Future Generation Computer Systems*, 20(3):475–487, 2004.

[123] L. Scheunemann. *Scale-bridging of elasto-plastic microstructures using statistically similar representative volume elements.* PhD thesis, Universität Duisburg-Essen, 2017.

[124] L. Scheunemann, D. Balzani, D. Brands, and J. Schröder. Design of 3D statistically similar representative volume elements based on Minkowski functionals. *Mechanics of Materials*, 90:185–201, 2015. doi: 10.1016/j.mechmat.2015.03.005.

[125] L. Scheunemann, D. Balzani, D. Brands, and J. Schröder. Construction of statistically similar RVEs. In S. Conti and K. Hackl, editors, *Analysis and Computation of Microstructure in Finite Plasticity (Lecture notes in applied and computational mechanics 78).* Springer, 2015.

[126] D. Schillinger, M. Ruess, N. Zander, Y. Bazilevs, A. Düster, and E. Rank. Small and large deformation analysis with the p-and b-spline versions of the finite cell method. *Computational Mechanics*, 50(4):445–478, 2012. doi: 10.1007/s00466-012-0684-z.

[127] B. Schmidt, F. Fraternali, and M. Ortiz. Eigenfracture: An Eigendeformation Approach to Variational Fracture. *Multiscale Modeling & Simulation*, 7(3):1237–1266, 2009. doi: 10.1137/080712568.

[128] K. Schneider, B. Klusemann, and S. Bargmann. Automatic three-dimensional geometry and mesh generation of periodic representative volume elements for matrix-inclusion composites. *Advances in Engineering Software*, 99:177–188, 2016. doi: 10.1016/j.advengsoft.2016.06.001.

[129] J. Schröder, D. Balzani, and D. Brands. Approximation of random microstructures by periodic statistically similar representative volume elements based on lineal-path functions. *Archive of Applied Mechanics*, 81(7):975–997, 2011. doi: 10.1007/s00419-010-0462-3.

[130] T. Schüler, R. Jänicke, and H. Steeb. Nonlinear modeling and computational homogenization of asphalt concrete on the basis of XRCT scans. *Construction and Building Materials*, 109:96–108, 2016. doi: 10.1016/j.conbuildmat.2016.02.012.

[131] A. Shahba and S. Ghosh. Coupled phase field finite element model for crack propagation in elastic polycrystalline microstructures. *International Journal of Fracture*, 219(1):31–64, 2019. doi: 10.1007/s10704-019-00378-6.

[132] M. Shakoor, V. M. T. Navas, D. P. Muñoz, M. Bernacki, and P.-O. Bouchard. Computational methods for ductile fracture modeling at the microscale. *Archives of Computational Methods in Engineering*, 26(4):1153–1192, 2019. doi: 10.1007/s11831-018-9276-1.

[133] S. A. Silling, M. Epton, O. Weckner, J. Xu, and E. Askari. Peridynamic states and constitutive modeling. *Journal of Elasticity*, 88(2):151–184, 2007. doi: 10.1007/s10659-007-9125-1.

[134] J. C. Simo. Algorithms for static and dynamic multiplicative plasticity that preserve the classical return mapping schemes of the infinitesimal theory. *Computer Methods in Applied Mechanics and Engineering*, 99(1):61–112, 1992. doi: 10.1016/0045-7825(92)90170-O.

[135] J. C. Simo and T. J. Hughes. *Computational Inelasticity*, volume 7. Springer Science, 2006.

[136] J. C. Simo and C. Miehe. Associative coupled thermoplasticity at finite strains: Formulation, numerical analysis and implementation. *Computer Methods in Applied Mechanics and Engineering*, 98(1):41–104, 1992. doi: 10.1016/0045-7825(92)0170-O.

[137] J. C. Simo, R. L. Taylor, and K. S. Pister. Variational and projection methods for the volume constraint in finite deformation elasto-plasticity. *Computer Methods in Applied Mechanics and Engineering*, 51:177 – 208, 1985. doi: 10.1016/0045-7825(85)90033-7.

[138] J. Storm, D. Supriatna, and M. Kaliske. The concept of representative crack elements for phase-field fracture: Anisotropic elasticity and thermo-elasticity. *International Journal for Numerical Methods in Engineering*, 121(5):779–805, 2020. doi: 10.1002/nme.6244.

[139] N. Sukumar, D. Srolovitz, T. Baker, and J.-H. Prevost. Brittle fracture in polycrystalline microstructures with the extended finite element method. *International Journal for Numerical Methods in Engineering*, 56(14):2015–2037, 2003. doi: 10.1002/nme.653.

[140] L. Susmel and P. Lazzarin. A bi-parametric Wöhler curve for high cycle multiaxial fatigue assessment. *Fatigue & Fracture of Engineering Materials & Structures*, 25(1):63–78, 2002. doi: 10.1046/j.1460-2695.2002.00462.x.

[141] R. Taylor and O. C. Zienkiewicz. *The Finite Element Method.* McGraw-Hill, 1989.

[142] R. L. Taylor. FEAP - Finite Element Analysis Program, 2014. URL `http://www.ce.berkeley/feap`.

[143] S. Torquato. *Random Heterogeneous Materials. Microstructure and Macroscopic Properties.* Springer, 2002. doi: 10.1007/s00466-014-1057-6.

[144] E. Voce. A practical strain hardening function. *Metallurgia*, 51:219–226, 1955.

[145] S. Walter. A history of fatigue. *Engineering Fracture Mechanics*, 54(2):263–300, 1996. doi: 10.1016/0013-7944(95)00178-6.

[146] E. Wiechert. Gesetze der elastischen Nachwirkung für constante Temperatur. *Annalen der Physik*, 286(11):546–570, 1893. doi: 10.1002/andp.18932861110.

[147] N. Wiener. Generalized harmonic analysis. *Acta Mathematica*, 55(1):117–258, 1930. doi: 10.1007\%2FBF02546511.

[148] D. Wingender and D. Balzani. Simulation of subcritical crack propagation in hard metal microstructures. *Proceedings in Applied Mathematics and Mechanics*, 19(1):e201900233, 2019. doi: 10.1002/pamm.201900233.

[149] D. Wingender and D. Balzani. Simulation of crack propagation through voxel-based, heterogeneous structures based on eigenerosion and finite cells. *Computational Mechanics*, 70:385–406, 2022. doi: 10.1007/s00466-022-02172-z.

[150] D. Wingender and D. Balzani. Simulation of crack propagation based on eigenerosion in brittle and ductile materials subject to finite strains. *Archive of Applied Mechanics*, 92:1199–1221, 2022. doi: 10.1007/s00419-021-02101-1.

[151] D. Wingender and D. Balzani. Application of statistically similar representative volume elements of metal matrix composites for the efficient simulation of crack propagation on the microscale. *Proceedings in Applied Mathematics and Mechanics*, accepted.

[152] D. Wingender, T. Schüler, and R. Jänicke. Computational generation of statistical volume elements of biphasic asphalt concrete and its material behavior. *Proceedings in Applied Mechanics and Mathematics*, 17(1):485–486, 2017. doi: 0.1002/pamm.201710212.

[153] D. Wingender, F. Fritzen, and R. Jänicke. Reduced order modeling of viscoelastic properties of asphalt concrete. *Proceedings in Applied Mathematics and Mechanics*, 18 (1):e201800240, 2018. doi: 10.1002/pamm.201800240.

[154] D. Wingender, L. Brackmann, A. Röttger, and D. Balzani. Simulation of ductile crack propagation in metal matrix composites – Comparison with cyclic experiments. *Proceedings in Applied Mathematics and Mechanics*, 21(1):e202100113, 2021. doi: 10.1002/pamm.202100113.

[155] P. Wriggers and S. Moftah. Mesoscale models for concrete: Homogenisation and damage behaviour. *Finite Elements in Analysis and Design*, 42(7):623–636, 2006. doi: 10.1016/j.finel.2005.11.008.

[156] J. Wulf, T. Steinkopff, and H. Fischmeister. Fe-simulation of crack paths in the real microstructure of an Al (6061)/SiC composite. *Acta Materialia*, 44(5):1765–1779, 1996. doi: 10.1016/1359-6454(95)00328-2.

[157] A. Wöhler. Über die Festigkeitsversuche mit Eisen und Stahl. *Zeitschrift für Bauwesen*, pages 73–106, 1870. doi: 10.1002/nme.6271.

[158] X.-P. Xu and A. Needleman. Numerical simulations of fast crack growth in brittle solids. *Journal of the Mechanics and Physics of Solids*, 42(9):1397–1434, 1994. doi: 10.1016/0022-5096(94)90003-5.

[159] Z. Yang, M. Ruess, S. Kollmannsberger, A. Düster, and E. Rank. An efficient integration technique for the voxel-based finite cell method. *International Journal for Numerical Methods in Engineering*, 91(5):457–471, 2012. doi: 10.1002/nme.4269.

[160] X. Yin, W. Chen, A. To, C. McVeigh, and W. K. Liu. Statistical volume element method for predicting microstructure–constitutive property relations. *Computer Methods in Applied Mechanics and Engineering*, 197(43-44):3516–3529, 2008. doi: 10.1016/j.cma.2008.01.008.

[161] N. Zaafarani, D. Raabe, R. N. Singh, F. Roters, and S. Zaefferer. Three-dimensional investigation of the texture and microstructure below a nanoindent in a cu single crystal using 3d ebsd and crystal plasticity finite element simulations. *Acta Materialia*, 54(7): 1863–1876, 2006. doi: 10.1016/j.actamat.2005.12.014.

[162] S. Zaefferer, S. Wright, and D. Raabe. Three-dimensional orientation microscopy in a focused ion beam–scanning electron microscope: A new dimension of microstructure characterization. *Metallurgical and Materials Transactions A*, 39(2):374–389, 2008. doi: 10.1007/s11661-007-9418-9.

[163] J. Zeman. *Analysis of composite materials with random microstructure.* PhD thesis, University of Prague, 2003.

[164] X. Zhang, S. W. Sloan, C. Vignes, and D. Sheng. A modification of the phase-field model for mixed mode crack propagation in rock-like materials. *Computer Methods in Applied Mechanics and Engineering*, 322:123–136, 2017. doi: 10.1016/j.cma.2017.04.028.

[165] O. C. Zienkiewicz, R. L. Taylor, and J. Z. Zhu. *The Finite Element Method: Its Basis and Fundamentals.* Elsevier, 1967.

Curriculum Vitae

Personal Data

Name:	Dennis Wingender
Born:	April 24th, 1991 in Essen

Professional Career

05/2016-12/2022	Research associate at the Chair of Continuum Mechanics at Ruhr-University Bochum
08/2015-04/2016 02/2014-12/2014 10/2012-09/2013	Teaching assistant at the Institute of Mechanics at Ruhr-University Bochum
10/2013-01/2014	Internship at ThyssenKrupp Rothe Erde, Dortmund

Education

04/2014-04/2016	Master of Science in Mechanical Engineering at Ruhr-University Bochum with specialization in Applied Mechanics
01/2015-06/2015	Semester abroad at Texas A&M University, TX, USA
10/2010-03/2014	Bachelor of Science in Mechanical Engineering at Ruhr-University Bochum with specialization in Applied Mechanics
09/2001-06/2010	Abitur at Helmhotz Gymnasium Essen
09/1997-07/2001	Käthe-Kollwitz Grundschule

Scholarship

01/2015-06/2015	Scholarship for semester abroad by DAAD
06/2013	ThyssenKrupp Student Award 2013, ThyssenKrupp AG
10/2011-09/2012	Deutschlandstipendium

List of Publications

- L. Brackmann, D. Wingender, S. Weber, D. Balzani, and A. Röttger. Influence of hard phase morphology on the fatigue crack propagation in tool steels - Numerical simulation and experimental validation. *Ruhr-Universität Bochum, Universitätsbibliothek*, pages 1–30, 2023. doi: 10.13154/294-9580
- L. Brackmann, A. Röttger, H. G. Bui, S. Butt, G. Hoormazdi, A. R. L. Bal, S. Priebe, D. Wingender, H. Yang, D. Balzani, K. Hackl, G. Meschke, I. Mueller, and J. Renner. *Excavation Simulations and Cutting Tool Wear.* Springer, 2023
- D. Wingender and D. Balzani. Application of statistically similar representative volume elements of metal matrix composites for the efficient simulation of crack propagation on the microscale. *Proceedings in Applied Mathematics and Mechanics*, accepted
- D. Wingender and D. Balzani. Simulation of crack propagation through voxel-based, heterogeneous structures based on eigenerosion and finite cells. *Computational Mechanics*, 70:385–406, 2022. doi: 10.1007/s00466-022-02172-z
- D. Wingender and D. Balzani. Simulation of crack propagation based on eigenerosion in brittle and ductile materials subject to finite strains. *Archive of Applied Mechanics*, 92:1199–1221, 2022. doi: 10.1007/s00419-021-02101-1
- S. Butt, L. Brackmann, H. Yang, G. Hoormazdi, D. Wingender, S. Priebe, G. Meschke, A. Vogel, A. Röttger, J. Renner, D. Balzani, K. Hackl, and I. Müller. Soil excavation and tool wear. *Tunnel*, 2:36–39, 2021
- D. Wingender, L. Brackmann, A. Röttger, and D. Balzani. Simulation of ductile crack propagation in metal matrix composites – Comparison with cyclic experiments. *Proceedings in Applied Mathematics and Mechanics*, 21(1):e202100113, 2021. doi: 10.1002/pamm.202100113
- D. Wingender and D. Balzani. Simulation of subcritical crack propagation in hard metal microstructures. *Proceedings in Applied Mathematics and Mechanics*, 19(1):e201900233, 2019. doi: 10.1002/pamm.201900233
- D. Wingender, F. Fritzen, and R. Jänicke. Reduced order modeling of viscoelastic properties of asphalt concrete. *Proceedings in Applied Mathematics and Mechanics*, 18 (1):e201800240, 2018. doi: 10.1002/pamm.201800240
- D. Wingender, T. Schüler, and R. Jänicke. Computational generation of statistical volume elements of biphasic asphalt concrete and its material behavior. *Proceedings in Applied Mechanics and Mathematics*, 17(1):485–486, 2017. doi: 0.1002/pamm.201710212

Mitteilungen aus dem Institut für Mechanik
RUHR-UNIVERSITÄT BOCHUM
Nr. 190

ISBN 978-3-935892-68-1